TECHNISCHE UNIVERSITÄT MÜNCHEN

TUM School of Engineering and Design

Biomechanical assessment of abdominal aortic aneurysm rupture risk and growth using clinical data: a probabilistic approach

Lukas Bruder

Vollständiger Abdruck der von der TUM School of Engineering and Design der Technischen Universität München zur Erlangung des akademischen Grades eines

Doktors der Ingenieurwissenschaften (Dr.-Ing.)

genehmigten Dissertation.

Vorsitz: apl. Prof. Dr.–Ing. habil. Christian Stemmer

Prüfer*innen der Dissertation:

1. Prof. Dr.-Ing. Michael W. Gee
2. Prof. Phaedon-Stelios Koutsourelakis, Ph.D.

Die Dissertation wurde am 25.01.2022 bei der Technischen Universität München eingereicht und durch die TUM School of Engineering and Design am 16.06.2022 angenommen.

Abstract

Pathological enlargements of the descending aorta, more commonly known as abdominal aortic aneurysms (AAAs), belong to the class of vascular diseases and are associated with typical risk factors such as age, tobacco use and what could be referred to as an unhealthy lifestyle. Although the clinical treatment of AAAs by either open or endovascular repair is an established procedure, the decision making for cases at the threshold of the maximum diameter criterion (55 mm for men, 50 mm for women) can be ambiguous, calling for additional, patient-specific rupture risk indicators. In particular, a better and predictive assessment of AAA growth is desirable, such that individual surveillance strategies can be applied and growth-related risks determined. With the growing amount of diagnostics data and an expanding digital infrastructure, these represent logical steps in the context of personalized medicine. At the same time, advances in the biomechanical modeling of the cardiovascular system and a growing availability of computational resources have encouraged detailed simulation models in order to predict in-vivo quantities of interest or the future progression of a disease.

Motivated by these developments and to address the aforementioned challenges in the clinical management of AAAs, biomechanical approaches to the rupture risk assessment have emerged as promising supplements to the clinically established maximum diameter criterion. This thesis builds upon these developments and proposes a comprehensive biomechanical rupture risk assessment framework, which makes use of personalized computational models and where special attention is paid to the probabilistic treatment of relevant, unknown model parameters using clinically accessible data. It is being argued that to take these uncertainties into account is crucial in clinical applications, when based on the model's predictions an educated decision needs to be made. In particular, it is shown that uncertainties can represent important statistical information that contribute to model understanding and more reliable results.

Many other computational biomechanics applications limit themselves to deterministic methods. This is mainly due to the additional computational effort associated with stochastic analyses, which further complicates a possible clinical use of such solutions. A major contribution of this work lies in the development of efficient uncertainty quantification (UQ) strategies for the biomechanical assessment of AAAs. Different approaches to the forward and inverse propagation of uncertainties are discussed, adjusted for the purposes of this thesis and demonstrated in several numerical examples involving retrospective AAA cases. Applications focus on a) the probabilistic, patient-specific description of invasive vessel wall quantities, b) the biomechanical rupture risk assessment at the time of data collection in the clinic based on these quantities, c) the Bayesian calibration of growth parameters based on two consecutive CTA scans, as well as d) the propagation of these parameters for a predictive rupture risk evaluation at future points in time.

Zusammenfassung

Pathologische Erweiterungen der absteigenden Aorta, besser bekannt als abdominale Aortenaneurysmen (AAAs), gehören zu den Gefäßkrankheiten und werden mit typischen Risikofaktoren wie Alter, Tabakkonsum und einem allgemein ungesunden Lebensstil in Verbindung gebracht. Obwohl die klinische Behandlung von AAAs durch offene oder endovaskuläre Therapie ein etabliertes Verfahren ist, kann die Entscheidungsfindung für Fälle im Randbereich des maximalen Durchmesserkriteriums (55 mm für Männer, 50 mm für Frauen) nicht eindeutig sein, sodass zusätzliche, patientenspezifische Indikatoren für die Beurteilung erforderlich sind. Insbesondere wäre eine bessere und prädiktive Bewertung des AAA-Wachstums wünschenswert, sodass individuelle Überwachungsstrategien angewandt und wachstumsbedingte Risiken bestimmt werden können. Mit der steigenden Menge an diagnostischen Daten und einer wachsenden digitalen Infrastruktur sind dies konsequente Schritte in Richtung personalisierte Medizin. Gleichzeitig haben Fortschritte in der biomechanischen Modellbildung des kardiovaskulären Systems und eine größere Verfügbarkeit von Computerressourcen detaillierte Simulationsmodelle ermöglicht, um in-vivo Zustände oder den zukünftigen Verlauf einer Krankheit vorherzusagen.

Motiviert durch diese Entwicklungen und zur Bewältigung der oben genannten Herausforderungen bei der klinischen Behandlung von AAAs haben sich biomechanische Ansätze zur Bewertung des Rupturrisikos als vielversprechende Ergänzung zum klinisch etablierten maximalen Durchmesserkriterium erwiesen. Die vorliegende Arbeit baut auf diesen Entwicklungen auf und stellt eine umfassende Vorgehensweise für die biomechanische Bewertung des Rupturrisikos vor, welche personalisierte Berechnungsmodelle verwendet und bei der besonderes Augenmerk auf die probabilistische Behandlung relevanter, unbekannter Modellparameter unter Verwendung klinisch zugänglicher Daten gelegt wird. Die Berücksichtigung dieser Unsicherheiten in klinischen Anwendungen wird als entscheidend eingestuft, da auf der Grundlage der Modellvorhersagen eine fundierte Entscheidung getroffen werden muss. Es wird gezeigt, dass Unsicherheiten wichtige statistische Informationen enthalten können, die zum Verständnis des Modells und zu zuverlässigeren Ergebnissen beitragen.

Verwandte Anwendungen aus der numerischen Biomechanik beschränken sich oftmals auf deterministische Methoden. Dies ist vor allem auf den zusätzlichen Rechenaufwand zurückzuführen, der mit stochastischen Analysen verbunden ist, was eine mögliche klinische Anwendung solcher Lösungen zusätzlich erschwert. Ein wesentlicher Beitrag dieser Arbeit liegt in der Entwicklung effizienter Methoden zur Quantifizierung von Unsicherheiten für die biomechanische Beurteilung von AAAs. Dazu werden verschiedene Ansätze zur Berechnung des Einflusses von Unsicherheiten diskutiert, für diese Arbeit angepasst und in mehreren numerischen Beispielen mit retrospektiven AAA-Fällen untersucht. Die Anwendungen konzentrieren sich auf a) die probabilistische, patientenspezifische Beschreibung invasiver Größen der Gefäßwand, b) die Rupturrisikoabschätzung zum Zeitpunkt der Datenerhebung in der Klinik, c) die Bayes'sche Kalibrierung von Wachstumsparametern basierend auf zwei aufeinanderfolgenden CTA-Scans, sowie d) die Vorwärtsausbreitung dieser Parameter für eine prädiktive Rupturrisikoabschätzung.

Contents

List of Figures

List of Tables

Acronyms

AA	aortic aneurysm
AAA	abdominal aortic aneurysm
ALM	active learning-MacKay
AMG	algebraic multigrid
ANOVA	analysis of variance
ASM	active subspace method
BC	boundary condition
BVP	boundary value problem
CDF	cumulative distribution function
CI	confidence interval
CT	computed tomography
CTA	computed tomography angiography
CV	coefficient of variation
DL	deep learning
ECM	extracellular matrix
ELBO	evidence lower bound
EM	expectation–maximization
EVAR	endovascular aneurysm repair
FD	finite differences
FE	finite element
FEM	finite element method
FSI	fluid-structure interaction
GMRES	generalized minimal residual method
GP	Gaussian process
hsCRP	high-sensitivity C-reactive protein
i.i.d.	independent and identically distributed
ILT	intraluminal thrombus
KDE	kernel density estimation

KL   Kullback-Leibler

L-BFGS   Limited-memory BFGS
LOOCV   leave-one-out-cross-validation

MALA   Metropolis-adjusted Langevin algorithm
MAP   maximum a posteriori probability
MC   Monte Carlo
MCH   mean corpuscular hemoglobin
MCHC   mean corpuscular hemoglobin concentration
MCMC   Markov chain Monte Carlo
MCV   mean corpuscular volume
MFMC   multi-fidelity Monte Carlo
ML   machine learning
MLMC   multi-level Monte Carlo
MRA   magnetic resonance angiography
MULF   modified updated Lagrangian formulation

NLS   nonlinear least squares

OED   optimal experimental design
OSR   open surgical repair

PAD   peripheral artery disease
PCA   principal component analysis
PDE   partial differential equation
PDF   probability density function
POD   proper orthogonal decomposition
PPE   patient predictive entropy
PRRI   probabilistic rupture risk index
PSMSE   patient standardized mean square error
PTC   pseudo-transient continuation

QoI   quantity of interest

rAAA   ruptured AAA
RB   reduced basis
ROC   receiver operating characteristic
RPI   rupture potential index

SA   sensitivity analysis
SG   stent graft
SGD   stochastic gradient descent
SMC   sequential Monte Carlo
SVD   singular value decomposition

SVI   stochastic variational inference

TAA   thoracic aortic aneurysm
TAAA   thoracoabdominal aortic aneurysm
TV   total variation

UQ   uncertainty quantification

VI   variational inference

Nomenclature

Continuum mechanics

$\mathcal{B}$	continuous body
Ω_0	continuum in its reference configuration
Ω	continuum in its current configuration
$\partial\Omega_0$	boundary of a continuum in its reference configuration
$\partial\Omega$	boundary of a continuum in its current configuration
Γ_u	Dirichlet boundary in reference configuration
γ_u	Dirichlet boundary in current configuration
Γ_σ	Neumann boundary in reference configuration
γ_σ	Neumann boundary in current configuration
$\underline{X}$	reference coordinates
$\underline{x}$	current coordinates
$\underline{\phi}$	deformation map from the reference to the current coordinates
$\underline{u}$	displacement field
$\underline{\underline{F}}$	deformation gradient
J	determinant of the deformation gradient
$\underline{N}$	reference surface normal
$\underline{n}$	current surface normal
$\underline{\underline{C}}$	right Cauchy-Green deformation tensor
$\underline{\underline{E}}$	Green-Lagrange strain tensor
$\underline{T}$	reference surface traction
$\underline{t}$	current surface traction
$\underline{\underline{\sigma}}$	Cauchy stress tensor
$\underline{\underline{P}}$	1st Piola-Kirchhoff stress tensor
$\underline{\underline{S}}$	2nd Piola-Kirchhoff stress tensor
Ψ	strain energy density function
I_1, I_2, I_3	1st, 2nd and 3rd invariant of the Green-Lagrange deformation tensor

Operators

$\underline{\boldsymbol{\nabla}}_X \otimes (\bullet)$	gradient of $(\bullet)$ with respect to the reference coordinates
$\underline{\boldsymbol{\nabla}}_X \cdot (\bullet)$	divergence of $(\bullet)$ with respect to the reference coordinates
$\underline{\boldsymbol{\nabla}}_x \otimes (\bullet)$	gradient of $(\bullet)$ with respect to the current coordinates
$\underline{\boldsymbol{\nabla}}_x \cdot (\bullet)$	divergence of $(\bullet)$ with respect to the current coordinates

Biomechanical model

$(\bullet)_{\mathrm{w}}$	quantity $(\bullet)$ in the arterial wall
$(\bullet)_{\mathrm{ILT}}$	quantity $(\bullet)$ in the intraluminal thrombus
p	blood pressure value
k_s	spring stiffness parameter
ϑ	growth field
c_ϑ	growth rate

Variational and Lagrangian formulation

$\delta\underline{\boldsymbol{u}}$	virtual displacement field
$\mathcal{R}$	weak form residual
$\underline{\boldsymbol{\lambda}}$	Lagrange multiplier field
$\mathcal{L}$	Lagrangian objective function

Finite element discretization

$(\bullet)^{(e)}$	quantity $(\bullet)$ of element e
n_{el}	number of elements
n_{nd}	number of nodes per element
n_{dof}	number of degrees of freedom
n_p	number of Gauss points
$\bar{\mathbf{X}}$	nodal coordinates
$\boldsymbol{N}$	shape function matrix
$\mathbf{d}$	local displacements
$\mathbf{D}$	global displacements
$\delta\mathbf{d}$	local virtual displacements
$\delta\mathbf{D}$	global virtual displacements
$\boldsymbol{J}$	Jacobi matrix
$\boldsymbol{B}$	B-operator matrix
$\boldsymbol{S}$	2nd Piola-Kirchhoff stress matrix
$\mathbf{r}$	local residual vector
$\mathbf{R}$	global residual vector
$\mathbf{k}$	local stiffness matrix
$\mathbf{K}$	global stiffness matrix
c_ϑ	local growth rate parameter
$\mathbf{c}_\vartheta$	global growth rate vector
A	assembly operator
L	discretized Lagrangian objective function
$\boldsymbol{\Lambda}$	global vector of Lagrange multipliers

Parameter-to-QoI map

$\boldsymbol{\theta}$	model parameters
Q	quantity of interest
$Q(\boldsymbol{\theta})$	parameter to quantity of interest map: $Q : \boldsymbol{\theta} \mapsto Q(\boldsymbol{\theta})$
$\nabla_{\boldsymbol{\theta}}(\bullet)$	gradient of the scalar quantity ($\bullet$) with respect to the model parameters
n_θ	number of model parameters
n_Q	number of quantities of interest

Probability theory

$(\Omega, \mathcal{A}, \mathbb{P})$	complete probability space
Ω	sample space
$\mathcal{A}$	σ-algebra associated with Ω
$\mathbb{P}$	probability measure
ω	element $\omega \in \Omega$
X	random variable $X : \omega \mapsto X(\omega)$
$\mathcal{X}$	range of $X : \Omega \to \mathcal{X}$
x	element $x \in \mathcal{X}$
$\mathcal{B}_\mathcal{X}$	Borel-σ-algebra induced by X
A	element of $\mathcal{B}_\mathcal{X}$ (also called event)
$\mathbb{P}_\mathcal{X}$	probability measure induced by X
$\mathbb{P}_\mathcal{X}(A)$	probability assigned to A by $\mathbb{P}_\mathcal{X}$
$\pi_\mathcal{X}$	probability density function associated with $\mathbb{P}_\mathcal{X}$
$\pi_\mathcal{X}(x)$	probability density assigned to x by $\pi_\mathcal{X}$
$\mathbb{E}_{\mathbb{P}_\mathcal{X}}[X]$	expected value of X under $\mathbb{P}_\mathcal{X}$
$\mathbb{V}_{\mathbb{P}_\mathcal{X}}[X]$	variance of X under $\mathbb{P}_\mathcal{X}$
$\text{Cov}_{\mathbb{P}_{\mathcal{X}_1, \mathcal{X}_2}}[X_1, X_2]$	covariance of two random variables X_1 and X_2 under $\mathbb{P}_{\mathcal{X}_1, \mathcal{X}_2}$
$\mathbb{P}_\mathcal{X}(A_2|A_1)$	conditional probability of $A_2 \in \mathcal{B}_\mathcal{X}$ given $A_1 \in \mathcal{B}_\mathcal{X}$
X_τ	random process $X_\tau : (\tau, \omega) \mapsto X_\tau(\omega)$

1. Introduction

1.1. Motivation

Abdominal aortic aneurysm

An abdominal aortic aneurysm (AAA) is a slowly progressing vascular disease in the descending aorta, which causes a regional weakening of the aortic wall and a corresponding dilatation. It is considered pathological if the aortic diameter exceeds 30 mm, which is twice the standard deviation above the male and female mean normal aortic diameter of 20 mm [148]. In the literature, maximum diameter sizes of up to 180 mm can be found [96]. Together with the less common thoracic aortic aneurysm (TAA) and thoracoabdominal aortic aneurysm (TAAA), the AAA belongs to the class of aortic aneurysms (AAs).

AAA prevalence has been reported within a range of 1.2% to 3.3% in men aged over 60 years in western societies, representing a slight decrease from numbers between 3.9% to 7.2% that have been published in the 1990s [55, 138]. In addition to age and male sex, the most important risk factors for the development of an AAA are smoking and familial predisposition [29]. From all cardiovascular diseases, the AAA and peripheral artery disease (PAD) are the ones showing the highest association with smoking [29]. AAAs can be further categorized into infrarenal, juxtarenal, pararenal or suprarenal [77], with shapes varying from simple and fusiform to sacciform, eccentric or highly irregular. In most AAAs an intraluminal thrombus (ILT) forms at the luminal aortic wall as a result of blood depositions, narrowing the lumen. Fig. 1.1 shows CT slices from two exemplary cases, where the lumen and ILT geometry can be clearly identified.

While most AAAs develop and grow asymptotically over several years, they can quickly turn into a serious clinical emergency in case of rupture. More than 50% of patients with a ruptured AAA (rAAA) die before reaching the hospital [24] and perioperative mortality rates for rAAAs range from 40% to 60% [118]. Since only very few AAA patients experience any symptoms beforehand, it is crucial to detect and treat AAAs prior to becoming dangerously large or prone to rupture.

Clinical guidelines

Today, elective open surgical repair (OSR) and endovascular aneurysm repair (EVAR) are established and effective strategies to prevent aneurysm rupture. Both methods are associated with certain operational risks and post-operative complications. In the famous UK small aneurysm trial [105], the risk of rupture for small AAAs (40-55 mm) was found to be significantly lower than for larger-sized aneurysms, justifying a surveillance strategy over elective repair for such cases. Further studies showed similar results and paved the way for today's clinical guidelines on the care of AAA patients [77]. While details can vary between different vascular surgery societies, there is near consensus on some fundamental recommendations [24, 29]:
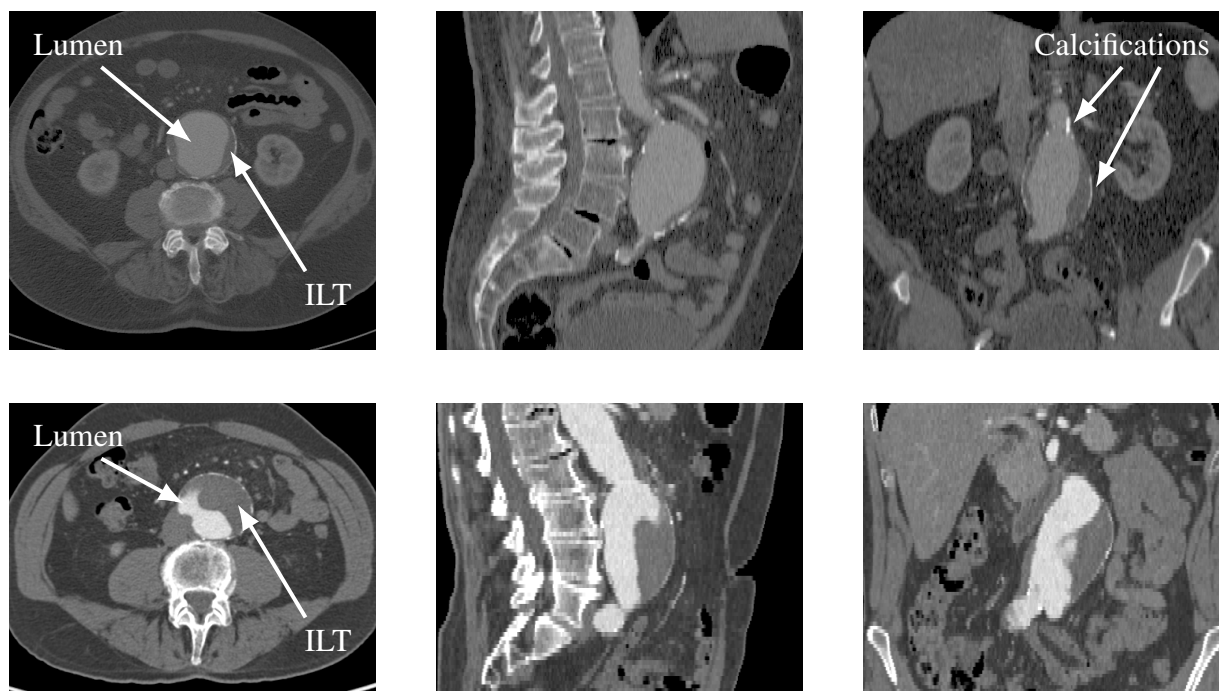
Figure 1.1.: Axial (left column), sagittal (center column) and coronal (right column) views of CT slices from two AAAs. The maximum diameters are 63 mm (top row) and 57 mm (bottom row). The lumen can usually be easily identified due to a contrast agent that is administered prior to CT imaging, while the ILT appears much darker and it can be hard to separate it from the surrounding tissue. The AAA vessel wall is too thin to be visible directly, but can be approximately determined via calcifications (tiny bright spots) in the wall or due to the contrast to the surrounding tissue.

- Immediate elective repair for patients with a symptomatic or rAAA.

- Elective repair for patients with an aortic diameter greater than or equal to 55 mm in men and 50 mm in women, or with a growth rate greater than 10 mm per year.

- Individual evaluation of irregular-shaped and exotic AAAs.

- Preferred treatment in high-volume hospital centers.

- Screening in men and women older than 65 years with a history of smoking.

- Regular screening intervals for patients with small-sized AAAs with maximum diameters up to 55 mm.

- Ultrasonography for screening and surveillance.

- Computed tomography angiography (CTA) or magnetic resonance angiography (MRA) for pre-procedural imaging, covering the area between the aortic arch and the inguinal vessels.

Treatment possibilities

Open surgical repair is the conventional therapy for AAAs and involves the replacement of the diseased aorta with a prosthetic graft. OSR has been the only option for elective repair for several decades and is associated with relatively high hospital mortality rates, especially for elderly patients. Since the 2000s, the minimally invasive procedure EVAR has increasingly been used. It requires the deployment of a stent graft (SG) via the patient's femoral arteries, with the goal to remove the blood pressure load from the AAA wall. Nowadays, endovascular aneurysm repair has clearly surpassed OSR in usage [136], which can be attributed to its significant short term mortality benefit (1.4% compared to 4.2%) [24]. Though clinical guidelines do not yet give a clear recommendation to favor one method over the other [29], with the growing customizability of SGs and improved technical equipment, the upward trend of EVAR is expected to continue.

Current limitations for the use of EVAR are mostly associated with the patient's anatomy and AAA shape [54]. For example, if there are no appropriate so-called landing zones for the SG deployment, there is a higher risk for leakages and subsequent re-interventions. While OSR can be applied almost universally, EVAR is the preferred choice for elderly people and rAAAs [104], and is associated with a shorter hospitalization.

Despite peri-operative mortality rates are undoubtedly smaller with EVAR, recent meta-analyses indicate equal or even higher numbers in the long term [1, 48, 79]. In [1], e.g., seven randomized control trials comparing the outcomes of EVAR and OSR were analyzed. According to this study, the 30 day and in-hospital mortality was significantly lower with EVAR, also six months after the procedure. With further follow-up, however, aneurysm related mortality, re-intervention and rupture risk rates increased and even exceeded those of OSR in the long term (> 8 years).

Independent from the type of therapy, it is being discussed whether screening for AAAs should be intensified. While a recent meta-study could not find an all-cause mortality benefit associated with screening in men aged 65 or older [55], data from Germany reveals that 30% of patients with a rAAA are not covered by the national screening program (which applies to men ≥ 65 years) and suggests to include further risk groups [137]. These studies emphasize the complex decisions surgeons are faced with today. While current guidelines provide recommendations for some standard AAA cases, the nature of the disease is manifold and patient-specific considerations imperative.

Computational biomechanics as an additional tool for decision making

Over the last decades, advances in biomechanical modeling, numerical methods and a tremendous increase in computational power have paved the way for the emerging field of computational biomechanics. Driven by the promises of personalized healthcare, a growing amount of available medical data and progress in related fields such as mechanobiology, there is still a tremendous potential for development. Applications range from modeling the vascular system and its diseases [60, 84, 134] to surgical intervention planning [2, 58] and biomedical engineering [65], just to name a few.

For the purposes of this thesis, which is concerned with the rupture risk assessment of AAAs, there are several shortcomings in clinical practice that can be addressed by appropriate computational approaches. In particular, these tools can be valuable in situations, where doctors are faced with an ambiguous situation. For example, the Society for Vascular Surgery's 55 mm recom-
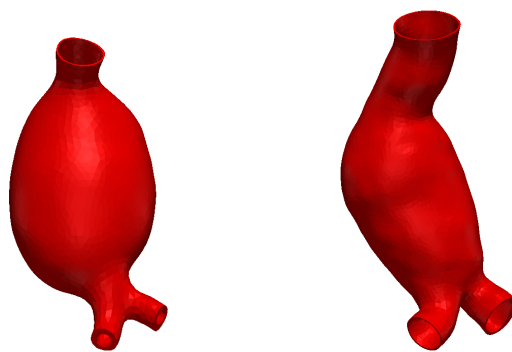
Figure 1.2.: 3D renderings of the two AAA cases from Fig. 1.1. These have been extracted from the CT scans via a segmentation software and provide the basis for a computational assessment.

mendation only holds for patients "at low or acceptable surgical risk with a fusiform AAA" [24]. Furthermore, there are no clear or only weak recommendations for women with AAAs of size 50-54 mm, aneurysms with non-fusiform geometries, smaller AAAs [132], or patients at higher surgical risk. Finally, not all AAAs are suitable for EVAR, with higher complication rates for cases that are not covered by the instructions for use [101]. A patient-specific modeling and simulation framework that makes use of the available clinical data could avoid unnecessary interventions [4], enable individual screening intervals and support the clinical decision process for cases that are not covered by the clinical guidelines. Fig. 1.2 shows 3D renderings of the two AAA cases from Fig. 1.1, which provide the basis for a computational assessment.

1.2. Research objectives

This thesis is based on previous work regarding the modeling, simulation and rupture risk assessment of AAAs. Past efforts by our group and collaborators have encompassed the modeling of the in-vivo mechanical state of AAAs [43, 46, 84], tensile testing and characterization of AAA tissue samples [8, 117] as well as the quantification of growth [68, 69] and model uncertainties [5–7]. Based on the progress achieved in these fields, the clinical motivation from above and promising studies indicating that biomechanical rupture risk indices are more accurate predictors than the clinically established maximum diameter criterion [30, 34, 35, 37, 42, 83, 107, 110], the objectives of this thesis are the following:

1. Establish a patient-specific framework for the quantification of AAA growth and rupture.

2. Incorporate available clinical data and make use of existing data sources.

3. Follow a probabilistic approach and quantify relevant uncertainties.

4. Aim for practical solutions that can be translated into clinical practice.

While patient-specific biomechanical models of AAAs are widely used for the purposes of a rupture risk assessment, these models can usually only quantify the risk at the time of data acquisition, e.g. at the time of the diagnosis. Moreover, different approaches exist on how to compute the risk of rupture, depending on model assumptions and the treatment of unknown parameters.

The goal of the first objective is to develop a consistent and general approach to rupture risk assessment and to incorporate a simple growth model in order to predict the risk of rupture at a future point in time and effectively be able to quantify the progression of the disease. For the construction of a patient-specific AAA model, any relevant data point will be considered as a piece of information that should be incorporated into the framework. To that end, a probabilistic approach will be pursued, where existing information about AAA properties can be combined with available clinical data of an individual patient to obtain a personalized statistical model. Efficient strategies for uncertainty quantification (UQ) will be employed to make the computations feasible. Following the concepts described in [17], an outline of a comprehensive rupture risk framework is illustrated in Fig. 1.3. All details regarding this methodology are established in the following chapter and later applied in several examples.
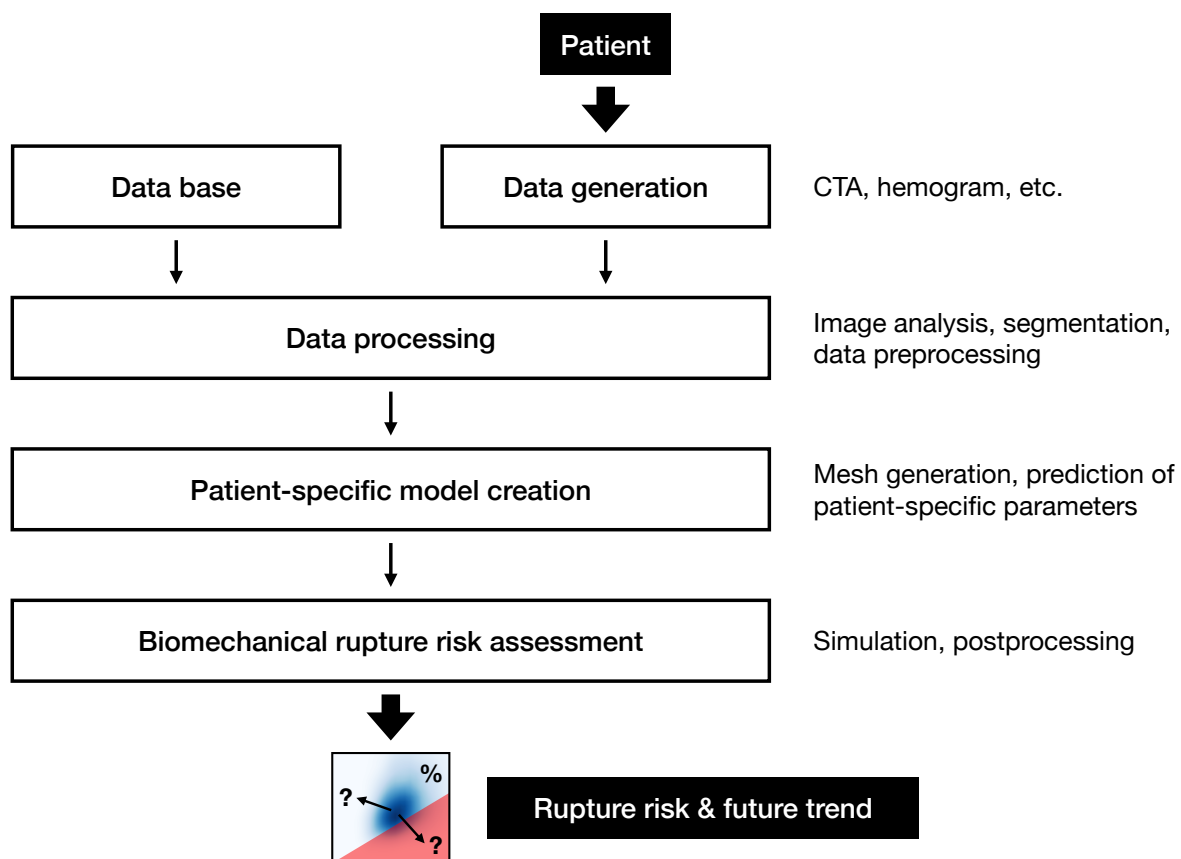
Figure 1.3.: Framework overview for the biomechanical rupture risk assessment of a prospective patient. After generating data as part of the clinical routine and some preprocessing, it is combined with existing information about invasive and non-invasive AAA-related properties from a database. Based on this, a patient-specific, stochastic model is created and employed for the purposes of rupture risk prediction.

1.3. Outline

The thesis is organized as follows. In Chapter 2, the theoretical background for the biomechanical rupture risk framework is established. This encompasses the definition of the biomechanical model, a numerical solution approach to be able to make predictions, as well as a formalism to deal with uncertainties. Based on this, a probabilistic rupture risk index is formulated that arises naturally from a mechanical failure criterion. The framework is applied in Chapter 3 and its feasibility demonstrated in several examples. After discussing the probabilistic treatment of the available clinical data, the rupture risk assessment is demonstrated on a cohort of retrospective AAA patients. Extensions for the incorporation of growth are investigated. Finally, relevant findings of this thesis are summarized in Chapter 4 and a short outlook for future work is provided. Further details on theoretical aspects and practical technicalities are provided in the appendix. Additionally, different evaluation methods for mechanical testing data are examined in order to determine elastic properties of the AAA vessel wall.

2. Theoretical Background

The theoretical background for the proposed biomechanical rupture risk framework is provided in this chapter. This includes the mathematical AAA model in Section 2.1, which is based on nonlinear solid mechanics, as well as the corresponding numerical finite element (FE) model in Section 2.2. To incorporate probabilistic information, stochastic forward and inverse problems are formulated in Section 2.3, which leads to the definition of a generalized rupture risk index in Section 2.4. Lastly, UQ tools for the efficient calculation of this index are discussed in Section 2.5.

2.1. Mathematical AAA model

Biomechanical rupture risk assessment for AAAs is based on the concept that local stress concentrations in the aneurysm wall lead to defects that can eventually propagate and cause a rupture. Hence, for the purposes of estimating a risk of rupture, the dominant effects responsible for the wall stress distribution need to be taken into account. At the same time, the model should only be as complex as absolutely necessary in order to make a clinical application feasible and to avoid the introduction of several parameters that cannot be specified on a patient-specific basis. On a macroscopic level, calculating mechanical AAA properties involves a fluid-structure interaction (FSI) problem, where the pulsating downward blood flow from the thoracic descending aorta interacts with the aortic wall in the abdominal aorta. In the computational study by [78], however, it was shown that the effect of fluid flow is negliglible in terms of the peak wall stress when compared to a simple static structural mechanics simulation. As a consequence, blood flow, dynamic effects and gravity are not considered in this work and it is being focused on the relevant effects based on the mathematical framework of nonlinear solid mechanics.

2.1.1. Continuum mechanical preliminaries

Continuum mechanics is concerned with the macroscopic behavior of matter, which is assumed a continuous body, consisting of infinitesimally spaced points and allowing for the application of mathematical analysis. The following sections review some fundamental continuum mechanical concepts based on the books [64, 133] and introduce the partial differential equations (PDEs) governing the biomechanical model of the AAA. The tensor notation applied below is explained in Section A.1.1.

Kinematics

Introducing a reference configuration Ω_0 for the continuous body $\mathcal{B}$, this configuration can be characterized by the coordinates $\underline{X}$ of all points that make up the body, so that any point can

be described as $\underline{\boldsymbol{X}} \in \Omega_0$. Correspondingly, a current configuration Ω for the same continuum is introduced, where each point is characterized by $\underline{\boldsymbol{x}} \in \Omega$. To describe the relationship between the reference coordinates $\underline{\boldsymbol{X}}$ of one point in Ω_0 to its current coordinates $\underline{\boldsymbol{x}}$ in Ω, a one-to-one correspondence $\underline{\boldsymbol{\phi}}(\underline{\boldsymbol{X}})$ is considered, where

$$\underline{\boldsymbol{\phi}} : \underline{\boldsymbol{X}} \to \underline{\boldsymbol{\phi}}(\underline{\boldsymbol{X}}) = \underline{\boldsymbol{x}}(\underline{\boldsymbol{X}}) \quad \text{with} \quad \underline{\boldsymbol{\phi}} : \mathbb{R}^3 \to \mathbb{R}^3. \tag{2.1}$$

Having the two configurations available, it is straightforward to define a displacement field $\underline{\boldsymbol{u}}$ as the difference between their corresponding coordinates

$$\underline{\boldsymbol{u}} = \underline{\boldsymbol{x}} - \underline{\boldsymbol{X}}. \tag{2.2}$$

In addition to quantifying the displacement, it is important to have a measure of deformation. For that purpose, the transformation

$$\mathrm{d}\underline{\boldsymbol{x}} = \underline{\underline{\boldsymbol{F}}} \cdot \mathrm{d}\underline{\boldsymbol{X}}. \tag{2.3}$$

of an infinitesimal line element $\mathrm{d}\underline{\boldsymbol{X}}$ from the reference to the current configuration $\mathrm{d}\underline{\boldsymbol{x}}$ is considered. The second-order tensor relating the two line elements is a point-wise measure of deformation – the deformation gradient – and is defined as

$$\underline{\underline{\boldsymbol{F}}} = \underline{\boldsymbol{\nabla}}_X \otimes \underline{\boldsymbol{x}} = \underline{\underline{\mathbf{1}}} + \underline{\boldsymbol{\nabla}}_X \otimes \underline{\boldsymbol{u}}, \tag{2.4}$$

where $\underline{\underline{\mathbf{1}}}$ is the identity tensor. Similarly to the deformation map $\underline{\boldsymbol{\phi}}$, the deformation gradient $\underline{\underline{\boldsymbol{F}}}$ is required to be invertible, such that its determinant $J = \det \underline{\underline{\boldsymbol{F}}}$ is nonzero. This implies that the line element $\mathrm{d}\underline{\boldsymbol{x}}$ can be transformed to the reference configuration as

$$\mathrm{d}\underline{\boldsymbol{X}} = \underline{\underline{\boldsymbol{F}}}^{-1} \cdot \mathrm{d}\underline{\boldsymbol{x}}. \tag{2.5}$$

Just like for infinitesimal line elements, it is possible to transform infinitesimal volume and surface elements using the relations

$$\mathrm{d}v = J \, \mathrm{d}V \tag{2.6}$$

and

$$\underline{\boldsymbol{n}} \, \mathrm{d}a = J \underline{\underline{\boldsymbol{F}}}^{-\mathsf{T}} \cdot \underline{\boldsymbol{N}} \, \mathrm{d}A, \tag{2.7}$$

respectively, where $\underline{\boldsymbol{N}}$ is the reference surface normal and $\underline{\boldsymbol{n}}$ the surface normal corresponding to the deformed surface in the current configuration. Finally, these relations illustrate that a negative deformation gradient determinant J is physically implausible, leading to the requirement $J > 0$.

Strain

For the characterization of material behavior, measures of strain, i.e. measures of changes in length, need to be established. Since there is no unique way to do so, different strain tensors have proven suitable for different applications. A popular choice for nonlinear solid mechanics

that will also be used in this work is the Green-Lagrange strain tensor defined as

$$\underline{\underline{E}} = \frac{1}{2}\left(\underline{\underline{C}} - \underline{\underline{1}}\right), \tag{2.8}$$

with the right Cauchy-Green deformation tensor $\underline{\underline{C}} = \underline{\underline{F}}^{\mathsf{T}} \cdot \underline{\underline{F}}$. It is symmetric and invariant with respect to rigid body motions, which makes it an appropriate choice for problems involving large displacements and rotations.

Stress

While measures of strain are concerned with describing the deformation of a continuum, stress is considered responsible for a deformation. Cauchy's stress theorem

$$\underline{t}(\underline{x}, \underline{n}) = \underline{\underline{\sigma}}(\underline{x}) \cdot \underline{n} \tag{2.9}$$

states that the relationship between the surface traction $\underline{t}$ and the outward surface normal $\underline{n}$ at an arbitrary point $\underline{x}$ on a cut surface through a deformed body is linear. The symmetric second order tensor $\underline{\underline{\sigma}}$ required for this linear transformation is called the Cauchy stress tensor, where symmetry stems from the conservation of angular momentum, which is not further discussed here. The theorem can also be formulated in terms of the surface traction $\underline{T}$ (i.e. with respect to the undeformed surface), outward surface normal $\underline{N}$ and reference coordinate $\underline{X}$, yielding

$$\underline{T}(\underline{X}, \underline{N}) = \underline{\underline{P}}(\underline{X}) \cdot \underline{N} \tag{2.10}$$

with the non-symmetric 1st Piola-Kirchhoff stress tensor $\underline{\underline{P}}$. Another stress tensor particularly useful for computational analysis is the symmetric 2nd Piola-Kirchhoff stress tensor $\underline{\underline{S}}$. It is fully expressed in the reference configuration and can be linked to $\underline{\underline{P}}$ and $\underline{\underline{\sigma}}$ as

$$\underline{\underline{P}} = \underline{\underline{F}} \cdot \underline{\underline{S}} \quad \text{and} \quad \underline{\underline{\sigma}} = J^{-1}\underline{\underline{F}} \cdot \underline{\underline{S}} \cdot \underline{\underline{F}}^{\mathsf{T}}. \tag{2.11}$$

Balance of linear momentum

In absence of body forces and dynamic effects, the balance of linear momentum for a continuous body in equilibrium reduces to the expression

$$\int_{\partial\Omega} \hat{\underline{t}} \, \mathrm{d}a = \underline{0}, \tag{2.12}$$

requiring the surface integral over all externally applied tractions $\hat{\underline{t}}$ at the boundary $\partial\Omega$ to be zero. With Eq. (2.9) this can be transformed into a volume integral, resulting in the more familiar relation

$$\int_{\Omega} \underline{\boldsymbol{\nabla}}_x \cdot \underline{\underline{\sigma}} \, \mathrm{d}v = \int_{\Omega_0} \underline{\boldsymbol{\nabla}}_X \cdot \underline{\underline{P}} \, \mathrm{d}V = \underline{0}, \tag{2.13}$$

where the second expression is formulated in the reference configuration.

Constitutive behavior

The linkage between stress and strain is accomplished via constitutive equations. In continuum mechanics these are usually phenomenological, i.e. based on fitting parameterized models to experimental data to describe the macroscopic stress-strain behavior of materials. For the purposes of this work, materials that can be described by a strain energy density function $\Psi(\underline{\underline{F}})$ and do not depend on their deformation history are considered. Such materials are called hyperelastic and their constitutive behavior is fully determined by $\Psi(\underline{\underline{F}})$. Under the additional assumption of isotropy, it can be shown that Ψ can be expressed as a function of the three principal invariants of $\underline{\underline{C}}$, i.e.

$$\Psi = \Psi(I_1(\underline{\underline{C}}), I_2(\underline{\underline{C}}), I_3(\underline{\underline{C}})) \tag{2.14}$$

with

$$I_1 = \operatorname{tr}\underline{\underline{C}}, \tag{2.15}$$

$$I_2 = \frac{1}{2}\left[(\operatorname{tr}\underline{\underline{C}})^2 - \operatorname{tr}\underline{\underline{C}}^2\right], \tag{2.16}$$

$$I_3 = \det\underline{\underline{C}} = J^2. \tag{2.17}$$

For some materials, it is beneficial to split the deformation gradient multiplicatively into a volumetric and isochoric part $\underline{\underline{F}} = \underline{\underline{F}}_{\text{vol}}\underline{\underline{F}}_{\text{iso}}$ in order to model the material behavior of both parts independently from each other, where

$$\underline{\underline{F}}_{\text{vol}} = J^{\frac{1}{3}}\underline{\underline{1}} \quad \text{and} \quad \underline{\underline{F}}_{\text{iso}} = \overline{\underline{\underline{F}}} \quad \text{with} \quad \det\overline{\underline{\underline{F}}} = 1. \tag{2.18}$$

This translates to the relation $\underline{\underline{C}} = J^{\frac{2}{3}}\overline{\underline{\underline{C}}}$. $\overline{\underline{\underline{F}}}$ and $\overline{\underline{\underline{C}}} = \overline{\underline{\underline{F}}}^{\mathsf{T}}\cdot\overline{\underline{\underline{F}}}$ are called the modified deformation gradient and right Cauchy-Green tensor, respectively. Motivated by this split, one can postulate a decoupled representation of the strain energy density

$$\Psi = \Psi_{\text{vol}}(J) + \Psi_{\text{iso}}(\overline{I}_1(\overline{\underline{\underline{C}}}), \overline{I}_2(\overline{\underline{\underline{C}}})), \tag{2.19}$$

with the modified invariants

$$\overline{I}_1 = \operatorname{tr}\overline{\underline{\underline{C}}} = J^{-\frac{2}{3}}I_1, \tag{2.20}$$

$$\overline{I}_2 = \frac{1}{2}\left[(\operatorname{tr}\overline{\underline{\underline{C}}})^2 - \operatorname{tr}\overline{\underline{\underline{C}}}^2\right] = J^{-\frac{4}{3}}I_2. \tag{2.21}$$

Finally, the 2nd Piola-Kirchhoff stress tensor $\underline{\underline{S}}$, corresponding to a deformation state $\underline{\underline{C}}$ for any hyperelastic material with strain energy density function Ψ, can be computed via the equation

$$\underline{\underline{S}} = 2\frac{\partial\Psi(\underline{\underline{C}})}{\partial\underline{\underline{C}}}. \tag{2.22}$$

With this, the most fundamental relations required for the mathematical modeling of quasi-static, hyperelastic bodies under external loads are provided.

2.1.2. Biomechanical modeling and boundary value problem formulation

While continuum mechanics provides the mathematical framework to create a detailed description of physical reality, using this framework to establish a model for practical purposes is far from trivial. For example, if too much attention is paid to all the physical and geometrical details, the model may become too complex, infeasible to evaluate and difficult to interpret. It might also be not possible to accurately model all the details due to a lack of knowledge about material properties, boundary conditions, etc. In the present case, we are confronted with both issues, complexity and uncertainty. At the beginning of this chapter, the AAA model has already been limited to a nonlinear elastostatics problem. Below, further modeling choices for the purposes of a biomechanical rupture risk assessment are briefly discussed. These encompass the models for the AAA wall and ILT constitutive behavior, the boundary conditions, a methodology for prestressing and an approach to incorporate growth.

Wall material model

The aortic vessel wall is a complex biological organ, which continuously adapts to environmental changes via growth and remodeling to maintain its functionality [39]. In a healthy state, the aortic wall is multi-layered, consisting of the intima, media and adventitia, and highly anisotropic, with an increased stiffness in circumferential direction. Its structural properties are mainly determined by the extracellular matrix (ECM) components elastin and collagen. While elastin is responsible for the stiffness at low strains as well as for the recoiling of the vessel wall during the diastolic phase, collagen fibers determine the mechanical properties at high strain levels. Due to its structural design, the aortic wall can be modeled as a fiber-reinforced composite with dispersed orientation [40, 62], allowing for a detailed description for the individual layers. It is being referred to [63] or [39] for a comprehensive description and overview over mechanical properties of the aorta.

The pathogenesis of an AAA goes along with a degradation of elastin in the aortic wall and a compensating increase in collagen. During the progression from a healthy to an aneurysmatic aorta, its anisotropic three-layer structure disperses into a collagen-dominated fibrous material, stimulating enlargement and local wall weakening [39]. To avoid complex material models with multiple parameters, the aneurysmatic vessel wall material is frequently chosen as single-layered and isotropic [38, 84]. While different formulations are available in the literature [109], a recent study suggests that the particular choice in the constitutive model does not have a major influence on the AAA wall stress as long as an initial and high-strain stiffness component is included [85]. In this work, the popular two-parameter strain energy function from [113] will therefore be employed. Using the decoupled isochoric/volumetric formulation in Eq. (2.19), this results in

$$\Psi_{\mathrm{w}}(\bar{I}_1, J) = \alpha_{\mathrm{w}}\left(\bar{I}_1 - 3\right) + \beta_{\mathrm{w}}\left(\bar{I}_1 - 3\right)^2 + \Psi_{\mathrm{vol}}(J), \tag{2.23}$$

with stiffness parameters α_{w} and β_{w}, which are in general spatially varying parameters $\alpha_{\mathrm{w}}(\underline{\boldsymbol{X}})$ and $\beta_{\mathrm{w}}(\underline{\boldsymbol{X}})$. This model is frequently used in the context of AAA biomechanics simulations and parameter values for α_{w} and β_{w} including their intra-patient variations have been reported by

different groups [8, 100, 113, 117]. Unfortunately, with the exception of [7], there is hardly any literature about the variation of these parameters among a single patient.

ILT material model

The majority of AAAs, especially those coming into question for a biomechanical rupture risk assessment, exhibit a narrowed lumen due to an aggregation of coagulated blood, called the ILT. It is assumed that the altered blood flow in an AAA plays a major role in thrombus development. For the purposes of this work, only the impact of an existing ILT on the stress distribution in the AAA wall is of interest and it is being referred to [150] for a detailed review of biomechanical thrombus formation. An ILT is an inhomogeneous, porous structure of fibrin bundles that can be very thin to centimeters thick. Often, a three-layer structure can be identified with different biomechanical properties, consisting of a luminal, medial and abluminal ILT layer [150]. In several experimental studies [41, 84, 140, 147], the mechanical behavior of ILT material was identified as almost isotropic and only slightly nonlinear. This motivates the usage of the strain energy proposed by [41], which can be expressed in terms of invariants and using a decoupled formulation as

$$\Psi_{\mathrm{ILT}}(\bar{I}_1, \bar{I}_2, J) = c_{\mathrm{ILT}}(\bar{I}_1^2 - 2\bar{I}_2 - 3) + \Psi_{\mathrm{vol}}(J). \tag{2.24}$$

To take into account the three-layer structure, the stiffness parameter c_{ILT} is chosen linearly decreasing from the luminal to the abluminal ILT surface following [84] and using the stiffness values from [41], i.e. 2.62 kPa for the luminal, 1.98 kPa for the medial and 1.73 kPa for the abluminal ILT layer.

The mechanical role of the ILT with respect to the AAA wall stress is controversial [150]. From a mechanical point of view, it has often been attributed with a cushioning effect for the blood pressure, reducing the load acting on the aortic wall. Measurements, however, could not verify this [127], showing a constant blood pressure distribution throughout the ILT and indicating a porous composition. In [108], this was further examined via a two-phase simulation model. While the observation in [127] could be verified, a significant reduction in the aortic wall stresses due to the ILT's presence was noted. Finally, the authors demonstrated that these results are comparable to those from single-phase simulations, which has only recently been confirmed in a different study [20], justifying the use of the simplified model in Eq. (2.24).

Volumetric component for slightly compressible behavior

The volumetric component in Eq. (2.23) and Eq. (2.24) is chosen following [84] as

$$\Psi_{\mathrm{vol}}(J) = \frac{\kappa}{4}\left(J^2 - 2\ln J - 1\right), \tag{2.25}$$

where the bulk modulus has the form

$$\kappa = \frac{E_{(\bullet)}}{3(1 - 2\nu)} \tag{2.26}$$

and ν denotes Poisson's ratio. For the employed material models for the vessel wall and ILT, Young's moduli can be determined as $E_{\mathrm{w}} = 6\alpha$ and $E_{\mathrm{ILT}} = 24c$, corresponding to the respective initial stiffness under the assumption of uniaxial stress and incompressibility (cf. Section A.1.2). Following [84], ν is fixed to 0.48.

Boundary conditions

The load associated with the arterial blood pressure p is simulated by means of an orthogonal surface traction

$$\hat{\underline{t}} = -p\underline{n} \tag{2.27}$$

on the Neumann boundary γ_σ (i.e. the luminal ILT surface) in the current configuration, representing a nonlinear follower load. At the proximal and distal end surfaces Γ_u, a Robin-type boundary condition (BC) with spring support

$$(\underline{\underline{F}} \cdot \underline{\underline{S}}) \cdot \underline{N} = -k_s \underline{u} \tag{2.28}$$

and stiffness parameter k_s is applied [92], which is set to 100 kPa/mm in this work. The influence of surrounding organs is not taken into account, such that there are no external loads acting on the outer surface of the aorta.

Growth

AAA growth is modeled following a phenomenological approach for the vessel wall as described in [68, 69], with the goal to provide an extrapolation of the current growth process. The aim is thus not to describe the growth and remodeling associated with the development of an AAA, which is a much more complex task, e.g. [15]. To that end, an isotropic volumetric growth description is incorporated via a multiplicative split of the deformation gradient

$$\underline{\underline{F}} = \underline{\underline{F}}_g \cdot \underline{\underline{F}}_e = \vartheta(\underline{X}, t)\underline{\underline{F}}_e \tag{2.29}$$

into a growth component $\underline{\underline{F}}_g = \vartheta(\underline{X}, t)\underline{\underline{1}}$ and an elastic component $\underline{\underline{F}}_e$ and where $\vartheta(\underline{X}, t)$ denotes the growth at point $\underline{X}$ and time t. Assuming a temporally constant growth rate $c_\vartheta(\underline{X})$, the evolution equation for $\vartheta(\underline{X}, t)$ is

$$\frac{\partial \vartheta(\underline{X}, t)}{\partial t} = \dot{\vartheta}(\underline{X}, t) = c_\vartheta(\underline{X}) \tag{2.30}$$

with the solution

$$\vartheta(\underline{X}, t) = \vartheta(\underline{X}, t = t_0) + \int_{t=t_0}^{t=\bar{t}} c_\vartheta(\underline{X}) \, \mathrm{d}t = \vartheta_0 + c_\vartheta(\underline{X})\,(\bar{t} - t_0)\,. \tag{2.31}$$

The initial value at the onset of growth is set to $\vartheta_0 = 1.0$ everywhere and $\bar{t}$ is the point in time for the evaluation of growth. The strain energy function is evaluated with the elastic component

of the deformation gradient $\underline{\underline{F}}_e$, which can be computed as

$$\underline{\underline{F}}_e = \underline{\underline{F}}_g^{-1} \cdot \underline{\underline{F}} = \frac{1}{\vartheta}\underline{\underline{F}}. \tag{2.32}$$

This means that any partial variation with respect to $c_\vartheta(\underline{X})$ only affects quantities derived from the elastic deformation gradient $\underline{\underline{F}}_e$, i.e. quantities associated with the strain energy $\Psi_{\mathrm{w}}(\underline{\underline{F}}_e)$, cf. Section A.2.2.

Boundary-value problem

To summarize, the governing equations for the quasi-static solid mechanics problem are

$$\underline{\boldsymbol{\nabla}}_X \cdot (\underline{\underline{F}} \cdot \underline{\underline{S}}) = \underline{0} \qquad \text{in} \quad \Omega_0, \tag{2.33}$$

$$\underline{\underline{\sigma}} \cdot \underline{n} = -p\underline{n} \qquad \text{on} \quad \gamma_\sigma, \tag{2.34}$$

$$(\underline{\underline{F}} \cdot \underline{\underline{S}}) \cdot \underline{N} = -k_s\underline{u} \qquad \text{on} \quad \Gamma_u. \tag{2.35}$$

A typical AAA geometry is shown in Fig. 2.1, illustrating where Eq. (2.33)−Eq. (2.35) of the boundary value problem (BVP) have to be satisfied.
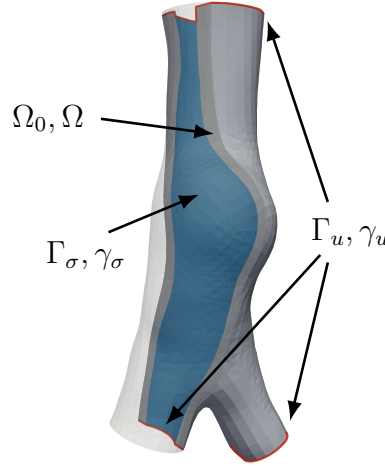
Figure 2.1.: A typical AAA geometry to illustrate the BVP. Eq. (2.33) has to be satisfied in Ω_0, with different stress responses for the AAA wall and ILT material. The pressure BC from Eq. (2.34) is applied on the current Neumann boundary, γ_σ, while the spring support BC from Eq. (2.35) is applied at the inlet and two outlet surfaces of the AAA.

2.1.3. Variational formulation of the boundary value problem

By multiplying the balance of linear momentum with a sufficiently smooth function $\delta\underline{u} = \delta\underline{u}(\underline{X})$, where $\delta\underline{u} : \mathbb{R}^3 \to \mathbb{R}^3$ and $\delta\underline{u} = \underline{0}$ on the Dirichlet boundary, a weighted residual for-

mulation of the BVP is obtained [64]

$$\mathcal{R}(\underline{\boldsymbol{u}}, \delta\underline{\boldsymbol{u}}) = \int_{\Omega_0} (\underline{\boldsymbol{\nabla}}_X \cdot (\underline{\underline{\boldsymbol{F}}} \cdot \underline{\underline{\boldsymbol{S}}})) \cdot \delta\underline{\boldsymbol{u}} \, \mathrm{d}V = 0 \quad \forall \, \delta\underline{\boldsymbol{u}}. \tag{2.36}$$

Using the identity

$$(\underline{\boldsymbol{\nabla}}_X \cdot (\underline{\underline{\boldsymbol{F}}} \cdot \underline{\underline{\boldsymbol{S}}})) \cdot \delta\underline{\boldsymbol{u}} = \underline{\boldsymbol{\nabla}}_X \cdot (\underline{\underline{\boldsymbol{F}}} \cdot \underline{\underline{\boldsymbol{S}}} \cdot \delta\underline{\boldsymbol{u}}) - (\underline{\underline{\boldsymbol{F}}} \cdot \underline{\underline{\boldsymbol{S}}}) : (\underline{\boldsymbol{\nabla}}_X \otimes \delta\underline{\boldsymbol{u}}) \tag{2.37}$$

and applying Gauss' divergence theorem, this becomes

$$\mathcal{R}(\underline{\boldsymbol{u}}, \delta\underline{\boldsymbol{u}}) = \int_{\Omega_0} (\underline{\underline{\boldsymbol{F}}} \cdot \underline{\underline{\boldsymbol{S}}}) : (\underline{\boldsymbol{\nabla}}_X \otimes \delta\underline{\boldsymbol{u}}) \, \mathrm{d}V + \int_{\gamma_\sigma} p\underline{\boldsymbol{n}} \cdot \delta\underline{\boldsymbol{u}} \, \mathrm{d}a + \int_{\Gamma_u} k_s \underline{\boldsymbol{u}} \cdot \delta\underline{\boldsymbol{u}} \, \mathrm{d}A = 0, \tag{2.38}$$

where the surface integral was split up and associated with the corresponding boundary conditions on Γ_u and γ_σ. In the context of solid mechanics, $\delta\underline{\boldsymbol{u}}$ is often referred to as virtual displacements and this one-field variational formulation is called the principle of virtual work. Making use of a basic property of double contractions and the symmetry of $\underline{\underline{\boldsymbol{S}}}$

$$\begin{aligned}
(\underline{\underline{\boldsymbol{F}}} \cdot \underline{\underline{\boldsymbol{S}}}) : (\underline{\boldsymbol{\nabla}}_X \otimes \delta\underline{\boldsymbol{u}}) &= (\underline{\underline{\boldsymbol{F}}}^\mathsf{T} \cdot (\underline{\boldsymbol{\nabla}}_X \otimes \delta\underline{\boldsymbol{u}})) : \underline{\underline{\boldsymbol{S}}} \\
&= \frac{1}{2}(\underline{\underline{\boldsymbol{F}}}^\mathsf{T} \cdot (\underline{\boldsymbol{\nabla}}_X \otimes \delta\underline{\boldsymbol{u}}) + \underline{\underline{\boldsymbol{F}}} \cdot (\underline{\boldsymbol{\nabla}}_X \otimes \delta\underline{\boldsymbol{u}})^\mathsf{T}) : \underline{\underline{\boldsymbol{S}}} \\
&= \delta\underline{\underline{\boldsymbol{E}}} : \underline{\underline{\boldsymbol{S}}} = \underline{\underline{\boldsymbol{S}}} : \delta\underline{\underline{\boldsymbol{E}}},
\end{aligned} \tag{2.39}$$

the final formulation is

$$\mathcal{R}(\underline{\boldsymbol{u}}, \delta\underline{\boldsymbol{u}}) = \int_{\Omega_0} \underline{\underline{\boldsymbol{S}}} : \delta\underline{\underline{\boldsymbol{E}}} \, \mathrm{d}V + \int_{\gamma_\sigma} p\underline{\boldsymbol{n}} \cdot \delta\underline{\boldsymbol{u}} \, \mathrm{d}a + \int_{\Gamma_u} k_s \underline{\boldsymbol{u}} \cdot \delta\underline{\boldsymbol{u}} \, \mathrm{d}A = 0. \tag{2.40}$$

Key to the application of the finite element method (FEM) in Section 2.2.1 is that a solution to Eq. (2.40) represents a weak solution to the BVP defined by Eq. (2.33)−(2.35).

2.1.4. Lagrangian formulation for gradient-based, PDE-constrained optimization

In addition to enabling a FEM-based numerical solution, the variational formulation can be employed in the context of PDE-constrained optimization. Consider a scalar objective function $\mathcal{F}(\underline{\boldsymbol{u}}(\theta), \theta)$ and the optimization problem

$$\min_\theta \mathcal{F}(\underline{\boldsymbol{u}}(\theta), \theta) \quad \text{subject to} \quad \mathcal{R}(\underline{\boldsymbol{u}}(\theta), \delta\underline{\boldsymbol{u}}, \theta) = 0 \quad \forall \, \delta\underline{\boldsymbol{u}}, \tag{2.41}$$

where θ are unspecified design parameters of the BVP. The notation implies that the parameters θ directly affect the displacements $\underline{\boldsymbol{u}} = \underline{\boldsymbol{u}}(\theta)$ as well as the weighted residual itself, such that $\mathcal{R}(\underline{\boldsymbol{u}}, \delta\underline{\boldsymbol{u}}) = \mathcal{R}(\underline{\boldsymbol{u}}(\theta), \delta\underline{\boldsymbol{u}}, \theta)$. The variational formulation ensures that independent of the choice of $\delta\underline{\boldsymbol{u}}$, the equality condition $\mathcal{R}(\underline{\boldsymbol{u}}(\theta), \delta\underline{\boldsymbol{u}}, \theta) = 0$ is always fulfilled. This turns out to be a particularly helpful property for gradient calculations. To that end and following [69], the Lagrangian

formulation

$$\mathcal{L}(\underline{\boldsymbol{u}}(\theta), \underline{\boldsymbol{\lambda}}, \theta) = \mathcal{F}(\underline{\boldsymbol{u}}(\theta), \theta) + \mathcal{R}(\underline{\boldsymbol{u}}(\theta), \underline{\boldsymbol{\lambda}}, \theta) \quad \forall \underline{\boldsymbol{\lambda}} \tag{2.42}$$

is introduced, where the virtual displacements $\delta\underline{\boldsymbol{u}}$ take the role of Lagrange multipliers $\underline{\boldsymbol{\lambda}}$. In Section 2.2, the numerical implementation of this concept for the purposes of gradient calculations is discussed, where the role of the Lagrange multipliers $\underline{\boldsymbol{\lambda}}$ will become apparent.

2.2. Numerical AAA model

In order to compute solutions to the BVP defined via Eq. (2.33)−Eq. (2.35), a FE-based numerical model for the AAA is constructed. After a short review of the FEM in Section 2.2.1, simulation details as well as practical considerations are discussed in Section 2.2.2 and the parameter-to-quantity of interest (QoI) map is introduced in Section 2.2.3. Finally, the adjoint method for discrete problems is presented in Section 2.2.4, allowing for the efficient calculation of parameter gradients of QoI of the numerical model, which is a fundamental requirement for many of the UQ tools presented in Section 2.5.

2.2.1. Finite element formulation

Applying the FEM involves the discretization of the reference domain Ω_0 into n_{el} sub-domains (finite elements), the choice of suitable functions (that are square-integrable with a square-integrable spatial first derivative) for the displacement field $\underline{\boldsymbol{u}}$ as well as for the virtual displacement field $\delta\underline{\boldsymbol{u}}$, and the utilization of the weak form in Eq. (2.40). Below, a brief summary of the FEM is provided, covering the basic formalism required for this work. For further details, it is being referred to the comprehensive works of [3, 151].

Discretization

The idea is to approximate the volume and surface integrals appearing in Eq. (2.40) as a sum over element-wise contributions and to choose functions for $\underline{\boldsymbol{u}}$ and $\delta\underline{\boldsymbol{u}}$ with local support on each element. As an example, the volume integrals can then be computed as

$$\int_{\Omega_0} (\bullet)(\underline{\boldsymbol{X}}) \, \mathrm{d}V \approx \sum_{\text{e}=1}^{n_{\text{el}}} \int_{\Omega_0^{(\text{e})}} (\bullet)(\underline{\boldsymbol{X}}) \, \mathrm{d}V. \tag{2.43}$$

In the following, a matrix notation will be employed for quantities associated with the FE approximation, cf. Section A.2 for all details. The geometry of each finite element is approximated via an interpolation of the element's nodal coordinates $\bar{\mathbf{X}}^{(\text{e})}$ such that

$$\underline{\boldsymbol{X}} \approx \boldsymbol{X}(\boldsymbol{\xi}) = \boldsymbol{N}(\boldsymbol{\xi}) \, \bar{\mathbf{X}}^{(\text{e})}. \tag{2.44}$$

The matrix $\boldsymbol{N}(\boldsymbol{\xi})$ consists of basis or shape functions, in our case Lagrange polynomials, in so-called natural coordinates $\boldsymbol{\xi}$. This implies a map $\boldsymbol{X} = \boldsymbol{X}(\boldsymbol{\xi})$ between the reference and natural coordinates, which has to fulfill the same conditions as the deformation map from Eq. (2.1), such

that the inverse map $\boldsymbol{\xi} = \boldsymbol{\xi}(\boldsymbol{X})$ exists. Following an isoparametric approach, the displacement field for each element is formulated using the same shape functions

$$\underline{\boldsymbol{u}} \approx \boldsymbol{u}(\boldsymbol{X}) = \boldsymbol{N}(\boldsymbol{\xi}(\boldsymbol{X})) \, \mathbf{d}^{(\mathrm{e})}, \tag{2.45}$$

where $\mathbf{d}^{(\mathrm{e})}$ is the vector of the nodal displacements, i.e. the nodal degrees of freedom. Finally, the same functions are also used for the virtual displacements

$$\delta \boldsymbol{u}(\boldsymbol{X}) = \boldsymbol{N}(\boldsymbol{\xi}(\boldsymbol{X})) \, \delta \mathbf{d}^{(\mathrm{e})}, \tag{2.46}$$

where $\delta \mathbf{d}^{(\mathrm{e})}$ corresponds to the nodal virtual displacements. With $\mathbf{u} \in H^1(\Omega_0)$ and $\delta \mathbf{u} \in H_0^1(\Omega_0)$, this approach results in the well-known Bubnov-Galerkin method, where $H^1(\Omega_0)$ denotes the Sobolev space on Ω_0 and $H_0^1(\Omega_0)$ a subspace of $H^1(\Omega_0)$ with functions that vanish on the Dirichlet boundary. All remaining quantities necessary for the element-wise integration follow as elaborated in Section A.2. Inserting the interpolation approaches above into the weak form in Eq. (2.40) and factoring out the virtual displacements $\delta \mathbf{d}^{(\mathrm{e})}$, summarized in $\delta \mathbf{D}$, a compact notation for the approximate weighted residual

$$\mathcal{R}(\underline{\boldsymbol{u}}, \delta \underline{\boldsymbol{u}}) \approx \delta \mathbf{D}^{\mathsf{T}} \mathbf{R}(\mathbf{D}) = 0, \quad \forall \, \delta \mathbf{D}. \tag{2.47}$$

is obtained. Since $\delta \mathbf{D}$ are arbitrary, this is equivalent to the set of nonlinear equations

$$\mathbf{R}(\mathbf{D}) = \mathbf{0}, \tag{2.48}$$

where $\mathbf{D}$ includes all nodal displacements $\mathbf{d}^{(\mathrm{e})}$ and $\mathbf{R} \in \mathbb{R}^{n_{\mathrm{dof}}}$ is the n_{dof}-sized global residual vector. It is constructed as

$$\mathbf{R}(\mathbf{D}) = \overset{n_{\mathrm{el}}}{\underset{\mathrm{e}=1}{\mathsf{A}}} \mathbf{r}^{(\mathrm{e})}(\mathbf{d}^{(\mathrm{e})}) \tag{2.49}$$

with the assembly operator A and element-wise contributions

$$\mathbf{r}^{(\mathrm{e})}(\mathbf{d}^{(\mathrm{e})}) = \int_{\Omega_0^{(\mathrm{e})}} \boldsymbol{B}^{\mathsf{T}} [\boldsymbol{S}]_{6 \times 1} \, \mathrm{d}V + \int_{\gamma_\sigma^{(\mathrm{e})}} p \boldsymbol{N}^{\mathsf{T}} \boldsymbol{n} \, \mathrm{d}a + \int_{\Gamma_u^{(\mathrm{e})}} k_s \boldsymbol{N}^{\mathsf{T}} \boldsymbol{N} \mathbf{d}^{(\mathrm{e})} \, \mathrm{d}A. \tag{2.50}$$

$\boldsymbol{B}$ and $\boldsymbol{S}$ are as defined in Eq. (A.23) and Eq. (A.24), respectively. The integration is carried out in the natural coordinates $\boldsymbol{\xi}$ using Gaussian quadrature. For the volume integrals, this translates to the expression

$$\int_{\Omega_0^{(\mathrm{e})}} (\cdot)(\boldsymbol{X}) \, \mathrm{d}V = \int_{\Omega_\square^{(\mathrm{e})}} (\cdot)(\boldsymbol{\xi}) \det \boldsymbol{J}(\boldsymbol{\xi}) \, \mathrm{d}\boldsymbol{\xi} \approx \sum_{p=1}^{n_p} (\cdot)(\boldsymbol{\xi}_p) \det \boldsymbol{J}(\boldsymbol{\xi}_p) w_p, \tag{2.51}$$

with n_p Gauss point coordinates $\boldsymbol{\xi}_p$ and corresponding weights w_p, as well as the Jacobi matrix $\boldsymbol{J}$ as specified in Eq. (A.20).

Linearization

The nonlinear system of equations from (2.48) is solved using Newton's method. To that end, the discretized residual $\mathbf{R}(\mathbf{D})$ is linearized at the current solution $\mathbf{D}^i$

$$\mathbf{R}(\mathbf{D}) \approx \mathbf{R}(\mathbf{D}^i) + \left.\frac{\partial \mathbf{R}(\mathbf{D})}{\partial \mathbf{D}}\right|_{\mathbf{D}=\mathbf{D}^i} \Delta\mathbf{D}^{i+1} = \mathbf{0} \tag{2.52}$$

$$\Leftrightarrow \mathbf{K}(\mathbf{D}^i)\Delta\mathbf{D}^{i+1} = -\mathbf{R}(\mathbf{D}^i), \tag{2.53}$$

where $\mathbf{K}$ is referred to as the stiffness matrix, with the element-wise contributions

$$\mathbf{K} = \overset{n_{\mathrm{el}}}{\underset{\mathrm{e}=1}{\mathbf{A}}} \mathbf{k}^{(\mathrm{e})} = \overset{n_{\mathrm{el}}}{\underset{\mathrm{e}=1}{\mathbf{A}}} \frac{\partial \mathbf{r}^{(\mathrm{e})}}{\partial \mathbf{d}^{(\mathrm{e})}}. \tag{2.54}$$

The resulting linear system in Eq. (2.53) is sparse and non-symmetric and can be solved for the displacement increment $\Delta\mathbf{D}^{i+1}$ to update the solution

$$\mathbf{D}^{i+1} = \mathbf{D}^i + \Delta\mathbf{D}^{i+1}. \tag{2.55}$$

Convergence is checked in terms of the residual vector norm $\|\mathbf{R}(\mathbf{D}^i)\|_2 < \varepsilon_{\mathrm{res}}$ and displacement increment norm $\|\Delta\mathbf{D}^{i+1}\|_2 < \varepsilon_{\mathrm{dis}}$.

2.2.2. Modeling and simulation details

The following section is a revised version of part of the author's work published in [19].

Segmentation and mesh generation

Patient-specific AAA geometries are extracted via a semi-automatic segmentation process from computed tomography (CT) imaging data using the software ScanIP[1] (Synopsys, Mountain View, California, version 2020.06) and based on a protocol as described in [84]. The minimal requirement for the spatial resolution of CT scans was 1 mm and for the slice thickness 3 mm. The upper boundary for the segmentation was the branching of the renal arteries and the lower boundary below the bifurcation at the iliac arteries. Due to the small thickness of the AAA wall, its low contrast and the limited resolution of the CT images, it is only possible to extract the blood lumen and ILT geometries. After segmentation, the ILT geometry is exported as a surface model for meshing.

In a next step, the software Trelis[2] (Coreform, Orem, Utah, version 16.5.4) is used to generate a mesh of bi-linear quadrilateral elements on the abluminal ILT surface. From this surface mesh, the arterial wall layer is extruded with a specified, spatially constant thickness t_{w}, resulting in a tri-linear, single layer, hexahedral mesh for the AAA wall. Finally, linear tetrahedral elements are employed for the meshing of the complex ILT geometry and a layer of linear pyramid elements as a transition for mesh compatibility between AAA wall and thrombus. Element sizes were set to 1.6 mm, corresponding to the median of measured thicknesses of AAA wall specimens in our

---

[1]https://www.synopsys.com/simpleware/software/scanip.html (accessed January 19, 2022)
[2]https://coreform.com/products/coreform-cubit/ (accessed January 19, 2022)

database and leading to hexahedral elements of shape 1.6 mm × 1.6 mm × t_{w} for the AAA wall. The meshing procedure is also described in [59] in more detail. To reduce volumetric locking effects arising from the employed nearly incompressible material models, the F-bar element technology [95] is used for the hexahedral elements in the arterial wall as well as for the pyramid transition layer.

Prestressing and load control

To obtain a pressurized in-vivo configuration, the modified updated Lagrangian formulation (MULF) prestressing method [43, 46] is used, where the applied load corresponds to the mean arterial pressure $\bar{p}$ defined as

$$\bar{p} = \frac{1}{3}p_{\mathrm{sys}} + \frac{2}{3}p_{\mathrm{dia}}. \tag{2.56}$$

Using a standard load control approach, MULF generates a prestressed state to approximate the wall stress distribution for the geometry obtained at the time of CTA or MRA imaging. From this prestressed configuration, the pressure is raised by 50% to simulate elevated blood pressure conditions [107]. Following [83], the values for the systolic and diastolic pressures were set to $p_{\mathrm{sys}} = 121$ mmHg and $p_{\mathrm{dia}} = 87$ mmHg for all cases, respectively, resulting in a mean arterial pressure $\bar{p} = 98.33$ mmHg.

Performance aspects

Disregarding computational overhead associated with the assembly of $\mathbf{K}(\mathbf{D}^i)$ and $\mathbf{R}(\mathbf{D}^i)$ or input/output operations, the numerical costs C_{fw} (in terms of wall-clock time) for one deterministic forward solve are governed by the costs C_{lin} associated with the solution of the sparse and non-symmetric linear system[3] in Eq. (2.53) for the displacement increment $\Delta \mathbf{D}^{i+1}$, i.e.

$$C_{\mathrm{fw}} = C_{\mathrm{lin}} n_t \bar{n}_{\mathrm{iter}}, \tag{2.57}$$

where n_t is the number of time or load steps and $\bar{n}_{\mathrm{iter}}$ the average number of Newton iterations per time step. To keep C_{lin} at a minimum, a parallel implementation[4] of the generalized minimal residual method (GMRES) method [123] is used, which is preconditioned using algebraic multigrid (AMG) [45]. For a reduction of the factor $n_t \bar{n}_{\mathrm{iter}}$, the pseudo-transient continuation (PTC) scheme [44] has proven as a robust modification of the classical Newton scheme, allowing for larger steps.

2.2.3. Parameter to QoI map

The growth rate parameter $c_\vartheta(\underline{\mathbf{X}})$ is assumed an element-wise constant parameter c_ϑ, summarized in the vector $\mathbf{c}_\vartheta \in \mathbb{R}^{n_{\mathrm{el}}}$. Wall thickness t_{w}, alpha stiffness α_{w} and beta stiffness β_{w} are assumed spatially constant parameters. In the following, any combination of these model parameters will be summarized in the vector $\boldsymbol{\theta} = [\theta_1, \ldots, \theta_{n_\theta}]^{\mathsf{T}} \in \mathbb{R}^{n_\theta}$, where n_θ is the total number

---

[3]Non-symmetric contributions arise from the pressure load term and the employed F-bar element implementation.
[4]https://trilinos.github.io/aztecoo.html (accessed Januar 19, 2022).

of model parameters. A concrete specification of $\boldsymbol{\theta}$ will be provided in the different examples in Chapter 3.

Since usually only a limited number n_Q of QoI are of interest, the evaluation of the deterministic forward problem is denoted by means of a parameter-to-QoI map

$$Q : \boldsymbol{\theta} \mapsto Q(\boldsymbol{\theta}) \quad \text{with} \quad Q : \mathbb{R}^{n_\theta} \to \mathbb{R}^{n_Q}. \tag{2.58}$$

In the context of rupture risk prediction, the relevant QoI is the maximum von Mises stress $\sigma_{\mathrm{vm}}^{\max}$, which is computed as a postprocessing step from the displacements $\mathbf{D}$, so that with

$$Q = \sigma_{\mathrm{vm}}^{\max} = \sigma_{\mathrm{vm}}^{\max}(\mathbf{D}(\boldsymbol{\theta})) = \sigma_{\mathrm{vm}}^{\max}(\boldsymbol{\theta}) \tag{2.59}$$

the evaluation of the QoI at parameters $\boldsymbol{\theta}$ is denoted, where

$$\sigma_{\mathrm{vm}}^{\max} : \boldsymbol{\theta} \mapsto \sigma_{\mathrm{vm}}^{\max}(\boldsymbol{\theta}) \quad \text{with} \quad \sigma_{\mathrm{vm}}^{\max} : \mathbb{R}^{n_\theta} \to \mathbb{R}^{+}. \tag{2.60}$$

2.2.4. Calculation of parameter gradients using the adjoint method

Frequently, UQ methods that make use of gradient information of the QoI or some objective function $f(\mathbf{D}, \boldsymbol{\theta})$, i.e.

$$\nabla_{\boldsymbol{\theta}} \, \sigma_{\mathrm{vm}}^{\max} = \frac{\mathrm{d}\sigma_{\mathrm{vm}}^{\max}}{\mathrm{d}\boldsymbol{\theta}} = \left[\frac{\mathrm{d}\sigma_{\mathrm{vm}}^{\max}}{\mathrm{d}\theta_1}, \dots, \frac{\mathrm{d}\sigma_{\mathrm{vm}}^{\max}}{\mathrm{d}\theta_{n_\theta}} \right]^{\mathsf{T}} \tag{2.61}$$

or

$$\nabla_{\boldsymbol{\theta}} \, f = \frac{\mathrm{d}f}{\mathrm{d}\boldsymbol{\theta}} = \left[\frac{\mathrm{d}f}{\mathrm{d}\theta_1}, \dots, \frac{\mathrm{d}f}{\mathrm{d}\theta_{n_\theta}} \right]^{\mathsf{T}}, \tag{2.62}$$

are preferred due to their superior performance and effectiveness. When dealing with nonlinear systems such as the one in Eq. (2.48), where one evaluation is associated with a considerable amount of numerical costs and where the number of model parameters n_θ is potentially very high, the adjoint method is the method of choice for gradient calculation.

Adjoint formulation for discrete, quasi-static problems

Let $f(\mathbf{D}, \boldsymbol{\theta})$ be a scalar objective function of the n_{dof} degrees of freedom $\mathbf{D}$ and n_θ model parameters $\boldsymbol{\theta}$, where

$$f : (\mathbf{D}, \boldsymbol{\theta}) \mapsto f(\mathbf{D}, \boldsymbol{\theta}) \quad \text{with} \quad f : \mathbb{R}^{n_{\mathrm{dof}}} \times \mathbb{R}^{n_\theta} \to \mathbb{R}. \tag{2.63}$$

Furthermore, let $f(\mathbf{D}, \boldsymbol{\theta})$ be subject to the conditions $\mathbf{R}(\mathbf{D}, \boldsymbol{\theta}) = \mathbf{0}$ from the discretized PDE. Then, following the Lagrangian formulation in Section 2.1.4, the objective function can be rewritten as

$$L(\mathbf{D}, \boldsymbol{\theta}, \boldsymbol{\Lambda}) = f(\mathbf{D}, \boldsymbol{\theta}) + \boldsymbol{\Lambda}^{\mathsf{T}} \mathbf{R}(\mathbf{D}, \boldsymbol{\theta}), \tag{2.64}$$

where

$$L : (\mathbf{D}, \boldsymbol{\theta}, \boldsymbol{\Lambda}) \mapsto L(\mathbf{D}, \boldsymbol{\theta}, \boldsymbol{\Lambda}) \quad \text{with} \quad L : \mathbb{R}^{n_{\mathrm{dof}}} \times \mathbb{R}^{n_\theta} \times \mathbb{R}^{n_{\mathrm{dof}}} \to \mathbb{R} \tag{2.65}$$

and $\boldsymbol{\Lambda} \in \mathbb{R}^{n_{\mathrm{dof}}}$ is a vector of n_{dof} Lagrange parameters. Here, $\boldsymbol{\Lambda}$ can be associated with the virtual displacements $\delta\mathbf{D}$, cf. Eq. (2.47). Taking into account the dependency $\mathbf{D} = \mathbf{D}(\boldsymbol{\theta})$, the total derivative with respect to the model parameters becomes

$$\begin{aligned} \frac{\mathrm{d}L(\mathbf{D}, \boldsymbol{\theta}, \boldsymbol{\Lambda})}{\mathrm{d}\boldsymbol{\theta}} &= \frac{\partial f}{\partial \mathbf{D}} \frac{\partial \mathbf{D}}{\partial \boldsymbol{\theta}} + \frac{\partial f}{\partial \boldsymbol{\theta}} + \boldsymbol{\Lambda}^\mathsf{T} \left[\frac{\partial \mathbf{R}}{\partial \mathbf{D}} \frac{\partial \mathbf{D}}{\partial \boldsymbol{\theta}} + \frac{\partial \mathbf{R}}{\partial \boldsymbol{\theta}} \right] = \\ &= \left[\frac{\partial f}{\partial \mathbf{D}} + \boldsymbol{\Lambda}^\mathsf{T} \frac{\partial \mathbf{R}}{\partial \mathbf{D}} \right] \frac{\partial \mathbf{D}}{\partial \boldsymbol{\theta}} + \frac{\partial f}{\partial \boldsymbol{\theta}} + \boldsymbol{\Lambda}^\mathsf{T} \frac{\partial \mathbf{R}}{\partial \boldsymbol{\theta}}. \end{aligned} \tag{2.66}$$

Since Eq. (2.47) holds for an arbitrary choice of $\delta\mathbf{D}$, the idea is to choose $\boldsymbol{\Lambda}$ such that the term involving the intractable derivative $\partial\mathbf{D}/\partial\boldsymbol{\theta}$ vanishes. This can be achieved by solving a linear system of equations, the so-called adjoint problem,

$$\frac{\partial \mathbf{R}}{\partial \mathbf{D}}^\mathsf{T} \boldsymbol{\Lambda} = \mathbf{K}^\mathsf{T}\boldsymbol{\Lambda} = -\frac{\partial f}{\partial \mathbf{D}} \tag{2.67}$$

for the parameters $\boldsymbol{\Lambda}$, resulting in the adjoint-based derivative

$$\frac{\mathrm{d}f(\mathbf{D}(\boldsymbol{\theta}), \boldsymbol{\theta})}{\mathrm{d}\boldsymbol{\theta}} = \frac{\mathrm{d}L(\mathbf{D}(\boldsymbol{\theta}), \boldsymbol{\theta})}{\mathrm{d}\boldsymbol{\theta}} = \frac{\partial f}{\partial \boldsymbol{\theta}} + \boldsymbol{\Lambda}^\mathsf{T} \frac{\partial \mathbf{R}}{\partial \boldsymbol{\theta}}. \tag{2.68}$$

The equivalence of $\mathrm{d}f/\mathrm{d}\boldsymbol{\theta}$ and $\mathrm{d}L/\mathrm{d}\boldsymbol{\theta}$ evolves from the fact that the total derivative $\mathrm{d}\mathbf{R}/\mathrm{d}\boldsymbol{\theta}$ must always be zero, such that the governing equations are satisfied [81]. Above, the assumption was made that the objective function only depends on the last displacement state. An extension to objective functions that involve n_t intermediate states $\{\mathbf{D}_t\}_{t=1}^{n_t}$ is straightforward. The objective function is rewritten as

$$L(\{\mathbf{D}_t\}_{t=1}^{n_t}, \boldsymbol{\theta}, \{\boldsymbol{\Lambda}_t\}_{t=1}^{n_t}) = f(\{\mathbf{D}_t\}_{t=1}^{n_t}, \boldsymbol{\theta}) + \sum_{t=1}^{n_t} \boldsymbol{\Lambda}_t^\mathsf{T} \mathbf{R}_t(\mathbf{D}_t, \boldsymbol{\theta}) \tag{2.69}$$

and there are n_t adjoint equation that need to be solved,

$$\frac{\partial \mathbf{R}_t}{\partial \mathbf{D}_t}^\mathsf{T} \boldsymbol{\Lambda}_t = \mathbf{K}_t^\mathsf{T}\boldsymbol{\Lambda}_t = -\frac{\partial f}{\partial \mathbf{D}_t}, \tag{2.70}$$

resulting in the gradient

$$\frac{\mathrm{d}f(\{\mathbf{D}_t(\boldsymbol{\theta})\}_{t=1}^{n_t}, \boldsymbol{\theta})}{\mathrm{d}\boldsymbol{\theta}} = \frac{\partial f}{\partial \boldsymbol{\theta}} + \sum_{t=1}^{n_t} \boldsymbol{\Lambda}_t^\mathsf{T} \frac{\partial \mathbf{R}_t}{\partial \boldsymbol{\theta}}. \tag{2.71}$$

For further theoretical considerations of the adjoint method, it is being referred to [129].

Practical considerations

While the derivative of the residuals **R** with respect to the displacements **D** can be identified as the well-known stiffness matrix **K**, there are three terms that require a manual derivation if no automatic differentiation tools are available:

$$\frac{\partial f}{\partial \mathbf{D}}, \quad \frac{\partial f}{\partial \boldsymbol{\theta}} \quad \text{and} \quad \frac{\partial \mathbf{R}}{\partial \boldsymbol{\theta}}. \tag{2.72}$$

Analytical expressions for these terms are presented in Section 2.5.5 and Section 2.5.7, when gradients appear in the context of UQ methods. To solve the adjoint problem in Eq. (2.67), the conditions $\mathbf{R}(\mathbf{D}(\boldsymbol{\theta}), \boldsymbol{\theta}) = \mathbf{0}$ need to be satisfied, which requires the solution of a standard forward problem. For time-dependent problems, if the objective function depends only on the last time step $f = f(\mathbf{D}_{n_t}, \boldsymbol{\theta})$, this means that only the corresponding adjoint problem needs to be solved for $\boldsymbol{\Lambda}_{n_t}$, since for all other time steps, $\boldsymbol{\Lambda}_t = \mathbf{0}$, $t = 1 \dots n_t - 1$. As mentioned before, the numerical costs for the solution of one forward problem $C_{\mathrm{fw}} = C_{\mathrm{lin}} n_t \bar{n}_{\mathrm{iter}}$ is governed by the effort C_{lin} it takes to solve the linear systems during each Newton iteration. For the calculation of $\nabla_{\boldsymbol{\theta}}\, \sigma_{\mathrm{vm}}^{\max}(\boldsymbol{\theta})$ or $\nabla_{\boldsymbol{\theta}}\, f(\boldsymbol{\theta})$, the costs using the adjoint method only increase by an additional linear system solve as

$$C_{\nabla_{\boldsymbol{\theta}}}^{\mathrm{ad}} = C_{\mathrm{fw}} + C_{\mathrm{lin}}. \tag{2.73}$$

The costs using finite differences (FD), on the other hand, are

$$C_{\nabla_{\boldsymbol{\theta}}}^{\mathrm{fd}} = C_{\mathrm{fw}} + n_\theta C_{\mathrm{fw}}, \tag{2.74}$$

making it obvious that the FD method is only a feasible choice for a very low number of parameters n_θ.

2.3. Stochastic AAA model

With the mathematical and numerical models in Section 2.1 and Section 2.2 it is possible to compute the mechanical state of an AAA given its exact geometry and model parameters $\boldsymbol{\theta}$. Since this is practically impossible for a prospective AAA patient, this thesis follows a probabilistic approach in order to deal with uncertainties. To that end, below some fundamental aspects of modern probability theory are presented. Afterwards, the general stochastic forward problem for QoI is formulated, as well as two types of inverse problems: the classical Bayesian inverse problem and a stochastic inverse problem based on density-matching. Corresponding applications in the context of an AAA rupture risk assessment are shortly introduced.

2.3.1. Fundamentals of probability theory

This introduction is based on the works [56, 74]. For an extensive reference book on modern probability theory, it is being referred to [11]. A more concise and practical treatment can be found in [32, 129].

Let $(\Omega, \mathcal{A}, \mathbb{P})$ be a complete probability space, where Ω is the sample space, $\mathcal{A}$ the associated σ-algebra and $\mathbb{P}$ a probability measure. The sample space Ω and probability measure $\mathbb{P}$ are abstract constructs and not further specified. They can be regarded as modeling the sources of uncertainties responsible for the random variables that can be observed and eventually end up in a model. A n-variate random variable X is defined as a measurable function of the elements $\omega \in \Omega$

$$X : \omega \mapsto X(\omega) \quad \text{with} \quad X : \Omega \to \mathcal{X} \subset \mathbb{R}^n, \tag{2.75}$$

such that the inverse image $X^{-1}(A) = \{\omega \in \Omega \mid X(\omega) \in A\}$ satisfies

$$X^{-1}(A) \in \mathcal{A} \quad \forall A \in \mathcal{B}_{\mathcal{X}} \tag{2.76}$$

and where $\mathcal{B}_{\mathcal{X}}$ is the Borel-σ-algebra induced by X [56]. It is being noted that in contrast to the inverse function $X^{-1}(X(\omega))$, which only exists in special cases, the inverse image $X^{-1}(A)$ always exists. For $n > 1$, X is also called a random vector. Together with the push-forward probability measure $\mathbb{P}_{\mathcal{X}}$ induced by X, the probability space $(\mathcal{X}, \mathcal{B}_{\mathcal{X}}, \mathbb{P}_{\mathcal{X}})$ is obtained [56]. Probability can then be defined by the function

$$\mathbb{P}_{\mathcal{X}} : A \mapsto \mathbb{P}_{\mathcal{X}}(A), \tag{2.77}$$

which assigns any subset $A \subset \mathcal{X}$, which is part of $\mathcal{B}_{\mathcal{X}}$, a value $\mathbb{P}_{\mathcal{X}}(A)$. It has the properties [129]

$$0 \le \mathbb{P}_{\mathcal{X}}(A) \le 1 \quad \forall A \in \mathcal{B}_{\mathcal{X}} \quad \text{with} \quad \mathbb{P}_{\mathcal{X}}(\mathcal{X}) = 1, \quad \mathbb{P}_{\mathcal{X}}(\emptyset) = 0 \tag{2.78}$$

and

$$\mathbb{P}_{\mathcal{X}}\Big(\bigcup_{i=1}^{\infty} A_i\Big) = \sum_{i=1}^{\infty} \mathbb{P}_{\mathcal{X}}(A_i) \text{ for } A_i \in \mathcal{B}_{\mathcal{X}} \text{ and } \{A_i\}_{i=1}^{\infty} \text{ pairwise disjoint.} \tag{2.79}$$

Thus, the value $\mathbb{P}_{\mathcal{X}}(A)$ denotes the probability that an element $x \in \mathcal{X}$ lies in the subset $A \in \mathcal{B}_{\mathcal{X}}$, or simply speaking the probability that event A happens. It is being assumed that all probability measures that are made use of in this work are absolutely continuous with respect to the Lebesgue measure, i.e. the standard volume measure, such that they have an associated probability density function (PDF)

$$\pi_{\mathcal{X}} : x \mapsto \pi_{\mathcal{X}}(x), \quad \text{with} \quad \pi_{\mathcal{X}} : \mathcal{X} \to [0, \infty[. \tag{2.80}$$

This allows to express the probability $\mathbb{P}_{\mathcal{X}}(A)$ in terms of a volume integral

$$\mathbb{P}_{\mathcal{X}}(A) = \int_A \mathrm{d}\mathbb{P}_{\mathcal{X}} = \int_A \pi_{\mathcal{X}}(x) \, \mathrm{d}x = \int \mathbb{1}_A(x) \, \pi_{\mathcal{X}}(x) \, \mathrm{d}x \quad \forall A \in \mathcal{B}_{\mathcal{X}}, \tag{2.81}$$

where $\mathbb{1}_A : \mathcal{X} \to \{0, 1\}$ is the indicator function

$$\mathbb{1}_A(x) = \begin{cases} 1 & \text{if } x \in A \\ 0 & \text{if } x \notin A \end{cases} \quad \forall x \in \mathcal{X}. \tag{2.82}$$

Calculations with random variables

In practice, the specification of $\mathbb{P}_\mathcal{X}$ is often part of an uncertainty modeling process for input parameters to a model, such that the random variables are transformed to m-dimensional model outputs $Y(X)$ as

$$Y : X \mapsto Y(X) \quad \text{with} \quad Y : \mathcal{X} \to \mathcal{Y} \subset \mathbb{R}^m. \tag{2.83}$$

Assuming Y is measurable, cf. Eq. (2.76), leads to the induced probability space $(\mathcal{Y}, \mathcal{B}_\mathcal{Y}, \mathbb{P}_\mathcal{Y})$ with the Borel-σ-algebra $\mathcal{B}_\mathcal{Y}$ and the push-forward probability measure $\mathbb{P}_\mathcal{Y}$. The calculation of integrals over a measurable function $f : y \mapsto f(y)$ with $f : \mathcal{Y} \to \mathbb{R}$ can then be carried out with respect to either measure $\mathbb{P}_\mathcal{X}$ or $\mathbb{P}_\mathcal{Y}$ using the relation

$$\int_B f(y) \, \mathrm{d}\mathbb{P}_\mathcal{Y} = \int_{Y^{-1}(B)} f(Y(x)) \, \mathrm{d}\mathbb{P}_\mathcal{X} \quad \forall B \in \mathcal{B}_\mathcal{Y}, \tag{2.84}$$

or, written in terms of PDFs

$$\int_B f(y) \, \pi_\mathcal{Y}(y) \, \mathrm{d}y = \int_{Y^{-1}(B)} f(Y(x)) \, \pi_\mathcal{X}(x) \, \mathrm{d}x \quad \forall B \in \mathcal{B}_\mathcal{Y}. \tag{2.85}$$

In practice, one can think about X as model inputs, Y as model outputs and f some function of the model outputs. Fundamental characteristics of random variables are:

- The expected value or mean value of the random variable X with respect to $\mathbb{P}_\mathcal{X}$:

$$\mathbb{E}_{\mathbb{P}_\mathcal{X}}[X] = \int x \, \pi_\mathcal{X}(x) \, \mathrm{d}x. \tag{2.86}$$

- The variance of the random variable X with respect to $\mathbb{P}_\mathcal{X}$:

$$\mathbb{V}_{\mathbb{P}_\mathcal{X}}[X] = \int (x - \mathbb{E}_{\mathbb{P}_\mathcal{X}}[X])^2 \, \pi_\mathcal{X}(x) \, \mathrm{d}x = \mathbb{E}_{\mathbb{P}_\mathcal{X}}[X^2] - (\mathbb{E}_{\mathbb{P}_\mathcal{X}}[X])^2. \tag{2.87}$$

- The covariance between two random variables X_1 and X_2 with respect to $\mathbb{P}_{\mathcal{X}_1, \mathcal{X}_2}$:

$$\begin{aligned} \mathrm{Cov}_{\mathbb{P}_{\mathcal{X}_1, \mathcal{X}_2}}(X_1, X_2) &= \int (x_1 - \mathbb{E}_{\mathbb{P}_{\mathcal{X}_1}}[X_1])(x_2 - \mathbb{E}_{\mathbb{P}_{\mathcal{X}_2}}[X_2]) \, \pi_{\mathcal{X}_1, \mathcal{X}_2}(x_1, x_2) \, \mathrm{d}x_1 \, \mathrm{d}x_2 \\ &= \mathbb{E}_{\mathbb{P}_{\mathcal{X}_1, \mathcal{X}_2}}[X_1 X_2] - \mathbb{E}_{\mathbb{P}_{\mathcal{X}_1}}[X_1] \, \mathbb{E}_{\mathbb{P}_{\mathcal{X}_2}}[X_2]. \end{aligned} \tag{2.88}$$

Conditional probability and Bayes' rule

An important concept is conditional probability. For $A_2 \in \mathcal{B}_\mathcal{X}$ with $\mathbb{P}_\mathcal{X}(A_2) > 0$, the conditional probability is defined as

$$\mathbb{P}_\mathcal{X}(A_1|A_2) = \frac{\mathbb{P}_\mathcal{X}(A_1 \cap A_2)}{\mathbb{P}_\mathcal{X}(A_2)} \quad \forall A_1 \in \mathcal{B}_\mathcal{X}. \tag{2.89}$$

The value $\mathbb{P}_\mathcal{X}(A_1|A_2)$ denotes the probability that event A_1 happens, given that event A_2 has happened. This concept gives rise to Bayes' rule, a formula to compute the conditional probability as

$$\mathbb{P}_\mathcal{X}(A_1|A_2) = \frac{\mathbb{P}_\mathcal{X}(A_2|A_1)\,\mathbb{P}_\mathcal{X}(A_1)}{\mathbb{P}_\mathcal{X}(A_2)} \tag{2.90}$$

In this context, $\mathbb{P}_\mathcal{X}(A_1|A_2)$ is called posterior and $\mathbb{P}_\mathcal{X}(A_1)$ prior probability. $\mathbb{P}_\mathcal{X}(A_1)$ can be thought of as an initial (prior) understanding of the probability of event A_1 happening, while $\mathbb{P}_\mathcal{X}(A_1|A_2)$ is the updated (posterior) probability, given new information (knowing that A_2 has happened). Conditional probability can also be written in terms of densities. To that end, making use of the two random variables X and Y with elements $x \in \mathcal{X}$ and $y \in \mathcal{Y}$, the conditional probability of A knowing $Y = y$ is

$$\mathbb{P}_\mathcal{X}(A|Y = y) = \int_A \pi_\mathcal{X}(x|y)\,\mathrm{d}x, \quad \forall A \in \mathcal{B}_\mathcal{X}. \tag{2.91}$$

The introduced conditional PDF $\pi_\mathcal{X}(x|y)$ is defined as

$$\pi_\mathcal{X}(x|y) = \frac{\pi_{\mathcal{X},\mathcal{Y}}(x,y)}{\pi_\mathcal{Y}(y)} \tag{2.92}$$

with the joint PDF $\pi_{\mathcal{X},\mathcal{Y}} : \mathcal{X} \times \mathcal{Y} \to [0, \infty[$. This allows the expression of Bayes' rule in terms of densities

$$\pi_\mathcal{X}(x|y) = \frac{\pi_\mathcal{Y}(y|x)\,\pi_\mathcal{X}(x)}{\pi_\mathcal{Y}(y)}, \tag{2.93}$$

where

- $\pi_\mathcal{X}(x|y)$ is the posterior PDF,

- $\pi_\mathcal{X}(x)$ the prior PDF,

- $\pi_\mathcal{Y}(y|x)$ the likelihood and

- $\pi_\mathcal{Y}(y) = \int \pi_\mathcal{Y}(y|x)\,\pi_\mathcal{X}(x)\,\mathrm{d}x$ the integration constant referred to as the model evidence.

Since $\pi_\mathcal{Y}(y)$ is constant with respect to x, the posterior density is often denoted as

$$\pi_\mathcal{X}(x|y) \propto \pi_\mathcal{Y}(y|x)\,\pi_\mathcal{X}(x). \tag{2.94}$$

Random processes

A random or stochastic process $X_\tau(\omega) = X(\tau, \omega)$ with

$$X : (\tau, \omega) \mapsto X(\tau, \omega), \quad X : \mathcal{T} \times \Omega \to \mathbb{R}^n, \tag{2.95}$$

is a function of two parameters $\tau \in \mathcal{T}$ and $\omega \in \Omega$ such that $\{X_\tau(\omega), \ \tau \in \mathcal{T}\}$ is a collection of random variables on a common probability space $(\Omega, \mathcal{A}, \mathbb{P})$. The set $\mathcal{T}$ can, e.g., represent a sequence ($\mathcal{T} = \mathbb{N}$), time ($\mathcal{T} = \mathbb{R}^+$) or space ($\mathcal{T} = \mathbb{R}^3$). If $n > 1$, $X_\tau(\omega)$ is called a multivariate random process. For a fixed $\omega \in \Omega$, the function $X_\tau : \tau \mapsto X_\tau(\omega)$ is called the path of ω and is also referred to as a realization of the random process. Random processes can be described in terms of the probability distributions they induce on a finite subset of random variables. For instance, a Gaussian process implies that the random vector $[X_1, X_2, \ldots, X_n]^\mathsf{T}$ follows a n-variate Gaussian distribution. The additional parameter τ makes random processes a popular modeling tool for physical problems involving spatially or temporally varying uncertainties.

Simplified notation

In most cases, the argument of a PDF or expected value already implies the associated probability measure, such that additional subscripts are not necessary. While these are adequate for specific purposes, the notation will be simplified whenever this seems appropriate for the remainder of this work. For example, by $\pi(x)$ the PDF associated with the random variable X and the probability space $(\mathcal{X}, \mathcal{B}_\mathcal{X}, \mathbb{P}_\mathcal{X})$ is denoted. Furthermore, the expectation, variance and covariance of random variables will simply be denoted by $\mathbb{E}[X]$, $\mathbb{V}[X]$ and $\mathrm{Cov}[X_1, X_2]$, respectively.

An analogy to solid mechanics

For a structural mechanics engineer, it may be helpful to think of a probability measure $\mathbb{P}$ as a more familiar type of measure like mass or area in order not to get too intimidated by the abstract formalism of probability theory. For example, let $\Omega_0 \subset \mathbb{R}^3$ be the set of points defining the reference configuration of a continuum (cf. Section 2.1). Then, one can define a measure $\mu_m : A \mapsto \mu_m(A)$, which assign any reasonable part $A \subset \Omega_0$ of the body a mass $\mu_m(A)$, while the total mass m_{Ω_0} of the continuous body is $\mu_m(\Omega_0)$. The term "reasonable part" is the actual reason, why σ-algebras had to be introduced, since formally there cannot exist a measure which is able to assign a value to *any* $A \subset \Omega_0$ [56]. Like the probability measures above, μ_m can be associated with a density $\rho_0 : \Omega_0 \to [0, \infty[$.

Instead of allowing any measurable function between the reference configuration $\underline{X}$ and the current configuration $\underline{x}$, however, there are tighter requirements on $\underline{x}(\underline{X})$, cf. the deformation map in Eq. (2.1). The total mass can be computed with respect to the density ρ_0 in the reference or ρ in the current configuration as

$$\mu_m(\Omega) = m_{\Omega_0} = \int_\Omega \rho(\underline{x}) \, \mathrm{d}\underline{x} = \int_{\Omega_0} \rho_0(\underline{X}) \, \mathrm{d}\underline{X} \tag{2.96}$$

with $\rho_0(\underline{X}) = J\rho(\underline{x})$, resembling the calculation with respect to different measures in Eq. (2.85) and $\mathrm{d}\underline{X} = \mathrm{d}V$ implying a volume integral. The only difference between $\mathbb{P}$ and μ_m is that the

probability measure is normalized. Moreover, the center of mass $\underline{\boldsymbol{x}}_c$ can be associated with the expected value of a random variable as

$$\underline{\boldsymbol{x}}_{\mathrm{c}} = \frac{1}{m_{\Omega_0}} \int_{\Omega} \underline{\boldsymbol{x}}\, \rho(\underline{\boldsymbol{x}})\, \mathrm{d}\underline{\boldsymbol{x}}, \tag{2.97}$$

implying that $\underline{\boldsymbol{x}}_c$ is the expected value of $\underline{\boldsymbol{x}}$, cf. Eq. (2.86), with respect to the mass measure μ_m divided by m_{Ω_0}. As a last example, the moment of inertia can be associated with the variance and covariance from Eq. (2.87) and Eq. (2.88), respectively. Consider the I_{11} entry of the inertia tensor from solid mechanics

$$I_{11} = \int_{\Omega} (x_2^2 + x_3^2)\, \rho(\underline{\boldsymbol{x}})\, \mathrm{d}\underline{\boldsymbol{x}} = \int_{\Omega} x_2^2\, \rho(\underline{\boldsymbol{x}})\, \mathrm{d}\underline{\boldsymbol{x}} + \int_{\Omega} x_3^2\, \rho(\underline{\boldsymbol{x}})\, \mathrm{d}\underline{\boldsymbol{x}}. \tag{2.98}$$

This expression corresponds to the sum of the variances $\mathbb{V}[X_2] + \mathbb{V}[X_3]$ of two random variables X_2 and X_3 with zero mean. Likewise,

$$I_{12} = \int_{\Omega} x_1 x_2\, \rho(\underline{\boldsymbol{x}})\, \mathrm{d}\underline{\boldsymbol{x}} \tag{2.99}$$

is equal to the covariance $\mathrm{Cov}(X_1, X_2)$ of two zero mean random variables X_1 and X_2. Thus, just like the center of mass and moment of inertia are characteristics of a continuous body, the expected value, variance and covariance are characteristics of random variables.

2.3.2. Stochastic forward problem

The stochastic forward problem is the determination of the push-forward probability measure $\mathbb{P}_{\mathcal{Y}}$ of a probability measure $\mathbb{P}_{\mathcal{X}}$ under the transformation Y, such that [22]

$$\mathbb{P}_{\mathcal{Y}}(B) = \mathbb{P}_{\mathcal{X}}(Y^{-1}(B)) \quad \forall B \in \mathcal{B}_{\mathcal{Y}}. \tag{2.100}$$

For practical cases it suffices to generate samples from the PDF $\pi_{\mathcal{Y}}$ associated with $\mathbb{P}_{\mathcal{Y}}$ such that one can resort to Monte Carlo (MC) approximation methods (cf. Section 2.5.3). Recalling the QoI map from Eq. (2.58), the model parameters $\boldsymbol{\theta} \in \mathbb{R}^{n_\theta}$ are identified as random variables transformed via the function $Y = Q(\boldsymbol{\theta})$, where $Q \in \mathbb{R}^{n_Q}$. A typical task is to calculate the probability that Q lies in some region B

$$\mathbb{P}(B) = \int \mathbb{1}_B(Q)\, \pi(Q)\, \mathrm{d}Q = \int \mathbb{1}_B(Q(\boldsymbol{\theta}))\, \pi(\boldsymbol{\theta})\, \mathrm{d}\boldsymbol{\theta} \tag{2.101}$$

or to compute the expected value of Q

$$\mathbb{E}[Q] = \int Q\, \pi(Q)\, \mathrm{d}Q = \int Q(\boldsymbol{\theta})\, \pi(\boldsymbol{\theta})\, \mathrm{d}\boldsymbol{\theta}. \tag{2.102}$$

More concrete examples will be discussed in detail in Section 2.4 in the context of biomechanical rupture risk assessment, while different strategies for approximating $\pi(Q)$ are presented in Section 2.5.

2.3.3. Bayesian inverse problem

The Bayesian approach to inverse problems results in a conditional measure

$$\mathbb{P}(A|Y = y) = \int \mathbb{1}_A(x)\,\pi(x|y)\,\mathrm{d}x \quad \forall A \in \mathcal{B}_\mathcal{X} \tag{2.103}$$

on the model input parameters X given a realization $Y = y$. In that sense, the posterior density $\pi(x|y)$ from Eq. (2.93) represent the solution to the inverse problem [67]. For any practical purposes, however, the posterior is usually not available in closed form, such that the biggest challenge in Bayesian inverse problems lies in the calculation of characteristics of the density $\pi(x|y)$, e.g. by generating samples using Markov chain Monte Carlo (MCMC) methods. Different methods addressing this challenge are presented in Section 2.5.5.

For the specification of the posterior in order to obtain growth parameters for the AAA vessel wall, the modeling approach from [68, 69] is being followed. While model parameters X are denoted by $\boldsymbol{\theta}$ as before, the realizations $Y = y$ are measurements from CTA and denoted by $\hat{\mathbf{S}}$. Both the model-predicted surfaces $\mathbf{S} = \mathbf{S}(\mathbf{D}(\boldsymbol{\theta}))$ and the surface measurements $\hat{\mathbf{S}}$ are represented via a triangulation [68]. The log posterior $\log \pi(\boldsymbol{\theta}|\hat{\mathbf{S}})$ becomes

$$\log \pi(\boldsymbol{\theta}|\hat{\mathbf{S}}) \propto \log \pi(\hat{\mathbf{S}}|\boldsymbol{\theta}) + \log \pi(\boldsymbol{\theta}), \tag{2.104}$$

where $\pi(\hat{\mathbf{S}}|\boldsymbol{\theta})$ denotes the likelihood and $\pi(\boldsymbol{\theta})$ the prior. The likelihood is formulated using a surface currents based similarity measure [68] as

$$\log \pi(\hat{\mathbf{S}}|\boldsymbol{\theta}) \propto -\frac{\|\hat{\mathbf{S}} - \mathbf{S}(\mathbf{D}(\boldsymbol{\theta}))\|_{\mathcal{W}^\star}^2}{2\sigma_N^2} = f_\ell(\mathbf{D}(\boldsymbol{\theta})), \tag{2.105}$$

with the measurement noise parameter σ_N. A total variation (TV) regularization prior [68] is chosen as

$$\log \pi(\boldsymbol{\theta}) \propto -\alpha_{\mathrm{tv}} \sum_{i=1}^{n_{\mathrm{el}}} \left[\sum_{j=1}^{n_i} w_{ij} \,(\theta_j - \theta_i)^2 + \varepsilon_{\mathrm{tv}}^2 \right]^{\frac{1}{2}} = f_p(\boldsymbol{\theta}), \tag{2.106}$$

with the weight w_{ij} attributed to the two parameters θ_i and θ_j, the number of parameters n_i adjacent to θ_i and the hyperparameters α_{tv} and $\varepsilon_{\mathrm{tv}}$. For notational convenience, the objective function

$$f(\mathbf{D}(\boldsymbol{\theta}), \boldsymbol{\theta}) = f_\ell(\mathbf{D}(\boldsymbol{\theta})) + f_p(\boldsymbol{\theta}) \tag{2.107}$$

will frequently be employed in the rest of this work. According to Section 2.2.4, the computation of the objective function total derivative requires the solution of the adjoint problem

$$\frac{\partial \mathbf{R}}{\partial \mathbf{D}}^\top \boldsymbol{\Lambda} = -\frac{\partial f_\ell}{\partial \mathbf{D}} \tag{2.108}$$

and the evaluation of

$$\nabla_{\boldsymbol{\theta}} f(\boldsymbol{\theta}) = \frac{\mathrm{d} f(\mathbf{D}(\boldsymbol{\theta}), \boldsymbol{\theta})}{\mathrm{d}\boldsymbol{\theta}} = \frac{\partial f_p}{\partial \boldsymbol{\theta}} + \boldsymbol{\Lambda}^{\mathsf{T}} \frac{\partial \mathbf{R}}{\partial \boldsymbol{\theta}}. \tag{2.109}$$

For the derivatives of the prior associated term $f_p(\boldsymbol{\theta})$ with respect to $\boldsymbol{\theta}$ and the likelihood associated term $f_\ell(\mathbf{D}(\boldsymbol{\theta}))$ with respect to $\mathbf{D}$, it is being referred to [68]. In Section 2.5.5, an approach that makes use of gradients $\nabla_{\boldsymbol{\theta}} f(\boldsymbol{\theta})$ in the context of stochastic optimization and results in an approximate posterior density $\pi(\boldsymbol{\theta}|\hat{\mathbf{S}})$ is presented and later applied in the context of AAA growth in Section 3.4.

2.3.4. Stochastic inverse problem

In accordance with the terminology of the stochastic forward problem, the stochastic inverse problem is the determination of the probability measure $\mathbb{P}_{\mathcal{X}}$, such that the induced push-forward measure $\mathbb{P}_{\mathcal{Y}}$ satisfies [22]

$$\mathbb{P}_{\mathcal{X}}(Y^{-1}(B)) = \mathbb{P}_{\mathcal{Y}}(B) \quad \forall B \in \mathcal{B}_{\mathcal{Y}}. \tag{2.110}$$

For the QoI map $Q(\boldsymbol{\theta})$ this corresponds to finding a probability measure $\mathbb{P}_{\mathcal{X}}$ for $\boldsymbol{\theta} \in \mathbb{R}^{n_\theta}$ such that the push-forward measure corresponds to the probability measure $\mathbb{P}_{\mathcal{Y}}$ for $Q \in \mathbb{R}^{n_Q}$. Such a solution is called a consistent solution to an inverse problem in the sense that Eq. (2.110) is satisfied. The nature of this particular inverse problem renders it appropriate for the case, where $\mathbb{P}_{\mathcal{Y}}$ can be determined from repeated experiments in order to obtain a probability measure $\mathbb{P}_{\mathcal{X}}$ that represents the statistical properties of the tested samples.

This addresses the problem of determining a PDF for the mechanical properties of AAA tissue samples from a cohort of patients. In particular, let $\boldsymbol{\theta}$ denote the stiffness parameters α_{w} and β_{w} of the AAA wall material model and $Q(\boldsymbol{\theta})$ the numerical or analytical model of the tensile test, where $Q(\boldsymbol{\theta})$ represents some QoI that can be associated with the measurement data. The stochastic inverse problem seeks a density $\pi(\boldsymbol{\theta})$, such that its push-forward density $\pi(Q(\boldsymbol{\theta}))$ corresponds to the observed density $\pi(\hat{Q})$ of measured responses $\hat{Q}$ of the QoI. A strategy to compute $\pi(\boldsymbol{\theta})$ is presented in Section 2.5.6 and applied for the purposes of determining a cohort-based density $\pi(\alpha_{\mathrm{w}}, \beta_{\mathrm{w}})$ in Section A.4.

2.4. Biomechanical rupture risk assessment of AAAs

The following section is a revised version of part of the author's work published in [19]. From a mechanical point of view, rupture is an event of local material failure at a point $\boldsymbol{x}$ in the aneurysm wall, which motivates its definition via a failure function $\phi(\boldsymbol{x})$ and the failure criterion

$$\phi(\boldsymbol{x}) > 0, \text{ at any } \boldsymbol{x}. \tag{2.111}$$

Here, only stress-based failure is considered and rupture defined as an event where the local wall stress measure $\sigma(\boldsymbol{x})$ exceeds the local wall strength $\sigma_\gamma(\boldsymbol{x})$. This results in the failure function

$\phi(\boldsymbol{x}) = \sigma(\boldsymbol{x}) - \sigma_\gamma(\boldsymbol{x})$, or the criterion

$$\sigma(\boldsymbol{x}) > \sigma_\gamma(\boldsymbol{x}), \text{ at any } \boldsymbol{x}. \tag{2.112}$$

Using the equivalent von Mises stress $\sigma_{\mathrm{vm}}(\boldsymbol{x})$ as the local stress measure $\sigma(\boldsymbol{x})$ and an assumed spatially constant wall strength σ_γ, this criterion can be evaluated as

$$\sigma_{\mathrm{vm}}^{\max} > \sigma_\gamma, \tag{2.113}$$

where $\sigma_{\mathrm{vm}}^{\max}$ is the maximum von Mises stress $\sigma_{\mathrm{vm}}^{\max} = \max_{\boldsymbol{x}} \sigma_{\mathrm{vm}}(\boldsymbol{x})$.

Rupture risk estimation for AAAs has been an ongoing research topic over several decades, with many attempts to establish decision criteria for clinical practice. The maximum diameter criterion [24] still represents the most widely used criterion for decision making today. It is often justified by Laplace's law, which states that the vessel wall stress is proportional to its diameter in spherical geometries. Based on this and with data obtained from several clinical studies, a very simple criterion,

$$d > d_{\max}, \tag{2.114}$$

has been formulated, relating the patient's AAA diameter d to a critical maximum diameter $d_{\max}$. While established in clinical practice and easy to apply using CT or ultrasound imaging, this criterion has often been criticized [144] and is an ongoing subject for discussion [132]. This issue is exemplified by the intra- and inter-observer variabilities in measuring the maximum diameter [87].

With growing computational resources and advances in the modeling of biomechanical material behavior, the simulation of patient-specific AAA models has been advanced by several research groups. Experiments on harvested AAA samples were able to reveal material parameters and failure properties. In addition with regression models [114, 117, 141] for the prediction of the individual wall strength, this enabled the definition of biomechanics-based indices [37, 42, 83, 139], such as the rupture potential index (RPI)

$$\mathrm{RPI} = \frac{\sigma_{\mathrm{vm}}^{\max}}{\sigma_\gamma} \quad \text{or} \quad \mathrm{RPI}(\boldsymbol{x}) = \frac{\sigma_{\mathrm{vm}}(\boldsymbol{x})}{\sigma_\gamma(\boldsymbol{x})}, \tag{2.115}$$

relating the von Mises stress to the wall strength. Furthermore, it could be shown [30, 42, 83] that these indices can be better rupture risk indicators than the maximum diameter criterion. Experimental testing [114, 117, 141] also revealed significant inter- and intra-patient variabilities in the mechanical properties of AAA tissue, motivating a probabilistic approach to rupture risk estimation [5, 7, 107] and resulting in the probabilistic rupture risk index (PRRI) [107]

$$\mathrm{PRRI} = \int_0^\infty \int_{\sigma_\gamma}^\infty \pi(\sigma_{\mathrm{vm}}^{\max}) \, \mathrm{d}\sigma_{\mathrm{vm}}^{\max} \, \pi(\sigma_\gamma) \, \mathrm{d}\sigma_\gamma, \tag{2.116}$$

where the authors used densities for the wall thickness and wall strength that were fitted on data published in [117].

The current work proposes a probabilistic rupture risk indicator that consistently incorporates all available statistical information and accounts for correlations among vessel wall properties. Fig. 2.2 (left) illustrates the rationale for this approach, showing how part of the available data from a patient is directly involved in the estimation of the risk of rupture, while another part affects the evaluation of the computational model. In general, this data will be correlated, resulting in correlated quantities for the evaluation of the rupture risk. As a consequence, the PRRI from Eq. (2.116) will be inadequate, since it assumes an independence between the biomechanical model and the wall strength.
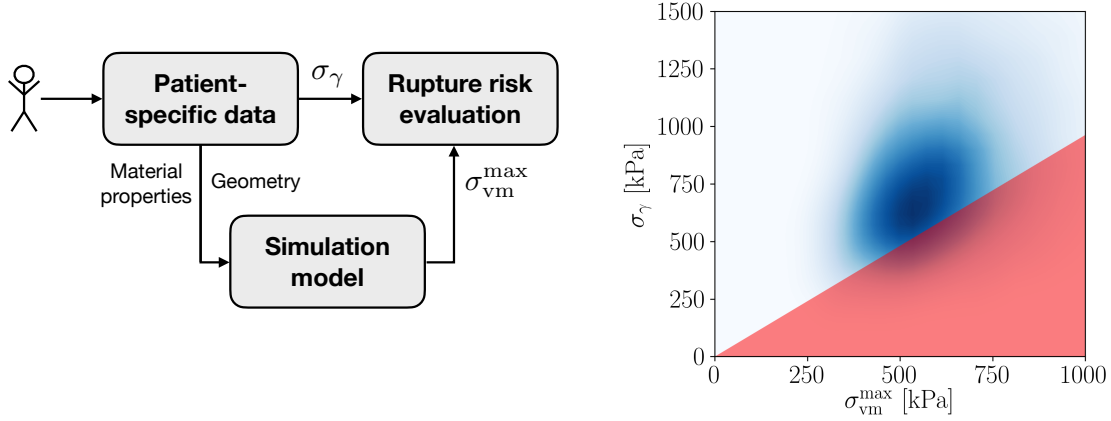
Figure 2.2.: Rationale for this novel formulation (left) and visualization of its estimation (right). The probability of rupture, $\mathbb{P}_{\mathrm{rupt}}$, is calculated as the volume of the PDF $\pi(\sigma_{\mathrm{vm}}^{\max}, \sigma_\gamma)$ within the triangular-shaped area marked in red. Reproduced with permission from [19].

To that end and recalling the rupture criterion from Eq. (2.113), the probability of rupture is calculated over the joint PDF $\pi(\sigma_{\mathrm{vm}}^{\max}, \sigma_\gamma)$ as

$$\mathbb{P}_{\mathrm{rupt}} = \int \mathbb{1}_{\sigma_{\mathrm{vm}}^{\max} > \sigma_\gamma} \, \pi(\sigma_{\mathrm{vm}}^{\max}, \sigma_\gamma) \, \mathrm{d}\sigma_{\mathrm{vm}}^{\max} \, \mathrm{d}\sigma_\gamma, \tag{2.117}$$

where $\mathbb{1}_{\sigma_{\mathrm{vm}}^{\max} > \sigma_\gamma}$ is defined as

$$\mathbb{1}_{\sigma_{\mathrm{vm}}^{\max} > \sigma_\gamma} = \begin{cases} 1 & \sigma_{\mathrm{vm}}^{\max} > \sigma_\gamma, \\ 0 & \text{otherwise.} \end{cases} \tag{2.118}$$

This formulation can be easily extended to, e.g., spatially varying vessel properties using Eq. (2.111) or Eq. (2.112) as failure events. Furthermore, it includes the PRRI in Eq. (2.116) as a special case, when choosing $\pi(\sigma_{\mathrm{vm}}^{\max}, \sigma_\gamma) = \pi(\sigma_{\mathrm{vm}}^{\max}) \, \pi(\sigma_\gamma)$. Lastly, it allows for a straightforward visual interpretation as illustrated in Fig. 2.2 (right). The plot shows the joint PDF $\pi(\sigma_{\mathrm{vm}}^{\max}, \sigma_\gamma)$ and visualizes the rupture event area in red. The blue area implies a high probability for the joint occurrence of the corresponding stress and strength values. The probability of rupture, $\mathbb{P}_{\mathrm{rupt}}$, is simply the volume of this density within the triangular rupture event area. Thus, the larger the overlap between $\pi(\sigma_{\mathrm{vm}}^{\max}, \sigma_\gamma)$ and the red area, the higher $\mathbb{P}_{\mathrm{rupt}}$.

Eq. (2.117) is general in the sense that it allows arbitrary models for $\sigma_{\mathrm{vm}}^{\max}$ and σ_γ. In particular, when growth of the AAA is taken into account, Eq. (2.117) can be evaluated over time, such that
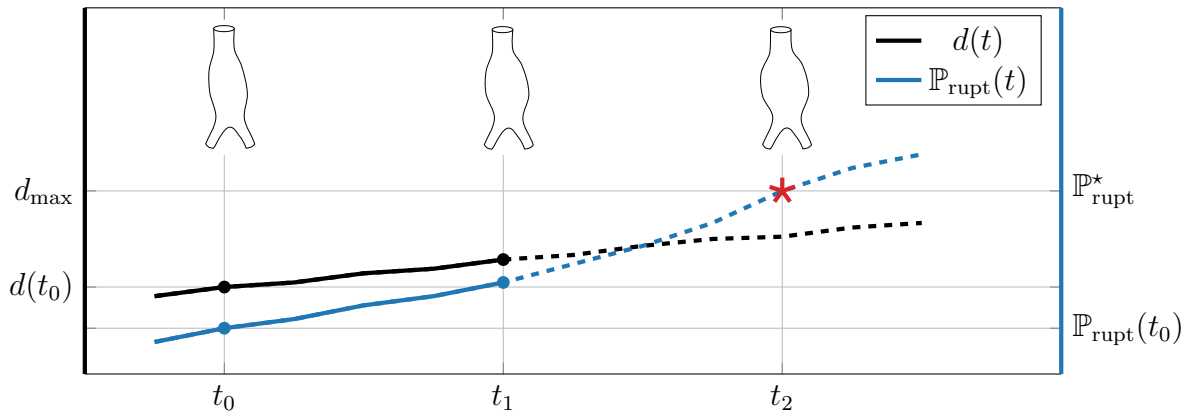
Figure 2.3.: Conceptual illustration for a predictive rupture risk assessment. Using a time-dependent biomechanical AAA model based on growth, both $\mathbb{P}_{\mathrm{rupt}}$ (blue, solid and dashed line) as well as the AAA maximum diameter d (black, solid and dashed) can be simulated and monitored over time. Here, the growth model involves a calibration phase based on consecutive CTA or MRA imaging (blue and black circles at t_0 and t_1) and a prediction phase. The plot shows exemplary model-estimated values for $\mathbb{P}_{\mathrm{rupt}}$ and d during the calibration (solid lines) as well as during the prediction phase (dashed lines). Surveillance intervals can be adapted individually and predictively based on when the rupture risk index exceeds the critical value $\mathbb{P}^{\star}_{\mathrm{rupt}}$ at a future point in time (indicated via the red star at t_2) or when $d(t)$ exceeds the value $d_{\max}$ from the maximum diameter criterion. Finally, the model may be re-calibrated at any time to increase the accuracy in the predictions given new clinical data.

a time-dependent probability of rupture $\mathbb{P}_{\mathrm{rupt}}(t)$ is obtained. Visually speaking and with regards to Fig. 2.2 (right), this allows an estimation about where the blue area representing $\pi(\sigma_{\mathrm{vm}}^{\max}, \sigma_{\gamma})$ moves over time. As a result, it is possible to identify trends about the progression of the AAA disease. While the interpretation of $\mathbb{P}_{\mathrm{rupt}}$ at one instance in time can be difficult (cf. Section 3.3), a negative trend in terms of an increasing probability of rupture can be directly translated to shorter surveillance intervals for that patient. A conceptual illustration for a predictive rupture risk assessment is described in Fig. 2.3.

2.5. Uncertainty quantification tools

This section introduces the Gaussian family of PDFs as well as different Gaussian processs (GPs) as statistical models in Section 2.5.1 and Section 2.5.2, respectively. Furthermore, the MC method (cf. Section 2.5.3) and a probabilistic multi-fidelity Monte Carlo (MFMC) (cf. Section 2.5.4) are presented in order to deal with stochastic forward problems. Strategies for Bayesian inverse problems are covered in Section 2.5.5 and consistent solutions to stochastic inverse problems in Section 2.5.6. Lastly, tools for dimensionality reduction of parameterized models are discussed in Section 2.5.7. There exist a variety of excellent books on modern UQ topics, which cover some of the presented methods or go far beyond the scope of this work. For a machine learning (ML) inspired approach, the works of [12, 93] are recommended. A more mathematical introduction is provided by [129].

2.5.1. Gaussian probability density functions

Univariate Gaussian

A random variable $X \in \mathbb{R}$ with the PDF

$$\pi(x) = \frac{1}{\sqrt{2\pi}\sigma} \exp\left[-\frac{1}{2}\left(\frac{x-\mu}{\sigma} \right)^2 \right] \tag{2.119}$$

is said to follow a Gaussian or normal distribution, denoted by $X \sim \mathcal{N}(\mu, \sigma^2)$, with mean $\mu \in \mathbb{R}$ and variance $\sigma^2 \in \mathbb{R}^+$.

Multivariate Gaussian

A random vector $X \in \mathbb{R}^n$ with the PDF

$$\pi(\boldsymbol{x}) = (2\pi)^{-\frac{n}{2}} |\boldsymbol{\Sigma}|^{-\frac{1}{2}} \exp\left[-\frac{1}{2}(\boldsymbol{x} - \boldsymbol{\mu})^{\mathsf{T}} \boldsymbol{\Sigma}^{-1} (\boldsymbol{x} - \boldsymbol{\mu}) \right], \tag{2.120}$$

follows a multivariate Gaussian distribution, i.e. $X \sim \mathcal{N}(\boldsymbol{\mu}, \boldsymbol{\Sigma})$, with the mean vector $\boldsymbol{\mu} \in \mathbb{R}^n$ and positive semi-definite covariance matrix $\boldsymbol{\Sigma} \in \mathbb{R}^{n \times n}$.

Matrix-variate Gaussian

A normally distributed random matrix $X \in \mathbb{R}^{n \times m}$, where $X \sim \mathcal{MN}_{n,m}(\boldsymbol{M}, \boldsymbol{\Sigma}, \boldsymbol{\Upsilon})$, has the PDF [25]

$$\pi(\boldsymbol{X}) = \frac{\exp\left\{ -\frac{1}{2}\mathrm{tr}\left[\boldsymbol{\Upsilon}^{-1}(\boldsymbol{X} - \boldsymbol{M})^{\mathsf{T}} \boldsymbol{\Sigma}^{-1} (\boldsymbol{X} - \boldsymbol{M}) \right] \right\}}{(2\pi)^{\frac{nm}{2}} |\boldsymbol{\Sigma}|^{\frac{n}{2}} |\boldsymbol{\Upsilon}|^{\frac{m}{2}}} \tag{2.121}$$

with mean $\boldsymbol{M} \in \mathbb{R}^{n \times m}$, positive semi-definite row covariance $\boldsymbol{\Sigma} \in \mathbb{R}^{n \times n}$ and positive semi-definite column covariance $\boldsymbol{\Upsilon} \in \mathbb{R}^{m \times m}$. The matrix-variate distribution $\mathcal{MN}_{n,m}(\boldsymbol{M}, \boldsymbol{\Sigma}, \boldsymbol{\Upsilon})$ can be reformulated as a multivariate Gaussian

$$\mathrm{vec}(\boldsymbol{X}^{\mathsf{T}}) \sim \mathcal{N}(\mathrm{vec}(\boldsymbol{M}^{\mathsf{T}}), \boldsymbol{\Sigma} \otimes \boldsymbol{\Upsilon}) \tag{2.122}$$

via vectorization using column-wise stacking.

2.5.2. Gaussian processes

Gaussian process regression

A Gaussian process is a random process with the property that any finite collection of random variables from the process has a multivariate Gaussian distribution [116]. It is fully specified by a mean $m(\tau) = \mathbb{E}[X_\tau]$ and covariance function $k(\tau, \tau') = \mathrm{Cov}[X_\tau, X_{\tau'}]$, where $\tau, \tau' \in \mathcal{T}$. In the context of regression, the GP is introduced as a Gaussian prior $\pi(f)$ over functions $f(\tau)$ and

denoted by

$$f(\tau) \sim \mathcal{GP}\left(m(\tau), k(\tau, \tau')\right). \tag{2.123}$$

The process is used for the purposes of approximating the relationship between f and τ based on a training data set $\{y_i, \tau_i\}_{i=1}^{n_{\text{train}}}$ consisting of n_{train} data points. The observed values of the function $f(\tau_i)$ are assumed to be contaminated by additive Gaussian noise as

$$y_i = f(\tau_i) + \epsilon_n, \quad \epsilon_n \sim \mathcal{N}(0, \sigma_n^2). \tag{2.124}$$

In Bayesian terminology, this gives rise to the likelihood

$$\pi(\boldsymbol{y}|f, \boldsymbol{\tau}) = \prod_{i=1}^{n_{\text{train}}} \mathcal{N}(y_i, \sigma_n^2) = \mathcal{N}(\boldsymbol{y}, \sigma_n^2 \boldsymbol{I}_{n_{\text{train}}}), \tag{2.125}$$

where $\boldsymbol{y}$ and $\boldsymbol{\tau}$ denote the training data and $\boldsymbol{I}_{n_{\text{train}}}$ is the $n_{\text{train}} \times n_{\text{train}}$ identity matrix. Conditioning the GP on $\boldsymbol{y}$ and $\boldsymbol{\tau}$ results in a posterior over the function $f(\tau)$, i.e. $\pi(f|\boldsymbol{y}, \boldsymbol{\tau})$, which can be used to obtain a predictive distribution for $y^\star = y(\tau^\star)$ at an arbitrary location $\tau^\star$

$$\pi(y^\star|\tau^\star, \boldsymbol{y}, \boldsymbol{\tau}) = \int \pi(y^\star|f, \tau^\star)\,\pi(f|\boldsymbol{y}, \boldsymbol{\tau})\,\mathrm{d}f. \tag{2.126}$$

For GPs, this predictive distribution is obtained by conditioning the multivariate Gaussian $\pi(y^\star, \boldsymbol{y}|\tau^\star, \boldsymbol{\tau})$ on the observed data and results in another Gaussian distribution [116]

$$y^\star \sim \pi(y^\star|\tau^\star, \boldsymbol{y}, \boldsymbol{\tau}) = \mathcal{N}(\mu^\star, \sigma^{\star^2}). \tag{2.127}$$

The mean $\mu^\star$ and variance $\sigma^{\star^2}$ are computed as

$$\mu^\star = m(\tau^\star) + \boldsymbol{k}^{\star\mathsf{T}}\boldsymbol{K}^{-1}\left(\boldsymbol{y} - \boldsymbol{m}\right), \tag{2.128}$$

$$\sigma^{\star^2} = k(\tau^\star, \tau^\star) - \boldsymbol{k}^{\star\mathsf{T}}\boldsymbol{K}^{-1}\boldsymbol{k}^\star, \tag{2.129}$$

with

- $\boldsymbol{k}^\star$: a vector of size n_{train} with entries $[k_i] = k(\tau^\star, \tau_i)$,

- $\boldsymbol{K}$: a matrix of size $n_{\text{train}} \times n_{\text{train}}$ with entries $[K_{ij}] = k(\tau_i, \tau_j) + \sigma_n^2 \delta_{ij}$ and where δ_{ij} is the Kronecker delta,

- $\boldsymbol{y}$: a vector of size n_{train} with entries $[y_i] = y_i$,

- $\boldsymbol{m}$: a vector of size n_{train} with entries $[m_i] = m(\tau_i)$.

The mean and covariance functions, $m(\tau)$ and $k(\tau, \tau')$, usually feature hyperparameters θ_m and θ_k, which need to be set appropriately. While it is possible to introduce further prior distributions [116, Section 5.2], the Bayesian view on GPs already provides a straightforward way for

optimizing these parameters along with σ_n via maximizing the model evidence

$$\pi(\boldsymbol{y}|\boldsymbol{\tau}) = \int \pi(\boldsymbol{y}, \boldsymbol{f}|\boldsymbol{\tau})\,\mathrm{d}\boldsymbol{f} = \int \pi(\boldsymbol{y}|\boldsymbol{f}, \boldsymbol{\tau})\,\pi(\boldsymbol{f}|\boldsymbol{\tau})\,\mathrm{d}\boldsymbol{f} \qquad (2.130)$$

with $\boldsymbol{f}$ containing the function values $f(\tau_i)$. For GPs, the log model evidence, which is also called the log marginal likelihood, becomes

$$L(\boldsymbol{\zeta}) = -\frac{1}{2}\log|\boldsymbol{K}| - \frac{1}{2}(\boldsymbol{y} - \boldsymbol{m})^{\mathsf{T}}\boldsymbol{K}^{-1}(\boldsymbol{y} - \boldsymbol{m}) - \frac{n_{\mathrm{train}}}{2}\log 2\pi \qquad (2.131)$$

with the hyperparameters $\boldsymbol{\zeta} = \{\theta_m, \theta_k, \sigma_n\}$.

Multivariate Gaussian process regression

A multivariate GP

$$X_\tau \sim \mathcal{MGP}(\boldsymbol{m}(\tau), k(\tau, \tau'), \boldsymbol{\Upsilon}) \qquad (2.132)$$

is a m-variate random process with $X_\tau \in \mathbb{R}^m$ such that the random matrix $[X_\tau^1, X_\tau^2, \ldots, X_\tau^n]^{\mathsf{T}} \in \mathbb{R}^{n \times m}$ of n random vectors X_τ^i follows a matrix-variate Gaussian distribution [25, 146]. As for the univariate case, it is defined via a mean $\boldsymbol{m}(\tau)$ and covariance function $k(\tau, \tau')$, but features an additional positive semi-definite matrix $\boldsymbol{\Upsilon} \in \mathbb{R}^{m \times m}$. The covariance function $k(\tau, \tau')$ is also called the row covariance and $\boldsymbol{\Upsilon}$ the column or parameter covariance. There are different possibilities on how to formulate multivariate GPs, especially on how to model the covariances and noise levels for the different outputs.

Below, the approach from [146] is presented, assuming a zero-mean function $\boldsymbol{m}(\tau) = \boldsymbol{0}$. As before, the GP will be defined as a prior over the unknown function $\boldsymbol{f}(\tau)$, where $\boldsymbol{f} \in \mathbb{R}^m$. It is being assumed that each component f_i of the function $\boldsymbol{f}$ follows the same univariate GP, i.e. $f_i \sim \mathcal{GP}(0, k(\tau, \tau'))$. To correlate the individual components f_i, the random vector $\boldsymbol{f}$ is described by a multivariate Gaussian distribution $\boldsymbol{f} \sim \mathcal{N}(\boldsymbol{0}, \boldsymbol{\Upsilon})$. Hence, the random matrix of n_{train} vectors $[\boldsymbol{f}^1, \ldots, \boldsymbol{f}^{n_{\mathrm{train}}}]^{\mathsf{T}}$ follows a matrix-variate Gaussian distribution

$$[\boldsymbol{f}^1, \ldots, \boldsymbol{f}^{n_{\mathrm{train}}}]^{\mathsf{T}} \sim \mathcal{MN}_{n_{\mathrm{train}}, m}(\boldsymbol{0}, \boldsymbol{K}, \boldsymbol{\Upsilon}). \qquad (2.133)$$

Given a data set $\{\boldsymbol{y}_i, \tau_i\}_{i=1}^{n_{\mathrm{train}}}$, the following noise model is assumed

$$\boldsymbol{y}_i = \boldsymbol{f}(\tau_i) + \boldsymbol{\epsilon}_n, \qquad (2.134)$$

with $\boldsymbol{\epsilon}_n \sim \mathcal{N}(\boldsymbol{0}, \boldsymbol{D})$. The diagonal matrix $\boldsymbol{D}$ contains different noise levels $D_{ii} \in \mathbb{R}_+, i = 1 \ldots m$, for the individual outputs. The matrix-variate Gaussian can be rewritten as a multivariate Gaussian via vectorization. Taking into account the noise levels, this results in

$$\mathrm{vec}(\boldsymbol{Y}) = [\boldsymbol{y}^{1\mathsf{T}}, \ldots, \boldsymbol{y}^{n_{\mathrm{train}}\mathsf{T}}]^{\mathsf{T}} \sim \mathcal{N}(\boldsymbol{0}, \boldsymbol{\Upsilon} \otimes \boldsymbol{K} + \boldsymbol{D} \otimes \boldsymbol{I}_{n_{\mathrm{train}}}), \qquad (2.135)$$

where $\otimes$ denotes the Kronecker product. Following [13, 25, 146], the matrix $\boldsymbol{\Upsilon}$ is parameterized via the entries L_{ij} of the Cholesky decomposition $\boldsymbol{\Upsilon} = \boldsymbol{L}\boldsymbol{L}^{\mathsf{T}}$. Then, the predictive distribution

at the arbitrary location $\tau^\star$ is a multivariate Gaussian such that

$$\boldsymbol{y}^\star \sim \mathcal{N}(\boldsymbol{\mu}^\star, \boldsymbol{\Sigma}^\star) \tag{2.136}$$

with

$$\boldsymbol{\mu}^\star = (\boldsymbol{\Upsilon} \otimes \boldsymbol{k}^\star)^\mathsf{T}(\boldsymbol{\Upsilon} \otimes \boldsymbol{K} + \boldsymbol{D} \otimes \boldsymbol{I}_{n_{\text{train}}})^{-1}\text{vec}(\boldsymbol{Y}), \tag{2.137}$$

$$\boldsymbol{\Sigma}^\star = \boldsymbol{\Upsilon}\, k(\tau^\star, \tau^\star) + \boldsymbol{D} - (\boldsymbol{\Upsilon} \otimes \boldsymbol{k}^\star)^\mathsf{T}(\boldsymbol{\Upsilon} \otimes \boldsymbol{K} + \boldsymbol{D} \otimes \boldsymbol{I}_{n_{\text{train}}})^{-1}(\boldsymbol{\Upsilon} \otimes \boldsymbol{k}^\star). \tag{2.138}$$

Finally, the log marginal likelihood becomes

$$
\begin{aligned}
L(\boldsymbol{\zeta}) = &-\frac{1}{2}\log|\boldsymbol{\Upsilon} \otimes \boldsymbol{K} + \boldsymbol{D} \otimes \boldsymbol{I}_{n_{\text{train}}}| \\
&-\frac{1}{2}\text{vec}(\boldsymbol{Y})^\mathsf{T}(\boldsymbol{\Upsilon} \otimes \boldsymbol{K} + \boldsymbol{D} \otimes \boldsymbol{I}_{n_{\text{train}}})^{-1}\text{vec}(\boldsymbol{Y}) - 2n_{\text{train}}\log 2\pi
\end{aligned}
\tag{2.139}
$$

and can be optimized with respect to the hyperparameters $\boldsymbol{\zeta}$, which in this case contain parameters θ_k from the covariance function, noise parameters D_{ii} as well as parameters L_{ij} from the Cholesky decomposition.

Gaussian process surrogate modeling incorporating explicit basis functions

GPs can also be employed as surrogate models by assuming noise-free observations, i.e. $y = f(\tau)$, to obtain cheap approximations to numerically expensive computational models [70]. In this case, the GP serves as an interpolator on a set of input-output values and the term Kriging is frequently used instead. Below, a GP-based interpolation model that incorporates explicit basis functions as proposed in [116] and exemplified by [14, 19] is presented. With such a model, it is possible to exactly represent functions that can be described by the provided basis. For the purposes of this work, the goal is to approximate the parameter-to-QoI map as

$$Q(\boldsymbol{\theta}) \approx f(\boldsymbol{\theta}) + \boldsymbol{h}(\boldsymbol{\theta})^\mathsf{T}\boldsymbol{\eta}, \tag{2.140}$$

where $f(\boldsymbol{\theta}) \sim \mathcal{GP}(0, k(\boldsymbol{\theta}, \boldsymbol{\theta}'))$ is a zero mean Gaussian process and $\boldsymbol{h}(\boldsymbol{\theta})$ denotes the chosen basis functions with coefficients $\boldsymbol{\eta}$. Assuming a Gaussian prior for the coefficients, $\boldsymbol{\eta} \sim \mathcal{N}(\boldsymbol{b}, \boldsymbol{B})$, this results in the Gaussian process

$$f(\boldsymbol{\theta}) + \boldsymbol{h}(\boldsymbol{\theta})^\mathsf{T}\boldsymbol{\eta} \sim \mathcal{GP}(\boldsymbol{h}(\boldsymbol{\theta})^\mathsf{T}\boldsymbol{b}, k(\boldsymbol{\theta}, \boldsymbol{\theta}') + \boldsymbol{h}(\boldsymbol{\theta})^\mathsf{T}\boldsymbol{B}\boldsymbol{h}(\boldsymbol{\theta}')). \tag{2.141}$$

The dependence on the prior parameters $\boldsymbol{b}$ and $\boldsymbol{B}$ can be resolved, if a vague prior for $\boldsymbol{\eta}$ is chosen, i.e. if the limiting case is considered, where $\boldsymbol{B}^{-1}$ approaches the zero matrix $\boldsymbol{0}$. In that case, the predicted mean and variance for an arbitrary point $\boldsymbol{\theta}^\star$ become

$$\mu_Q^\star = \boldsymbol{k}^{\star\mathsf{T}}\boldsymbol{K}^{-1}\boldsymbol{y} + \boldsymbol{r}^\mathsf{T}\bar{\boldsymbol{\eta}}, \tag{2.142}$$

$$\sigma_Q^{\star 2} = k(\boldsymbol{\theta}^\star, \boldsymbol{\theta}^\star) - \boldsymbol{k}^{\star\mathsf{T}}\boldsymbol{K}^{-1}\boldsymbol{k}^\star + \boldsymbol{r}^\mathsf{T}(\boldsymbol{H}\boldsymbol{K}^{-1}\boldsymbol{H}^\mathsf{T})^{-1}\boldsymbol{r}, \tag{2.143}$$

where $\bar{\boldsymbol{\eta}} = (\boldsymbol{HK}^{-1}\boldsymbol{H}^{\mathsf{T}})^{-1}\boldsymbol{HK}^{-1}\boldsymbol{y}$, $\boldsymbol{r} = \boldsymbol{h}^{\star} - \boldsymbol{HK}^{-1}\boldsymbol{k}^{\star}$ and $\boldsymbol{y} = [Q(\boldsymbol{\theta}_1), \ldots, Q(\boldsymbol{\theta}_{n_{\text{train}}})]^{\mathsf{T}}$ is the vector of n_{train} model evaluations. $\boldsymbol{H}$ is a matrix containing vectors $\boldsymbol{h}(\boldsymbol{\theta})$ at all training data points and $\boldsymbol{h}^{\star} = \boldsymbol{h}(\boldsymbol{\theta}^{\star})$. Finally, the log marginal likelihood is

$$L(\boldsymbol{\zeta}) = -\frac{1}{2}\boldsymbol{y}^{\mathsf{T}}\boldsymbol{K}^{-1}\boldsymbol{y} + \frac{1}{2}\boldsymbol{y}^{\mathsf{T}}\boldsymbol{C}\boldsymbol{y} - \frac{1}{2}\log|\boldsymbol{K}| - \frac{1}{2}\log|\boldsymbol{A}|$$
$$- \frac{n_{\text{train}} - \text{rank}(\boldsymbol{H}^{\mathsf{T}})}{2}\log 2\pi, \tag{2.144}$$

where $\boldsymbol{C} = \boldsymbol{K}^{-1}\boldsymbol{H}^{\mathsf{T}}\boldsymbol{A}^{-1}\boldsymbol{H}\boldsymbol{K}^{-1}$ and $\boldsymbol{A} = \boldsymbol{H}\boldsymbol{K}^{-1}\boldsymbol{H}^{\mathsf{T}}$.

2.5.3. Monte Carlo method

The Monte Carlo method [88, 130] can be considered an approach to approximate integrals of the general form

$$I = \int f(x)\,\pi(x)\,\mathrm{d}x. \tag{2.145}$$

The application of the MC method relies on the law of large numbers [129], which states that the arithmetic mean of N independent samples from the density $\pi(x)$ converges to the expected value

$$I_N = \frac{1}{N}\sum_{i=1}^{N} f(x_i) \to I \tag{2.146}$$

as $N \to \infty$ and where x_i are independent and identically distributed (i.i.d.) samples from $\pi(x)$. I_N is called an estimator and is a random variable itself, since it is composed of a sum of random variables. The estimator is unbiased in the sense that the expected value of the estimator is the exact value of the integral

$$\mathbb{E}[I_N] = \int I_N\,\pi(I_N)\,\mathrm{d}I_N = \frac{1}{N}\sum_{i=1}^{N}\int f(x_i)\,\pi(f)\,\mathrm{d}f = \mathbb{E}[f(x)] = I. \tag{2.147}$$

The variance of the estimator is

$$\mathbb{V}[I_N] = \frac{\mathbb{V}[f(x)]}{N}. \tag{2.148}$$

Hence, it depends on the variance of the function $f(x)$ itself and decays with $1/N$. The actual distribution of the random variable I_N is provided by the central limit theorem [129], which states for the sum of X_i i.i.d. random variables

$$\frac{\sum_{i=1}^{N} X_i - N\mu_X}{\sqrt{N}\sigma_X} \to \mathcal{N}(0, 1), \quad \text{as} \quad N \to \infty, \tag{2.149}$$

where $\mu_X = \mathbb{E}[X_i]$ and $\sigma_X = \sqrt{\mathbb{V}[X_i]}$. This means that the Monte Carlo error $\varepsilon_{\mathrm{MC}} = I_N - I$ follows a Gaussian distribution $\varepsilon_{\mathrm{MC}} \sim \mathcal{N}(0, \sigma_X^2/N)$ as $N \to \infty$. In practice it usually suffices that N is large enough in order for $\varepsilon_{\mathrm{MC}}$ to be approximately Gaussian. Then, using MC estimates for the variance σ_X^2, the MC error can be controlled up to a desired tolerance by choosing a corresponding sample size N. For the parameter-to-QoI map $Q(\boldsymbol{\theta})$ used in this work, one can compute integrals using MC sampling as

$$I = \int f(Q)\,\pi(Q)\,\mathrm{d}Q \approx \frac{1}{N}\sum_{i=1}^{N} f(Q(\boldsymbol{\theta}^{(i)})) \tag{2.150}$$

with i.i.d. $\boldsymbol{\theta}_i \sim \pi(\boldsymbol{\theta})$. Although simple and inherently parallel, MC sampling can quickly become infeasible for practical problems, where the parameter-to-QoI map $Q(\boldsymbol{\theta}^{(i)})$ is numerically expensive to evaluate. To that end, frequently surrogate models that are cheap to evaluate, such as the GP models above, are used for MC integration.

2.5.4. Probabilistic multi-fidelity Monte Carlo method

In Section 2.5.3, it was shown how integrals with respect to an unknown PDF $\pi(x)$ can be approximated using the MC method. Due to the high computational costs associated with MC sampling directly on the high-fidelity model, the objective of this section is to generate approximate yet accurate samples x_i from the density $\pi(x)$ at a fraction of the original costs by employing numerical models of varying fidelity. Existing multi-level Monte Carlo (MLMC) and MFMC methods [49, 50, 106] usually only provide moment estimates or are limited to parametric density estimation [9, 51]. Furthermore, surrogate models and response surface approximation techniques typically suffer from a poor stochastic scalability and become infeasible when the number of random input variables is large. To that end, a probabilistic MFMC method is presented below as a general and flexible strategy for UQ purposes. Following the idea of Bayesian MC [115], the method was introduced in [75], applied to large-scale problems in [5, 7, 111] and has recently been generalized [98].

The following section is a revised version of part of the author's work published in [18]. Below, the parameter-to-QoI map $Q = Q(\boldsymbol{\theta})$ will be referred to as the high-fidelity model and it is assumed that an additional low-fidelity solver $q = q(\boldsymbol{\theta})$ is available, providing a cheap approximation to the QoI. The joint distribution of both models is denoted as $\pi(Q, q)$. It is being noted that the low-fidelity approximation of the QoI can be very poor as long as there is some statistical dependence between the low-fidelity and the high-fidelity outputs, $q(\boldsymbol{\theta})$ and $Q(\boldsymbol{\theta})$. By basic rules of probability theory, for the density of the high-fidelity QoI one can write

$$\pi(Q) = \int \pi(Q, q)\,\mathrm{d}q = \int \pi(Q|q)\,\pi(q)\,\mathrm{d}q. \tag{2.151}$$

Thus, calculating $\pi(Q)$ involves constructing a conditional density $\pi(Q|q)$ between the high-fidelity and low-fidelity and averaging over q. In practice, a large amount of samples q_i are drawn from $\pi(q)$, samples $Q_i|q_i$ generated using the conditional density and it is made use of kernel density estimation (KDE) to obtain an approximate $\pi(Q)$. It is critical to mention that while the parameterization of the random variables $\boldsymbol{\theta}$ is not required to be the same for both levels of

fidelity, it is required that the parameters for the low-fidelity model be a subset of the parameters of the high-fidelity model, or that there exists a relationship between the parameters of the different models. This is necessary if one wants to construct $\pi(Q|q)$ using a regression model, since a training set with corresponding model evaluations needs to be created as demonstrated below.

The density $\pi(q)$ can be obtained via simple MC sampling, since every model evaluation $q(\boldsymbol{\theta})$ is assumed to be relatively cheap. The key ingredient thus is the construction of the conditional density $\pi(Q|q)$. The goal is to achieve this using regression models, trained on a sampling set $\{Q(\boldsymbol{\theta}_i), q(\boldsymbol{\theta}_i)\}_{i=1}^{n_{\text{train}}}$ involving n_{train} high-fidelity and corresponding low-fidelity model evaluations at the same parameter realization $\boldsymbol{\theta}_i$. Creating this training set naturally is the computationally most demanding part in the process. In addition to the type of regression model, the choice of model parameter realizations $\boldsymbol{\theta}_i$ can be a nontrivial task. Finally, using Eq. (2.151), the classical MC integration tasks from Eq. (2.150) can be expressed via

$$
\begin{aligned}
I &= \int f(Q)\,\pi(Q)\,\mathrm{d}Q = \int f(Q)\left(\int \pi(Q|q)\,\pi(q)\,\mathrm{d}q\right)\mathrm{d}Q \\
&= \int\int f(Q)\,\pi(Q|q)\,\mathrm{d}Q\,\pi(q)\,\mathrm{d}q = \int \mathbb{E}[f(Q|q)]\,\pi(q)\,\mathrm{d}q.
\end{aligned}
\tag{2.152}
$$

Approximating the conditional densities

While [7, 75] employ a Bayesian regression model for the conditional density $\pi(Q|q)$, this work follows [111, 115] and considers GP models due to their simple structure, but great flexibility. It is being noted, however, that any method providing probabilistic estimates $Q|q$ could be used. While in their standard formulation, GPs assume a Gaussian likelihood and homoscedastic noise, produce single-output responses and are limited in their scalability, generalizations to heteroscedastic noise, non Gaussian likelihoods, multiple output variables and scalable versions have been developed [10, 25, 116, 146]. Using the mean of the GP as a regression model for the trend of the mapping between two models Q and q is straightforward.

Unfortunately, the assumption of a Gaussian noise model may fail to capture the correct conditional distribution, even for simple models. For the models that appear to have non-Gaussian conditional distributions, the results using the GP model can be compared with a simple approach based on a KDE of the noise. This comparison does not require any additional model evaluations and provides a reasonable indication of the validity of the Gaussian noise assumption. As a further remedy, the generalized approach from [98] can be pursued for non-Gaussian conditionals $\pi(Q|q)$. The random process is defined as a link between the high-fidelity and the low-fidelity outputs, $Q(\boldsymbol{\theta})$ and $q(\boldsymbol{\theta})$. The resulting predictive density will serve the MFMC framework as the conditional density $\pi(Q|q)$ to generate high-fidelity samples $Q^\star$ given low-fidelity samples $q^\star$.

Training set selection strategies

When it comes to the selection of appropriate training data points for the construction of the GP, the simplest approach is based on MC sampling, i.e., generating n_{train} samples $\{\boldsymbol{\theta}_i\}_{i=1}^{n_{\text{train}}}$ from the density $\pi(\boldsymbol{\theta})$ and evaluating high- and low-fidelity model responses.While this is generally applicable and possibly the only feasible approach for a high number of QoI, it will lead to a

relatively slow convergence since only few training points will fall in the regions of the regression model corresponding to the tails of the high-fidelity push-forward. Areas with a high probability density, on the other hand, will be identified relatively quickly.

An alternative strategy is to try to cover the support of the low-fidelity density $\pi(q)$ by creating a set of evenly spaced points, e.g., on a grid, and evaluating the high-fidelity model at a representative set of corresponding model parameters. This procedure leads to a more stable surrogate creation process, since the GP captures the trend of the data relatively fast. On the other hand, a grid-based approach becomes infeasible, as the number of QoI grows. In particular, since the support of the low-fidelity push-forward is typically not a hypercube and can be highly correlated, constructing a grid of points may be impractical. In this case, one should resort to different design of experiment strategies.

Algorithmic steps and diagnostics

Applying the probabilistic MFMC framework in practice requires a few simple steps, cf. Alg. (1):

1. Define a high-fidelity model $Q(\boldsymbol{\theta})$ and a low-fidelity model $q(\boldsymbol{\theta})$.

2. Generate N samples from the input density $\pi(\boldsymbol{\theta})$ and compute the low-fidelity push-forward of this density using a standard KDE model.

3. Generate a training data set $\{q_i, Q_i\}_{i=1}^{n_{\text{train}}}$.

4. Train a regression model on the training set, generate high-fidelity samples Q_i using $\pi(Q|q)$ and approximate the high-fidelity push-forward.

To conclude this section, some diagnostics are discussed that are helpful to quantify the epistemic uncertainty introduced by the MFMC framework. This uncertainty is due to the trained regression model and will be dominated by its covariance structure. To simplify the discussion, the mean estimator

$$
\begin{aligned}
\mathbb{E}[Q] &= \int Q\,\pi(Q)\,\mathrm{d}Q = \int\int Q\,\pi(Q|q)\,\mathrm{d}Q\,\pi(q)\,\mathrm{d}q \\
&= \int \mathbb{E}[Q|q]\,\pi(q)\,\mathrm{d}q \approx \int \mu_Q(q)\,\pi(q)\,\mathrm{d}q \approx \frac{1}{N}\sum_{i=1}^{N}\mu_Q(q_i) = \hat{Q}
\end{aligned}
\tag{2.153}
$$

is considered. The first approximation is due to the GP regression model, the second one due to MC sampling. The mean estimator $\hat{Q}$ is thus simply an average of the GP predicted means μ_Q given q_i. To obtain a variance estimate of the mean estimator, one can compute

$$
\begin{aligned}
\mathbb{E}[(Q - \mu_Q(q))^2] &= \int \mathbb{E}[(Q|q - \mu_Q(q))^2]\,\pi(q)\,\mathrm{d}q \\
&\approx \int \sigma_Q^2(q)\,\pi(q)\,\mathrm{d}q \approx \frac{1}{N}\sum_{i=1}^{N}\sigma_Q^2(q_i) = \mathbb{V}_{\hat{Q}}.
\end{aligned}
\tag{2.154}
$$

The mean estimator variance $\mathbb{V}_{\hat{Q}}$ is thus the average of GP predicted variance σ_Q^2 given q_i. Estimator variances can be computed for any expectation as

$$\mathbb{E}[h(Q)] = \int \mathbb{E}[h(Q|q)] \, \pi(q) \, \mathrm{d}q \approx \frac{1}{N} \sum_{i=1}^{N} h(Q_i|q_i) = \hat{h}_Q. \tag{2.155}$$

With $h_Q(q) = \mathbb{E}[h(Q|q)]$, corresponding estimator variances are

$$\begin{aligned}
\mathbb{E}[(h(Q) - h_Q(q))^2] &= \int \mathbb{E}[(h(Q|q) - h_Q(q))^2] \, \pi(q) \, \mathrm{d}q \\
&\approx \frac{1}{N} \sum_{i=1}^{N} (h(Q_i) - h_Q(q_i))^2 = \mathbb{V}_{\hat{h}_Q},
\end{aligned} \tag{2.156}$$

providing a helpful diagnostic value to assess the uncertainty of the regression model and high-fidelity predictions. To conclude, the following diagnostics can be utilized:

1. The estimated QoI mean $\hat{Q}$, the absolute and relative mean estimator errors $\varepsilon_{\hat{Q}}^{\mathrm{abs}}$ and $\varepsilon_{\hat{Q}}^{\mathrm{rel}}$, defined as

$$\varepsilon_{\hat{Q}}^{\mathrm{abs}} = \mathbb{V}_{\hat{Q}}^{1/2} \quad \text{and} \quad \varepsilon_{\hat{Q}}^{\mathrm{rel}} = \frac{\mathbb{V}_{\hat{Q}}^{1/2}}{|\hat{Q}|}. \tag{2.157}$$

2. The estimated QoI standard deviations $\hat{V}_Q^{1/2}$, where $\hat{V}_Q$ is the variance estimate $\mathbb{E}[(Q - \hat{Q})^2]$, the absolute and the relative standard deviation estimator errors $\varepsilon_{\hat{V}_Q^{1/2}}^{\mathrm{abs}}$ and $\varepsilon_{\hat{V}_Q^{1/2}}^{\mathrm{rel}}$, defined as

$$\varepsilon_{\hat{V}_Q^{1/2}}^{\mathrm{abs}} = \sqrt{\hat{V}_Q + \mathbb{V}[\hat{V}_Q]^{1/2}} - \hat{V}_Q^{1/2} \quad \text{and} \quad \varepsilon_{\hat{V}_Q^{1/2}}^{\mathrm{rel}} = \frac{\sqrt{\hat{V}_Q + \mathbb{V}[\hat{V}_Q]^{1/2}} - \hat{V}_Q^{1/2}}{\hat{V}_Q^{1/2}}. \tag{2.158}$$

These diagnostics provide a quantitative estimate of the uncertainties of the first and second moment for the approximated push-forward density $\pi(Q)$.

Algorithm 1: Generating high-fidelity samples

1: **Input:** $Q(\boldsymbol{\theta})$, $q(\boldsymbol{\theta})$
2: Compute N samples $\{q_i\}_{i=1}^{N}$ using the input density $\pi(\boldsymbol{\theta})$.
3: Create a training data set $\{q_i, Q_i\}_{i=1}^{n_{\mathrm{train}}}$
4: Train a regression model on the data set $\{q_i, Q_i\}_{i=1}^{n_{\mathrm{train}}}$.
5: **for** $i = 1, \ldots, N$ **do**
6:     Obtain the GP-based predictive density $\pi(Q_i|q_i)$ and generate a sample $Q_i^\star$.
7: **end for**
8: Approximate $\pi(Q)$ from $\{Q_i^\star\}_{i=1}^{N}$ using a KDE.
9: **Output:** $\pi(Q)$, $\{Q_i^\star\}_{i=1}^{N}$

2.5.5. Bayesian inference

Bayesian inference is the process of updating beliefs (specified via the prior) using Bayes' rule as new information (specified via the likelihood) becomes available. In practice and for the purposes of this work, Bayesian inference implies exploring the posterior PDF from Section 2.3.3

$$\log \pi(\boldsymbol{\theta}|\hat{\mathbf{S}}) \propto \log \pi(\hat{\mathbf{S}}|\boldsymbol{\theta}) + \log \pi(\boldsymbol{\theta}), \tag{2.159}$$

i.e. generating samples, computing statistical moments, etc. The greatest challenge when it comes to applying the Bayesian paradigm to practical problems with computationally expensive numerical models is the relatively high number of model evaluations that are usually required. Hence, limited computational budgets and time constraints require an appropriate model choice or adequate approximation technique. In this section, different methods of varying approximation capabilities are discussed. Further details on Bayesian inference in general and the individual methods can be found in the works [12, 129].

MAP estimation and Laplace approximation

Fitting a Gaussian distribution at the maximum a posteriori probability (MAP) of the posterior $\pi(\boldsymbol{\theta}|\hat{\mathbf{S}})$ is called Laplace approximation. The MAP $\boldsymbol{\theta}^{\mathrm{MAP}}$ is the point at maximum probability density, i.e. the mode of the posterior, defined as

$$\boldsymbol{\theta}^{\mathrm{MAP}} = \arg \max_{\boldsymbol{\theta}} \log \pi(\boldsymbol{\theta}|\hat{\mathbf{S}}) \tag{2.160}$$

and can be found via non-convex optimization. In particular, for problems involving a high-dimensional parameter space $\mathbb{R}^{n_\theta}$, the Limited-memory BFGS (L-BFGS) [99] algorithm is a popular choice. As a quasi-Newton method, it approximates the Hessian of the objective function using gradient information. Here, the objective function is $f(\boldsymbol{\theta})$, with expressions for the gradient $\nabla_{\boldsymbol{\theta}} f(\boldsymbol{\theta})$ readily available using the adjoint method, cf. Section 2.3.3. In [47], a comprehensive discussion of the Laplace approximation method and its application to large-scale inverse problems is provided.

Markov chain Monte Carlo

The MCMC method was originally introduced for statistical mechanics problems [57, 89] and has evolved to a popular tool for Bayesian inference with applications to almost all fields of science and engineering. It is based on the idea of constructing an ergodic Markov chain, which produces a sequence of samples $\boldsymbol{\theta}_i$ that asymptotically satisfy $\boldsymbol{\theta}_i \sim \pi(\boldsymbol{\theta}|\hat{\mathbf{S}})$ after the chain has become stationary.

A major challenge with almost all MCMC methods in a high-dimensional parameter setting is the proper design of proposal densities $\pi(\boldsymbol{\theta}_{i+1}|\boldsymbol{\theta}_i)$ for consecutive samples, which can significantly affect the number of steps until stationarity. This is particularly important when the costs for each model evaluation is high. Faster convergence in comparison to the standard Metropolis-Hastings MCMC algorithm can, e.g., be achieved via the Metropolis-adjusted Langevin algorithm (MALA) [122] that incorporates gradient information of the posterior with respect to $\boldsymbol{\theta}$ into the proposal density. A further issue is the definition of a proper stopping criterion for the

chain, since asymptotic convergence in practice always implies an approximation error since computation time is limited.

Sequential Monte Carlo

Sequential Monte Carlo (SMC) methods follow an approach, where, starting from an initial distribution $\pi_0(\boldsymbol{\theta})$, multiple intermediate distributions $\pi_t(\boldsymbol{\theta})$ are constructed via simulated annealing [94], with the posterior $\pi(\boldsymbol{\theta}|\hat{\mathbf{S}})$ as the final distribution. It involves a set of particles that are updated from one step to another using transition kernels. In contrast to MCMC methods, SMC can be straightforwardly parallelized and does not have to be checked for stationarity. However, the same challenges with high-dimensional parameters arise in the construction of the transition kernel.

Variational inference

Variational inference (VI) [66, 145] is a method to approximate the posterior $\pi(\boldsymbol{\theta}|\hat{\mathbf{S}})$ using a parameterized PDF $q_{\boldsymbol{\phi}}(\boldsymbol{\theta})$ that is available in closed form. Key to this approach is the efficient optimization of the parameters $\boldsymbol{\phi}$ of the density $q_{\boldsymbol{\phi}}(\boldsymbol{\theta})$ such that $q_{\boldsymbol{\phi}}(\boldsymbol{\theta}) \approx \pi(\boldsymbol{\theta}|\hat{\mathbf{S}})$ can be used in place of the actual posterior. To that end, the Bayesian framework provides a natural optimization objective via the model evidence [12]

$$
\begin{aligned}
\log \pi(\hat{\mathbf{S}}) = \log \int \pi(\boldsymbol{\theta}, \hat{\mathbf{S}}) \, \mathrm{d}\boldsymbol{\theta} &= \log \int q_{\boldsymbol{\phi}}(\boldsymbol{\theta}) \frac{\pi(\boldsymbol{\theta}, \hat{\mathbf{S}})}{q_{\boldsymbol{\phi}}(\boldsymbol{\theta})} \, \mathrm{d}\boldsymbol{\theta} \\
&\geq \int q_{\boldsymbol{\phi}}(\boldsymbol{\theta}) \log \frac{\pi(\boldsymbol{\theta}, \hat{\mathbf{S}})}{q_{\boldsymbol{\phi}}(\boldsymbol{\theta})} \, \mathrm{d}\boldsymbol{\theta} = \mathcal{L}(\boldsymbol{\phi}).
\end{aligned}
\tag{2.161}
$$

$\mathcal{L}(\boldsymbol{\phi})$ is called the evidence lower bound (ELBO) and it can be shown that the inequality above becomes an equality if the optimal $q_{\boldsymbol{\phi}}$ corresponds to the posterior $\pi(\boldsymbol{\theta}|\hat{\mathbf{S}})$. Moreover, maximizing the ELBO is equivalent to minimizing the Kullback-Leibler (KL) divergence [76]

$$
\mathrm{KL}[q_{\boldsymbol{\phi}}(\boldsymbol{\theta}) \| \pi(\boldsymbol{\theta}|\hat{\mathbf{S}})] = -\int q_{\boldsymbol{\phi}}(\boldsymbol{\theta}) \log \frac{\pi(\boldsymbol{\theta}|\hat{\mathbf{S}})}{q_{\boldsymbol{\phi}}(\boldsymbol{\theta})} \, \mathrm{d}\boldsymbol{\theta},
\tag{2.162}
$$

which is a popular measure of closeness between two probability densities. The ELBO can be rewritten as

$$
\begin{aligned}
\mathcal{L}(\boldsymbol{\phi}) &= \int q_{\boldsymbol{\phi}}(\boldsymbol{\theta}) (\log \pi(\boldsymbol{\theta}, \hat{\mathbf{S}}) - \log q_{\boldsymbol{\phi}}(\boldsymbol{\theta})) \, \mathrm{d}\boldsymbol{\theta} \\
&= \mathbb{E}_{q_{\boldsymbol{\phi}}}[\log \pi(\hat{\mathbf{S}}|\boldsymbol{\theta}) + \log \pi(\boldsymbol{\theta})] + \mathbb{H}[q_{\boldsymbol{\phi}}(\boldsymbol{\theta})]
\end{aligned}
\tag{2.163}
$$

where $\mathbb{H}[q_{\boldsymbol{\phi}}(\boldsymbol{\theta})]$ is the entropy of $q_{\boldsymbol{\phi}}(\boldsymbol{\theta})$ defined as

$$
\mathbb{H}[q_{\boldsymbol{\phi}}(\boldsymbol{\theta})] = -\int \log q_{\boldsymbol{\phi}}(\boldsymbol{\theta}) q_{\boldsymbol{\phi}}(\boldsymbol{\theta}) \, \mathrm{d}\boldsymbol{\theta}.
\tag{2.164}
$$

Hence, the VI optimization problem can be formulated as

$$\boldsymbol{\phi}^{\star} = \arg\max_{\boldsymbol{\phi}} \mathcal{L}(\boldsymbol{\phi}). \tag{2.165}$$

For cases, where the measurement noise σ_N of the likelihood $\pi(\hat{\mathbf{S}}|\boldsymbol{\theta})$ is unknown, a non-informative Jeffrey's prior

$$\pi(\sigma_N) \propto \frac{1}{\sigma_N} \tag{2.166}$$

is added [12]. Point estimates corresponding to the MAP value of σ_N can then be computed based on the lower bound [16, 36]

$$
\begin{aligned}
\log \pi(\sigma_N|\hat{\mathbf{S}}) &= \log \int \pi(\boldsymbol{\theta}, \sigma_N|\hat{\mathbf{S}}) \, \mathrm{d}\boldsymbol{\theta} = \log \int q_{\boldsymbol{\phi}}(\boldsymbol{\theta}) \frac{\pi(\boldsymbol{\theta}, \sigma_N|\hat{\mathbf{S}})}{q_{\boldsymbol{\phi}}(\boldsymbol{\theta})} \, \mathrm{d}\boldsymbol{\theta} \\
&\geq \int q_{\boldsymbol{\phi}}(\boldsymbol{\theta}) \log \frac{\pi(\boldsymbol{\theta}, \sigma_N|\hat{\mathbf{S}})}{q_{\boldsymbol{\phi}}(\boldsymbol{\theta})} \, \mathrm{d}\boldsymbol{\theta} = \mathcal{L}(\boldsymbol{\phi}) + \log \pi(\sigma_N).
\end{aligned}
\tag{2.167}
$$

As before, it is straightforward to verify that the above inequality becomes an equality if $q_{\boldsymbol{\phi}}$ corresponds to the posterior $\pi(\boldsymbol{\theta}|\hat{\mathbf{S}})$. This suggests an iterative expectation–maximization (EM) scheme [12]:

- E-step: the noise parameter σ_N is fixed and $\mathcal{L}(\boldsymbol{\phi})$ is maximized with respect to $\boldsymbol{\phi}$.

- M-step: the parameters $\boldsymbol{\phi}$ remain fixed and $\mathcal{L}(\boldsymbol{\phi}) + \log \pi(\sigma_N)$ is maximized with respect to σ_N.

Even though arbitrary forms of approximating densities $q_{\boldsymbol{\phi}}$ are allowed, in this work the focus is on multivariate Gaussian distributions $\mathcal{N}(\boldsymbol{\mu}, \boldsymbol{\Sigma})$, parameterized by $\boldsymbol{\phi} = \{\boldsymbol{\mu}, \boldsymbol{\Sigma}\}$, with the mean $\boldsymbol{\mu} \in \mathbb{R}^{n_\theta}$ and positive semi-definite covariance matrix $\boldsymbol{\Sigma} \in \mathbb{R}^{n_\theta \times n_\theta}$.

Stochastic variational inference

Even for Gaussian densities, the optimization objective $\mathcal{L}(\boldsymbol{\phi})$ is analytically intractable due to nonlinearities in $\boldsymbol{\theta}$ in the likelihood $\pi(\hat{\mathbf{S}}|\boldsymbol{\theta})$ and prior $\pi(\boldsymbol{\theta})$. Classical VI can thus not be directly applied, but would require an iterative optimization approach using linearized expression for the prior and likelihood [36]. To that end, stochastic variational inference (SVI) [61, 103] is employed, which is based on stochastic optimization. The particular choice for $q_{\boldsymbol{\phi}}$ from above enables the application of the reparameterization trick [73, 120, 135] and a reformulation of the objective function in order to allow gradient estimation using MC sampling. In general, it expresses $\boldsymbol{\theta} = \boldsymbol{\theta}(\boldsymbol{\phi}, \boldsymbol{\varepsilon})$ as a function of the optimization parameters $\boldsymbol{\phi}$ and a random variable $\boldsymbol{\varepsilon}$ with known density $\pi(\boldsymbol{\varepsilon})$, which is independent from the parameters $\boldsymbol{\phi}$ and easy to sample from.

With this, the ELBO $\mathcal{L}(\boldsymbol{\phi})$ and its gradient can be computed using the estimates

$$
\begin{aligned}
\mathbb{E}_{q_{\boldsymbol{\phi}}}[\log \pi(\hat{\mathbf{S}}, \boldsymbol{\theta})] &= \mathbb{E}_{\pi(\boldsymbol{\varepsilon})}[\log \pi(\hat{\mathbf{S}}|\boldsymbol{\theta}(\boldsymbol{\phi}, \boldsymbol{\varepsilon})) + \log \pi(\boldsymbol{\theta}(\boldsymbol{\phi}, \boldsymbol{\varepsilon}))] \\
&\approx \frac{1}{N} \sum_{i=1}^{N} \log \pi(\hat{\mathbf{S}}|\boldsymbol{\theta}^{(i)}) + \log \pi(\boldsymbol{\theta}^{(i)})
\end{aligned}
\tag{2.168}
$$

and

$$
\begin{aligned}
\nabla_{\boldsymbol{\phi}} \mathbb{E}_{q_{\boldsymbol{\phi}}}[\log \pi(\hat{\mathbf{S}}, \boldsymbol{\theta})] &= \mathbb{E}_{\pi(\boldsymbol{\varepsilon})}[\nabla_{\boldsymbol{\theta}}(\log \pi(\hat{\mathbf{S}}|\boldsymbol{\theta}(\boldsymbol{\phi}, \boldsymbol{\varepsilon})) + \log \pi(\boldsymbol{\theta}(\boldsymbol{\phi}, \boldsymbol{\varepsilon})))\nabla_{\boldsymbol{\phi}}\boldsymbol{\theta}(\boldsymbol{\phi}, \boldsymbol{\varepsilon})] \\
&\approx \frac{1}{N} \sum_{i=1}^{N} \nabla_{\boldsymbol{\theta}}(\log \pi(\hat{\mathbf{S}}|\boldsymbol{\theta}^{(i)}) + \log \pi(\boldsymbol{\theta}^{(i)}))\nabla_{\boldsymbol{\phi}}\boldsymbol{\theta}^{(i)},
\end{aligned}
\tag{2.169}
$$

where $\boldsymbol{\theta}^{(i)} = \boldsymbol{\theta}(\boldsymbol{\phi}, \boldsymbol{\varepsilon}^{(i)})$ and $\boldsymbol{\varepsilon}^{(i)}$ i.i.d. samples from $\pi(\boldsymbol{\varepsilon})$. The gradient $\nabla_{\boldsymbol{\theta}}(\log \pi(\hat{\mathbf{S}}|\boldsymbol{\theta}(\boldsymbol{\phi})) + \log \pi(\boldsymbol{\theta}(\boldsymbol{\phi})))$ can be identified as $\nabla_{\boldsymbol{\theta}} f(\boldsymbol{\theta})$ from Section 2.3.3 and $\nabla_{\boldsymbol{\phi}}\boldsymbol{\theta}(\boldsymbol{\phi}, \boldsymbol{\varepsilon})$ is derived in Section A.3.2. As an unconstrained optimization problem, stochastic gradient descent (SGD) can be applied to construct sequences of the form

$$
\boldsymbol{\phi}^{(k+1)} = \boldsymbol{\phi}^{(k)} + \rho^{(k)} \nabla_{\boldsymbol{\phi}} \mathcal{L}(\boldsymbol{\phi}^{(k)}) = \boldsymbol{\phi}^{(k)} + \Delta \boldsymbol{\phi}^{(k)},
\tag{2.170}
$$

with step size $\rho^{(k)}$ and where $k = 0, 1, 2, 3, \ldots$. Convergence to a local maximum is guaranteed, provided that the Robbins-Monro criteria [121] for the step size sequence $\rho^{(k)}$

$$
\sum_{k=0}^{\infty} \rho^{(k)} = \infty, \quad \sum_{k=0}^{\infty} (\rho^{(k)})^2 < \infty
\tag{2.171}
$$

are satisfied. The celebrated Adam [72] algorithm is employed to obtain exponentially decaying averages of the first and second moments of the gradient $g_j^{(k)} = \partial \mathcal{L}(\boldsymbol{\phi}^{(k)})/\partial \phi_j$

$$
m_j^{(k)} = \beta_{1,a} m_j^{(k-1)} + (1 - \beta_{1,a}) g_j^{(k)},
\tag{2.172}
$$

$$
v_j^{(k)} = \beta_{2,a} v_j^{(k-1)} + (1 - \beta_{2,a}) (g_j^{(k)})^2.
\tag{2.173}
$$

With the initialization $m_j^0 = 0$ and $v_j^0 = 0$, a bias correction

$$
\hat{m}_j^{(k)} = \frac{m_j^{(k)}}{1 - \beta_{1,a}^k}, \quad \hat{v}_j^{(k)} = \frac{v_j^{(k)}}{1 - \beta_{2,a}^k}
\tag{2.174}
$$

is required[5], resulting in the component-wise parameter update

$$
\Delta \phi_j^{(k)} = \eta_a \frac{\hat{m}_j^{(k)}}{\sqrt{\hat{v}_j^{(k)}} + \varepsilon_a}.
\tag{2.175}
$$

---

[5]Note: $\beta_{1,a}^k$ and $\beta_{2,a}^k$ truly means $\beta_{1,a}$ and $\beta_{2,a}$ to the power of k in this case.

Appropriate values for the hyperparameters η_a, $\beta_{1,a}$ and $\beta_{2,a}$ will be provided for the example in Section 3.4, while the stability parameter ε_a is set to 10^{-8} [72]. To summarize, the ELBO estimate becomes

$$\mathcal{L}(\boldsymbol{\phi}) \approx \frac{1}{N} \sum_{i=1}^{N} f(\boldsymbol{\theta}^{(i)}) + \mathbb{H}[q_{\boldsymbol{\phi}}(\boldsymbol{\theta})] \tag{2.176}$$

and its derivatives with respect to the parameters $\boldsymbol{\phi}$

$$\nabla_{\boldsymbol{\phi}}\mathcal{L} \approx \frac{1}{N} \sum_{i=1}^{N} \nabla_{\boldsymbol{\theta}} f(\boldsymbol{\theta}^{(i)}) \nabla_{\boldsymbol{\phi}} \boldsymbol{\theta}^{(i)} + \nabla_{\boldsymbol{\phi}} \mathbb{H}[q_{\boldsymbol{\phi}}(\boldsymbol{\theta})], \tag{2.177}$$

where the entropy terms $\mathbb{H}[q_{\boldsymbol{\phi}}(\boldsymbol{\theta})]$ and $\nabla_{\boldsymbol{\phi}} \mathbb{H}[q_{\boldsymbol{\phi}}(\boldsymbol{\theta})]$ remain analytically tractable, cf. Section A.3.2. The basic algorithmic steps for the application of SVI for the solution of inverse problems are provided in Alg. (2).

Algorithm 2: SVI for Bayesian inference

1: Initialize $\boldsymbol{\phi}$ randomly
2: **while** not converged **do**
3:     Estimate the gradient: $\boldsymbol{\nabla}_{\boldsymbol{\phi}}\mathcal{L}(\boldsymbol{\phi}^{(k)})$ using Eq. (2.177)
4:     Update the parameters: $\boldsymbol{\phi}^{(k+1)} \leftarrow \boldsymbol{\phi}^{(k)} + \Delta\boldsymbol{\phi}^{(k)}$ using Eq. (2.175)
5:     Estimate the objective function: $\mathcal{L}(\boldsymbol{\phi}^{(k+1)})$ using Eq. (2.176)
6: **end while**

As mentioned before, a Gaussian distribution $\mathcal{N}(\boldsymbol{\mu}, \boldsymbol{\Sigma})$, parameterized by $\boldsymbol{\phi} = \{\boldsymbol{\mu}, \boldsymbol{\Sigma}\}$, is utilized as $q_{\boldsymbol{\phi}}$. While full or banded covariance parameterizations of $\boldsymbol{\Sigma}$ are possible and discussed in [16], these quickly become infeasible as n_θ becomes large. Hence, for reasons of computational efficiency, a scalable covariance formulation [91, 102] is utilized, which is based on a diagonal plus low-rank structure and where the number of ranks can be chosen as a trade off between efficiency and accuracy. Details are presented in Section A.3.2.

2.5.6. Unique solutions to stochastic inverse problems

The following section is a revised version of part of the author's work published in [18]. In Section 2.3.4 above, a stochastic inverse problem that seeks consistent solutions was formulated. Unfortunately, there exist many measures $\mathbb{P}_{\mathcal{X}}$ that satisfy this condition. To obtain a unique solution, the approach developed in [21, 22] is made use of, which imposes additional structure to the problem. Recalling Section 2.3.4, given an observed probability measure $\mathbb{P}_{\mathcal{Y}}^{\mathrm{obs}}$ with density $\pi_{\mathcal{Y}}^{\mathrm{obs}}$, the stochastic inverse problem seeks a probability measure $\mathbb{P}_{\mathcal{X}}$ with density $\pi_{\mathcal{X}}$ such that the subsequent push-forward measure $\mathbb{P}_{\mathcal{Y}}^{Q}$ induced by the map $Q(\boldsymbol{\theta})$ satisfies

$$\mathbb{P}_{\mathcal{X}}(Q^{-1}(B)) = \mathbb{P}_{\mathcal{Y}}^{Q}(B) = \mathbb{P}_{\mathcal{Y}}^{\mathrm{obs}}(B), \quad \forall B \in \mathcal{B}_{\mathcal{Y}}. \tag{2.178}$$

As a constraint on the space of solutions, an initial probability measure $\mathbb{P}_{\mathcal{X}}^{\mathrm{init}}$ with density $\pi_{\mathcal{X}}^{\mathrm{init}}$ is introduced. Together with the map $Q(\boldsymbol{\theta})$, the initial probability measure induces a push-forward

measure

$$\mathbb{P}_{\mathcal{Y}}^{Q(\text{init})}(B) = \mathbb{P}_{\mathcal{X}}^{\text{init}}(Q^{-1}(B)), \quad \forall B \in \mathcal{B}_{\mathcal{Y}}, \tag{2.179}$$

and a push-forward density $\pi_{\mathcal{Y}}^{Q(\text{init})}$. [21] make use of Bayes' rule to construct a unique solution to the stochastic inverse problem, which is referred to as the updated probability measure $\mathbb{P}_{\mathcal{X}}^{\text{up}}$. The updated density follows as

$$\pi_{\mathcal{X}}^{\text{up}}(\boldsymbol{\theta}) = \pi_{\mathcal{X}}^{\text{init}}(\boldsymbol{\theta}) \frac{\pi_{\mathcal{Y}}^{\text{obs}}(Q(\boldsymbol{\theta}))}{\pi_{\mathcal{Y}}^{Q(\text{init})}(Q(\boldsymbol{\theta}))}. \tag{2.180}$$

The existence of this solution requires a predictability assumption [21], i.e. it is assumed that there exists a constant $C > 0$ such that $\pi_{\mathcal{Y}}^{\text{obs}}(Q) \leq C\pi_{\mathcal{Y}}^{Q(\text{init})}(Q)$, $\forall Q \in \mathbb{R}^{n_Q}$. In practice, this assumption simply requires that the observations have to be predictable by the model. Various properties of this approach addressing the uniqueness and stability of the consistent solution are discussed in [21, 22]. A further interesting observation is that the updated density removes the regularization induced by the initial density within the manifold informed by the data [23]. Lastly, the approach has recently been generalized to allow for non-deterministic maps $Q(\boldsymbol{\theta})$ subject to noise or other sources of uncertainties.

Algorithmic steps and diagnostics

Approximating the push-forward $\pi_{\mathcal{Y}}^{Q(\text{init})}$ using MC sampling is simple, but computationally very demanding. This approach involves sampling from the initial density, computing the model responses and utilizing KDE to obtain the push-forward density. It is being noted that KDE methods can quickly become infeasible for multiple QoI due to their poor scalability in higher dimensions. In most practical cases, however, the number of parameters n_θ is large, while the number of QoI n_Q will be relatively small. Having calculated the push-forward of the initial density, a mechanism to generate samples from the updated density is required in order to infer updated statistics about the model parameters $\boldsymbol{\theta}$ and to make predictions. Since the updated density can be interrogated directly, this can easily be accomplished via rejection sampling [22], cf. Alg. (3). For a given parameter realization $\boldsymbol{\theta}$, the ratio of the updated density divided by the initial density is computed and normalized by an estimate of the maximum of the ratio over the whole space $\mathcal{X}$. For the updated density given in Eq. (2.180), this ratio is given by

$$r(\boldsymbol{\theta}) = \frac{\pi_{\mathcal{X}}^{\text{up}}(\boldsymbol{\theta})}{\pi_{\mathcal{X}}^{\text{init}}(\boldsymbol{\theta})} = \frac{\pi_{\mathcal{Y}}^{\text{obs}}(Q(\boldsymbol{\theta}))}{\pi_{\mathcal{Y}}^{Q(\text{init})}(Q(\boldsymbol{\theta}))}. \tag{2.181}$$

Thus, applying rejection sampling to generate samples from the updated density using samples from the initial density is equivalent to generating samples from the observed density using samples generated from the push-forward of the initial. The value of this ratio is then compared with a sample from the uniform distribution $\mathcal{U}(0, 1)$, accepted if the ratio is larger and rejected otherwise. Rejection sampling is applied to the samples from the initial density and therefore comes at no additional costs, since model evaluations at the initial samples were already computed in the calculation of the push-forward. As a result of this, the updated samples will be a subset of the

initial samples. This makes the approach very attractive to optimal experimental design (OED) problems as further discussed in [23].

Algorithm 3: Generate samples from the updated density using rejection sampling

1: **Input:** $\{\boldsymbol{\theta}_i\}_{i=1}^N$, $\{Q_i\}_{i=1}^N$, $\pi_{\mathcal{Y}}^{Q(\text{init})}(Q)$, $\pi_{\mathcal{Y}}^{\text{obs}}(Q)$
2: Calculate $M = \max_i \pi_{\mathcal{Y}}^{\text{obs}}(Q_i)/\pi_{\mathcal{Y}}^{Q(\text{init})}(Q_i)$
3: **for** $i = 1, \ldots, N$ **do**
4:     Compute: $r_i = \pi_{\mathcal{Y}}^{\text{obs}}(Q_i)/\pi_{\mathcal{Y}}^{Q(\text{init})}(Q_i)$
5:     Generate a random number from a uniform distribution: $\xi_i \sim \mathcal{U}(0,1)$
6:     Compute: $\eta_i = r_i/M$
7:     **if** $\eta_i > \xi_i$ **then**
8:         Accept $\boldsymbol{\theta}_i$
9:     **else**
10:        Reject $\boldsymbol{\theta}_i$
11:     **end if**
12: **end for**
13: **Output:** Accepted samples

An appealing property of this framework for stochastic inverse problems is the possibility to compute several diagnostic values to examine the obtained updated solution. The following diagnostics are considered:

(D1) The integral of the updated density

$$\int \pi_{\mathcal{X}}^{\text{up}}(\boldsymbol{\theta})\, \mathrm{d}\boldsymbol{\theta} = \int r(\boldsymbol{\theta})\, \pi_{\mathcal{X}}^{\text{init}}(\boldsymbol{\theta})\, \mathrm{d}\boldsymbol{\theta} \approx \frac{1}{N} \sum_{i=1}^N r_i, \qquad (2.182)$$

where $r(\boldsymbol{\theta})$ is the ratio from Eq. (2.181) and $r_i = r(\boldsymbol{\theta}_i)$. This quantity should integrate to approximately one.

(D2) The push-forward of the updated density, $\pi_{\mathcal{Y}}^{Q(\text{up})}$, can be compared with the observed density. If the observed density has a parametric form, e.g., Gaussian, then the relevant parameters can be compared. More generally, the push-forward of the updated density can be estimated using KDE on the model evaluations corresponding to the samples from the updated solution and this should match the observed density $\pi_{\mathcal{Y}}^{\text{obs}}$. This can be checked quantitatively by calculating the KL divergence

$$\begin{aligned}
\text{KL}[\pi_{\mathcal{Y}}^{Q(\text{up})} : \pi_{\mathcal{Y}}^{Q(\text{obs})}] &= \int \pi_{\mathcal{Y}}^{Q(\text{up})}(Q) \log \frac{\pi_{\mathcal{Y}}^{Q(\text{up})}(Q)}{\pi_{\mathcal{Y}}^{Q(\text{obs})}(Q)}\, \mathrm{d}Q \\
&\approx \frac{1}{N_{\text{up}}} \sum_{i=1}^{N_{\text{up}}} \log \frac{\pi_{\mathcal{Y}}^{Q(\text{up})}(Q_i)}{\pi_{\mathcal{Y}}^{Q(\text{obs})}(Q_i)},
\end{aligned} \qquad (2.183)$$

which should be close to zero and where N_{up} is the number of accepted samples from the rejection sampling algorithm.

(D3) The information gained between the initial and updated densities, measured by the KL divergence

$$\mathrm{KL}[\pi_{\mathcal{X}}^{\mathrm{up}} : \pi_{\mathcal{X}}^{\mathrm{init}}] = \int \pi_{\mathcal{X}}^{\mathrm{up}}(\boldsymbol{\theta}) \log \frac{\pi_{\mathcal{X}}^{\mathrm{up}}(\boldsymbol{\theta})}{\pi_{\mathcal{X}}^{\mathrm{init}}(\boldsymbol{\theta})} \, \mathrm{d}\boldsymbol{\theta}$$
$$= \int r(\boldsymbol{\theta}) \log(r(\boldsymbol{\theta})) \, \pi_{\mathcal{X}}^{\mathrm{init}}(\boldsymbol{\theta}) \, \mathrm{d}\boldsymbol{\theta} \approx \frac{1}{N} \sum_{i=1}^{N} r_i \log r_i. \tag{2.184}$$

(D4) The acceptance rate

$$\tau = \frac{N_{\mathrm{up}}}{N}. \tag{2.185}$$

Diagnostics (D1) and (D2) numerically verify that the predictability assumption was not violated. Diagnostic (D3) provides insight about how much the solution was updated by the data and (D4) gives an indication of the effectiveness of the rejection sampling scheme.

Calculating the push-forward density using probabilistic MFMC

As mentioned above, simple MC sampling to approximate the push-forward density $\pi_{\mathcal{Y}}^{Q(\mathrm{init})}(Q)$ is computationally prohibitive for practical purposes. To that end, the utilization of the probabilistic MFMC method from above is proposed. This approach is demonstrated in detail in the author's work published in [18] and relies on Eq. (2.151) to compute the push-forward via a low-fidelity model $q(\boldsymbol{\theta})$ as

$$\pi_{\mathcal{Y}}^{Q(\mathrm{init})}(Q) = \int \pi(Q|q) \, \pi^{q(\mathrm{init})}(q) \, \mathrm{d}q. \tag{2.186}$$

Hence, the numerically expensive MC sampling is only necessary for the calculation of the push-forward $\pi^{q(\mathrm{init})}(q)$ of the low-fidelity model $q(\boldsymbol{\theta})$. The high-fidelity model, $Q(\boldsymbol{\theta})$, only needs to be evaluated a few times for the construction of the conditional $\pi(Q|q)$, cf. Alg. (1), resulting in significant speed-ups compared to direct MC sampling on the high-fidelity model.

2.5.7. Dimensionality reduction of parameterized models

A frequent challenge in doing UQ with problems of practical interest is the high number of stochastic parameters n_θ, since many established methods suffer from the infamous curse of dimensionality [12]. While MC methods are not affected by this phenomenon, their applicability is usually numerically infeasible, requiring model evaluations in the order of thousands. Thus, reducing the number of parameters is a popular strategy to avoid the curse of dimensionality in forward and inverse UQ problems, allowing for the application of methods that perform well in lower dimensional settings, such as surrogate or reduced-order models and grid-based approaches.

Principal component analysis

Principal component analysis (PCA) is a dimensionality reduction approach that arises from the problem of finding the directions of largest variation in a data set $\{\boldsymbol{x}^{(k)}\}_{k=1}^{n}$, with data points $\boldsymbol{x}^{(k)} \in \mathbb{R}^{m}$. It can be shown [12] that this problem corresponds to solving an eigenvalue problem on the data covariance matrix $\boldsymbol{C}^{m} \in \mathbb{R}^{m \times m}$ with entries

$$C_{ij}^{m} = \frac{1}{n} \sum_{k=1}^{n} (x_i^{(k)} - \bar{x}_i)(x_j^{(k)} - \bar{x}_j) \tag{2.187}$$

and where $\bar{x}_i = \frac{1}{n} \sum_{i=1}^{n} x_i$ is the arithmetic mean for dimension i. The spectrum of $\boldsymbol{C}_m$ can then be examined for gaps in order to define a threshold at which directions contributing negligible amounts to the variance are truncated. Finally, the $r \leq \mathrm{rank}(\boldsymbol{C}^m)$ eigenvectors $\boldsymbol{\zeta}_i \in \mathbb{R}^m$, $i = 1 \dots r$, corresponding to the r largest eigenvalues λ_i^2 form a matrix $\boldsymbol{P} \in \mathbb{R}^{m \times r}$, which can be used to project data points $\boldsymbol{x} \in \mathbb{R}^m$ from the original to the reduced space and vice versa,

$$\boldsymbol{\psi} = \boldsymbol{P}^{\mathsf{T}} \boldsymbol{x} \quad \text{and} \quad \boldsymbol{x} = \boldsymbol{P}\boldsymbol{\psi}, \quad \boldsymbol{\psi} \in \mathbb{R}^r. \tag{2.188}$$

PCA is referred to as an unsupervised method in the context of ML and is frequently used in a preprocessing step upstream to a supervised ML method. For the case where $m > n$, the covariance matrix

$$C_{ij}^{n} = \frac{1}{m} \sum_{k=1}^{m} (x_k^{(i)} - \bar{x}_k)(x_k^{(j)} - \bar{x}_k) \tag{2.189}$$

with $\boldsymbol{C}^n \in \mathbb{R}^{n \times n}$ can be used, since the non-zero eigenvalues of $\boldsymbol{C}^n$ and $\boldsymbol{C}^m$ are identical [112]. In particular, let $\boldsymbol{X} \in \mathbb{R}^{m \times n}$ denote the centered data matrix, i.e. with entries $X_{ij} = x_i^{(j)} - \bar{x}_i$, then

$$\boldsymbol{C}^m = \boldsymbol{X}\boldsymbol{X}^{\mathsf{T}}, \quad \boldsymbol{C}^n = \boldsymbol{X}^{\mathsf{T}}\boldsymbol{X} \tag{2.190}$$

and

$$\boldsymbol{C}^m \boldsymbol{\zeta}_i = \lambda_i^2 \boldsymbol{\zeta}_i, \quad \boldsymbol{C}^n \boldsymbol{\xi}_i = \lambda_i^2 \boldsymbol{\xi}_i, \tag{2.191}$$

with eigenvalues λ_i^2 and corresponding eigenvectors $\boldsymbol{\zeta}_i \in \mathbb{R}^m$ and $\boldsymbol{\xi}_i \in \mathbb{R}^n$, respectively. From the singular value decomposition (SVD) on $\boldsymbol{X}$, it is known that

$$\boldsymbol{X}\boldsymbol{\xi}_i = \lambda_i \boldsymbol{\zeta}_i, \tag{2.192}$$

implying that the columns of the projection matrix $\boldsymbol{P} \in \mathbb{R}^{m \times r}$ can be computed using

$$\boldsymbol{\zeta}_i = \frac{1}{\lambda_i} \boldsymbol{X}\boldsymbol{\xi}_i. \tag{2.193}$$

To summarize, for the construction of $\boldsymbol{P}$, an eigendecomposition of either $\boldsymbol{C}^m$ or $\boldsymbol{C}^n$ can be employed, whichever is computationally more convenient. In the context of reduced basis (RB)

methods, $m > n$ is the standard case and the process is referred to as proper orthogonal decomposition (POD).

Sensitivity analysis

While PCA is solely based on the input parameters, for the case of parameterized models such as the parameter-to-QoI map $Q(\boldsymbol{\theta})$, it is more common to use sensitivity analysis (SA) methods in order to quantify the influence of model outputs Q with respect to model inputs $\boldsymbol{\theta}$. If the sensitivity with respect to one parameter θ_i is estimated around a fixed value $\bar{\boldsymbol{\theta}}$, the sensitivity metric S_i is referred to as a local sensitivity, e.g.

$$S_i = \left.\frac{\mathrm{d}Q}{\mathrm{d}\theta_i}\right|_{\boldsymbol{\theta}=\bar{\boldsymbol{\theta}}}. \tag{2.194}$$

In contrast, if the sensitivity is computed across the whole parameter domain of $\boldsymbol{\theta}$, these are called global sensitivities. The latter sensitivity metrics are particularly needed, if the degree of nonlinearity in the model $Q(\boldsymbol{\theta})$ as well as the uncertainty about the parameters $\boldsymbol{\theta}$ is large. In this case, local SA is no longer an appropriate option.

A class of particularly powerful global sensitivity metrics are Sobol's indices [125, 131]. They are based on the analysis of variance (ANOVA) decomposition of the function $Q(\boldsymbol{\theta})$ into a sum of variances, allowing for the computation of so-called nth-order and total effect global sensitivity indices. While the former quantifies the nth-order contribution of the variance associated with variable θ_i, the latter represents the total amount of variance due to θ_i. The computation of these indices allows for a straightforward ranking of the input parameters $\boldsymbol{\theta}$ in terms of their contributions to the variance of the function $Q(\boldsymbol{\theta})$. Unfortunately, their MC approximation comes at the cost of a considerable amount of numerical effort, which is in the order of thousands per parameter.

Active subspace method

A recently proposed, novel approach to dimensionality reduction and global SA of parameterized models is provided via the active subspace method (ASM) [26]. It is based on a covariance matrix defined as

$$\boldsymbol{C}^{n_\theta} = \int (\nabla_{\boldsymbol{\theta}} Q)(\nabla_{\boldsymbol{\theta}} Q)^{\mathsf{T}} \pi(\boldsymbol{\theta}) \, \mathrm{d}\boldsymbol{\theta}, \tag{2.195}$$

which represents an average of the outer product of gradients $\nabla_{\boldsymbol{\theta}} Q(\boldsymbol{\theta}) \in \mathbb{R}^{n_\theta}$ with themselves, i.e.

$$C_{ij}^{n_\theta} = \int \frac{\mathrm{d}Q}{\mathrm{d}\theta_i} \frac{\mathrm{d}Q}{\mathrm{d}\theta_j} \pi(\boldsymbol{\theta}) \, \mathrm{d}\boldsymbol{\theta}. \tag{2.196}$$

The idea behind this definition of $\boldsymbol{C}^{n_\theta}$ is to capture the dominating directions of high sensitivity across the parameter domain. In practice, a MC estimate of $\boldsymbol{C}^{n_\theta}$ is employed

$$\boldsymbol{C}^{n_\theta} \approx \frac{1}{N} \sum_{i=1}^{N} (\nabla_{\boldsymbol{\theta}} Q_i)(\nabla_{\boldsymbol{\theta}} Q_i)^{\mathsf{T}}, \qquad (2.197)$$

with gradient evaluations $\nabla_{\boldsymbol{\theta}} Q_i = \nabla_{\boldsymbol{\theta}} Q(\boldsymbol{\theta})|_{\boldsymbol{\theta}=\boldsymbol{\theta}_i}$, based on i.i.d. samples $\boldsymbol{\theta}_i \sim \pi(\boldsymbol{\theta})$. As before, a covariance matrix $\boldsymbol{C}^N \in \mathbb{R}^{N \times N}$ can also be used, if $n_\theta > N$. Finally, carrying out a PCA on the covariance matrix, a projection of the original parameter space to the active subspace can be carried out as

$$\boldsymbol{\psi} = \boldsymbol{P}^{\mathsf{T}} \boldsymbol{\theta}, \qquad (2.198)$$

with $\boldsymbol{\psi} \in \mathbb{R}^r$ and $\boldsymbol{P} \in \mathbb{R}^{n_\theta \times r}$ containing the eigenvectors associated with the highest r eigenvalues, allowing for lower-dimensional approximations $Q(\boldsymbol{\psi}) \approx Q(\boldsymbol{\theta})$. To choose an adequate number N of MC samples, [26] developed the formula

$$N = \alpha \, r \log n_\theta, \quad \alpha \in [2, 10], \qquad (2.199)$$

for the approximation of the r first eigenvalues of $\boldsymbol{C}^{n_\theta}$ and propose bootstrapping to assess the variability in the respective estimates. Further applications of the ASM have been presented in the context of accelerated MCMC [28, 128] and global SA [27]. For a more rigorous mathematical analysis of the method and discussion regarding its properties, it is referred to [26].

Maximum von Mises stress derivative for the application of the ASM

The application of derivative-based parameter reduction methods such as the ASM requires gradient information $\nabla_{\boldsymbol{\theta}} Q(\boldsymbol{\theta})$ of the parameter-to-QoI map. For the case where $Q(\boldsymbol{\theta})$ corresponds to the maximum von Mises stress $\sigma_{\mathrm{vm}}^{\max}$, the adjoint method from Section 2.2.4 can readily be applied. The general objective function then simply corresponds to

$$f(\mathbf{D}(\boldsymbol{\theta}), \boldsymbol{\theta}) = \sigma_{\mathrm{vm}}^{\max}(\mathbf{D}(\boldsymbol{\theta}), \boldsymbol{\theta}) = \max_{\mathrm{e}} \boldsymbol{\Sigma}_{\mathrm{vm}}(\mathbf{D}(\boldsymbol{\theta}), \boldsymbol{\theta}), \qquad (2.200)$$

where $\boldsymbol{\Sigma}_{\mathrm{vm}} = \{\sigma_{\mathrm{vm}}{}^{(\mathrm{e})}\}_{\mathrm{e}=1}^{n_{\mathrm{el}}}$ are the element-wise von Mises stresses. The computation of the objective function total derivative requires the solution of the adjoint problem

$$\frac{\partial \mathbf{R}}{\partial \mathbf{D}}^{\mathsf{T}} \boldsymbol{\Lambda} = -\frac{\partial \sigma_{\mathrm{vm}}^{\max}}{\partial \mathbf{D}} \qquad (2.201)$$

and the evaluation of

$$\frac{\mathrm{d} f(\mathbf{D}(\boldsymbol{\theta}), \boldsymbol{\theta})}{\mathrm{d} \boldsymbol{\theta}} = \frac{\partial \sigma_{\mathrm{vm}}^{\max}}{\partial \boldsymbol{\theta}} + \boldsymbol{\Lambda}^{\mathsf{T}} \frac{\partial \mathbf{R}}{\partial \boldsymbol{\theta}}. \qquad (2.202)$$

The partial derivatives of $\sigma_{\mathrm{vm}}^{\max}$ with respect to $\mathbf{D}$ and $\boldsymbol{\theta}$ can be derived on an element-wise basis, cf. Section A.2.3 for details. All remaining terms are already known from Section 2.2.4.

In Section 3.5, the ASM will be used for a predictive rupture risk assessment using the calibrated growth parameters from Section 3.4.

3. Framework Application

In the following, the biomechanical rupture risk assessment as presented in Section 2.4 will be exemplified in several numerical examples. The main purpose of this section is to demonstrate two possible scenarios resulting from this approach:

I. *In momento* rupture risk: snapshot in time assessment using clinical data from one point in time. This corresponds to the classical scenario, where one is interested in the risk of rupture of a prospective patient.

II. *In posterum* rupture risk: predictive assessment by making use of longitudinal data as part of a surveillance strategy. This allows for an estimate about the future trend of the risk of rupture.

The section is organized as follows. After carrying out a correlation analysis between non-invasive and invasive features from an existing database in Section 3.1, the most relevant properties are employed for the prediction of the invasive properties of a prospective patient in Section 3.2. With this, the rupture risk framework is demonstrated in detail for one patient and afterwards applied to a cohort of patients with asymptomatic and symptomatic/ruptured AAA in Section 3.3 (scenario I.). While this analysis did not take into account any effects related to growth and thus only allows the assessment at the time of data acquisition, a methodology for the calibration of growth parameters based on consecutive CT images is presented in Section 3.4. Finally, it is demonstrated how a predictive rupture risk index based on the previous growth model can be computed in Section 3.5 (scenario II.).

Employed methods and software implementations

In Section A.5, for each of the presented result, an overview of the employed methods from Section 2.5 is provided, as well as information regarding the software implementation. In addition, related publications from the Mechanics & High Performance Computing Group are listed for contextual reasons or to refer to more details.

Acknowledgements

3.1. Correlation analysis between invasive vessel wall properties and non-invasively accessible clinical parameters

This section is a revised version of part of the author's work published in [19]. The presented results make use of clinical and experimental data that has been collected during multiple research projects on the mechanobiological behavior of AAAs between 2008 and 2017. In particular, AAA patients undergoing elective OSR at the University Hospital rechts der Isar in Munich, Germany, were added to the database, whenever one or more tissue samples of the AAA vessel wall could be extracted. Each data point contains clinically accessible patient information from anamnesis, CT imaging and a total blood count, as well as results from mechanical testing of the harvested AAA tissue sample. Details on data collection and experimental testing have been reported in [8, 117]. In total, the database contains 305 entries from an equal number of tissue samples that were collected from 139 patients.

t_{w}	Wall thickness	[mm]
α_{w}	Alpha stiffness	[kPa]
β_{w}	Beta stiffness	[kPa]
σ_{γ}	Wall strength	[kPa]

Table 3.1.: Invasive properties represent key vessel wall characteristics for a biomechanical rupture risk assessment. They cannot be obtained prospectively by using clinically established methods and will be provided via the statistical model proposed in Section 3.2.

The data can be split into two groups. Invasive properties (cf. Table 3.1), denoted by $\boldsymbol{\Theta}$, represent key vessel wall characteristics, which have been determined retrospectively from AAA tissue samples and cannot be obtained for a prospective patient by using clinically established methods. They are, however, essential for the biomechanical modeling and simulation of AAAs and the calculation of the probability of rupture using Eq. (2.117). In contrast, non-invasive properties (cf. Table 3.2), denoted by $\boldsymbol{\xi}$, can be determined with standard methods in the clinic.

Prior to any analysis, a preprocessing operation on the dataset is essential, since values are missing both in the invasive and non-invasive properties for several cases in the database. Similar to [8], the following preparatory steps are conducted. Non-invasive features, where more than 30% of the data points had missing values and patients with more than 30% of missing features were excluded and all other missing non-invasive properties imputed with the corresponding median value across the population. As a consequence, the four parameters calcium, hsCRP, creatine kinase and fibrinogen were disregarded. Finally, all non-invasive features were normalized. The resulting dataset $\mathcal{D} = \{\boldsymbol{\xi}_i, \boldsymbol{\Theta}_i\}_{i=1}^{n_{\mathrm{data}}}$, that was used for the analysis, consisted of $n_{\mathrm{data}} = 251$ data points from 113 individual patients.

To examine possible correlations between the non-invasive and invasive properties, an approach based on Spearman's rank correlation coefficient and bootstrapping is pursued. In contrast to the Pearson correlation coefficient

$$r_{\mathrm{P}}(X, Y) = \frac{\sum_{i=1}^{n_{\mathrm{data}}}(x_i - \bar{x})(y_i - \bar{y})}{\sqrt{\sum_{i=1}^{n_{\mathrm{data}}}(x_i - \bar{x})^2}\sqrt{\sum_{i=1}^{n_{\mathrm{data}}}(y_i - \bar{y})^2}} \tag{3.1}$$

General	Sex	m=1, w=0
	Age	y
	Symptomatic	yes=1, no=0
	Ruptured	yes=1, no=0
Geometry	Maximum AAA diameter	mm
	Maximum thrombus thickness	mm
	AAA length	mm
	Subrenal diameter	mm
Medication	Acetylsalicylic acid (ASA) / clopidogrel	yes=1, no=0
	Angiotensin-converting enzyme (ACE) inhibitors	yes=1, no=0
	Statins	yes=1, no=0
	Beta blockers	yes=1, no=0
	Antihypertensives	yes=1, no=0
	Diuretics	yes=1, no=0
	Oral hypoglycemic agents / insulin	yes=1, no=0
Anamnesis	Hypertension	yes=1, no=0
	Diabetes mellitus	yes=1, no=0
	Hyperlipidemia	yes=1, no=0
	Smoking status	yes=1, no=0
	Chronic kidney disease (CKD)	yes=1, no=0
	Coronary heart disease (CHD)	yes=1, no=0
	Peripheral vascular disease (PVD)	yes=1, no=0
Hemogram	Sodium	mmol/l
	Potassium	mmol/l
	Calcium	mmol/l
	high-sensitivity C-reactive protein (hsCRP)	mg/l
	Fibrinogen	mg/dl
	Urea	mg/dl
	Creatinine	mg/dl
	Creatine kinase	1/l
	Leukocytes	$1{,}000/\mu l$
	Erythrocytes	$Mio/\mu l$
	Thrombocytes	$1{,}000/\mu l$
	Hemoglobin	g/dl
	Mean corpuscular hemoglobin (MCH)	pg/cell
	Mean corpuscular volume (MCV)	fl
	Mean corpuscular hemoglobin concentration (MCHC)	gHb/100ml

Table 3.2.: Non-invasive properties overview. These can be determined with standard methods in the clinic and will be used as feature variables to predict the invasive properties of a prospective AAA patient. The subrenal diameter is measured directly below the renal arteries. If the aneurysm reached the renal arteries, the aortic diameter between the celiac artery and the superior mesenteric artery minus 2.5 mm was used instead [84]. Reproduced with permission from [19].

between the samples $\{x_i, y_i\}_{i=1}^{n_{\text{data}}}$ of two variables X and Y, which is a measure of linear correlation, Spearman's rank correlation coefficient

$$r_{\text{S}}(X, Y) = r_{\text{P}}(\text{rg}(X), \text{rg}(Y)) \tag{3.2}$$

assesses the monotonicity of the relationship between X and Y. Spearman's rank correlation coefficient is thus not limited to linear relationships. It is computed identically to the Pearson correlation coefficient, but uses the ranks $\text{rg}(X)$ and $\text{rg}(Y)$ of X and Y instead of their values. For an ordered collection of data points, $\{x_i\}_{i=1}^{n_{\text{data}}}$, the rank $\text{rg}(x_i)$ is simply the position of x_i in the collection.

Correlation coefficients are often referred to as r-values and reported along with so-called p-values, which indicate the probability that the observed correlations were produced by an uncorrelated dataset $\{x_i, y_i\}_{i=1}^{n_{\text{data}}}$. Hence, if the p-value associated with a computed r-value is very small, the null hypothesis of uncorrelated data can be rejected and the alternative hypothesis of an existing correlation accepted. In view of the known issues associated with interpreting r- and p-values [142, 149], however, especially when obtained from a small and noisy dataset, the correlation analysis is carried out using the bootstrapping resampling method. To that end, N new datasets $\{\tilde{\mathcal{D}}_j\}_{j=1}^{N}$ of the same size are created from the original dataset $\mathcal{D}$ via sampling with replacement. Then, the r- and p-values are computed N times for the individual bootstrap datasets $\tilde{\mathcal{D}}_j$, allowing for a straightforward computation of uncertainty estimates.

Here, $\mathcal{D} = \{x_i, y_i\}_{i=1}^{n_{\text{data}}} = \{\boldsymbol{\xi}_i, \boldsymbol{\Theta}_i\}_{i=1}^{n_{\text{data}}}$, while $N = 100$ has proven a reasonable choice. Results are provided in Fig. 3.1, where in the upper row the bootstrapping analysis is visualized for Spearman's rank correlation coefficient r_{S} between each invasive property and its six corresponding highest correlating non-invasive properties. Additionally, in the lower row, corresponding p-values are visualized in order to assess the confidence in the correlations. The figure reveals a relatively large scattering of the r- and p-value for many of the correlates, especially those involving the beta stiffness. Apart from that, the results suggest that the geometric parameters as well as some of the hemogram parameters are associated with almost all of the invasive properties. In particular, strongest correlations with reasonable scatter in the p-values can be observed between:

- Wall thickness and AAA length, maximum AAA diameter, subrenal diameter, MCV.

- Alpha stiffness and subrenal diameter, MCV, MCH, AAA length.

- Beta stiffness and thrombocytes, MCH.

- Wall strength and MCH, MCV, hemoglobin.

While a direct comparison to the correlations in previous works [8, 117] is not possible due to the extended database and different methodology used here, most of these correlations have been identified before. However, [8] didn't provide any quantitative results regarding r- and p-values, such that Fig. 3.1 may provide further insights on the possible correlations as well as their remaining uncertainty in the current dataset. It is being noted that the importance of geometric features has also been confirmed in the recent works of [80, 97, 119], where different approaches for rupture risk assessment based on the AAA geometry are discussed.
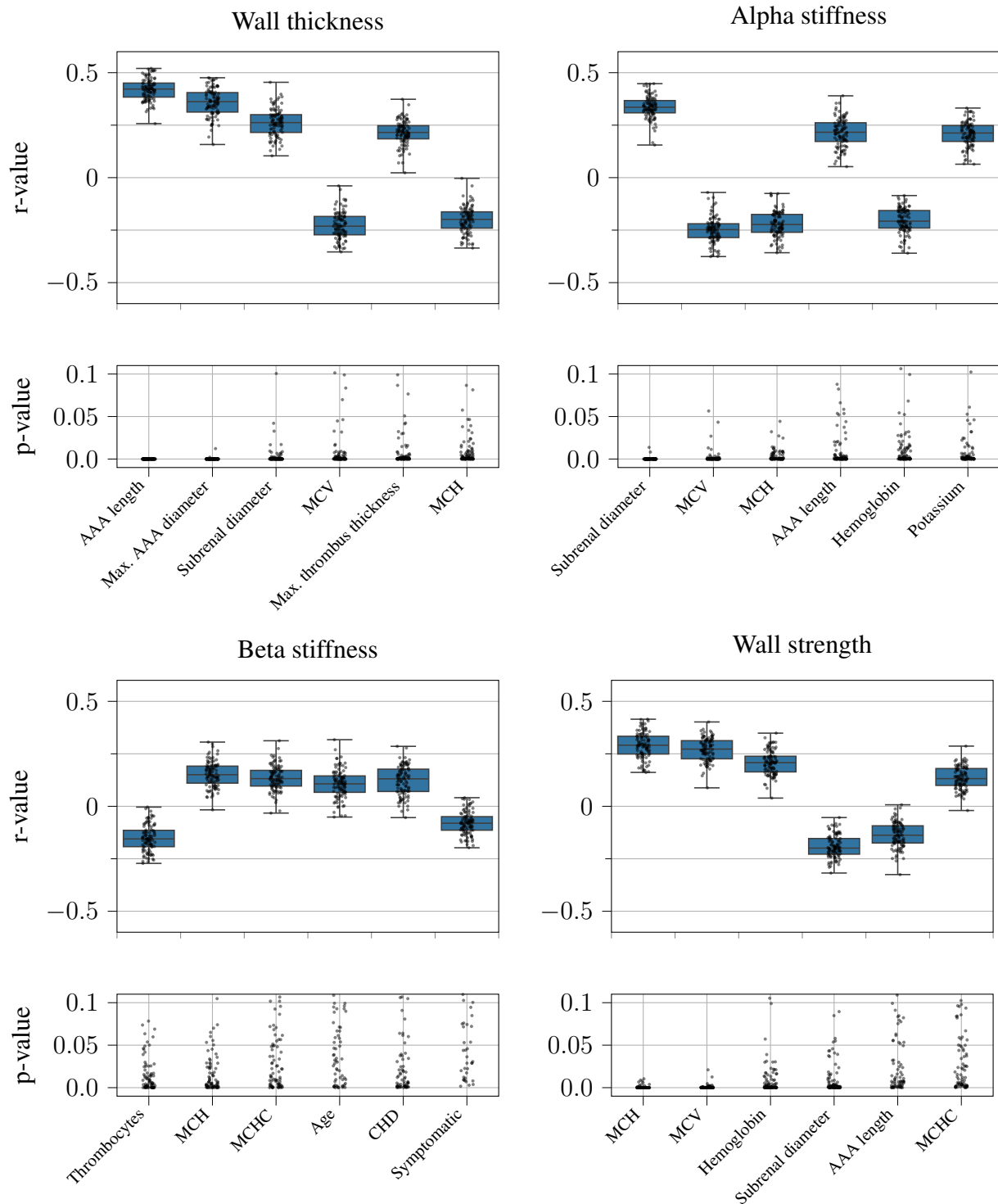
Figure 3.1.: Computed r- and p-values for the invasive vessel wall properties and corresponding most important non-invasive properties using Spearman's rank correlation coefficient. Boxplots in the upper rows indicate median values, 25% and 75% percentiles as well as maximum and minimum values, while the black dots represent all $N = 100$ computed points from the bootstrapping analysis.

3.2. Patient-specific probabilistic modeling of invasive vessel wall properties

This section is a revised version of part of the author's work published in [19]. Based on the correlation analysis from the previous section, the goal is to construct a statistical model for the vessel wall properties $\Theta(\boldsymbol{\xi})$ for a prospective new patient with non-invasive properties $\boldsymbol{\xi}$, under the following desiderata:

1. Patient-specific modeling: obtain personalized estimates for the vessel wall quantities Θ based on correlations with the non-invasive properties $\boldsymbol{\xi}$ of a specific, prospective patient.

2. Probabilistic treatment: take into account the uncertainties in the predictions for Θ (do not ignore statistical information).

3. Dependencies: model the correlations among the invasive properties Θ in order to obtain a more accurate probabilistic description and avoid physically implausible parameter configurations.

Previous approaches were either deterministic [84, 141], based on cohort statistics [107], or did not account for correlations among the vessel wall quantities [8]. While the first point can be addressed by using any regression model instead of cohort statistics, the latter two points require a closer examination of the invasive properties. To that end, summary statistics using boxplots as well as correlations between all possible combinations of t_{w}, α_{w}, β_{w} and σ_{γ} are visualized in Fig. 3.2 and Fig. 3.3. Fig. 3.2 reveals a significant variance in all of the four invasive properties, which is a result of intra- and inter-patient variabilities and has been reported before on previous datasets [8, 117]. This reinforces the importance of a probabilistic treatment. In Fig. 3.3, relatively strong correlations among almost all invasive properties can be observed, which calls for an approach that is able to take these dependencies into account.

Motivated by [8], where GPs were used as a regression model for the individual invasive properties, a multivariate GP model (cf. Section 2.5.2 and Section A.3.1) is used for the purposes of this work and to address the three desiderata above. The relatively small number of available data, but high number of non-invasive properties, requires a feature selection process to identify the most important properties in $\boldsymbol{\xi}$. The results in Fig. 3.1 indicate that a small subset of noninvasive properties suffices to account for the dominating correlations and already suggest a pre-selection of features. In an attempt to keep the number of non-invasive parameters small and employing a sequential forward selection algorithm as in [8], the total number of features was reduced to a final selection of 8 variables: maximum AAA diameter, maximum thrombus thickness, AAA length, subrenal diameter, thrombocytes, hemoglobin, MCH, MCV. It is being noted that this does not imply that other non-invasive features such as sex, medication or anamnesis parameters do not have an influence on the biomechanical properties of the AAA wall.

As a result, given the non-invasive properties $\boldsymbol{\xi}$ of a prospective AAA patient, the natural logarithm (acting as a positivity constraint) of the corresponding prediction $\Theta(\boldsymbol{\xi})$ will follow a multivariate Gaussian distribution with predicted mean $\boldsymbol{\mu}_{\log \Theta}$ and covariance matrix $\boldsymbol{\Sigma}_{\log \Theta}$, i.e.

$$\log \Theta(\boldsymbol{\xi}) \sim \mathcal{N}(\boldsymbol{\mu}_{\log \Theta}, \boldsymbol{\Sigma}_{\log \Theta}) = \pi(\log \Theta). \tag{3.3}$$
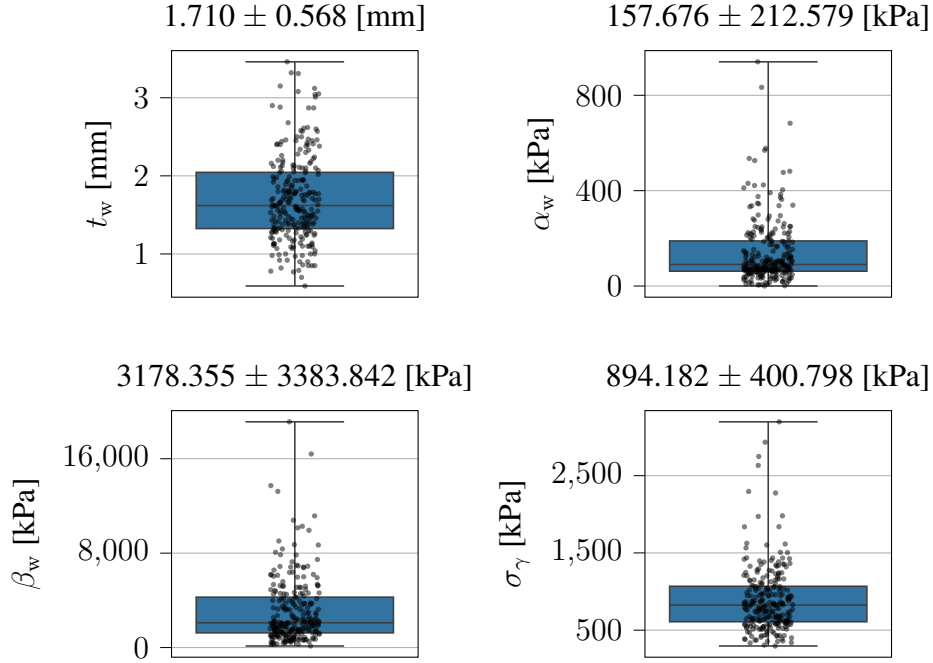
Figure 3.2.: Summary statistics for the invasive properties t_{w}, α_{w}, β_{w} and σ_γ obtained from mechanical testing. Boxplots indicate median values, 25% and 75% percentiles as well as maximum and minimum values, while the black dots represent all available data points. Mean values and standard deviations are provided in the individual plot titles.

Regression model benchmark

Below, a brief comparison between the multivariate GP regression model with existing probabilistic modeling approaches used in the context of AAA rupture risk is provided. To that end, leave-one-out-cross-validation (LOOCV) is applied to the dataset $\mathcal{D}$ to test the predictive capabilities of three different models for $\pi(\log \boldsymbol{\Theta})$:

- Model 1: assuming all variables are log-normally distributed and independent, the joint distribution

$$\pi(\log \boldsymbol{\Theta}) = \prod_{\kappa} \mathcal{N}(\mu_{\log \kappa}, \sigma^2_{\log \kappa}) \tag{3.4}$$

is obtained, with $\kappa \in \{t_{\mathrm{w}}, \alpha_{\mathrm{w}}, \beta_{\mathrm{w}}, \sigma_\gamma\}$. The means and variances are calculated across the whole population using the dataset $\mathcal{D}$, that is

$$\mu_{\log \kappa} = \frac{1}{n_{n_{\mathrm{data}}}} \sum_{i=1}^{n_{\mathrm{data}}} \log \kappa_i \quad \text{and} \quad \sigma^2_{\log \kappa} = \frac{1}{n_{\mathrm{data}}} \sum_{i=1}^{n_{\mathrm{data}}} \left(\log \kappa_i - \mu_{\log \kappa} \right)^2. \tag{3.5}$$

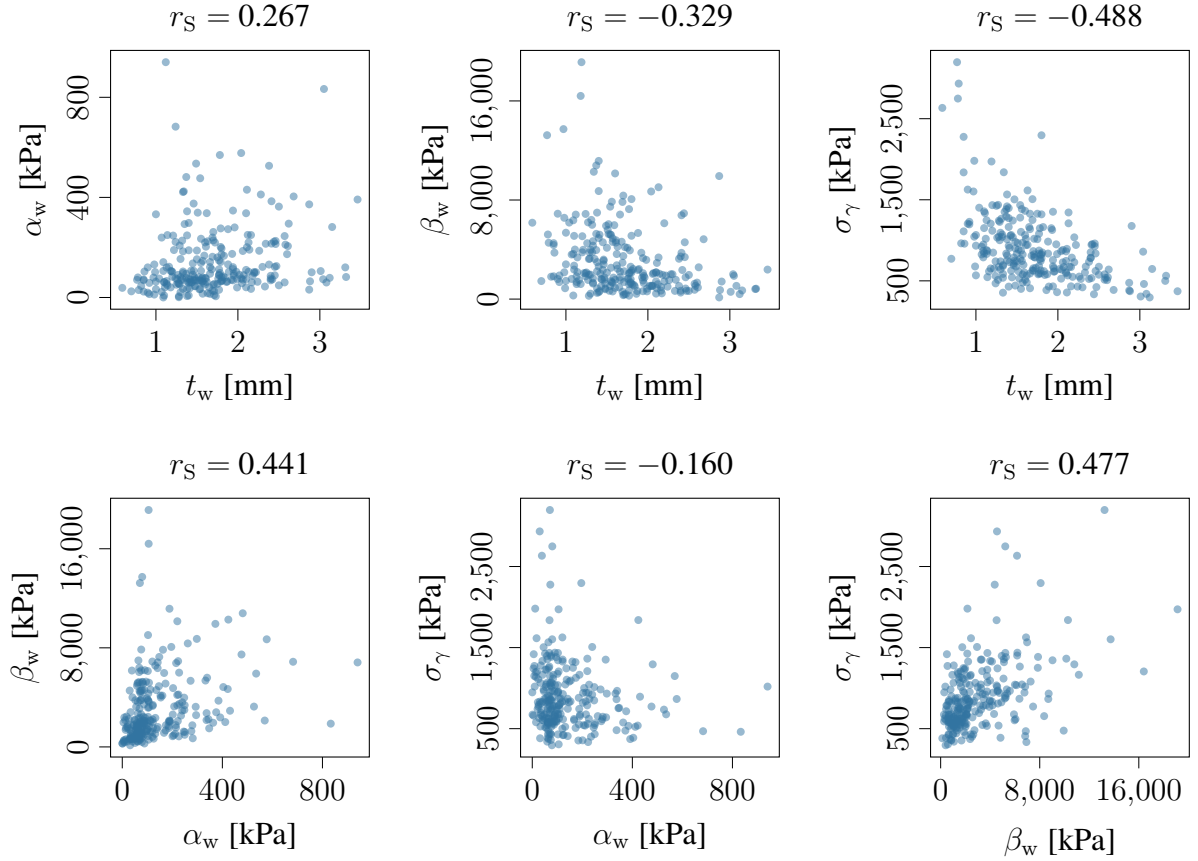This corresponds to the approach chosen in [107].

Figure 3.3.: Scatter plots for all combinations of the invasive properties t_w, α_w, β_w and σ_γ. Corresponding computed Spearman correlations are provided in the titles.

- Model 2: by training single-output GPs for each output variable separately following [8], the same decomposition of Gaussian distributions as in Eq. (3.4) is obtained, however, with means and variances predicted individually for each patient.

- Model 3: the proposed multivariate GP resulting in Eq. (3.3).

In addition to the mean of the patient standardized mean square error (PSMSE) [8], the mean of the patient predictive entropy (PPE)

$$\mathbb{E}[\text{PPE}] = \frac{1}{n_\text{pat}} \sum_{i=1}^{n_\text{pat}} \mathbb{H}[\pi_i(\log \boldsymbol{\Theta})] \tag{3.6}$$

is reported, where $\mathbb{H}[\pi(\log \boldsymbol{\Theta})]$ is the entropy of the distribution $\pi(\log \boldsymbol{\Theta})$ and a measure of uncertainty or variance for multivariate distributions. With regards to the different measures, it is desirable for both PSMSE and PPE to be small, corresponding to a model which is accurate and produces low-variance estimates. For conciseness, values for the mean of the PSMSE are averaged over the four predictive variables $\boldsymbol{\Theta}$. It is being referred to [8] for an exhaustive discussion of the LOOCV and calculation of the PSMSE. The obtained results for the three models

are shown in Table 3.3, where it can be seen that the model proposed here (Model 3) is able to consistently achieve the lowest scores, although the differences are rather small.

	Model 1	Model 2	Model 3
$\mathbb{E}[\text{PSMSE}]$	0.9480	0.9315	0.9226
$\mathbb{E}[\text{PPE}]$	3.5778	3.4300	3.3353

Table 3.3.: LOOCV results for the three probabilistic models. The table compares the calculated mean ($\mathbb{E}[\text{PSMSE}]$) of the PSMSE averaged over the four predictive variables Θ as well as the mean of the patient predictive entropy ($\mathbb{E}[\text{PPE}]$). Reproduced with permission from [19].

3.3. Biomechanical rupture risk assessment at the time of data collection in the clinic

This section is a revised version of part of the author's work published in [19]. The focus lies on the biomechanical rupture risk assessment at the time of data collection in the clinic using Eq. (2.117) and the parameter-to-QoI map $Q(\boldsymbol{\theta}) = \sigma_{\text{vm}}^{\max}(\boldsymbol{\theta})$ with $\boldsymbol{\theta} = [t_{\text{w}}, \alpha_{\text{w}}, \beta_{\text{w}}]^{\mathsf{T}}$. Since the calculation of the probability of rupture $\mathbb{P}_{\text{rupt}}$ using the high-fidelity, nonlinear finite element model from Section 2.2.1 is infeasible for a clinical application, a Kriging surrogate model is proposed to speed up computations inspired by the pioneering works of [70, 124]. It is being noted that Kriging is by far not the only possible method. In [126], e.g., a POD-based approach is established for a very similar AAA model. The surrogate model will effectively serve as a proxy for the maximum von Mises stress $\sigma_{\text{vm}}^{\max}(\boldsymbol{\theta})$ in the AAA vessel wall (cf. Eq. (2.59)) and allows to make computationally cheap predictions at an arbitrary point $\boldsymbol{\theta}$, i.e.

$$\log \sigma_{\text{vm}}^{\max}(\boldsymbol{\theta}) \sim \mathcal{N}(\mu_{\log \sigma_{\text{vm}}^{\max}}, \delta_{\log \sigma_{\text{vm}}^{\max}}^2), \tag{3.7}$$

with the predicted mean $\mu_{\log \sigma_{\text{vm}}^{\max}}$ and standard deviation $\delta_{\log \sigma_{\text{vm}}^{\max}}$, respectively. For all relevant details, it is being referred to Section 2.5.2 and Section A.3.1. The high-fidelity model can then be simply approximated as $\log \sigma_{\text{vm}}^{\max}(\boldsymbol{\theta}) \approx \mu_{\log \sigma_{\text{vm}}^{\max}}(\boldsymbol{\theta})$, allowing for a direct MC estimation of the probability of rupture

$$\mathbb{P}_{\text{rupt}} = \mathbb{E}_{\pi(\log \boldsymbol{\Theta})}\big[\mathbb{1}_{\log \sigma_{\text{vm}}^{\max}(\boldsymbol{\theta}) > \log \sigma_{\gamma}}\big] \approx \frac{1}{n_{\text{eval}}} \sum_{i=1}^{n_{\text{eval}}} \mathbb{1}_{\log \sigma_{\text{vm}}^{\max}(\boldsymbol{\theta}_i) > \log \sigma_{\gamma,i}}, \tag{3.8}$$

where

$$\mathbb{1}_{\log \sigma_{\text{vm}}^{\max}(\boldsymbol{\theta}_i) > \log \sigma_{\gamma,i}} = \begin{cases} 1 & \log \sigma_{\text{vm}}^{\max}(\boldsymbol{\theta}_i) > \log \sigma_{\gamma,i}, \\ 0 & \text{otherwise} \end{cases} \tag{3.9}$$

and $\boldsymbol{\Theta}_i \sim \pi(\log \boldsymbol{\Theta})$, $i = 1 \dots n_{\text{eval}}$. The Kriging surrogate training process is carried out under the two demands:

1. As few as possible high-fidelity model evaluations.

2. Ensure that the Kriging model is accurate where necessary.

To that end, the active learning-MacKay (ALM) strategy from [53] is adopted and extended by choosing points for high-fidelity model evaluations such as to minimize a density- and stress-weighted predictive standard deviation objective function

$$\psi(\boldsymbol{\Theta}) = \delta_{\log \sigma_{\mathrm{vm}}^{\max}}(\boldsymbol{\theta}) \, \pi(\log \boldsymbol{\Theta}) \, \mu_{\log \sigma_{\mathrm{vm}}^{\max}}(\boldsymbol{\theta}), \tag{3.10}$$

where $\pi(\log \boldsymbol{\Theta})$ is the patient-specific PDF for the invasive model parameters $\boldsymbol{\Theta} = [t_{\mathrm{w}}, \alpha_{\mathrm{w}}, \beta_{\mathrm{w}}, \sigma_{\gamma}]^{\mathsf{T}}$ from the regression model. The reasoning behind this choice follows from the ALM approach, where only the predictive standard deviations $\delta_{\log \sigma_{\mathrm{vm}}^{\max}}(\boldsymbol{\theta})$ are considered in the objective function. In the present case, the PDF $\pi(\log \boldsymbol{\Theta})$ is available, so that a higher weight can be attributed to the more probable regions in $\boldsymbol{\Theta}$. Additionally, special attention is paid to points in the input space, where the predicted maximum von Mises stresses $\mu_{\log \sigma_{\mathrm{vm}}^{\max}}$ are high to ensure the surrogate model accurately replicates the full model in these regions. The problem of choosing an appropriate point $\boldsymbol{\theta}^{\mathrm{next}}$ for evaluation results in the optimization problem

$$\boldsymbol{\Theta}^{\mathrm{next}} = \arg \max_{\boldsymbol{\Theta}} \, \psi(\boldsymbol{\Theta}), \tag{3.11}$$

which is approximated by creating a grid $\{\boldsymbol{\Theta}_i\}_{i=1}^{n_{\mathrm{grid}}}$ over the input space, calculating $\{\psi(\boldsymbol{\Theta}_i)\}_{i=1}^{n_{\mathrm{grid}}}$ using the Kriging surrogate and determining

$$\boldsymbol{\Theta}^{\mathrm{next}} \approx \arg \max_{\boldsymbol{\Theta}} \, \{\psi(\boldsymbol{\Theta}_i)\}_{i=1}^{n_{\mathrm{grid}}}. \tag{3.12}$$

The next evaluation point $\boldsymbol{\theta}^{\mathrm{next}} = [t_{\mathrm{w}}^{\mathrm{next}}, \alpha_{\mathrm{w}}^{\mathrm{next}}, \beta_{\mathrm{w}}^{\mathrm{next}}]^{\mathsf{T}}$ can then simply be extracted from $\boldsymbol{\Theta}^{\mathrm{next}}$. During the active learning, the average

$$\hat{\psi} = \frac{1}{n_{\mathrm{grid}}} \sum_{i=1}^{n_{\mathrm{grid}}} \psi(\boldsymbol{\Theta}_i) \tag{3.13}$$

is monitored and the training process stopped, when there are no more significant changes in $\hat{\psi}$ with an increasing number of high-fidelity model evaluations.

Framework summary

Based on the retrospective AAA database of non-invasive and invasive data pairs and a multi-output GP model fitted to this dataset (cf. Section 3.2), the necessary steps to estimate the probability of rupture for a prospective patient are:

- **Step 1:** Data generation in the clinic: CT imaging, determination of the non-invasive parameters $\boldsymbol{\xi}$ from Table 3.2

- **Step 2:** Geometry creation: segmentation and meshing of the AAA geometry

- **Step 3:** Model specification: modeling of the invasive properties $\boldsymbol{\Theta}(\boldsymbol{\xi})$ using the multi-output GP model from Section 2.5.2

- **Step 4:** Surrogate training: fitting of the Kriging model using active learning

- **Step 5:** Post-processing: estimating the probability of rupture

While CT imaging is essential for geometry creation, the rupture risk analysis can also be carried out if no non-invasive properties $\boldsymbol{\xi}$ are available for a prospective patient by using cohort statistics (cf. Model 1) without personalization. The computational procedure is summarized in Alg. (4). In practice, it has proven feasible to choose $n_{\mathrm{init}} = 8$ (where it makes sense to include the predicted mean $\boldsymbol{\mu}_{\log \Theta}$ in the set of initial samples), $n_{\mathrm{grid}} = n_{\mathrm{eval}} = 10{,}000$ and $\mathrm{tol} = 1.0 \times 10^{-4}$.

Algorithm 4: Calculating the probability of rupture $\mathbb{P}_{\mathrm{rupt}}$

1: **Input:** Input uncertainties $\pi(\log \Theta(\boldsymbol{\xi}))$, simulation model $\sigma_{\mathrm{vm}}^{\max}(\boldsymbol{\theta})$, tol, n_{init}, n_{grid}, n_{eval}
2: Set $\mathrm{iter} = 1, \hat{\psi}_0 = 0$
3: Generate n_{init} samples $\{\log \boldsymbol{\theta}_i\}_{i=1}^{n_{\mathrm{init}}}$ and calculate $\{\log \sigma_{\mathrm{vm}}^{\max}(\boldsymbol{\theta}_i)\}_{i=1}^{n_{\mathrm{init}}}$
4: Train a Kriging surrogate using the training data $\{\boldsymbol{\theta}_i, \log \sigma_{\mathrm{vm}}^{\max}(\boldsymbol{\theta}_i)\}_{i=1}^{n_{\mathrm{init}}}$
5: Create a grid $\{\log \Theta_i\}_{i=1}^{n_{\mathrm{grid}}}$ over the input space and calculate $\hat{\psi}_1$ (cf. Eq. (3.13))
6: **while** $|\hat{\psi}_{\mathrm{iter}} - \hat{\psi}_{\mathrm{iter}-1}| > \mathrm{tol}$ **do**
7:     Determine $\boldsymbol{\theta}^{\mathrm{next}}$ using Eq. (3.12) and calculate $\sigma_{\mathrm{vm}}^{\max}(\boldsymbol{\theta}^{\mathrm{next}})$
8:     Update the Kriging model with the new data $\{\boldsymbol{\theta}^{\mathrm{next}}, \log \sigma_{\mathrm{vm}}^{\max}(\boldsymbol{\theta}^{\mathrm{next}})\}$ and calculate $\hat{\psi}_{\mathrm{iter}}$
9:     Set $\mathrm{iter} = \mathrm{iter} + 1$
10: **end while**
11: Generate n_{eval} samples $\{\log \Theta_i\}_{i=1}^{n_{\mathrm{eval}}}$ and calculate $\mathbb{P}_{\mathrm{rupt}}$ according to Eq. (3.8) using the Kriging surrogate
12: **Output:** $\mathbb{P}_{\mathrm{rupt}}$

Framework demonstration for AAA Pat17

To illustrate the application of the proposed framework, all steps are demonstrated in detail below, following the outline as presented in the framework summary above. It is being assumed that CT imaging data and non-invasive properties $\boldsymbol{\xi}$ for one specific prospective AAA (**Step 1**), referred to as Pat17 in the following, are provided. Fig. 3.4 shows the AAA as seen via CT imaging (I), a 3D rendering of the segmentation result (II) as well as the generated finite element mesh (III) (**Step 2**). The mesh consists of 117,218 finite elements and 93,840 nodal degrees of freedom, with an approximate element size of 1.6 mm.

Table 3.4 shows the relevant 8 non-invasive properties $\boldsymbol{\xi}$ that are used by the regression model (cf. Section 3.2) to obtain the predictive density $\pi(\log \Theta(\boldsymbol{\xi}))$, which is specific to Pat17. Along with that, means and standard deviations based on all 113 patients in $\mathcal{D}$ are provided. Based on this data, the mean $\boldsymbol{\mu}_{\log \Theta}$ and covariance $\Sigma_{\log \Theta}$ for Pat17 can be predicted (**Step 3**). The obtained density is visualized in Fig. 3.5 and the predictive means and standard deviations are provided in Table 3.5 along with reference values from the cohort. The entropy of $\pi(\log \Theta)$ is 3.3050 and thus slightly lower than the LOOCV mean (cf. Table 3.3).

Given $\pi(\log \Theta)$, the stochastic forward problem (cf. Section 2.3.2) for Pat17 is defined. The probability of rupture for this AAA is approximated using the Kriging surrogate model (**Step 4**). Fig. 3.4 (IV) provides a visualization of the von Mises stresses corresponding to $\boldsymbol{\mu}_{\log \Theta}$, the mean
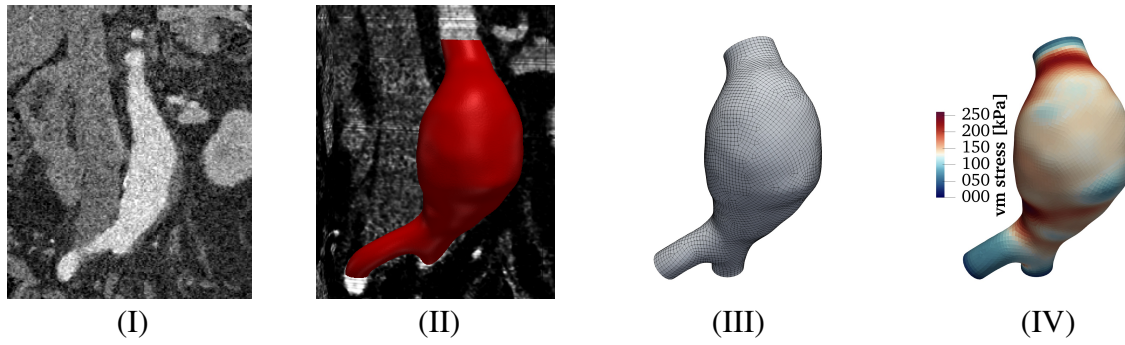
(I)   (II)   (III)   (IV)

Figure 3.4.: AAA Pat17 as seen via CT imaging (I), a 3D rendering of the segmentation result (II), the generated finite element mesh (III) and a visualization of the von Mises stress field corresponding to the mean $\boldsymbol{\mu}_{\log\boldsymbol{\Theta}}$ of the predictive density $\pi(\log\boldsymbol{\Theta})$ for that AAA (IV). Reproduced with permission from [19].

		Pat17	Cohort (mean $\pm$ std)
Maximum AAA diameter	[mm]	53.75	62.91 $\pm$ 17.57
Subrenal diameter	[mm]	21.88	24.58 $\pm$ 6.55
AAA length	[mm]	85.0	111.84 $\pm$ 28.30
Maximum thrombus thickness	[mm]	19.11	24.10 $\pm$ 11.19
Thrombocytes	[1,000/μl]	182.0	221.33 $\pm$ 82.10
Hemoglobin	[g/dl]	15.1	13.27 $\pm$ 2.20
Mean corpuscular hemoglobin (MCH)	[pg/cell]	29.0	30.39 $\pm$ 2.46
Mean corpuscular volume (MCV)	[fl]	85.0	89.95 $\pm$ 6.61

Table 3.4.: Non-invasive properties $\boldsymbol{\xi}$ for AAA Pat17 as well as cohort means and standard deviations (based on all 113 patients in $\mathcal{D}$) for comparison. Reproduced with permission from [19].

		Pat17 (mean $\pm$ std)	Cohort (mean $\pm$ std)
$\log t_{\mathrm{w}}$		0.415 $\pm$ 0.088	0.484 $\pm$ 0.105
t_{w}	[mm]	1.583 $\pm$ 0.481	1.710 $\pm$ 0.568
$\log \alpha_{\mathrm{w}}$		4.504 $\pm$ 0.967	4.543 $\pm$ 1.036
α_{w}	[kPa]	146.529 $\pm$ 187.106	157.676 $\pm$ 212.579
$\log \beta_{\mathrm{w}}$		7.723 $\pm$ 0.817	7.685 $\pm$ 0.758
β_{w}	[kPa]	3399.204 $\pm$ 811.469	3178.355 $\pm$ 3383.842
$\log \sigma_{\gamma}$		6.729 $\pm$ 0.174	6.704 $\pm$ 0.183
σ_{γ}	[kPa]	912.004 $\pm$ 397.176	894.182 $\pm$ 400.798

Table 3.5.: Predicted means and standard deviations for the invasive properties of AAA Pat17 along with cohort values over all $n_{\mathrm{data}} = 251$ samples for comparison. Reproduced with permission from [19]. The notation was adjusted to be consistent with the one used in this thesis.

parameter combination of $\pi(\log\boldsymbol{\Theta})$. Fig. 3.6 shows the decrease of the objective function over the number of iterations on the left as well as a comparison of the Kriging-based approximate density $\pi(\sigma_{\mathrm{vm}}^{\max})$ together with a Monte Carlo reference calculated using 10,000 samples on the right.
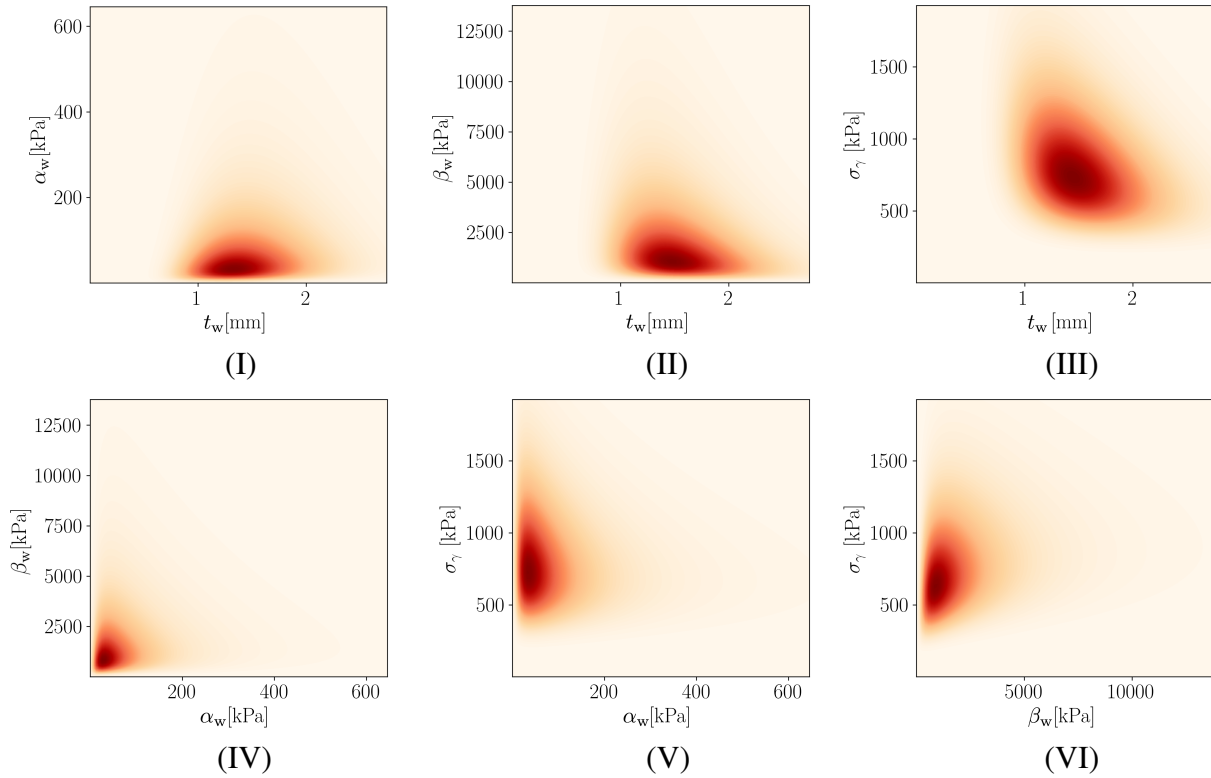
Figure 3.5.: Visualization of the predictive density $\pi(\log \boldsymbol{\Theta})$ transformed to the physical parameter range for AAA Pat17. Plots (I)-(VI) show 2D marginal densities over all possible parameter combinations between t_{w}, α_{w}, β_{w} and σ_γ. Reproduced with permission from [19]. The notation was adjusted to be consistent with the one used in this thesis.

Lastly, the probability of rupture can be estimated using the Kriging surrogate (**Step 5**), which amounts to 0.47% for Pat17 (cf. Fig. 3.9 for a visualization). It is important to note that this value must not be compared to the operative risks associated with OSR or EVAR in order to make decisions. Rather, it needs to be put into context with results for other AAA patients that have been computed using the same methodology, which is discussed below.

Comparative case-control study using diameter matched groups

To test the efficacy of the framework as a rupture risk indicator and to compare it with existing biomechanical indices, diameter matched groups of asymptomatic (group 1, $n = 18$) and known symptomatic/ruptured (group 2, $n = 18$) AAA patients from the database are considered. The groups were chosen such that their maximum diameter mean and standard deviation approximately match (group 1: 62.17 ± 7.18 mm, group 2: 63.06 ± 7.56 mm), rendering a differentiation between the groups based on the maximum diameter criterion ineffective.

For a detailed overview regarding the selection of the two groups, it is being refer to Table 3.6. After preprocessing of the original dataset, the cohort is restricted to AAAs with a maximum diameter between 50 and 80 mm in order to obtain an intermediate-sized group of patients. As a result, 64 patients remained, of which 47 had asymptomatic and 17 had symptomatic or ruptured AAAs. The latter were put into one group, since symptomatic AAAs are known to be at
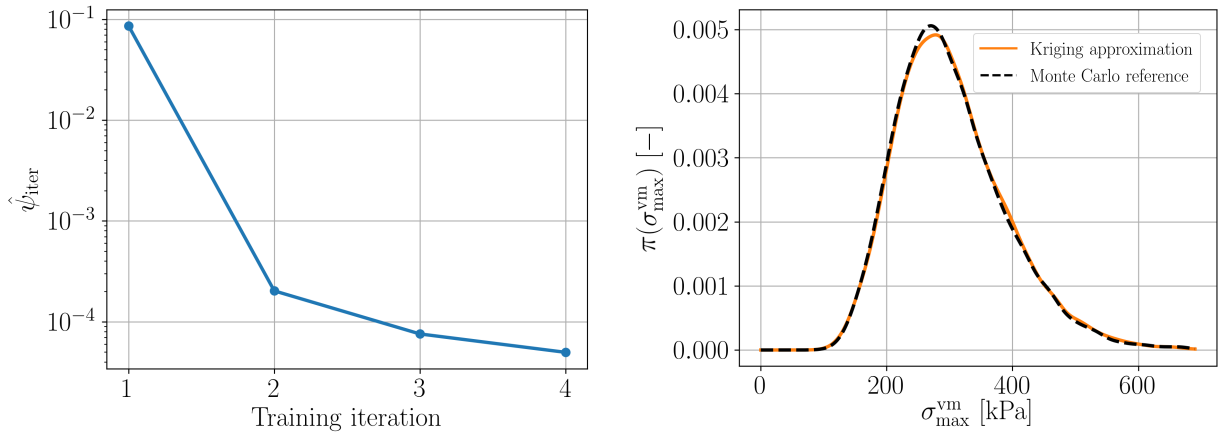
Figure 3.6.: Left: Decrease of the objective function over the number of training iterations, where the first training iteration corresponds to the Kriging surrogate after $n_{\text{init}} = 8$ model evaluations. 11 model evaluations were used for the surrogate creation. Right: Estimated Kriging-based density $\pi(\sigma_{\text{vm}}^{\text{max}})$ along with a Monte Carlo reference. All densities were calculated using kernel density estimation with Gaussian kernels based on 10,000 samples of the maximum von Mises stress $\sigma_{\text{vm}}^{\text{max}}$. Reproduced with permission from [19]. The notation was adjusted to be consistent with the one used in this thesis.

	total no.	m	w	asympt	sympt/rupt
original database	139	122	17	100	39
after preprocessing	113	99	14	83	30
diameter filter	64	58	6	47	17
manual selection	19	19	0	10	9
added from [83]	17	12	5	8	9
final cohort	36	31	5	18	18

Table 3.6.: Overview: selection process for the diameter matched groups. Reproduced with permission from [19].

an elevated risk of rupture [86]. The reason for the much lower number of symptomatic/ruptured AAAs is that these AAAs often have very large diameters (>80 mm). AAA patients from a previous case-control study [83], which examined 13 asymptomatic and 12 symptomatic AAA patients, are included. Finally, 18 asymptomatic and 18 symptomatic/ruptured patients are manually selected based on the following criteria:

- Find two groups with the best match in diameter.

- Preferably include cases where non-invasive data is available and thus patient-specific invasive properties can be predicted.

- Disregard cases, where CT images are not available or lack a sufficient image quality to create simulation models.

Detailed information for all AAAs of both groups is provided in Table 3.8. No patient had known connective tissue disorders. For 10 out of 18 AAAs in group 1 and for 9 out of 18 AAAs in

group 2 non-invasive data was available and it was thus possible to determine a personalized input density $\pi(\log \boldsymbol{\Theta})$. For the remaining 8 (group 1) and 9 (group 2) AAAs, the cohort density (i.e. Model 1) was used.

The framework is applied to all 36 AAAs using an individual prospective scenario, i.e. before starting the analysis for one AAA, this patient is removed from the database, while the other 35 AAAs are included. In order to provide a comparison of $\mathbb{P}_{\mathrm{rupt}}$ with other biomechanical indices, the following additional quantities are calculated:

- Maximum von Mises stress at the input parameter mean (neglects any statistical information):

$$\sigma_{\mathrm{vm}}^{\mathrm{max}}(\boldsymbol{\mu}_{\log \boldsymbol{\theta}}). \tag{3.14}$$

- Rupture potential index [139] at the input parameter mean (neglects any statistical information, but takes into account the wall strength):

$$\mathrm{RPI} = \frac{\sigma_{\mathrm{vm}}^{\mathrm{max}}(\boldsymbol{\mu}_{\log \boldsymbol{\theta}})}{\mu_{\sigma_\gamma}}. \tag{3.15}$$

- Probabilistic rupture risk index [107] (takes into account cohort-based uncertainties in the wall thickness and wall strength according to Model 1):

$$\mathrm{PRRI} = \mathbb{E}_{\mathcal{N}(\mu_{\log t}, \sigma_{\log t}^2) \mathcal{N}(\mu_{\log \sigma_\gamma}, \sigma_{\log \sigma_\gamma}^2)} \left[\mathbb{1}_{\log \sigma_{\mathrm{vm}}^{\mathrm{max}}(\mu_{\log t}) > \mu_{\log \sigma_\gamma}} \right]. \tag{3.16}$$

Comprehensive results for all patients are listed in Table 3.8 and Table 3.9 and a visualization of their rupture risk indices, $\mathbb{P}_{\mathrm{rupt}}$, is provided in Fig. 3.9 and Fig. 3.10. The average number of high-fidelity model evaluations to train the Kriging surrogate was 11. Based on these results and to evaluate the performance of the individual quantities, the following is examined:

I. Relative mean and median differences between group 1 and group 2 (cf. Table 3.7).

II. Boxplots for both groups (cf. Fig. 3.7).

III. receiver operating characteristic (ROC) curves and the area under the ROC curve (AUC) [33] (cf. Fig. 3.8).

		d_{max}	$\sigma_{\mathrm{vm}}^{\mathrm{max}}$	RPI	PRRI	$\mathbb{P}_{\mathrm{rupt}}$
Δ mean	[%]	1.42	20.84	23.15	122.17	204.45
Δ median	[%]	0.81	8.15	9.75	43.24	266.02

Table 3.7.: Relative mean and median differences (in %) of d_{max}, $\sigma_{\mathrm{vm}}^{\mathrm{max}}$, RPI, PRRI and $\mathbb{P}_{\mathrm{rupt}}$ between the asymptomatic and the symptomatic/ruptured group. Relative differences for a quantity q between the asymptomatic group result q_{a} and the symptomatic/ruptured group result $q_{\mathrm{s/r}}$ are calculated as $\Delta q = |q_{\mathrm{s/r}} - q_{\mathrm{a}}|/q_{\mathrm{a}}$. Reproduced with permission from [19].
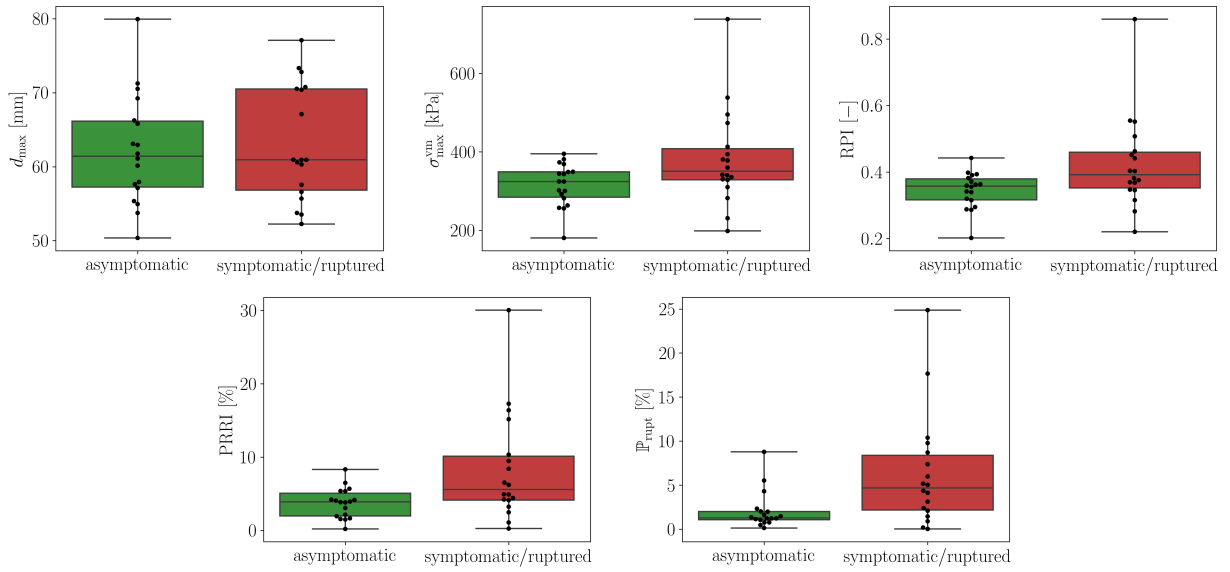
Figure 3.7.: Boxplots comparing $d_{\max}$, $\sigma_{\mathrm{vm}}^{\max}$, RPI, PRRI and $\mathbb{P}_{\mathrm{rupt}}$ for the asymptomatic and symptomatic/ruptured group. The plots illustrate the interquartile range (green and red color) including the sample median as well as the first and third quartiles. Whiskers indicate minimum and maximum values and black dots represent all values from the respective group. Reproduced with permission from [19].
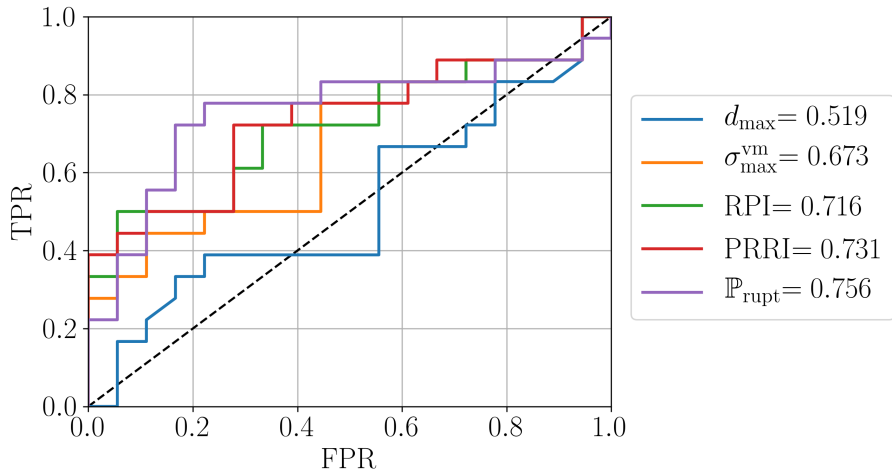

Figure 3.8.: Receiver operating characteristic (ROC) curves showing true positive rates (TPR) over false positive rates (FPR) and area under the ROC curve (AUC) scores for $d_{\max}$, $\sigma_{\mathrm{vm}}^{\max}$, RPI, PRRI and $\mathbb{P}_{\mathrm{rupt}}$. Reproduced with permission from [19].

Discussion

The obtained values for the relative mean and median differences in Table 3.7 confirm that group 1 and group 2 are indistinguishable based on the maximum diameter criterion. While the relative differences are higher for $\sigma_{\mathrm{vm}}^{\max}$ and RPI, PRRI and in particular the proposed index $\mathbb{P}_{\mathrm{rupt}}$ feature a significantly larger mean and median difference. A similar trend as in Table 3.7

can be observed in Fig. 3.7, with RPI and PRRI providing a slightly better separation between the two groups than $\sigma_{\mathrm{vm}}^{\max}$, while for $\mathbb{P}_{\mathrm{rupt}}$ the interquartile ranges of the two groups are non-overlapping. Finally, in Fig. 3.8 one can observe that $\mathbb{P}_{\mathrm{rupt}}$ outperforms the remaining classifiers and achieves the best performance among all quantities in terms of the AUC score, followed by PRRI, RPI and $\sigma_{\mathrm{vm}}^{\max}$. It is further noted that from the 18 patients in the symptomatic/ruptured group, 11 had ruptured AAAs (Pat19, Pat23, Pat24, Pat26, Pat27, Pat28, Pat29, Pat30, Pat32, Pat34, Pat35). The mean $\mathbb{P}_{\mathrm{rupt}}$ scores for the 11 ruptured AAAs is 6.57 and thus slightly higher than the mean 5.89 for the 7 symptomatic AAAs. To summarize the key observations:

- The maximum diameter criterion, by design, clearly fails to separate the two groups in all the comparisons.

- The proposed index $\mathbb{P}_{\mathrm{rupt}}$ consistently achieves the best separation.

- The results indicate that the more statistical information taken into account, the better the capability to distinguish between group 1 and group 2.

Before translating these findings into any clinical application, however, there are several limitations that have to be kept in mind. First, this is a non-randomized, retrospective case-control study with a relatively small cohort size (group 1: n=18, group 2: n=18) and the database described above. Second, there was no matching based on other risk factors such as sex, age or family history, which could be a confounder. Third, since only access to electively repaired or symptomatic/ruptured AAAs for mechanical testing was possible, the mean diameters of the two groups (group 1: 62.17 mm, group 2: 63.03 mm) are larger than the Society for Vascular Surgery's decision criterion for elective repair (55 mm) [24]. In the future, due to the increasing use of EVAR, it will be even harder to obtain representative tissue samples from AAAs of relevant size for a database. As a result, caution is advised when interpreting the results presented here for smaller AAAs, e.g. of size 45-55 mm. Furthermore, all approaches discussed in this section are unable to make any prediction about the future development of the AAA, such that the rupture risk assessment only holds for the point in time of data generation. In addition to that, the biomechanical model does not take into account factors like calcifications and surrounding organs, which might have an impact on the analysis [71, 82].

Nr.	$d_{\max}$ [mm]	$\sigma_{\max}^{\mathrm{vm}}$ [kPa]	RPI [$-$]	PRRI [%]	$\mathbb{P}_{\mathrm{rupt}}$ [%]
Pat1	63.09	373.14	0.398	6.48	2.01
Pat2	69.23	180.21	0.202	0.20	0.13
Pat3	61.76	368.65	0.362	4.20	1.04
Pat4	50.37	257.04	0.288	1.55	1.22
Pat5	62.94	349.00	0.371	4.15	1.34
Pat6	61.10	324.35	0.363	3.81	4.30
Pat7	54.94	301.55	0.339	3.06	0.76
Pat8	60.14	348.62	0.390	5.36	5.52
Pat9	57.12	380.97	0.382	5.68	1.63
Pat10	57.94	263.15	0.295	1.65	1.46
Pat11	57.63	324.06	0.359	3.93	1.14
Pat12	55.35	343.26	0.356	3.84	1.22
Pat13	66.25	281.44	0.315	2.14	2.32
Pat14	71.25	255.60	0.286	1.49	1.21
Pat15	70.52	394.89	0.442	8.32	8.77
Pat16	79.94	300.20	0.342	4.06	0.76
Pat17	53.75	291.70	0.320	1.93	0.47
Pat18	65.81	344.30	0.393	5.37	1.98
mean	62.17	315.67	0.345	3.73	2.07
std	7.18	53.18	0.053	1.99	2.07
25th percentile	57.25	284.00	0.316	1.98	1.07
50th percentile	61.43	324.21	0.357	3.89	1.28
75th percentile	66.14	348.90	0.379	5.07	2.00

Table 3.8.: Group 1 (asymptomatic, 18 m, 0 f) overview and obtained results for $\sigma_{\max}^{\mathrm{vm}}$, RPI, PRRI and $\mathbb{P}_{\mathrm{rupt}}$. Reproduced with permission from [19].

Nr.	$d_{\max}$ [mm]	$\sigma_{\max}^{\mathrm{vm}}$ [kPa]	RPI [−]	PRRI [%]	$\mathbb{P}_{\mathrm{rupt}}$ [%]
Pat19	57.55	230.60	0.282	1.08	0.18
Pat20	70.40	473.52	0.551	16.38	9.77
Pat21	70.76	538.30	0.507	15.16	7.37
Pat22	73.32	380.57	0.452	9.47	4.12
Pat23	77.09	738.58	0.860	30.03	24.87
Pat24	72.80	377.91	0.404	6.51	2.38
Pat25	52.26	197.94	0.220	0.25	0.02
Pat26	60.95	335.47	0.376	4.92	5.02
Pat27	60.30	359.65	0.403	6.21	5.98
Pat28	53.75	309.83	0.347	3.23	3.12
Pat29	55.69	340.56	0.381	4.90	5.16
Pat30	53.53	281.85	0.316	2.47	2.09
Pat31	60.93	412.86	0.462	10.33	10.38
Pat32	70.52	495.17	0.555	17.27	17.66
Pat33	67.10	393.87	0.441	8.40	8.70
Pat34	56.59	328.43	0.368	4.21	4.35
Pat35	60.58	329.85	0.369	4.41	1.44
Pat36	60.93	341.59	0.346	4.11	0.89
mean	63.06	381.47	0.424	8.30	6.31
std	7.56	119.61	0.135	7.18	6.21
25th percentile	56.83	328.78	0.352	4.14	2.16
50th percentile	60.93	350.62	0.392	5.57	4.69
75th percentile	70.49	408.12	0.460	10.12	8.37

Table 3.9.: Group 2 (symptomatic/ruptured, 13 m, 5 f) overview and obtained results for $\sigma_{\max}^{\mathrm{vm}}$, RPI, PRRI and $\mathbb{P}_{\mathrm{rupt}}$. Reproduced with permission from [19].

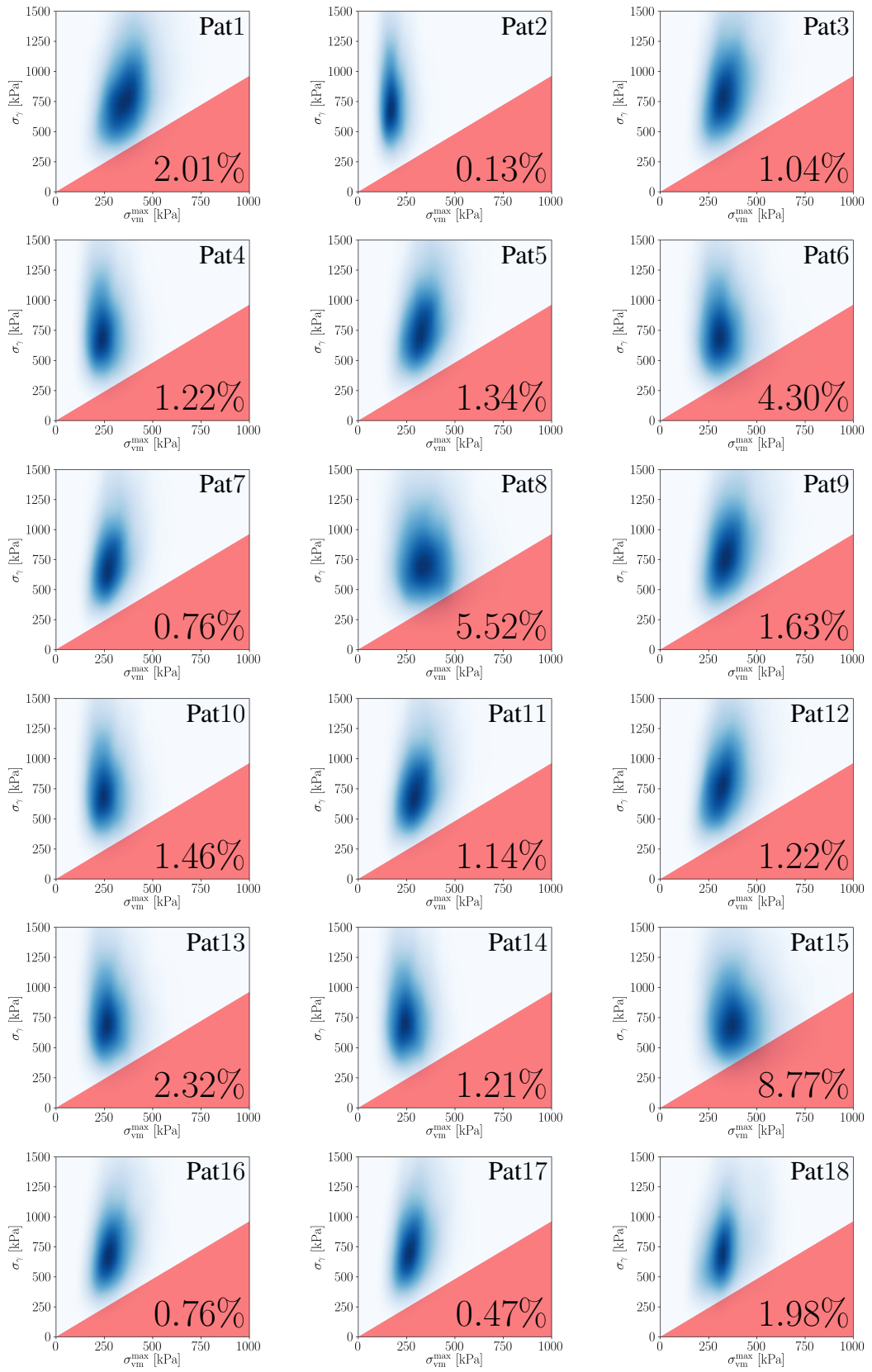Figure 3.9.: Visualization of $\mathbb{P}_{\text{rupt}}$ for all AAAs in group 1. Reproduced with permission from [19].
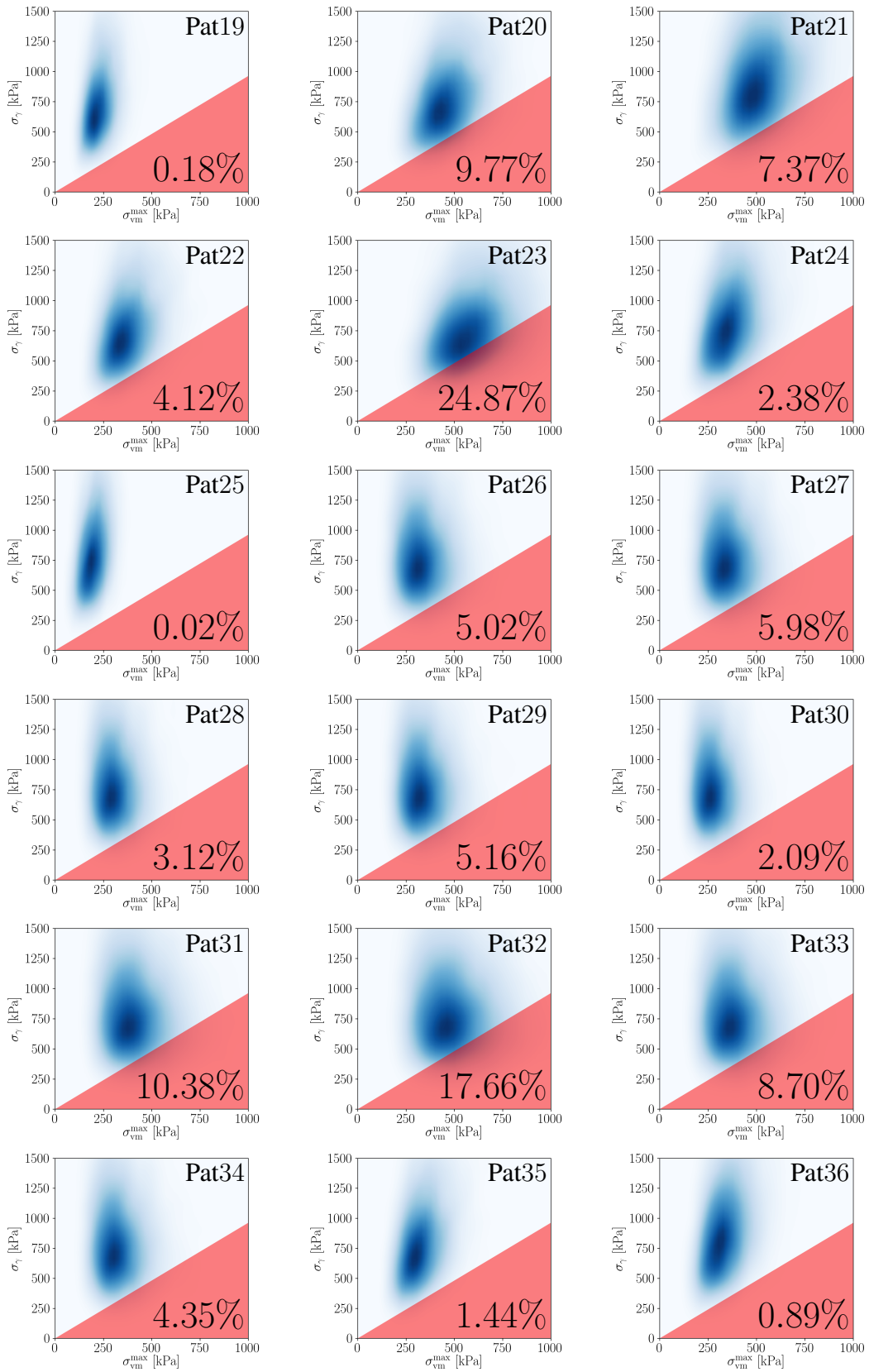
Figure 3.10.: Visualization of $\mathbb{P}_{\text{rupt}}$ for all AAAs in group 2. Reproduced with permission from [19].

3.4. Estimation of AAA growth based on consecutive imaging

The previous section demonstrated the assessment of an *in momento* risk of rupture at the point of data generation in the clinic. While this may already provide a useful piece of information for clinical decision making, an undeniable shortcoming is its limited predictive power, since only one data point in time is considered. Fortunately, the framework from Section 2.4 also allows for an *in posterum* assessment when given a suitable growth model. The biggest challenge associated with such a model, however, lies in the determination of the parameters to adequately describe the temporal changes of an AAA associated with growth. The goal of the next two sections is to enable an efficient *in posterum* rupture risk assessment with minimal requirements on the amount of necessary data and at a low added model complexity in comparison to Section 3.3.

To that end, the estimation of AAA growth will be based on the Bayesian inverse problem from Section 2.3.3, with the likelihood and prior defined in Eq. (2.105) and Eq. (2.106), respectively. Hence, the approach in this thesis follows the modeling framework from [69], where a simple growth law (cf. Section 2.1.2) is employed and only two consecutive CTA or MRA scans are necessary for parameter calibration. Starting from this, the following modifications are proposed:

- Application of the SVI framework (cf. Section 2.5.5) for inference in order to keep the number of required model evaluations significantly lower in comparison to MCMC methods, while being more accurate than the Laplace approximation.

- MAP estimation of the measurement noise as part of the inference process as described in Section 2.5.5. The measurement noise σ_N of the surface current-based likelihood from Eq. (2.106) is a priori not known and difficult to estimate in practice, such that this quantity will be inferred as part of the calibration.

- Spring boundary conditions instead of Dirichlet constraints at the inlet and outlets of the AAA as well as material and simulation models corresponding to Section 2.1.2 and Section 2.2.2.

The result will be an approximate posterior Gaussian PDF $\pi(\boldsymbol{\theta})$ on the growth parameters $\boldsymbol{\theta} = \{c_\vartheta^{(e)}\}_{e=1}^{n_\theta} = \mathbf{c}_\vartheta$, which is easy to sample from for uncertainty propagation purposes and where n_θ corresponds to the number of elements of the arterial wall. In particular, this density can be used in a subsequent step (cf. Section 3.5) to calculate QoI $Q(\boldsymbol{\theta}, t)$ like the maximum von Mises stress in the arterial wall at a certain point in time t, and a time-dependent probability of rupture $\mathbb{P}_{\text{rupt}}(t)$ as suggested in Fig. 2.3.

Example AAA case for growth estimation and prediction

The example AAA case for demonstrating growth and prediction in the context of a biomechanical rupture risk assessment is a relatively small aneurysm with a maximum diameter of 36.7 mm[1]. Such a case is typically uncritical and too small to be considered for elective repair

---

[1]For consistency with the results below, all maximum diameter values are computed in the same way based on the computational model including the vessel wall, and are not determined directly from the CTA images.

and hence needs to be monitored as part of a surveillance strategy. CTA imaging data is available for this patient with a time difference of 2 years and the time instances of data collection will be referred to as t_0 and $t_1 = t_0 + 2$ years, respectively. Over this time span, the maximum diameter increased to about 39.2 mm, corresponding to a growth rate of approximately 1.25 mm per year. The example has been studied before in [68, 69], where further details regarding the CTA data are provided. Axial CT slices at the maximum AAA diameter as well as generated finite element meshes with an approximate element size of 1.6 mm are visualized in Fig. 3.11. While the mesh at t_0 will be used as the forward model for calibration purposes, the abluminal ILT surface of the discretization at t_1 corresponds to the measurement data $\hat{\mathsf{S}}$ used for the evaluation of the surface current likelihood.
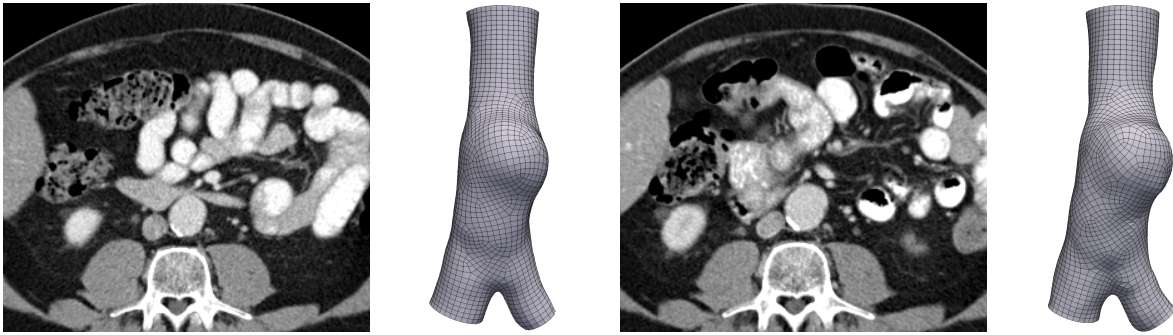

Figure 3.11.: Axial CT slices at the maximum AAA diameter as well as finite element meshes of the example case. First snapshot (left two images) taken at time t_0. Second snapshot (right two images) taken at time $t_1 = t_0 + 2$ years.

Calibration process and parameter settings

Starting from a geometry at time instance t_0, the calibration process is based on the objective to find model parameters $\boldsymbol{\theta}$, such that the simulated geometry at time t_1 matches the CTA extracted geometry from this instance under specific prior assumptions on $\boldsymbol{\theta}$. The quality of the match is quantified via the surface currents based similarity measure of the abluminal ILT surfaces corresponding to the two AAA geometries. The AAA is first prestressed to the mean arterial pressure $\bar{p} = 98.33$ mmHg (cf. Section 2.2.2) to simulate the physiological conditions at the time of imaging, t_0. Afterwards, growth is initiated using the model from Section 2.1.2 with the current set of parameters $\boldsymbol{\theta}$ until t_1. For simplicity and to focus on the effects of growth, the uncertainties associated with the vessel wall parameters are not taken into account here and fixed to $t_{\mathrm{w}} = 1.6$ mm, $\alpha_{\mathrm{w}} = 52.33$ kPa and $\beta_{\mathrm{w}} = 3112$ kPa, corresponding to the median values reported in [84]. The kernel parameter associated with the surface current likelihood [68] is set to $\sigma_W = 1.0$ mm and the parameters of the prior to $\alpha_{\mathrm{tv}} = 100.0$ t/mm and $\varepsilon_{\mathrm{tv}} = 1.0 \times 10^{-2}$ mm/t, respectively.

The number of samples for the estimation of $\mathcal{L}(\boldsymbol{\phi})$ and its gradient is set to $N = 1$, which is a common choice for practical purposes when the reparameterization gradient (cf. Section 2.5.5) is used. The parameters $\beta_{1,a}$ and $\beta_{2,a}$ from the Adam update rule have proven reliable for $\beta_{1,a} = \beta_{2,a} = 0.5$ and are fixed to this value for all numerical examples. Similarly, the step size parameter η_a leads to a stable optimization process for the value $\eta_a = 1 \times 10^{-3}$. Due to the

Parameter	Value
Surface current likelihood kernel scale σ_W	1.0 mm
TV prior weight α_{tv}	100.0 t/mm
TV prior parameter ε_{tv}	1.0×10^{-2} mm/t
Number of MC samples N	1
Adam parameter $\beta_{1,a}$	0.5
Adam parameter $\beta_{2,a}$	0.5
Adam step size parameter η_a	1.0×10^{-3}
Step size factor $\tilde{\eta}_{a,\boldsymbol{\mu}}$	$1.0\,\eta_a$
Step size factor for $\tilde{\eta}_{a,\boldsymbol{\omega}}$	$10.0\,\eta_a$
Step size factor for $\tilde{\eta}_{a,\boldsymbol{B}}$	$0.05\,\eta_a$
Step size factor for $\tilde{\eta}_{a,\omega_N}$	$5.0\,\eta_a$
Wall thickness t_{w}	1.6 mm
Alpha stiffness α_{w}	52.33 kPa
Beta stiffness β_{w}	3112 kPa

Table 3.10.: Overview of SVI and model parameters used in this section.

different nature of the parameters $\boldsymbol{\phi} = \{\boldsymbol{\mu}, \boldsymbol{\omega}, \boldsymbol{B}\}$ and $\omega_N = \log \sigma_N$, individual step size factors were found useful and determined as $\tilde{\eta}_{a,\boldsymbol{\mu}} = 1.0\eta_a$, $\tilde{\eta}_{a,\boldsymbol{\omega}} = 10.0\,\eta_a$, $\tilde{\eta}_{a,\boldsymbol{B}} = 0.05\,\eta_a$ and $\tilde{\eta}_{a,\omega_N} = 5\,\eta_a$. After 100 iterations, the step size is gradually lowered to $\eta_a = 1.0 \times 10^{-4}$ using a cosine function in order to reduce parameter fluctuations due to the stochastic nature of the optimization and make it easier to check the convergence behavior. Finding optimal values for these parameters for a specific problem can be tedious, which is certainly a shortcoming of SVI. However, this is a general issue with almost all optimization algorithms or other inference methods. In the author's experience, even with non-optimal values, the optimization is relatively robust and it is easy to recognize if the step size η_a was chosen too large or too small. As a summary, all relevant parameters are provided in Table 3.10.

MAP estimate of the measurement noise

As discussed in [68], the measurement noise σ_N in the surface current-based likelihood from Eq. (2.105) is usually unknown and nontrivial to choose. To that end, σ_N can be treated as a further optimization parameter in the modified ELBO

$$\tilde{\mathcal{L}}(\tilde{\boldsymbol{\phi}}) = \mathcal{L}(\boldsymbol{\phi}, \sigma_N) + \log \pi(\sigma_N), \tag{3.17}$$

where $\tilde{\boldsymbol{\phi}} = [\boldsymbol{\phi}, \omega_N]^{\mathsf{T}}$ (with $\omega_N = \log \sigma_N$ to allow for unconstrained optimization methods) and where the dependency of $\mathcal{L}$ on σ_N was made explicit. However, this requires a more precise definition of the likelihood in terms of σ_N, which is provided for the surface current framework [31] in the follow-up work [52] as

$$\log \pi(\hat{\mathbf{S}}|\boldsymbol{\theta}) \propto -n_\Delta \log \sigma_N - \frac{\|\hat{\mathbf{S}} - \mathbf{S}(\mathbf{D}(\boldsymbol{\theta}))\|_{\mathcal{W}^\star}^2}{2\sigma_N^2}. \tag{3.18}$$

Here, n_Δ corresponds to the number of triangles in the triangulation of the source geometry used for the evaluation of the norm $\| \cdot \|_{\mathcal{W}^\star}$. The derivative with respect to ω_N is straightforward

$$\frac{\partial \log \pi(\hat{\mathbf{S}}|\boldsymbol{\theta})}{\partial \omega_N} \propto -n_\Delta + \frac{\|\hat{\mathbf{S}} - \mathbf{S}(\mathbf{D}(\boldsymbol{\theta}))\|_{\mathcal{W}^\star}^2}{\sigma_N^2}, \tag{3.19}$$

such that ω_N can be treated like the remaining optimization parameters $\boldsymbol{\mu}$ and $\boldsymbol{\omega}$ in the SVI framework. It is being noted, that this modified formulation of the likelihood does not change the inference if σ_N is fixed, since the additional constant factor $n_\Delta \log \sigma_N$ is independent from the parameters $\boldsymbol{\theta}$.

Choosing a variational model

The following models for the Gaussian covariance matrix are considered:

- Diagonal covariance: $\boldsymbol{\Sigma_\theta} = \boldsymbol{D}^2$, where $\boldsymbol{D} \in \mathbb{R}_+^{n_\theta \times n_\theta}$ is a diagonal matrix.

- Diagonal plus rank-r covariance: $\boldsymbol{\Sigma_\theta} = \boldsymbol{D}^2 + \boldsymbol{B}\boldsymbol{B}^\mathsf{T}$, where $\boldsymbol{B} \in \mathbb{R}^{n_\theta \times n_r}$ is a lower triangular matrix.

- Smoothed diagonal plus rank-r covariance: $\boldsymbol{\Sigma_\theta} = \boldsymbol{L}(\boldsymbol{D}^2 + \boldsymbol{B}\boldsymbol{B}^\mathsf{T})\boldsymbol{L}^\mathsf{T}$, where $\boldsymbol{L} \in \mathbb{R}^{n_\theta \times n_\theta}$ is a linear smoothing operator.

While the diagonal covariance model is simple and efficient, its usage for the purposes of this work is limited, since the fitted density $q_\phi(\boldsymbol{\theta})$ does not account for any dependencies between the growth parameters $\boldsymbol{\theta}$. This becomes obvious, when generating approximate posterior samples from the fitted variational model in order to predict aneurysm growth. The independence assumption ignores any neighborhood relationship, i.e. it effectively contradicts the TV prior assumption, leading to non-smooth samples of the growth rate field and implausible predictions. For that reason and to allow for a more accurate variational approximation at a minimal computational overhead, the diagonal plus rank-r covariance is implemented, as well as a structure-imposing approach, which enforces a smoothing of the variance via averaging adjacent element-based parameters based on the available TV neighborhood graph. All relevant derivations regarding these models are provided in Section A.3.2.

For model selection purposes, a benchmark is carried out to compare the three approaches. Fixing the measurement noise to $\sigma_N = 1.0$ mm^2, different models can easily be compared in terms of their ELBO, cf. Section 2.5.5. The higher the ELBO, the higher the model evidence and thus the better the available observation can be explained by the model. To keep the numerical costs moderate for this benchmark, the AAA is discretized with an approximate element size of 2.5 mm, resulting in $n_\theta = 1{,}260$ growth parameters. The prior weight is adjusted to $\alpha_{\text{tv}} = 50$ t/mm for this coarser discretization. The optimizer is run for 500 iterations and the ELBO from the last 100 iterations are averaged and reported in Table 3.11. The table clearly demonstrates that more accurate approximations are possible using the smoothed covariance approach, while rank updates to the diagonal covariance only seem to result in minor improvements. The latter observation is probably an effect from the chosen stochastic optimization approach, which results in a fairly slow convergence behavior of the additional rank update parameters $\boldsymbol{B}$, such that adding many additional components does not pay off with a limited

Model	n_ϕ	$\bar{\mathcal{L}}(\phi)$
Diagonal covariance	2,520	-14,432.870
Diagonal plus rank-r covariance ($n_r = 1$)	3,780	-14,434.998
Diagonal plus rank-r covariance ($n_r = 2$)	5,040	-14,448.375
Diagonal plus rank-r covariance ($n_r = 3$)	6,300	-14,442.581
Diagonal plus rank-r covariance ($n_r = 10$)	15,120	-14,494.413
Smoothed diagonal covariance	2,520	-13,440.135
Smoothed diagonal plus rank-r covariance ($n_r = 1$)	**3,780**	**-13,412.788**
Smoothed diagonal plus rank-r covariance ($n_r = 2$)	5,040	-13,411.381
Smoothed diagonal plus rank-r covariance ($n_r = 3$)	6,300	-13,424.968
Smoothed diagonal plus rank-r covariance ($n_r = 10$)	15,120	-13,443.036

Table 3.11.: Benchmark between different variational models after 500 iterations. The provided scores, $\bar{\mathcal{L}}(\phi)$, are averaged values over the last 100 MC estimates of $\mathcal{L}(\phi)$. The selected model is highlighted in bold letters.

computational budget. Hence, the smoothed diagonal plus rank-1 covariance model was chosen over the rank-2 one as a trade-off between the number n_ϕ of optimization parameters and accuracy.

Results for the example AAA

The numerical model for the AAA case from Fig. 3.11 consists of 19,892 finite elements and 28,116 degrees of freedom, implying $n_\theta = 2,992$ model and $n_\phi = 8,976$ optimization parameters for the chosen variational approximation. The stochastic optimization is stopped after 500 iterations. In total, the calibration took about 640 minutes on a workstation with an Intel Xeon W-2133 (3.60GHz) processor using 10 cores, i.e. on average 1.28 minutes per iteration. In this case, each iteration involves the solution of one forward problem to estimate the objective function $\tilde{\mathcal{L}}$ and the solution of one adjoint problem for its gradient – besides some computational overhead.
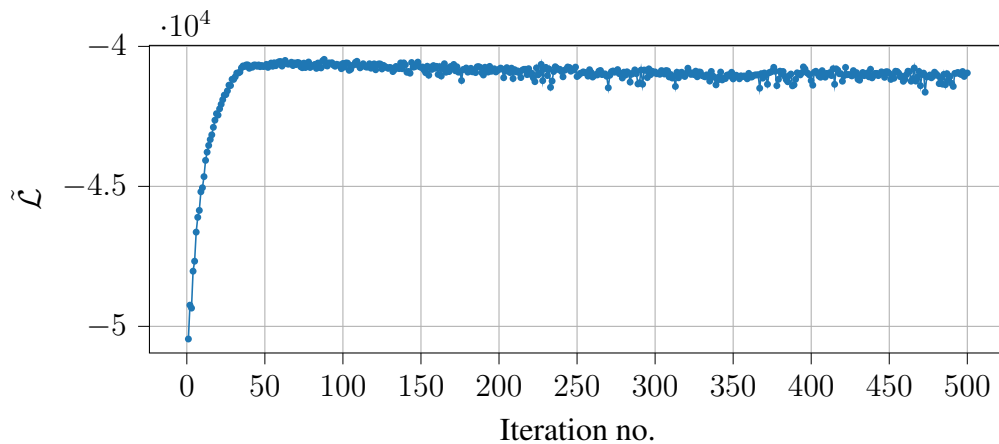

Figure 3.12.: Objective function over the number of iterations.

The stochastic optimization progress is visualized in Fig. 3.12 and Fig. 3.13, where the objective function, L2 norms of the mean, diagonal covariance and rank-1 update as well as the measurement noise over the number of iterations are plotted. In general, these serve as a helpful diagnostic to assess convergence, which is not always easy due to the stochastic nature of the process. Fig. 3.12 displays typical results with a steep increase in $\tilde{\mathcal{L}}$ at the beginning and a subsequent flattening. Since the objective function itself is estimated via MC sampling, there is an inherent variability between consecutive estimates $\tilde{\mathcal{L}}$. It is being noted, that in contrast to following the EM scheme from Section 2.5.5, a direct optimization approach is chosen, such that the measurement noise σ_N^2 and variational parameters ϕ are optimized at the same time. As a consequence, $\tilde{\mathcal{L}}$ may show an unfamiliar behavior when compared to a classical deterministic optimization objective. For example, at iteration number 60 in Fig. 3.12, the estimates for $\tilde{\mathcal{L}}$ drop slightly. Looking at the measurement noise σ_N^2 in Fig. 3.13, this can be explained via the maximum that is reached at iteration 34 and the significant decrease afterwards, implying a rapid change in the likelihood and reflecting the poor variational approximation at the beginning of the optimization.
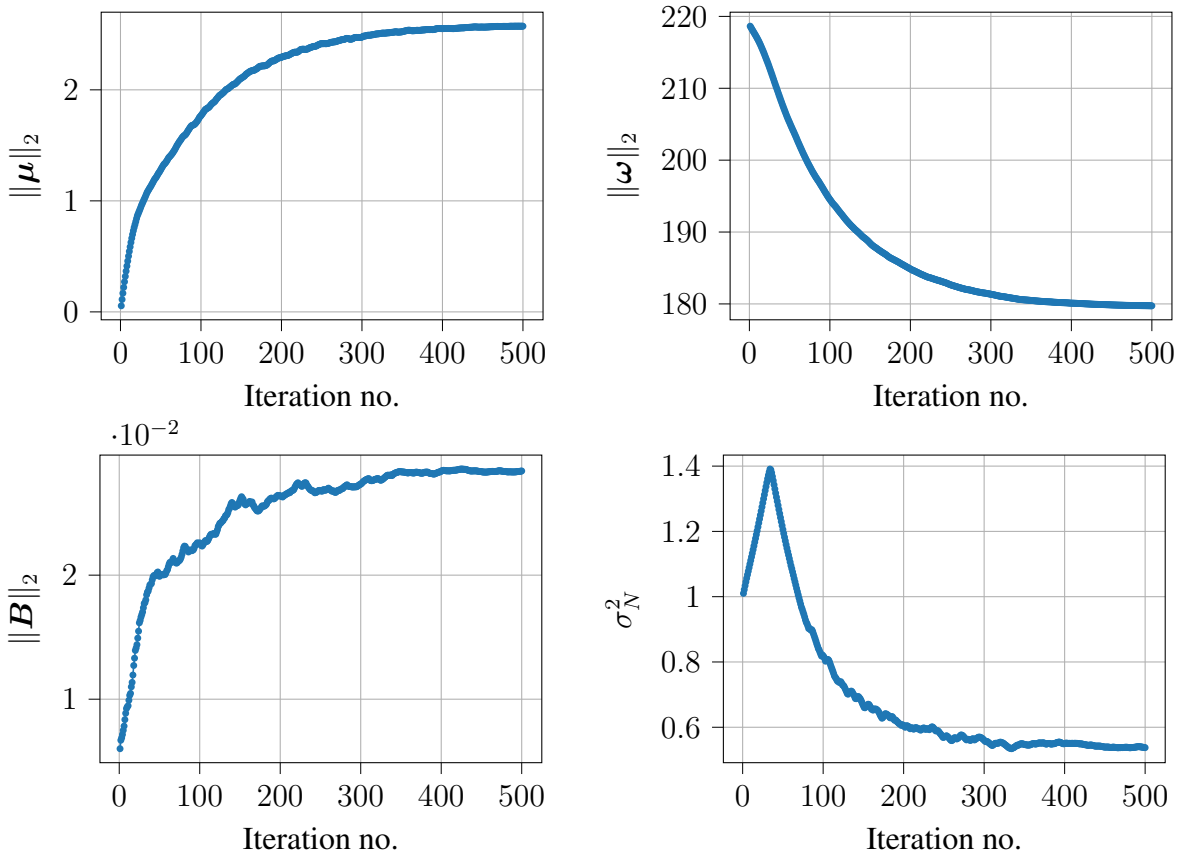

Figure 3.13.: L2 norms of the mean (top left), diagonal covariance (top right) and rank-1 update (bottom left) as well as the measurement noise (bottom right) over the number of iterations.

After about 50 iterations, it becomes increasingly hard to make out any progress by only monitoring $\tilde{\mathcal{L}}$, while the L2 norms of the parameter vectors still change considerably. Finally, the effect of the decreasing time step size is reflected in smaller fluctuations from iteration to

iteration and a trend towards a constant value can be made out. Estimated means $\boldsymbol{\mu_\theta}$ and standard deviations $\sqrt{\text{diag}\left(\boldsymbol{\Sigma_\theta}\right)}$ of the approximate posterior $q_\phi(\boldsymbol{\theta}) \approx \pi(\boldsymbol{\theta}|\hat{\mathbf{S}})$ are visualized in Fig. 3.14, while three different realizations $\mathbf{c}_\vartheta^{(i)} = \boldsymbol{\theta}^{(i)}$ from $q_\phi = \mathcal{N}(\boldsymbol{\mu_\theta}, \boldsymbol{\Sigma_\theta})$ $(i = 1, 2, 3)$ are shown in Fig. 3.15.
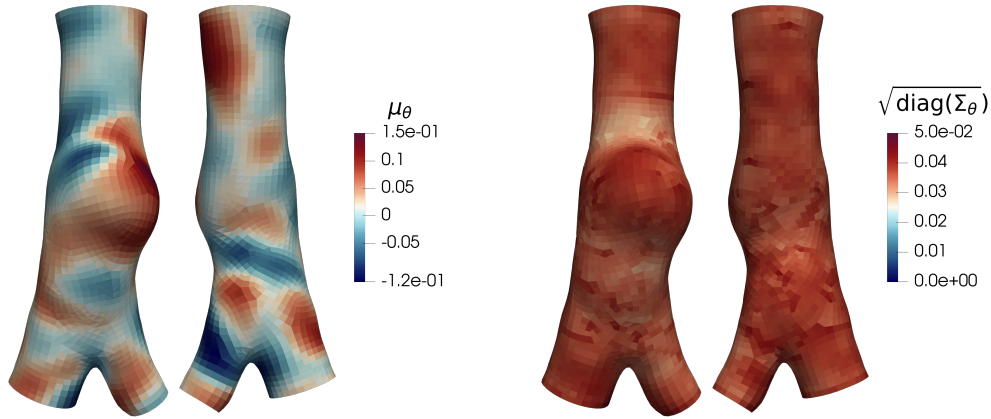

Figure 3.14.: Approximate posterior means (left) and standard deviations (right) of the parameters $\mathbf{c}_\vartheta$. Highest growth rates concentrate around the aneurysm sac, which is also where the largest changes in the two geometries from Fig. 3.11 occur.
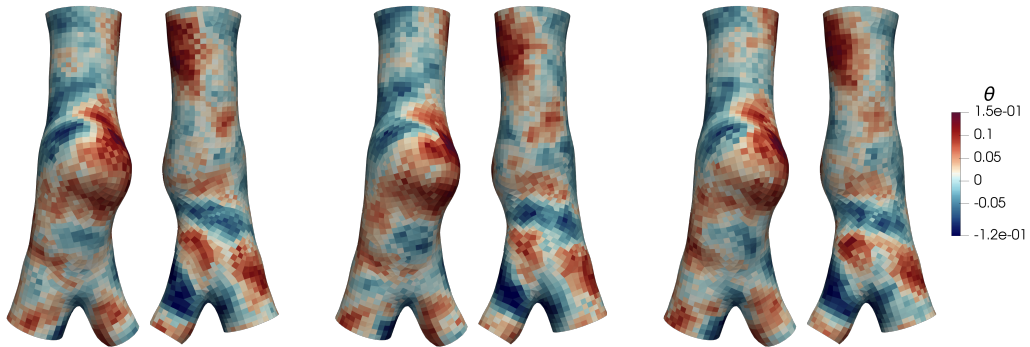

Figure 3.15.: Three exemplary samples from the approximate posterior. The samples mostly follow the mean from Fig. 3.14, but introduce an additional noise component.

Discussion

A comparison to the results reported in [68] is not straightforward. Although qualitatively, the inferred mean values are comparable, quantitative differences are expected due to the modified numerical model, parameters associated with the posterior, as well as approximation method. In particular, the optimized measurement noise in Fig. 3.13 is approximately $\sigma_N^2 \approx 0.54\,\text{mm}^4$, while [68] used a value of $\sigma_N^2 = 2.0\,\text{mm}^4$ (physical units were adapted[2]). Furthermore, the vessel

---

[2]The parameter σ_N quantifies the variance of the distance measure $\|\hat{\mathbf{S}} - \mathbf{S}(\mathbf{D}(\boldsymbol{\theta}))\|_{\mathcal{W}^\star}^2$ originating from the CTA imaging process and the uncertainty associated with $\hat{\mathbf{S}}$. Since the distance measure has physical units mm^4, σ_N needs to be specified in mm^2.

wall thickness in this work was set to $t_{\mathrm{w}} = 1.6$ mm ([68] used 1.0 mm), a different ILT material model was employed, as well as different stiffness parameters for the wall material model in order to be consistent with the AAA models throughout this thesis. Hence, it is possible that the present results and those from [68] perform equally good in terms of matching the two AAA geometries, however, with different values for the inferred growth rates.

From a methodological point of view, [68] uses a PCA (cf. Section 2.5.7) to reduce the number of parameters for calibration purposes. In this case, no data points $\boldsymbol{\theta}_i = \boldsymbol{x}_i$ are available, however, information about the input parameters are encoded into the TV prior $\pi(\boldsymbol{\theta})$. As the covariance matrix for PCA analysis, [68] proposes to utilize the sparse and symmetric Hessian resulting from a local quadratic approximation of $\pi(\boldsymbol{\theta})$ at the MAP (cf. Section 2.5.5). This allows the reparameterization

$$\boldsymbol{\theta} = \boldsymbol{\theta}^{\mathrm{MAP}} + \boldsymbol{P}\boldsymbol{\psi}, \tag{3.20}$$

where $\boldsymbol{\psi} \in \mathbb{R}^r$ denotes the reduced parameters. The original posterior $\pi(\boldsymbol{\theta}|\hat{\mathbf{S}})$ can then be reformulated in terms of the reduced parameters $\pi(\boldsymbol{\psi}|\hat{\mathbf{S}})$, making a SMC-based sampling approach feasible. With this approach, it could be demonstrated that a reduction from 7,428 to $r = 30$ parameters is possible. While being much more efficient than sampling on the full parameter space, the numerical costs are still tremendous and the approximation accuracy difficult to assess. The example provided in [68] required 192 SMC steps for 1,680 particles, implying a total of 322,560 model evaluations – a computational task that is only feasible using a highly parallelized implementation on a supercomputer such as the Munich-based SuperMUC, where the runtime was approximately 15 h.

In the end, there will always be a trade off between accuracy and practicality and it is important to assess the results in the context of their intended use case. Here, the inferred growth rates $\mathbf{c}_\vartheta$ are to be used in a predictive rupture risk assessment as presented in the next section. For this purpose, efficiency is the major concern, while the uncertainty estimates are sufficient to be representative. A complete analysis should be possible overnight without having to rely on a high-performance computing cluster. This section proposed a methodology to get closer to this target. Looking at Fig. 3.13, the 500 iterations employed for this example are probably too much and it is expected that a maximum of 300 iterations would suffice. For prediction purposes, it is important that the employed growth rate field is relatively smooth in order to produce meaningful von Mises stress estimates. In comparison to the estimated mean in Fig. 3.14, the samples in Fig. 3.15 using the smoothed diagonal plus rank-1 covariance model still appear a little noisy, but represent a major improvement to previous results that were obtained using just the diagonal covariance model.

3.5. Predictive rupture risk assessment

With the calibration result from the previous section, i.e. a PDF $q_{\boldsymbol{\phi}}(\boldsymbol{\theta}) = \mathcal{N}(\boldsymbol{\mu}_{\boldsymbol{\theta}}, \boldsymbol{\Sigma}_{\boldsymbol{\theta}})$ on the growth rate parameters $\mathbf{c}_\vartheta$, the next steps towards an *in posterum* rupture risk assessment can be taken. Here, a predictive rupture risk assessment implies the quantification of $\mathbb{P}_{\mathrm{rupt}}$ over time using a growth model. Since $\mathbb{P}_{\mathrm{rupt}}$ corresponds to an integral involving the density $\pi(\sigma_{\mathrm{vm}}^{\max}, \sigma_\gamma)$

(cf. Section 2.4), there are several possibilities with regards to which uncertainties should be incorporated:

- No model uncertainties: the growth rate parameters $\mathbf{c}_\vartheta$ are reduced to their mean value $\mathbf{c}_\vartheta = \boldsymbol{\mu_\theta}$, such that $\sigma_{\mathrm{vm}}^{\max}(\mu_{\boldsymbol{\theta}}, t)$ is deterministic and the rupture risk index becomes

$$\mathbb{P}_{\mathrm{rupt}}(t) = \int \mathbb{1}_{\sigma_{\mathrm{vm}}^{\max}(\boldsymbol{\mu_\theta},t)>\sigma_\gamma} \, \pi(\sigma_\gamma) \, \mathrm{d}\sigma_\gamma. \tag{3.21}$$

  Only one deterministic forward model evaluation is required.

- Growth-based model uncertainties: the approximate posterior from the previous section is used for propagating the uncertainties from the calibration

$$\mathbb{P}_{\mathrm{rupt}}(t) = \int \mathbb{1}_{\sigma_{\mathrm{vm}}^{\max}(\mathbf{c}_\vartheta,t)>\sigma_\gamma} \, \pi(\mathbf{c}_\vartheta) \, \pi(\sigma_\gamma) \, \mathrm{d}\mathbf{c}_\vartheta \, \mathrm{d}\sigma_\gamma. \tag{3.22}$$

  A stochastic forward problem with a high number of stochastic parameters $\mathbf{c}_\vartheta$ needs to be solved ($n_\theta = 2{,}992$) for each time step.

- Full model uncertainties: in addition to including $q_\phi(\boldsymbol{\theta})$, the uncertain vessel wall parameters $t_{\mathrm{w}}, \alpha_{\mathrm{w}}$ and β_{w} are taken into account via the density $\pi(\boldsymbol{\Theta}) = \pi(t_{\mathrm{w}}, \alpha_{\mathrm{w}}, \beta_{\mathrm{w}}, \sigma_\gamma)$ from Section 3.2, such that

$$\mathbb{P}_{\mathrm{rupt}}(t) = \int \mathbb{1}_{\sigma_{\mathrm{vm}}^{\max}(\mathbf{c}_\vartheta,t_{\mathrm{w}},\alpha_{\mathrm{w}},\beta_{\mathrm{w}},t)>\sigma_\gamma} \, \pi(\mathbf{c}_\vartheta) \, \pi(\boldsymbol{\Theta}) \, \mathrm{d}\mathbf{c}_\vartheta \, \mathrm{d}\boldsymbol{\Theta}. \tag{3.23}$$

  As before, a high-dimensional stochastic forward problem with 2,995 input parameters needs to be solved for each time step.

- Vessel-wall uncertainties: the growth rate parameters $\mathbf{c}_\vartheta$ are reduced to their mean value $\mathbf{c}_\vartheta = \boldsymbol{\mu_\theta}$ as above, but the uncertainties in the parameters $t_{\mathrm{w}}, \alpha_{\mathrm{w}}$ and β_{w} are included

$$\mathbb{P}_{\mathrm{rupt}}(t) = \int \mathbb{1}_{\sigma_{\mathrm{vm}}^{\max}(\boldsymbol{\mu_\theta},t_{\mathrm{w}},\alpha_{\mathrm{w}},\beta_{\mathrm{w}},t)>\sigma_\gamma} \, \pi(\boldsymbol{\Theta}) \, \mathrm{d}\boldsymbol{\Theta}. \tag{3.24}$$

  For each time step, a stochastic forward problem corresponding to the one from Section 3.3 needs to be solved.

While the first approach is straightforward, it neglects any uncertainties associated with the growth model and captured in $q_\phi(\boldsymbol{\theta})$. For the last two approaches, the calibration in Section 3.4 should incorporate the additional uncertainties in $t_{\mathrm{w}}, \alpha_{\mathrm{w}}$ and β_{w} for consistency. Thus, the second approach, i.e. Eq. (3.22), will be considered in the following.

Prediction strategy

Although generating samples from $q_\phi(\boldsymbol{\theta})$ is straightforward (cf. Section A.3.2), the computation of the rupture risk at some time instance t is computationally prohibitive due to the large amount of required samples and thus model evaluations using plain MC. As a remedy, the following procedure is proposed to estimate $\mathbb{P}_{\mathrm{rupt}}(\bar{t})$ at a point in time $t = \bar{t}$:

1. Reduce the number of input parameters $\boldsymbol{\theta}$ at $t = \bar{t}$ using the ASM for $Q(\boldsymbol{\theta}, \bar{t}) = \sigma_{vm}^{max}(\boldsymbol{\theta}, \bar{t})$, such that an approximation $Q(\boldsymbol{\psi}, \bar{t}) \approx Q(\boldsymbol{\theta}, \bar{t})$ is possible, where $n_\psi \ll n_\theta$ (cf. Section 2.5.7).

2. Create a surrogate model for $Q(\boldsymbol{\psi}, \bar{t})$ based on the evaluations required for the ASM above.

3. Evaluate $\mathbb{P}_{rupt}(\bar{t})$.

The first step involves a sampling stage, where N gradient samples $\{\nabla_{\boldsymbol{\theta}} Q(\boldsymbol{\theta}^{(i)}, \bar{t})\}_{i=1}^N$ using MC sampling from the density $q_\phi(\boldsymbol{\theta})$ are computed. For the example AAA case from Fig. 3.11, N is set to 32, corresponding to the minimum recommended number of samples using Eq. (2.199) for $\alpha = 2$, $n_\theta = 2{,}992$ and with the goal to adequately approximate the $r = 2$ first eigenvalue and eigenvector pairs. Each sample evaluation involves the solution of a forward problem for calculating $Q = \sigma_{vm}^{max}(\boldsymbol{\theta}, \bar{t})$ as well as the solution of an adjoint problem to evaluate the gradient $\nabla_{\boldsymbol{\theta}} Q$. Following Section 2.5.7, the $N \times N$ covariance matrix $\boldsymbol{C}^N$ is estimated via the computed gradient samples and a PCA is carried out to obtain the eigenvalues $\{\lambda_i\}_{i=1}^N$ and corresponding eigenvectors forming the $n_\theta \times r$ projection matrix $\boldsymbol{P}$.
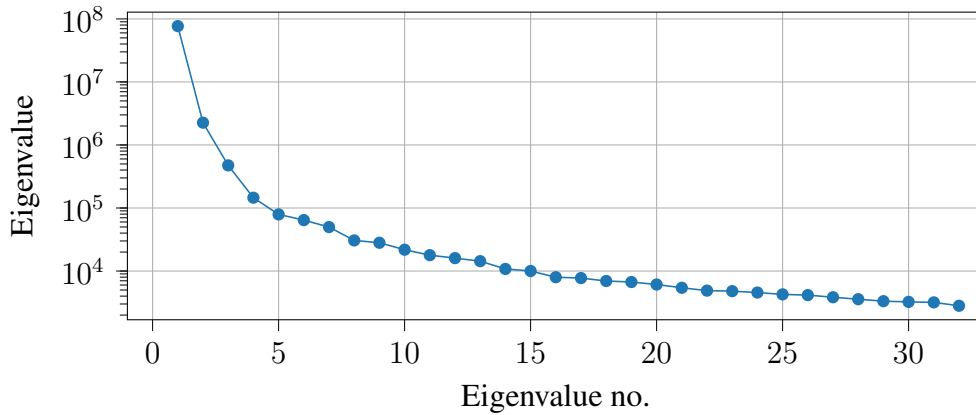

Figure 3.16.: Eigenvalue spectrum of the covariance matrix $\boldsymbol{C}^N$ for $t_1 = t_0 + 2$ y using $N = 32$ MC samples.

As an example, this is demonstrated for $\bar{t} = t_1 = t_0 + 2$ y, i.e. for the point in time of the second CTA screening, while results for further time steps are discussed at the end of the section below. In Fig. 3.16, the computed eigenvalues of the covariance matrix $\boldsymbol{C}^N$ are plotted. The significant drop after the first few eigenvalues suggests the existence of a low-dimensional active subspace. This is supported by the scatter plots in Fig. 3.17, where the maximum von Mises stress is plotted over the $r = 2$ projected variables $\boldsymbol{\psi} = [\psi_1, \psi_2]^{\mathsf{T}} = \boldsymbol{P}^{\mathsf{T}} \boldsymbol{\theta}$. The data implies that ψ_1, i.e. a one-dimensional active subspace, already explains most of the variability of the QoI with respect to $\boldsymbol{\theta}$. Hence, a one-dimensional approximation $Q(\boldsymbol{\theta}, \bar{t}) \approx Q(\psi_1, \bar{t})$ appears possible.

While a significant reduction in the input parameters n_θ does not lower the costs for MC sampling, it makes an efficient construction of approximate models feasible. To that end, a simple GP-based surrogate (cf. Section 2.5.2) is fitted on the training data $\{Q(\boldsymbol{\theta}^{(i)}, \bar{t}), \psi_1^{(i)}\}_{i=1}^N$ in order to model the relationship between the maximum von Mises stress σ_{vm}^{max} and the active variable ψ_1 probabilistically. The trained GP model is visualized in Fig. 3.18 in terms of the training data,
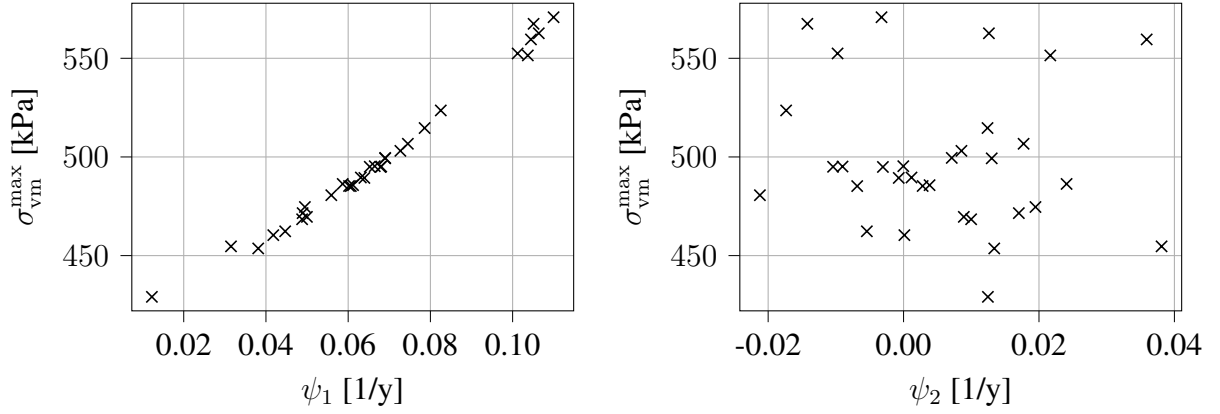
Figure 3.17.: Maximum von Mises stress over the first and second active variables for t_1.

predicted means and 95% confidence interval (CI). With this, predictions for the QoI at arbitrary input samples $\psi_1^{(i)} = \boldsymbol{P}_1^\mathsf{T} \boldsymbol{\theta}^{(i)}$ are available at negligible numerical costs

$$Q^{(i)} = \sigma_{\mathrm{vm}}^{\mathrm{max}(i)} \sim \mathcal{N}(\mu_Q(\psi_1^{(i)}), \sigma_Q^2(\psi_1^{(i)})) \tag{3.25}$$

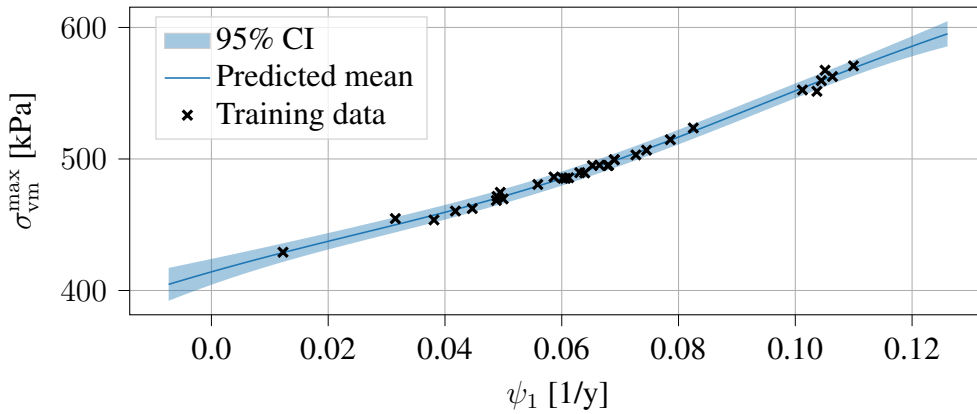and where $\boldsymbol{P}_1$ denotes the first column of $\boldsymbol{P}$.

Figure 3.18.: Surrogate model to approximate the relationship $\sigma_{\mathrm{vm}}^{\mathrm{max}}(\psi_1, \bar{t} = t_1)$ based on $N = 32$ MC samples.

It is being noted that by choosing a probabilistic model as a surrogate, there is a connection to the probabilistic MFMC method from Section 2.5.4. The active variable ψ_1 simply takes the role of the low-fidelity model in Eq. (2.151), such that

$$\pi(Q) = \pi(\sigma_{\mathrm{vm}}^{\mathrm{max}}) = \int \pi(\sigma_{\mathrm{vm}}^{\mathrm{max}}|\psi_1)\,\pi(\psi_1)\,\mathrm{d}\psi_1. \tag{3.26}$$

Thus, the tools developed in Section 2.5.4 can be applied here as well, in particular the diagnostics quantifying the estimator uncertainty introduced by applying the dimensionality reduction.

Furthermore, the GP- and ASM-based approximation of the rupture risk can be rewritten as

$$
\mathbb{P}_{\mathrm{rupt}}(\bar{t}) \approx \int \int \mathbb{1}_{\sigma_{\mathrm{vm}}^{\max}(\psi_1,\bar{t})>\sigma_\gamma}\, \pi(\sigma_{\mathrm{vm}}^{\max}|\psi_1)\, \pi(\sigma_\gamma)\, \pi(\psi_1)\, \mathrm{d}\sigma_{\mathrm{vm}}^{\max}\, \mathrm{d}\sigma_\gamma\, \mathrm{d}\psi_1
$$
$$
= 1 - \int \int \Phi\left(\frac{\sigma_\gamma - \mu_Q(\psi_1)}{\sigma_Q(\psi_1)}\right) \pi(\sigma_\gamma)\, \pi(\psi_1)\, \mathrm{d}\sigma_\gamma\, \mathrm{d}\psi_1,
\tag{3.27}
$$

where $\Phi(x)$ is the cumulative distribution function (CDF) of the standard normal defined as

$$
\Phi(x) = \frac{1}{\sqrt{2\pi}} \int_{-\infty}^{x} \exp\left(-\frac{z^2}{2}\right)\, \mathrm{d}z.
\tag{3.28}
$$

Results

The prediction strategy from above is applied to five additional time steps, which are equally spaced between t_1 and $t_1+ 1$ y, i.e. $t_2 = t_1+ 0.2$ y, $t_3 = t_1+ 0.4$ y, $t_4 = t_1+ 0.6$ y, $t_5 = t_1+ 0.8$ y and $t_6 = t_1+ 1$ y. For each time step, $N = 32$ MC samples of the QoI gradient are computed, a one-dimensional active subspace created and a GP-surrogate fitted in order to obtain $\mathbb{P}_{\mathrm{rupt}}(\bar{t})$, where $\bar{t} \in \{t_1, \ldots, t_6\}$. Since no non-invasive properties for this AAA case are available, the cohort-based wall strength density $\pi(\sigma_\gamma)$ from Eq. (3.4) is employed. The results for the individual rupture risks are visualized in Fig. 3.19. Additionally, the evolution of $\mathbb{P}_{\mathrm{rupt}}$ as well as the maximum diameter d over time are shown in Fig. 3.20, following the concept from Fig. 2.3 in Section 2.4. The means and standard deviations of d are computed based on the respective $N = 32$ MC samples and can therefore only be regarded as very rough estimates.
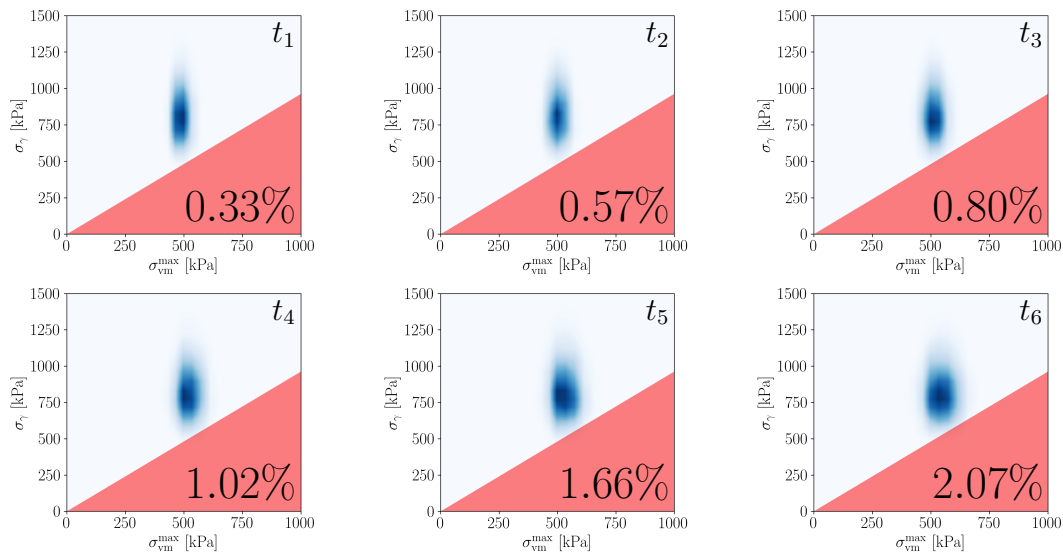

Figure 3.19.: Visualization of the predictive $\mathbb{P}_{\mathrm{rupt}}$ at different times in the future. t_1 corresponds to the time where the second CTA screening was carried out, while t_6 lies one year away from t_1.

Discussion

From Fig. 3.19 and Fig. 3.20 the propagation of the uncertainties in the growth rates $\mathbf{c}_\vartheta$ over time can be observed by means of $\mathbb{P}_{\mathrm{rupt}}$ and d. For $\mathbb{P}_{\mathrm{rupt}}$ this is expressed via a spread of the blue-colored density $\pi(\sigma_{\mathrm{vm}}^{\mathrm{max}}, \sigma_\gamma)$ towards higher stress values – and as a consequence a higher rupture risk – in Fig. 3.19. For d this can be seen in Fig. 3.20 through the increasing error bars corresponding to one standard deviation. While the maximum diameter increases almost perfectly linearly over time as a result of the employed growth law with a constant growth rate (cf. Section 2.1.2), the rupture risk index deviates from its initial linear trend towards higher values. Fig. 3.19 also illustrates that the wall strength density $\pi(\sigma_\gamma)$ is assumed constant over time, which is why there is no change of $\pi(\sigma_{\mathrm{vm}}^{\mathrm{max}}, \sigma_\gamma)$ along the σ_γ axis.
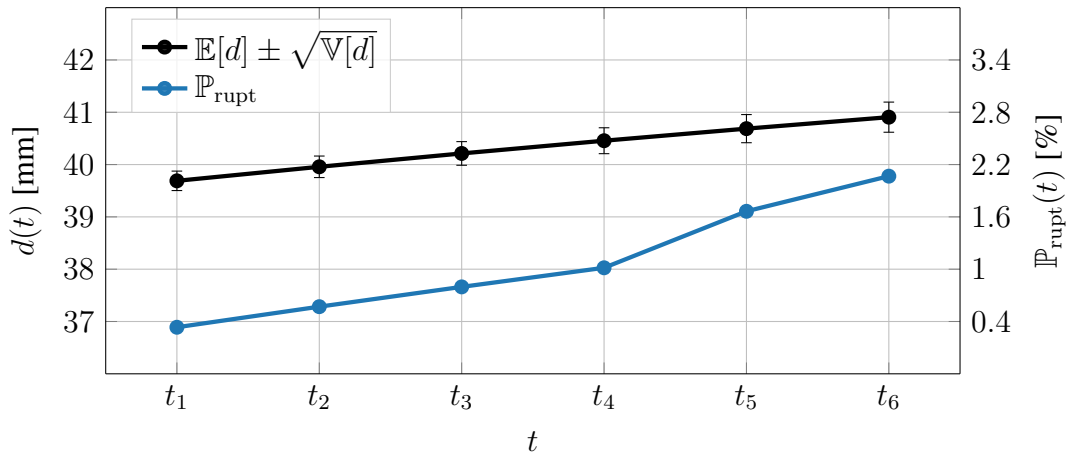

Figure 3.20.: Predictive rupture risk assessment following the concept from Fig. 2.3. Temporal evolution of the rupture risk $\mathbb{P}_{\mathrm{rupt}}$ and the maximum diameter d. t_1 corresponds to the time where the second CTA screening was carried out, while t_6 lies one year from that in the future.

The relative change in the maximum diameter between t_1 and t_6 is 3.1% and 518.9% for $\mathbb{P}_{\mathrm{rupt}}$, suggesting that the latter is much more sensitive towards growth than d. The MC-based estimated maximum diameter at t_1 is 39.7 mm and 40.9 mm at t_6, implying an increase of 1.2 mm after one year. Both values are in very good agreement with those from Section 3.4, where a maximum diameter of 39.2 mm at t_1 and a rate of change of 1.25 mm were estimated based on the two segmented geometries at t_0 and t_1. However, the predictions for the maximum diameters here are based on a relatively low number of MC samples, so that there is some remaining uncertainty in these estimates.

4. Summary and outlook

4.1. Framework summary

A comprehensive framework for the biomechanical assessment of AAA rupture risk and growth that incorporates available clinical data using a probabilistic approach was presented and demonstrated in several numerical examples of retrospective AAA cases. To summarize, the major contributions of this work are:

- The formulation of a general, biomechanical rupture risk index $\mathbb{P}_{\mathrm{rupt}}$ that is based on a simple failure criterion and allows to incorporate existing uncertainties.

- The development of several tools for the quantification of forward and inverse uncertainties that enable an efficient calculation of $\mathbb{P}_{\mathrm{rupt}}$ for different scenarios.

- An approach for the patient-specific, probabilistic prediction of invasive vessel wall properties based on non-invasively accessible clinical data that takes into account correlations in the predicted outputs.

- A retrospective case-control study for an *in momento* rupture risk assessment of 36 AAA cases, which demonstrated competitive performance in comparison to existing approaches.

- The Bayesian calibration of growth parameters using SVI to optimize a scalable variational model as an approximation to the posterior.

- The efficient forward propagation of the uncertainties associated with the inferred growth parameters using the ASM for dimensionality reduction and allowing for an *in posterum*, predictive rupture risk assessment $\mathbb{P}_{\mathrm{rupt}}(t)$ at a future point of time.

- A quantitative comparison of different approaches to the evaluation of elastic AAA wall properties based on tensile testing data (cf. Section A.4).

While it is argued that a deterministic approach to the rupture risk assessment is not purposeful due to unknown model parameters that have a significant influence on the estimated wall stress distribution, the results in this thesis have shown that a probabilistic treatment is not only more robust, but can also be more accurate by making use of statistical information. Although computational costs will always be higher compared to deterministic analyses, the developed UQ strategies provide a feasible alternative and an added value. Hence, the rupture risk index $\mathbb{P}_{\mathrm{rupt}}$ can be introduced as a relevant additional piece of information in the clinical decision process for AAA cases that are not or not unambiguously covered by existing guidelines and recommendations.

4.2. Outlook

In order to advance this framework to a clinical application, several further aspects need to be examined. A major challenge lies in the automatic segmentation of the CTA imaging data, which at the moment requires manual steps by a trained expert and can be time consuming. With the increasing use of deep learning (DL) methods for medical imaging data, it is expected that this problem can be dealt with in the future. A promising software framework for this purpose, that is currently under active development, is MONAI[1].

In view of the limitations discussed in Chapter 3, additional studies involving further AAA cases are desirable to confirm the predictive capabilities of $\mathbb{P}_{\mathrm{rupt}}$ and its clinical use for decision making. In particular, a larger, randomized study with risk factor matched groups is desirable. To validate the growth model, a retrospective case with at least three CTA images or a follow-up study, where the predicted growth rates can be directly compared to the actual growth of the AAA, is necessary.

In terms of framework extensions, there is still potential in the methods used for the estimation and prediction of AAA growth. For example, individual vessel wall uncertainties for t_{w}, α_{w} and β_{w} could be included in the calibration and prediction process. Furthermore, MAP estimates could also be computed for additional parameters from the likelihood and prior such as the kernel scale parameter σ_W during the calibration process. To reduce the costs associated with the stochastic optimization, the ASM parameter reduction scheme could already be applied during the inference as proposed by [28]. Lastly, geometry-based approaches that do not rely on a growth model, e.g. geodesic shooting [31], could be considered for the purposes of a predictive rupture risk assessment, allowing for a treatment according to Section 3.3 for the extrapolated geometries.

---

[1] https://monai.io/ (accessed January 19, 2022)

A. Appendix

A.1. Mathematical model details

A.1.1. Tensor notation

The symbolic tensor notation employed in Section 2.1 is summarized in Table A.1.

order	notation
0th	a or A
1st	$\underline{\boldsymbol{a}}$ or $\underline{\boldsymbol{A}}$
2nd	$\underline{\underline{\boldsymbol{a}}}$ or $\underline{\underline{\boldsymbol{A}}}$
4th	$\underline{\underline{\mathbb{A}}}$

Table A.1.: Symbolic tensor notation employed in Section 2.1.

The dot operator $(\cdot)$ defines a contraction between two tensors of order m and n such that a tensor of order $m + n - 2$ is returned. The contraction is computed over the last index of the first tensor and the first index of the second tensor, e.g.

$$c = \underline{\boldsymbol{a}} \cdot \underline{\boldsymbol{b}} = \sum_i a_i b_i, \tag{A.1}$$

$$\underline{\boldsymbol{c}} = \underline{\underline{\boldsymbol{A}}} \cdot \underline{\boldsymbol{b}} = \sum_j A_{ij} b_j = c_i, \tag{A.2}$$

$$\underline{\underline{\boldsymbol{C}}} = \underline{\underline{\boldsymbol{A}}} \cdot \underline{\underline{\boldsymbol{B}}} = \sum_j A_{ij} B_{jk} = C_{ik}. \tag{A.3}$$

The double dot symbol $(:)$ denotes a double contraction between two tensors such that a tensor of order $m + n - 4$ is returned. The double contraction is computed over the last two indices of the first tensor and the first two indices of the second tensor, e.g.

$$c = \underline{\underline{\boldsymbol{A}}} : \underline{\underline{\boldsymbol{B}}} = \sum_i \sum_j A_{ij} B_{ij}, \tag{A.4}$$

$$\underline{\underline{\boldsymbol{C}}} = \underline{\underline{\mathbb{A}}} : \underline{\underline{\boldsymbol{B}}} = \sum_k \sum_l A_{ijkl} B_{kl} = C_{ij}. \tag{A.5}$$

The tensor product is denoted by $\otimes$ and results in a tensor of order $m + n$, e.g.

$$\underline{\underline{\boldsymbol{C}}} = \underline{\boldsymbol{a}} \otimes \underline{\boldsymbol{b}} = a_i b_j = C_{ij}. \tag{A.6}$$

The spatial derivatives in reference and current configuration are expressed via

$$\underline{\boldsymbol{\nabla}}_X = \begin{bmatrix} \frac{\partial}{\partial X} \\ \frac{\partial}{\partial Y} \\ \frac{\partial}{\partial Z} \end{bmatrix} \quad \text{and} \quad \underline{\boldsymbol{\nabla}}_x = \begin{bmatrix} \frac{\partial}{\partial x} \\ \frac{\partial}{\partial y} \\ \frac{\partial}{\partial z} \end{bmatrix}, \tag{A.7}$$

respectively, such that $\underline{\boldsymbol{\nabla}}_X \otimes (\bullet)$ represents the gradient and $\underline{\boldsymbol{\nabla}}_X \cdot (\bullet)$ the divergence of $(\bullet)$ with respect to the reference coordinates.

A.1.2. Analytical derivation of Young's modulus for the volumetric component of slightly compressible behavior

Below, a short derivation of Young's moduli E_w and E_ILT for the volumetric component of the AAA's wall and ILT material model from Section 2.1.2 is provided. Imagine a rectangular cuboid under uniaxial load. Under the assumptions of incompressibility, the deformation gradient determinant becomes $J = \lambda_1 \lambda_2 \lambda_3 = 1$, where λ_i are the principal stretches such that λ_1 corresponds to the direction of the applied load. Assuming a uniaxial stress state and isotropic material behavior, $\lambda_2 = \lambda_3$, such that $\lambda_2 = 1/\sqrt{\lambda_1}$ and the first and second invariants of the Cauchy-Green tensor become

$$I_1 = \lambda_1^2 + \lambda_2^2 + \lambda_3^2 = \lambda_1^2 + \frac{2}{\lambda_1}, \tag{A.8}$$

$$I_2 = \lambda_1^2\lambda_2^2 + \lambda_2^2\lambda_3^2 + \lambda_3^2\lambda_1^2. \tag{A.9}$$

With this, the strain energy density function for the wall material model is

$$\Psi_\text{w}(\lambda_1) = \alpha_\text{w}\left(\lambda_1^2 + \frac{2}{\lambda_1} - 3\right) + \beta_\text{w}\left(\lambda_1^2 + \frac{2}{\lambda_1} - 3\right)^2, \tag{A.10}$$

and the relevant first Piola-Kirchhoff stress component

$$P_{11}(\lambda_1) = \frac{\partial\Psi_\text{w}(\lambda_1)}{\partial\lambda_1} = \left(2\alpha_\text{w} + 4\beta_\text{w}\left(\lambda_1^2 + \frac{2}{\lambda_1} - 3\right)\right)\left(\lambda_1 - \frac{1}{\lambda_1^2}\right). \tag{A.11}$$

Finally, Young's modulus evaluates to

$$E_\text{w} = C_{1111} = \left.\frac{\partial^2\Psi_\text{w}(\lambda_1)}{\partial\lambda_1^2}\right|_{\lambda_1=1} = 6\alpha_\text{w}. \tag{A.12}$$

Applying the same procedure to the ILT material model results in the strain energy

$$\Psi_\text{ILT}(\lambda_1) = c_\text{ILT}\left(\lambda_1^4 + \frac{2}{\lambda_1^2} - 3\right), \tag{A.13}$$

the first Piola-Kirchhoff stress component

$$P_{11}(\lambda_1) = \frac{\partial \Psi_{\mathrm{ILT}}(\lambda_1)}{\partial \lambda_1} = c_{\mathrm{ILT}} \left(4\lambda_1^3 - \frac{4}{\lambda_1^3} \right) \tag{A.14}$$

and a Young's modulus of

$$E_{\mathrm{ILT}} = C_{1111} = \left. \frac{\partial^2 \Psi_{\mathrm{ILT}}(\lambda_1)}{\partial \lambda_1^2} \right|_{\lambda_1=1} = 24c_{\mathrm{ILT}}. \tag{A.15}$$

A.2. Finite element method details

Below, further details regarding the FEM are provided, as well as additional derivations necessary for some of the methods in Section 2.5. Furthermore, the employed matrix-vector notation is clarified to allow for a straightforward implementation in a FE code.

A.2.1. Notation and fundamental quantities

Two-dimensional arrays of dimension $m \times n$ are referred to as matrices and denoted with bold-faced letters, e.g. $\boldsymbol{A} \in \mathbb{R}^{m \times n}$. Vectors are matrices where either m or n equals to one, e.g. $\boldsymbol{b} \in \mathbb{R}^{n \times 1}$. Matrix multiplication is denoted as $\boldsymbol{c} = \boldsymbol{A}\boldsymbol{b}$, where

$$[\boldsymbol{c}]_i = [\boldsymbol{A}\boldsymbol{b}]_i = \sum_{j=1}^{n} [\boldsymbol{A}]_{ij}[\boldsymbol{b}]_j. \tag{A.16}$$

Whenever discrete quantities that have no dependency on spatial coordinates occur, these will be highlighted using sans-serif bold-faced letters, e.g. the element degree of freedom vector $\mathsf{d}^{(\mathrm{e})}$, or the global stiffness matrix K (in contrast to spatially varying quantities such as the deformation gradient $\boldsymbol{F} = \boldsymbol{F}(\boldsymbol{\xi})$). To be precise with matrix dimensions, the following notation will be used to make the transformation of a symmetric matrix into the Voigt notation and the vectorization of an arbitrary matrix apparent:

- Apply the Voigt notation to a symmetric 3×3 matrix $\boldsymbol{A}$: $[\boldsymbol{A}]_{3\times3\to6\times1}$ or simply $[\boldsymbol{A}]_{6\times1}$, if the dimensions of $\boldsymbol{A}$ are obvious.

- "Undo" the Voigt notation of a 6×1 vector $\boldsymbol{a}$ that is known to have a symmetric matrix representation: $[\boldsymbol{a}]_{6\times1\to3\times3}$ or simply $[\boldsymbol{a}]_{3\times3}$.

- Vectorize the 3×3 matrix $\boldsymbol{B}$ using column-wise stacking: $[\boldsymbol{B}]_{3\times3\to9\times1}$, $[\boldsymbol{B}]_{3\times3\to1\times9}$ or simply $[\boldsymbol{B}]_{9\times1}$, $[\boldsymbol{B}]_{1\times9}$.

- "Undo" the vectorization of a 9×1 vector $\boldsymbol{b}$: $[\boldsymbol{b}]_{9\times1\to3\times3}$ or simply $[\boldsymbol{b}]_{3\times3}$.

Specifics regarding the application of the Voigt notation as well as the vectorization of matrices can be found in [3, Appendix 1]. Before stating the finite element residual equation and its linearized form, some fundamental quantities are introduced:

- The $3n_{\mathrm{nd}} \times 1$ vectors of the element nodal degrees of freedom and coordinates

$$
\mathbf{d}^{(\mathrm{e})} = \begin{bmatrix} \mathsf{d}_1^1 \\ \mathsf{d}_2^1 \\ \mathsf{d}_3^1 \\ \mathsf{d}_1^2 \\ \vdots \\ \mathsf{d}_3^{n_{\mathrm{nd}}} \end{bmatrix} \quad \text{and} \quad \bar{\mathbf{X}}^{(\mathrm{e})} = \begin{bmatrix} \bar{\mathsf{X}}_1^1 \\ \bar{\mathsf{X}}_2^1 \\ \bar{\mathsf{X}}_3^1 \\ \bar{\mathsf{X}}_1^2 \\ \vdots \\ \bar{\mathsf{X}}_3^{n_{\mathrm{nd}}} \end{bmatrix}, \tag{A.17}
$$

  respectively.

- The $3 \times 3n_{\mathrm{nd}}$ shape function matrix

$$
\boldsymbol{N} = \begin{bmatrix} N^1 & 0 & 0 & \ldots & N^{n_{\mathrm{nd}}} & 0 & 0 \\ 0 & N^1 & 0 & \ldots & 0 & N^{n_{\mathrm{nd}}} & 0 \\ 0 & 0 & N^1 & \ldots & 0 & 0 & N^{n_{\mathrm{nd}}} \end{bmatrix}. \tag{A.18}
$$

- The $3 \times 3n_{\mathrm{nd}}$ matrix of shape function derivatives with respect to the natural coordinates

$$
\boldsymbol{N}_{,\boldsymbol{\xi}} = \begin{bmatrix} \frac{\partial N^1}{\partial \xi_1} & 0 & 0 & \ldots & \frac{\partial N^{n_{\mathrm{nd}}}}{\partial \xi_1} & 0 & 0 \\ 0 & \frac{\partial N^1}{\partial \xi_2} & 0 & \ldots & 0 & \frac{\partial N^{n_{\mathrm{nd}}}}{\partial \xi_2} & 0 \\ 0 & 0 & \frac{\partial N^1}{\partial \xi_3} & \ldots & 0 & 0 & \frac{\partial N^{n_{\mathrm{nd}}}}{\partial \xi_3} \end{bmatrix}. \tag{A.19}
$$

- The 3×3 Jacobi matrix

$$
\boldsymbol{J} = \boldsymbol{N}_{,\boldsymbol{\xi}} \bar{\mathbf{X}}^{(\mathrm{e})} = \begin{bmatrix} \frac{\partial X_1}{\partial \xi_1} & \frac{\partial X_2}{\partial \xi_1} & \frac{\partial X_3}{\partial \xi_1} \\ \frac{\partial X_1}{\partial \xi_2} & \frac{\partial X_2}{\partial \xi_2} & \frac{\partial X_3}{\partial \xi_2} \\ \frac{\partial X_1}{\partial \xi_3} & \frac{\partial X_2}{\partial \xi_3} & \frac{\partial X_3}{\partial \xi_3} \end{bmatrix}. \tag{A.20}
$$

- The $3 \times 3n_{\mathrm{nd}}$ matrix of shape function derivatives with respect to the reference coordinates

$$
\boldsymbol{N}_{,\boldsymbol{X}} = \begin{bmatrix} \frac{\partial N^1}{\partial X_1} & 0 & 0 & \ldots & \frac{\partial N^{n_{\mathrm{nd}}}}{\partial X_1} & 0 & 0 \\ 0 & \frac{\partial N^1}{\partial X_2} & 0 & \ldots & 0 & \frac{\partial N^{n_{\mathrm{nd}}}}{\partial X_2} & 0 \\ 0 & 0 & \frac{\partial N^1}{\partial X_3} & \ldots & 0 & 0 & \frac{\partial N^{n_{\mathrm{nd}}}}{\partial X_3} \end{bmatrix}. \tag{A.21}
$$

- The 3×3 deformation gradient matrix

$$
\boldsymbol{F} = \mathbf{1} + \boldsymbol{N}_{,\boldsymbol{X}} \mathbf{d}^{(\mathrm{e})} = \begin{bmatrix} F_{11} & F_{12} & F_{13} \\ F_{21} & F_{22} & F_{23} \\ F_{31} & F_{32} & F_{33} \end{bmatrix}. \tag{A.22}
$$

- The $6 \times 3n_{\mathrm{nd}}$ B-operator matrix [3, Chapter 4.9.2]

$$
\boldsymbol{B} = \begin{bmatrix}
F_{11}\frac{\partial N^1}{\partial X_1} & F_{21}\frac{\partial N^1}{\partial X_1} & F_{31}\frac{\partial N^1}{\partial X_1} & \cdots \\
F_{12}\frac{\partial N^1}{\partial X_2} & F_{22}\frac{\partial N^1}{\partial X_2} & F_{32}\frac{\partial N^1}{\partial X_2} & \cdots \\
F_{13}\frac{\partial N^1}{\partial X_3} & F_{23}\frac{\partial N^1}{\partial X_3} & F_{33}\frac{\partial N^1}{\partial X_3} & \cdots \\
F_{11}\frac{\partial N^1}{\partial X_2} + F_{12}\frac{\partial N^1}{\partial X_1} & F_{21}\frac{\partial N^1}{\partial X_2} + F_{22}\frac{\partial N^1}{\partial X_1} & F_{31}\frac{\partial N^1}{\partial X_2} + F_{32}\frac{\partial N^1}{\partial X_1} & \cdots \\
F_{12}\frac{\partial N^1}{\partial X_3} + F_{13}\frac{\partial N^1}{\partial X_2} & F_{22}\frac{\partial N^1}{\partial X_3} + F_{23}\frac{\partial N^1}{\partial X_2} & F_{32}\frac{\partial N^1}{\partial X_3} + F_{33}\frac{\partial N^1}{\partial X_2} & \cdots \\
F_{11}\frac{\partial N^1}{\partial X_3} + F_{13}\frac{\partial N^1}{\partial X_1} & F_{21}\frac{\partial N^1}{\partial X_3} + F_{23}\frac{\partial N^1}{\partial X_1} & F_{31}\frac{\partial N^1}{\partial X_3} + F_{33}\frac{\partial N^1}{\partial X_1} & \cdots
\end{bmatrix}. \tag{A.23}
$$

- The 3×3 2nd Piola-Kirchhoff stress matrix

$$
\boldsymbol{S} = \begin{bmatrix}
S_{11} & S_{12} & S_{13} \\
 & S_{22} & S_{23} \\
\mathrm{sym.} & & S_{33}
\end{bmatrix}. \tag{A.24}
$$

- The 6×6 constitutive matrix, which is obtained by applying the Voigt notation to the fourth order elasticity tensor [3, Appendix 1]

$$
\boldsymbol{C}_{\mathrm{mat}} = \begin{bmatrix}
C_{11} & C_{12} & C_{13} & C_{14} & C_{15} & C_{16} \\
 & C_{22} & C_{23} & C_{24} & C_{25} & C_{26} \\
 & & C_{33} & C_{34} & C_{35} & C_{36} \\
 & & & C_{44} & C_{45} & C_{46} \\
 & \mathrm{sym.} & & & C_{55} & C_{56} \\
 & & & & & C_{66}
\end{bmatrix}. \tag{A.25}
$$

A.2.2. Derivatives of the residual vector

To calculate the adjoint-based derivative for an arbitrary objective function $f(\mathbf{D}, \boldsymbol{\theta})$, partial derivatives of the residual vector have to be calculated with respect to both $\mathbf{D}$ and the parameters $\boldsymbol{\theta}$. In the following, these derivation will be made for the growth rate parameters c_ϑ and on an element-wise basis for clarity. With the above, the $3n_{\mathrm{nd}} \times 1$ vector of element-wise residuals

$$
\mathbf{r}^{(\mathrm{e})}(\mathbf{d}^{(\mathrm{e})}) = \int_{\Omega_0^{(e)}} \boldsymbol{B}^{\mathsf{T}}[\boldsymbol{S}]_{6\times 1} \, \mathrm{d}V + \int_{\gamma_\sigma^{(e)}} p\boldsymbol{N}^{\mathsf{T}}\boldsymbol{n} \, \mathrm{d}a + \int_{\Gamma_u^{(e)}} k_s \boldsymbol{N}^{\mathsf{T}}\boldsymbol{N}\mathbf{d} \, \mathrm{d}A \tag{A.26}
$$

from Section 2.2.1 can be evaluated. The integral involving the blood pressure p features a 3×1 normal vector $\boldsymbol{n}$ of the surface element $\mathrm{d}a$ in the current configuration and can be computed following the approach in [3, Section 6.4.5]. Finally, the linearized residuals result in the $3n_{\mathrm{nd}} \times 3n_{\mathrm{nd}}$ element stiffness matrix

$$
\begin{aligned}
\mathbf{k}^{(\mathrm{e})}(\mathbf{d}^{(\mathrm{e})}) = {} & \int_{\Omega_0^{(e)}} \boldsymbol{B}^{\mathsf{T}}\boldsymbol{C}_{\mathrm{mat}}\boldsymbol{B} \, \mathrm{d}V + \int_{\Omega_0^{(e)}} \boldsymbol{N}_{,\boldsymbol{X}}{}^{\mathsf{T}}\boldsymbol{S}\boldsymbol{N}_{,\boldsymbol{X}} \, \mathrm{d}V \\
& + \frac{\partial}{\partial \mathbf{d}^{(\mathrm{e})}} \int_{\gamma_\sigma^{(e)}} p\boldsymbol{N}^{\mathsf{T}}\boldsymbol{n} \, \mathrm{d}a + \int_{\Gamma_u^{(e)}} k_s\boldsymbol{N}^{\mathsf{T}}\boldsymbol{N} \, \mathrm{d}A,
\end{aligned} \tag{A.27}
$$

where for the linearization of the pressure term it is again referred to [3, Section 6.4.5]. For the derivative with respect to c_ϑ, only the internal forces term is non-zero [68]

$$\frac{\partial \mathbf{r}^{(e)}(c_\vartheta)}{\partial c_\vartheta} = \frac{\partial}{\partial c_\vartheta} \int_{\Omega_0^{(e)}} \boldsymbol{B}^\mathsf{T}[\boldsymbol{S}]_{6\times 1} \, \mathrm{d}V = \int_{\Omega_0^{(e)}} \boldsymbol{B}^\mathsf{T} \frac{\partial [\boldsymbol{S}]_{6\times 1}}{\partial c_\vartheta} \, \mathrm{d}V, \tag{A.28}$$

where $\boldsymbol{S} = \vartheta^{-2}\boldsymbol{S}_e = \vartheta^{-2}\partial\Psi_\mathrm{w}(\boldsymbol{E}_e)/\partial\boldsymbol{E}_e$ and

$$\boldsymbol{E}_e = \frac{1}{2}\left(\frac{1}{\vartheta^2}\boldsymbol{C} - \boldsymbol{I}\right), \quad \boldsymbol{C} = \boldsymbol{F}^\mathsf{T}\boldsymbol{F}. \tag{A.29}$$

The stress derivative follows as

$$\begin{aligned}
\frac{\partial [\boldsymbol{S}]_{6\times 1}}{\partial c_\vartheta} &= \left(-\frac{2}{\vartheta^3}[\boldsymbol{S}_e]_{6\times 1} + \frac{1}{\vartheta^2}\frac{\partial[\boldsymbol{S}_e]_{6\times 1}}{\partial[\boldsymbol{E}_e]_{6\times 1}}\frac{\partial[\boldsymbol{E}_e]_{6\times 1}}{\partial c_\vartheta}\right)\frac{\partial\vartheta}{\partial c_\vartheta} \\
&= -\frac{1}{\vartheta}\frac{\partial\vartheta}{\partial c_\vartheta}\left(2[\boldsymbol{S}]_{6\times 1} + \boldsymbol{C}_\mathrm{mat}[\boldsymbol{C}]_{6\times 1}\right),
\end{aligned} \tag{A.30}$$

making use of

$$\frac{\partial[\boldsymbol{S}_e]_{6\times 1}}{\partial[\boldsymbol{E}_e]_{6\times 1}} = \boldsymbol{C}_{e,\mathrm{mat}} = \vartheta^{-4}\boldsymbol{C}_\mathrm{mat}. \tag{A.31}$$

Summarizing, the derivative of the element residuals with respect to c_ϑ is

$$\frac{\partial\mathbf{r}^{(e)}(c_\vartheta)}{\partial c_\vartheta} = -\int_{\Omega_0^{(e)}}\frac{1}{\vartheta}\frac{\partial\vartheta}{\partial c_\vartheta}\boldsymbol{B}^\mathsf{T}\left(2[\boldsymbol{S}]_{6\times 1} + \boldsymbol{C}_\mathrm{mat}[\boldsymbol{C}]_{6\times 1}\right)\,\mathrm{d}V. \tag{A.32}$$

Finally, the partial derivative of ϑ with respect to c_ϑ is time-dependent and follows from the growth law (2.30) as

$$\frac{\partial\vartheta}{\partial c_\vartheta} = \frac{\partial\vartheta(t_n)}{\partial c_\vartheta} = \frac{\partial}{\partial c_\vartheta}\left(\vartheta(t_0) + \int_{t_0}^{t_n}c_\vartheta\,\mathrm{d}t\right) = \frac{\partial}{\partial c_\vartheta}(t_n - t_0)c_\vartheta = t_n - t_0 \tag{A.33}$$

at an arbitrary point in time t_n.

A.2.3. Von Mises stress derivatives

In order to compute the parameter gradient $\nabla_{\boldsymbol\theta}\sigma_\mathrm{vm}^\mathrm{max}$ of the maximum von Mises stress using the adjoint method, again partial derivatives with respect to both $\mathbf{D}$ and $\boldsymbol\theta$ are required. In the following, these derivation will be made for the growth rate parameters c_ϑ and on an element-wise for clarity. To that end, first the 3×3 Cauchy stress matrix is

$$\boldsymbol\sigma = \begin{bmatrix} \sigma_{11} & \sigma_{12} & \sigma_{13} \\ \sigma_{12} & \sigma_{22} & \sigma_{23} \\ \sigma_{13} & \sigma_{23} & \sigma_{33} \end{bmatrix} = J^{-1}\boldsymbol{F}\boldsymbol{S}\boldsymbol{F}^\mathsf{T} \tag{A.34}$$

is introduced. The element-wise constant von Mises stress $\sigma_{\mathrm{vm}}{}^{(\mathrm{e})}(\mathbf{d}^{(\mathrm{e})}(\mathbf{c}_\vartheta), \mathbf{c}_\vartheta)$ is computed from the Gauss point averaged element Cauchy stresses $\boldsymbol{\sigma} = 1/n_p \sum_{p=1}^{n_p} \boldsymbol{\sigma}_p$ as

$$\sigma_{\mathrm{vm}}{}^{(\mathrm{e})} = \sqrt{\sigma_{11}^2 + \sigma_{22}^2 + \sigma_{33}^2 - \sigma_{11}\sigma_{22} - \sigma_{22}\sigma_{33} - \sigma_{11}\sigma_{33} + 3\left(\sigma_{12}^2 + \sigma_{23}^2 + \sigma_{13}^2\right)}. \quad \text{(A.35)}$$

Furthermore, making use of the chain rule

$$\frac{\partial \sigma_{\mathrm{vm}}^{\max}(\cdot)}{\partial(\cdot)} = \frac{\partial \sigma_{\mathrm{vm}}^{\max}(\cdot)}{\partial \sigma_{\mathrm{vm}}{}^{(\mathrm{e})}} \frac{\partial \sigma_{\mathrm{vm}}{}^{(\mathrm{e})}}{\partial \boldsymbol{\sigma}} \frac{\partial \boldsymbol{\sigma}}{\partial(\cdot)}, \quad \text{(A.36)}$$

where

$$\frac{\partial \sigma_{\mathrm{vm}}^{\max}(\cdot)}{\partial \sigma_{\mathrm{vm}}{}^{(\mathrm{e})}} = \begin{cases} 1 & \mathrm{e} = \arg\max_{\mathrm{e}} \boldsymbol{\Sigma}_{\mathrm{vm}}, \\ 0 & \text{otherwise} \end{cases} \quad \text{(A.37)}$$

and $\boldsymbol{\Sigma}_{\mathrm{vm}} = \{\sigma_{\mathrm{vm}}{}^{(\mathrm{e})}\}_{\mathrm{e}=1}^{n_{\mathrm{el}}}$. The von Mises stress derivatives with respect to the individual Cauchy stresses are

$$\begin{aligned} \frac{\partial \sigma_{\mathrm{vm}}}{\partial \sigma_{11}} &= \frac{1}{2\sigma_{\mathrm{vm}}}\left(2\sigma_{11} - \sigma_{22} - \sigma_{33}\right), \\ \frac{\partial \sigma_{\mathrm{vm}}}{\partial \sigma_{22}} &= \frac{1}{2\sigma_{\mathrm{vm}}}\left(2\sigma_{22} - \sigma_{11} - \sigma_{33}\right), \\ \frac{\partial \sigma_{\mathrm{vm}}}{\partial \sigma_{33}} &= \frac{1}{2\sigma_{\mathrm{vm}}}\left(2\sigma_{33} - \sigma_{11} - \sigma_{22}\right) \end{aligned} \quad \text{(A.38)}$$

and

$$\frac{\partial \sigma_{\mathrm{vm}}}{\partial \sigma_{12}} = \frac{3}{\sigma_{\mathrm{vm}}}\sigma_{12}, \quad \frac{\partial \sigma_{\mathrm{vm}}}{\partial \sigma_{23}} = \frac{3}{\sigma_{\mathrm{vm}}}\sigma_{23}, \quad \frac{\partial \sigma_{\mathrm{vm}}}{\partial \sigma_{13}} = \frac{3}{\sigma_{\mathrm{vm}}}\sigma_{13}. \quad \text{(A.39)}$$

Finally, the derivative with respect to the local degree of freedom d^i becomes

$$\begin{aligned} \frac{\partial [\boldsymbol{\sigma}]_{6\times1}}{\partial \mathrm{d}^i} = &- J^{-1}[\boldsymbol{F}\boldsymbol{S}\boldsymbol{F}^{\mathsf{T}}]_{3\times3\to6\times1}[\boldsymbol{F}^{-\mathsf{T}}]_{1\times9}\tilde{\boldsymbol{N}}_{,\boldsymbol{X}}^i \\ &+ J^{-1}\left[\boldsymbol{F}[\boldsymbol{C}_{\mathrm{mat}}\boldsymbol{B}^i]_{6\times1\to3\times3}\boldsymbol{F}^{\mathsf{T}}\right]_{3\times3\to6\times1} \\ &+ J^{-1}\left[[\tilde{\boldsymbol{N}}_{,\boldsymbol{X}}^i]_{3\times3}\boldsymbol{S}\boldsymbol{F}^{\mathsf{T}} + \boldsymbol{F}\boldsymbol{S}[\tilde{\boldsymbol{N}}_{,\boldsymbol{X}}^i]_{3\times3}^{\mathsf{T}}\right]_{3\times3\to6\times1}, \end{aligned} \quad \text{(A.40)}$$

where $\boldsymbol{B}^i$ and $\tilde{\boldsymbol{N}}^i_{,\boldsymbol{X}}$ refer to the ith column of $\boldsymbol{B}$ and the $9 \times 3n_{\mathrm{nd}}$ shape function derivative matrix

$$\tilde{\boldsymbol{N}}_{,\boldsymbol{X}} = \begin{bmatrix} \frac{\partial N^1}{\partial X_1} & 0 & 0 & \dots & \frac{\partial N^{n_{\mathrm{nd}}}}{\partial X_1} & 0 & 0 \\ 0 & \frac{\partial N^1}{\partial X_1} & 0 & \dots & 0 & \frac{\partial N^{n_{\mathrm{nd}}}}{\partial X_1} & 0 \\ 0 & 0 & \frac{\partial N^1}{\partial X_1} & \dots & 0 & 0 & \frac{\partial N^{n_{\mathrm{nd}}}}{\partial X_1} \\ \frac{\partial N^1}{\partial X_2} & 0 & 0 & \dots & \frac{\partial N^{n_{\mathrm{nd}}}}{\partial X_2} & 0 & 0 \\ 0 & \frac{\partial N^1}{\partial X_2} & 0 & \dots & 0 & \frac{\partial N^{n_{\mathrm{nd}}}}{\partial X_2} & 0 \\ 0 & 0 & \frac{\partial N^1}{\partial X_2} & \dots & 0 & 0 & \frac{\partial N^{n_{\mathrm{nd}}}}{\partial X_2} \\ \frac{\partial N^1}{\partial X_3} & 0 & 0 & \dots & \frac{\partial N^{n_{\mathrm{nd}}}}{\partial X_3} & 0 & 0 \\ 0 & \frac{\partial N^1}{\partial X_3} & 0 & \dots & 0 & \frac{\partial N^{n_{\mathrm{nd}}}}{\partial X_3} & 0 \\ 0 & 0 & \frac{\partial N^1}{\partial X_3} & \dots & 0 & 0 & \frac{\partial N^{n_{\mathrm{nd}}}}{\partial X_3} \end{bmatrix}, \tag{A.41}$$

respectively, i.e. $\boldsymbol{B}^i$ is 6×1 and $\tilde{\boldsymbol{N}}^i_{,\boldsymbol{X}}$ is 9×1. From above, it is already known that

$$\frac{\partial [\boldsymbol{S}]_{6 \times 1}}{\partial \mathsf{c}_\vartheta} = -\frac{1}{\vartheta} \frac{\partial \vartheta}{\partial \mathsf{c}_\vartheta} \left(2[\boldsymbol{S}]_{6 \times 1} + \boldsymbol{C}_{\mathrm{mat}}[\boldsymbol{C}]_{6 \times 1} \right) \tag{A.42}$$

and since only $\boldsymbol{S}$ has an explicit dependency on c_ϑ, it follows that

$$\frac{\partial \boldsymbol{\sigma}}{\partial \mathsf{c}_\vartheta} = J^{-1} \boldsymbol{F} \left[\frac{\partial [\boldsymbol{S}]_{6 \times 1}}{\partial \mathsf{c}_\vartheta} \right]_{6 \times 1 \to 3 \times 3} \boldsymbol{F}^{\mathsf{T}}. \tag{A.43}$$

A.3. Uncertainty quantification tools details

A.3.1. Gaussian process applications

Multivariate Gaussian process regression

For the purposes of Section 3.2, where $\boldsymbol{\xi}$ denotes the non-invasive and $\boldsymbol{\Theta} = [t_{\mathrm{w}}, \alpha_{\mathrm{w}}, \beta_{\mathrm{w}}, \sigma_\gamma]^{\mathsf{T}}$ the invasive vessel wall properties, the covariance function

$$k(\tau, \tau') = k(\boldsymbol{\xi}, \boldsymbol{\xi}') = \zeta_1 + \zeta_2 \boldsymbol{\xi}^{\mathsf{T}} \boldsymbol{\xi}' + \zeta_3 \exp \left[-\zeta_4 (\boldsymbol{\xi} - \boldsymbol{\xi}')^{\mathsf{T}} (\boldsymbol{\xi} - \boldsymbol{\xi}') \right] \tag{A.44}$$

with hyperparameters $\zeta_1, \zeta_2, \zeta_3$ and ζ_4 was chosen. Together with the entries in $\boldsymbol{L}$ from the Cholesky decomposition and the noise parameters from the matrix $\boldsymbol{D}$ (cf. Section 2.5.2), this results in the hyperparameter vector

$$\boldsymbol{\zeta} = [\zeta_1, \zeta_2, \zeta_3, \zeta_4, D_{11}, D_{22}, D_{33}, D_{44}, L_{11}, L_{22}, L_{33}, L_{44}, L_{21}, L_{31}, L_{41}, L_{32}, L_{42}, L_{43}]^{\mathsf{T}}, \tag{A.45}$$

where $\zeta_1, \zeta_2, \zeta_3, \zeta_4, D_{11}, D_{22}, D_{33}, D_{44}, L_{11}, L_{22}, L_{33}, L_{44} \in \mathbb{R}_+$ and $L_{21}, L_{31}, L_{41}, L_{32}, L_{42}, L_{43} \in \mathbb{R}$. Details regarding the optimization of the marginal log likelihood with respect to the hyperparameters $\boldsymbol{\zeta}$ are available in [146].

Gaussian process surrogate modeling incorporating explicit basis functions

The GP surrogate model in Section 3.3 makes use of a simple squared exponential kernel

$$k(\boldsymbol{\theta}, \boldsymbol{\theta}') = \zeta_1 \exp\left[-\frac{1}{2}(\boldsymbol{\theta} - \boldsymbol{\theta}')^\mathsf{T} \boldsymbol{\Lambda}^{-1}(\boldsymbol{\theta} - \boldsymbol{\theta}')\right], \tag{A.46}$$

where the matrix $\boldsymbol{\Lambda} = \mathrm{diag}\,(\zeta_2, \zeta_3, \zeta_4) \in \mathbb{R}^{3\times3}$ is diagonal, leading to the vector of hyperparameters $\boldsymbol{\zeta} = [\zeta_1, \zeta_2, \zeta_3, \zeta_4]^\mathsf{T}$, with $\boldsymbol{\zeta} \in \mathbb{R}_+^4$. Furthermore, trilinear basis functions are used for the model parameters $\boldsymbol{\theta} = [t_\mathrm{w}, \alpha_\mathrm{w}, \beta_\mathrm{w}]^\mathsf{T}$, i.e.

$$\boldsymbol{h}(\boldsymbol{\theta}) = [1, t_\mathrm{w}, \alpha_\mathrm{w}, \beta_\mathrm{w}, t_\mathrm{w}\alpha_\mathrm{w}, t_\mathrm{w}\beta_\mathrm{w}, \alpha_\mathrm{w}\beta_\mathrm{w}, t_\mathrm{w}\alpha_\mathrm{w}\beta_\mathrm{w}]^\mathsf{T}. \tag{A.47}$$

Recalling the log marginal likelihood from Section 2.5.2,

$$
\begin{aligned}
L(\boldsymbol{\zeta}) = {}& -\frac{1}{2}\boldsymbol{y}^\mathsf{T} \boldsymbol{K}^{-1}\boldsymbol{y} + \frac{1}{2}\boldsymbol{y}^\mathsf{T} \boldsymbol{C}\boldsymbol{y} - \frac{1}{2}\log|\boldsymbol{K}| - \frac{1}{2}\log|\boldsymbol{A}| \\
& - \frac{n_\mathrm{train} - \mathrm{rank}(\boldsymbol{H}^\mathsf{T})}{2}\log 2\pi
\end{aligned}
\tag{A.48}
$$

with $\boldsymbol{C} = \boldsymbol{K}^{-1}\boldsymbol{H}^\mathsf{T}\boldsymbol{A}^{-1}\boldsymbol{H}\boldsymbol{K}^{-1}$ and $\boldsymbol{A} = \boldsymbol{H}\boldsymbol{K}^{-1}\boldsymbol{H}^\mathsf{T}$, the derivative with respect to the individual hyperparmeters becomes

$$
\begin{aligned}
\frac{\partial L}{\partial \zeta_i} = {}& \frac{1}{2}\boldsymbol{y}^\mathsf{T}\boldsymbol{K}^{-1}\frac{\partial \boldsymbol{K}}{\partial \zeta_i}\boldsymbol{K}^{-1}\boldsymbol{y} \\
& + \frac{1}{2}\boldsymbol{y}^\mathsf{T}\boldsymbol{K}^{-1}\left[-\frac{\partial \boldsymbol{K}}{\partial \zeta_i}\boldsymbol{K}^{-1}\boldsymbol{H}^\mathsf{T}\boldsymbol{A}^{-1}\boldsymbol{H}\right. \\
& \qquad\qquad\qquad + \boldsymbol{H}^\mathsf{T}\boldsymbol{A}^{-1}\boldsymbol{H}\boldsymbol{K}^{-1}\frac{\partial \boldsymbol{K}}{\partial \zeta_i}\boldsymbol{K}^{-1}\boldsymbol{H}^\mathsf{T}\boldsymbol{A}^{-1}\boldsymbol{H} \\
& \qquad\qquad\qquad \left. - \boldsymbol{H}^\mathsf{T}\boldsymbol{A}^{-1}\boldsymbol{H}\boldsymbol{K}^{-1}\frac{\partial \boldsymbol{K}}{\partial \zeta_i}\right]\boldsymbol{K}^{-1}\boldsymbol{y} \\
& - \frac{1}{2}\mathrm{tr}\left(\boldsymbol{K}^{-1}\frac{\partial \boldsymbol{K}}{\partial \zeta_i}\right) \\
& + \frac{1}{2}\mathrm{tr}\left(\boldsymbol{A}^{-1}\boldsymbol{H}\boldsymbol{K}^{-1}\frac{\partial \boldsymbol{K}}{\partial \zeta_i}\boldsymbol{K}^{-1}\boldsymbol{H}^\mathsf{T}\right).
\end{aligned}
\tag{A.49}
$$

It is being noted that the numerical costs for evaluating this expression remain relatively low, since the size of the matrix $\boldsymbol{K}$ is usually very small (on average 11×11 in Section 3.3).

A.3.2. Gaussian variational models for SVI

Below, the variational models employed in Section 3.4 are outlined in detail, including all expressions necessary for the application of SVI. Starting from the classical diagonal covariance model, rank updates are discussed, followed by the employed diagonal plus smoothed rank-r covariance.

Diagonal covariance

A Gaussian PDF with a diagonal covariance matrix $\boldsymbol{\Sigma} = \boldsymbol{D}^2$, where $\boldsymbol{D}^2 = \text{diag}\,(\boldsymbol{\sigma}^2)$ and $\boldsymbol{\sigma} \in \mathbb{R}^{n_\theta}_+$, corresponds to a product of independent Gaussian PDFs

$$q_\phi(\boldsymbol{\theta}) = \mathcal{N}(\boldsymbol{\mu}, \boldsymbol{D}^2) = \prod_{i=1}^{n_\theta} \mathcal{N}(\mu_i, \sigma_i^2), \tag{A.50}$$

i.e. any correlations are neglected. To apply unconstrained optimization, the standard deviations are parameterized as $\boldsymbol{\sigma} = \exp(\boldsymbol{\omega})$, with $\boldsymbol{\omega} \in \mathbb{R}^{n_\theta}$ and where the exponential function is applied component-wise, i.e. $\sigma_i = \exp(\omega_i)$, $i = 1 \ldots n_\theta$. Hence, the optimization parameters are $\boldsymbol{\phi} = \{\boldsymbol{\mu}, \boldsymbol{\omega}\}$ and q_ϕ simplifies to

$$q_\phi(\boldsymbol{\theta}) = \prod_{i=1}^{n_\theta} q_i(\theta_i) = \prod_{i=1}^{n_\theta} \frac{\exp(-\omega_j)}{\sqrt{2\pi}} \exp\left[-\frac{\exp(-2\omega_i)}{2}(\theta_i - \mu_i)^2\right]. \tag{A.51}$$

The associated entropy is

$$\mathbb{H}[q_\phi(\boldsymbol{\theta})] = \frac{n_\theta}{2}(1 + \log 2\pi) + \sum_{i=1}^{n_\theta} \omega_i, \tag{A.52}$$

with derivatives

$$\frac{\partial \mathbb{H}[q_\phi(\boldsymbol{\theta})]}{\partial \mu_i} = 0 \quad \text{and} \quad \frac{\partial \mathbb{H}[q_\phi(\boldsymbol{\theta})]}{\partial \omega_i} = 1. \tag{A.53}$$

The reparameterization $\boldsymbol{\theta} = \boldsymbol{\theta}(\boldsymbol{\phi}, \boldsymbol{\varepsilon})$ for this model reduces to

$$\theta_i = \mu_i + \exp(\omega_i)\,\varepsilon_i, \tag{A.54}$$

where $\varepsilon_i \sim \pi(\varepsilon_i) = \mathcal{N}(0, 1)$. For the objective function gradient $\nabla_\phi f(\boldsymbol{\theta})$, the following component-wise expressions follow

$$\frac{\partial f}{\partial \mu_i} = \frac{\partial f}{\partial \theta_j}\frac{\partial \theta_j}{\partial \mu_i} = \sum_{j=1}^{n_\theta} \frac{\partial f}{\partial \theta_j}\delta_{ji} = \frac{\partial f}{\partial \theta_i}, \tag{A.55}$$

$$\frac{\partial f}{\partial \omega_i} = \frac{\partial f}{\partial \theta_j}\frac{\partial \theta_j}{\partial \omega_i} = \sum_{j=1}^{n_\theta} \frac{\partial f}{\partial \theta_j}\delta_{ji} \exp(\omega_i)\,\varepsilon_{\theta,i} = \frac{\partial f}{\partial \theta_i} \exp(\omega_i)\,\varepsilon_{\theta,i}. \tag{A.56}$$

Diagonal plus rank-r covariance

The diagonal plus rank-r covariance model has been independently proposed by [102] and [91]. It aims at an approximation to the full rank $n_\theta \times n_\theta$ covariance matrix as

$$\boldsymbol{\Sigma} = \boldsymbol{D}^2 + \boldsymbol{B}\boldsymbol{B}^\mathsf{T}, \tag{A.57}$$

where $\boldsymbol{B} \in \mathbb{R}^{n_\theta \times n_r}$ is a lower triangular matrix with n_r rank updates as column vectors. For the inverse of this matrix, it can be shown that

$$\left(\boldsymbol{D}^2 + \boldsymbol{B}\boldsymbol{B}^\mathsf{T}\right)^{-1} = \boldsymbol{D}^{-2} - \boldsymbol{D}^{-2}\boldsymbol{B}(\boldsymbol{I}_r + \boldsymbol{B}^\mathsf{T}\boldsymbol{D}^{-2}\boldsymbol{B})^{-1}\boldsymbol{B}^\mathsf{T}\boldsymbol{D}^{-2} \tag{A.58}$$

and for the determinant

$$|\boldsymbol{D}^2 + \boldsymbol{B}\boldsymbol{B}^\mathsf{T}| = |\boldsymbol{D}^2||\boldsymbol{I}_r + \boldsymbol{B}^\mathsf{T}\boldsymbol{D}^{-2}\boldsymbol{B}|. \tag{A.59}$$

Fortunately, the dense $n_\theta \times n_\theta$ inverse $\left(\boldsymbol{D}^2 + \boldsymbol{B}\boldsymbol{B}^\mathsf{T}\right)^{-1}$ does not need to be calculated explicitly, since it suffices to compute its action on a vector. E.g., the operation $\boldsymbol{y} = \left(\boldsymbol{D}^2 + \boldsymbol{B}\boldsymbol{B}^\mathsf{T}\right)^{-1}\boldsymbol{x}$ with two vectors $\boldsymbol{x}$ and $\boldsymbol{y}$ evaluates to

$$y_i = \sigma_i^{-2} - \sigma_i^{-4} \sum_{k=1}^{n_r} \sum_{j=1}^{n_r} \sum_{l=1}^{n_\theta} B_{ij}[(\boldsymbol{I}_r + \boldsymbol{B}^\mathsf{T}\boldsymbol{D}^{-2}\boldsymbol{B})^{-1}]_{jk} B_{lk} x_l. \tag{A.60}$$

Along with the computation of the $n_r \times n_r$ inverse $\left(\boldsymbol{I}_r + \boldsymbol{B}^\mathsf{T}\boldsymbol{D}^{-2}\boldsymbol{B}\right)^{-1}$ and determinant $|\boldsymbol{I}_r + \boldsymbol{B}^\mathsf{T}\boldsymbol{D}^{-2}\boldsymbol{B}^\mathsf{T}|$ this task is computationally feasible as long as n_r remains relatively small. With this, the entropy term can be readily evaluated as

$$\mathbb{H}[q_\phi(\boldsymbol{\theta})] = \frac{n_\theta}{2}(1 + \log 2\pi) + \sum_{i=1}^{n_\theta} \omega_i + \frac{1}{2} \log |\boldsymbol{I}_r + \boldsymbol{B}^\mathsf{T}\boldsymbol{D}^{-2}\boldsymbol{B}^\mathsf{T}|, \tag{A.61}$$

with the parameter derivatives

$$\frac{\partial \mathbb{H}[q_\phi(\boldsymbol{\theta})]}{\partial \mu_i} = 0, \tag{A.62}$$

$$\frac{\partial \mathbb{H}[q_\phi(\boldsymbol{\theta})]}{\partial \omega_i} = [(\boldsymbol{D}^2 + \boldsymbol{B}\boldsymbol{B}^\mathsf{T})^{-1}]_{ii} \exp(2\omega_i), \tag{A.63}$$

$$\frac{\partial \mathbb{H}[q_\phi(\boldsymbol{\theta})]}{\partial B_{ij}} = \sum_{k=1}^{n_\theta} [(\boldsymbol{D}^2 + \boldsymbol{B}\boldsymbol{B}^\mathsf{T})^{-1}]_{ik} B_{kj}. \tag{A.64}$$

For the computation of $\partial \mathbb{H}[q_\phi(\boldsymbol{\theta})]/\partial \omega_i$, it suffices to determine the diagonal entries

$$[(\boldsymbol{D}^2 + \boldsymbol{B}\boldsymbol{B}^\mathsf{T})^{-1}]_{ii} = \sigma_i^{-2} - \sigma_i^{-4} \sum_{j=1}^{n_r} \sum_{k=1}^{n_r} B_{ij}[(\boldsymbol{I}_r + \boldsymbol{B}^\mathsf{T}\boldsymbol{D}^{-2}\boldsymbol{B})^{-1}]_{jk} B_{ik}, \tag{A.65}$$

while $\nabla_{\boldsymbol{B}}\mathbb{H}[q_\phi(\boldsymbol{\theta})]$ involves a n_r-fold application of the inverse $\left(\boldsymbol{D}^2 + \boldsymbol{B}\boldsymbol{B}^\mathsf{T}\right)^{-1}$ to the columns of $\boldsymbol{B}$. The reparameterization transformation is

$$\boldsymbol{\theta}(\boldsymbol{\phi}, \boldsymbol{\varepsilon}_\theta, \boldsymbol{\varepsilon}_r) = \boldsymbol{\mu} + \boldsymbol{D}\boldsymbol{\varepsilon}_\theta + \boldsymbol{B}\boldsymbol{\varepsilon}_r, \tag{A.66}$$

with $\varepsilon_\theta \sim \mathcal{N}(\mathbf{0}, \boldsymbol{I}_\theta)$, $\varepsilon_r \sim \mathcal{N}(\mathbf{0}, \boldsymbol{I}_r)$ and where $\pi(\varepsilon) = \pi(\varepsilon_\theta)\pi(\varepsilon_r)$. Finally, the corresponding objective function derivatives are

$$\frac{\partial f}{\partial \mu_i} = \frac{\partial f}{\partial \theta_i}, \quad \frac{\partial f}{\partial \omega_i} = \frac{\partial f}{\partial \theta_i} \exp(\omega_i)\, \varepsilon_{\theta,i}, \tag{A.67}$$

$$\frac{\partial f}{\partial B_{ij}} = \frac{\partial f}{\partial \theta_k} \frac{\partial \theta_k}{\partial B_{ij}} = \sum_{k=1}^{n_\theta} \frac{\partial f}{\partial \theta_k} \delta_{ki}\, \varepsilon_{r,j} = \frac{\partial f}{\partial \theta_i} \varepsilon_{r,j}, \tag{A.68}$$

where $\partial f / \partial B_{ij}$ is set to zero, if $j > i$ in order to preserve the lower triangular structure of $\boldsymbol{B}$.

Smoothed diagonal plus rank-r covariance

The idea is to smooth the variance term in the reparameterization as

$$\boldsymbol{\theta}(\boldsymbol{\phi}, \varepsilon_\theta, \varepsilon_r) = \boldsymbol{\mu} + \boldsymbol{L}(\boldsymbol{D}\varepsilon_\theta + \boldsymbol{B}\varepsilon_r), \tag{A.69}$$

where $\boldsymbol{L} \in \mathbb{R}^{n_\theta \times n_\theta}$ is a linear smoothing operator that averages entries from adjacent elements, in order to avoid discontinuities during the stochastic optimization. This results in a Gaussian with covariance

$$\boldsymbol{\Sigma} = \boldsymbol{L}(\boldsymbol{D}^2 + \boldsymbol{B}\boldsymbol{B}^\mathsf{T})\boldsymbol{L}^\mathsf{T}. \tag{A.70}$$

and determinant

$$|\boldsymbol{L}(\boldsymbol{D}^2 + \boldsymbol{B}\boldsymbol{B}^\mathsf{T})\boldsymbol{L}^\mathsf{T}| = |\boldsymbol{L}|^2 |\boldsymbol{D}^2||\boldsymbol{I}_r + \boldsymbol{B}^\mathsf{T}\boldsymbol{D}^{-2}\boldsymbol{B}|. \tag{A.71}$$

The entropy of this Gaussian is

$$\mathbb{H}[q_\phi(\boldsymbol{\theta})] = \frac{n_\theta}{2}(1 + \log 2\pi) + \sum_{i=1}^{n_\theta} \omega_i + \frac{1}{2}\log|\boldsymbol{I}_r + \boldsymbol{B}^\mathsf{T}\boldsymbol{D}^{-2}\boldsymbol{B}^\mathsf{T}| + \log|\boldsymbol{L}|, \tag{A.72}$$

which implies that derivatives of the entropy remain the same as for the standard diagonal plus smoothed rank-r covariance approach. Regarding the entropy itself, it suffices to evaluate it up to the constant term $\log|\boldsymbol{L}|$. The reparameterization gradient can be straightforwardly computed, resulting in the objective function derivatives

$$\frac{\partial f}{\partial \mu_i} = \frac{\partial f}{\partial \theta_i}, \quad \frac{\partial f}{\partial \omega_i} = \sum_{j=1}^{n_\theta} \frac{\partial f}{\partial \theta_j} L_{ji} \exp(\omega_i)\, \varepsilon_{\theta,i} \quad \text{and} \quad \frac{\partial f}{\partial B_{ij}} = \sum_{k=1}^{n_\theta} \frac{\partial f}{\partial \theta_k} L_{ki}\, \varepsilon_{r,j}. \tag{A.73}$$

A.4. Determining stiffness parameters based on tensile tests of AAA tissue samples

In order to characterize the material behavior of the AAA vessel wall, tensile tests were performed on tissue samples harvested during OSR as already described in Section 3.1. Due to the

significant inter- and intra-patient variabilities in the obtained mechanical properties and relatively small data set, a careful evaluation is required. Below, the focus is on the determination of the α_w- and β_w-stiffness parameters from Section 2.1.2. In previous work [8, 117] and for the purposes of Chapter 3, the evaluation was based on an analytical model for the stress-stretch relation of the tensile test, cf. Section A.1.2, where the parameters α_w- and β_w were fitted to the measured force-displacement data of rectangular shaped tissue samples with length l_0, width b_0 and thickness t_0. This approach, however, has the following limitations:

- Uniaxial stress state: since in most cases only samples of relatively small dimension could be obtained [84], the assumption of uniaxial stress is expected to be violated.

- Incompressibility: even though human tissue has a high water content, it is not a perfectly incompressible material.

- Deterministic results: no estimates about the variance due to noisy measurement data have been reported.

The purpose of this section is to provide a comprehensive investigation of these deficiencies. In particular, the goal is to:

1. Examine the impact of the assumptions made by the analytical model by comparing it to a numerical FEM model in terms of parameter estimates.

2. Investigate the variance of the estimated parameters by treating the fitting procedure as a Bayesian inverse problem.

3. Provide data-consistent population-based densities for the stiffness parameters using a stochastic inverse problem.

To that end, the measured data is briefly described and the different calibration methods discussed. Afterwards, the analytical model and numerical FEM model are introduced and employed for the evaluation of all tested samples using the deterministic approach for comparison. Finally, results for the Bayesian and data-consistent approaches are presented.

Mechanical testing and data description

Uniaxial tests were carried out on rectangular shaped tissue samples with undeformed length l_0, width b_0 and thickness t_0. As testing machines, an ElectroForce 3100 (Bose Corporation, Eden Prairie, USA) and Zwick/Roell mediX0.1 (Messphysik Materials Testing, Fürstenried Austria) were used. A sinusoidal load was applied and the 20th cycle used for evaluation purposes [117]. In contrast to Section 3.1, several samples that could not be accurately described by the considered material model were not considered for the evaluation, resulting in $n = 191$ remaining datasets. Force-displacement curves from 50 exemplary samples are shown in Fig. A.1.
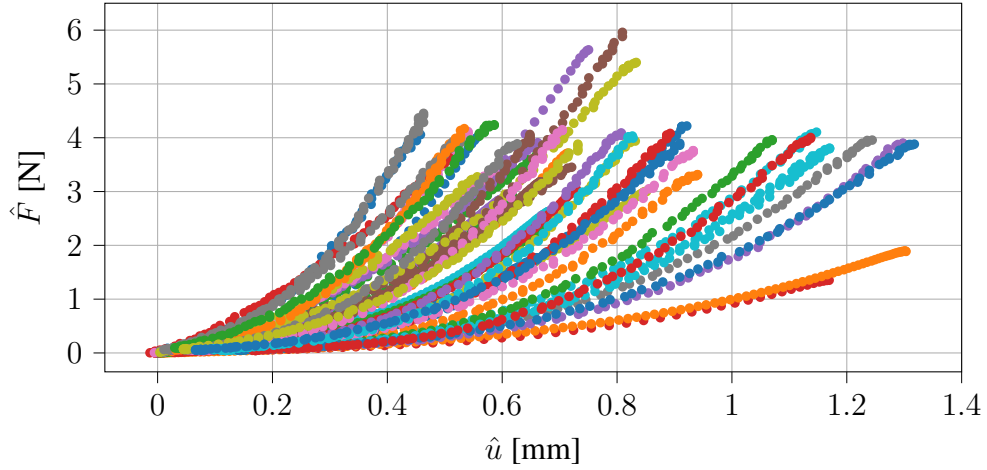
Figure A.1.: Force-displacement curves from 50 exemplary samples.

Deterministic approach using nonlinear least squares

The deterministic approach is based on a nonlinear least squares (NLS) fit algorithm following [117]. The corresponding optimization problem for finding optimal values $\alpha_{\mathrm{w}}^{\star}$ and $\beta_{\mathrm{w}}^{\star}$ is

$$\log \alpha_{\mathrm{w}}^{\star}, \log \beta_{\mathrm{w}}^{\star} = \arg \min_{\log \alpha_{\mathrm{w}}, \log \beta_{\mathrm{w}}} \|\hat{\boldsymbol{u}} - \boldsymbol{u}\|_2^2, \tag{A.74}$$

where $\hat{\boldsymbol{u}} = [\hat{u}_1, \ldots, \hat{u}_i, \ldots, \hat{u}_n]$ are the measured displacements and $\boldsymbol{u} = [u_1, \ldots, u_i, \ldots, u_n]$ the displacements with $u_i = u_i(\hat{F}_i)$ computed at the force $\hat{F}_i$ that corresponds to the measurement $\hat{u}_i$. The parameters α_{w} and β_{w} are log-transformed to be able to apply unconstrained optimization.

Stochastic approach via a Bayesian inverse problem

The stochastic approach utilizes a Bayesian formulation of the inverse problem and MCMC for inference. The likelihood is

$$\pi(\hat{\boldsymbol{u}} | \log \alpha_{\mathrm{w}}, \log \beta_{\mathrm{w}}) = \frac{1}{(\sqrt{2\pi}\sigma_u)^n} \exp\left(-\frac{1}{2\sigma_u^2} \|\hat{\boldsymbol{u}} - \boldsymbol{u}\|_2^2\right) \tag{A.75}$$

and for the prior

$$\pi(\log \alpha_{\mathrm{w}}, \log \beta_{\mathrm{w}}) = \mathcal{N}(\mu_{\log \alpha_{\mathrm{w}}}, \sigma_{\log \alpha_{\mathrm{w}}}^2)\mathcal{N}(\mu_{\log \beta_{\mathrm{w}}}, \sigma_{\log \beta_{\mathrm{w}}}^2) \tag{A.76}$$

is used, where the means and variances are calculated from the deterministic analysis as

$$\mu_{\log \alpha_{\mathrm{w}}} = \frac{1}{n}\sum_{i=1}^{n} \log \alpha_{\mathrm{w},i}^{\star}, \quad \mu_{\log \beta_{\mathrm{w}}} = \frac{1}{n}\sum_{i=1}^{n} \log \beta_{\mathrm{w},i}^{\star}, \tag{A.77}$$

$$\sigma_{\log \alpha_{\mathrm{w}}}^2 = \frac{1}{n}\sum_{i=1}^{n}(\log \alpha_{\mathrm{w},i}^{\star} - \mu_{\log \alpha_{\mathrm{w}}})^2, \quad \sigma_{\log \beta_{\mathrm{w}}}^2 = \frac{1}{n}\sum_{i=1}^{n}(\log \beta_{\mathrm{w},i}^{\star} - \mu_{\log \beta_{\mathrm{w}}})^2. \tag{A.78}$$

An additional chain is run for the measurement noise σ_u of the likelihood in order to get an impression about its variability across the tested samples and two testing machines. Moreover, the delayed rejection adaptive Metropolis (DRAM) implementation from [90] is used as the MCMC algorithm to generate posterior samples.

Data-consistent cohort density for the stiffness parameters

The task of finding a cohort PDF for the stiffness parameters α_{w} and β_{w} that is consistent with all available measurements and where the measurement noise is negligible represents a stochastic inverse problem of the sort as described in Section 2.3.4. Hence, the framework presented in Section 2.5.6 is used to find a unique solution to this particular inverse problem. The sought density is given by

$$\pi^{\mathrm{up}}(\log \alpha_{\mathrm{w}}, \log \beta_{\mathrm{w}}) = \pi^{\mathrm{init}}(\log \alpha_{\mathrm{w}}, \log \beta_{\mathrm{w}}) \frac{\pi^{\mathrm{obs}}(Q)}{\pi^{Q(\mathrm{init})}(Q)}, \tag{A.79}$$

where $Q = Q(\boldsymbol{\theta})$ with $\boldsymbol{\theta} = [\alpha_{\mathrm{w}}, \beta_{\mathrm{w}}]^{\mathsf{T}}$. For the initial density, $\pi^{\mathrm{init}}(\log \alpha_{\mathrm{w}}, \log \beta_{\mathrm{w}})$, the same choice as for the prior from Eq. (A.76) is made. To determine the observed density, appropriate QoI need to be computed from the available data $\{\hat{u}_i, \hat{F}_i\}_{i=1}^n$. The number of QoI, n_{Q}, should be as low as possible and the QoI should ideally be statistically independent from each other to provide as much information as possible.
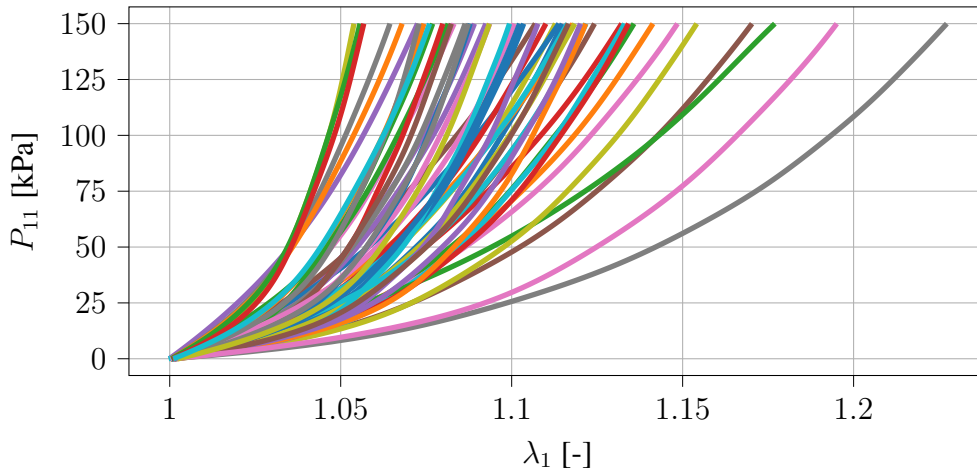

Figure A.2.: Preprocessed stress-strain curves from 50 exemplary samples.

In this section, different characteristics of the stress-strain curves are chosen as the QoI:

1. The area under the curve:

$$Q_1 = \int_1^{\lambda_1^{\mathrm{max}}} P_{11} \, \mathrm{d}\lambda_1, \tag{A.80}$$

which corresponds to a strain energy.

2. The length of the curve:

$$Q_2 = \int_1^{\lambda_1^{\max}} \sqrt{1 + \left(\frac{\partial P_{11}}{\partial \lambda_1}\right)^2} \, d\lambda_1, \tag{A.81}$$

which includes the stiffness $\partial P_{11}/\partial \lambda_1$.

To obtain representative values for Q_1 and Q_2, a preprocessing operation is carried out, where the sample data is smoothly interpolated between 0 and 150 kPa. 25 samples, which either didn't reach 150 kPa during testing or where negative stiffness values appeared, were disregarded from the analysis, resulting in $n = 166$ QoI. The results for 50 exemplary stress-strain curves are shown in Fig. A.2. Finally, both QoI can be approximated via numerical integration of the interpolated or model-predicted stress-stretch data, where the derivative $\partial P_{11}/\partial \lambda_1$ is computed using forward differences. The observed density $\pi^{\mathrm{obs}}(Q) = \pi^{\mathrm{obs}}(Q_1, Q_2)$ can then be obtained using KDE. Note that for evaluation purposes, densities involving logarithmized quantities of the stiffness parameters can be readily transformed to the physical domain as

$$\pi(\alpha_{\mathrm{w}}, \beta_{\mathrm{w}}) = \frac{1}{\alpha_{\mathrm{w}} \beta_{\mathrm{w}}} \pi(\log \alpha_{\mathrm{w}}, \log \beta_{\mathrm{w}}). \tag{A.82}$$

Analytical model of the tensile test

The analytical AAA wall material model has been derived in Section A.1.2 as

$$P_{11}(\lambda_1) = \left(2\alpha_{\mathrm{w}} + 4\beta_{\mathrm{w}}\left(\lambda_1^2 + \frac{2}{\lambda_1} - 3\right)\right)\left(\lambda_1 - \frac{1}{\lambda_1^2}\right), \tag{A.83}$$

where $P_{11} = F_1/(b_0 l_0)$ is the first Piola-Kirchhoff stress and $\lambda_1 = 1 + u_1/l_0$ the stretch in axial direction. Note that $P_{11}(\lambda_1)$ is a strictly monotonic function for $\lambda_1 \geq 1, \alpha_{\mathrm{w}} > 0, \beta_{\mathrm{w}} > 0$, such that the inverse $\lambda_1(P_{11})$ exists. Hence, for a given sample geometry with undeformed length l_0, width b_0 and thickness t_0, parameter choice α_{w} and β_{w} and measured force $\hat{F}$, a corresponding displacement $u = u_1(\hat{F})$ can be computed and compared to the measurement data $\hat{u}$.

Numerical model of the tensile test

For the numerical model, a finite deformation FEM model of the tensile test is utilized, where the strain energy function to describe the constitutive behavior is the same as in Eq. (2.23) and where a Possion's ratio of $\nu = 0.495$ is used. The left boundary of the tissue sample model is fixed via a Dirichlet boundary condition and at the right boundary a Neumann boundary condition with a surface load corresponding to the measured force $\hat{F}$ is applied. A quasi-static, load-controlled simulation yields force-displacement curves, consisting of computed axial displacements $u(F)$ for an applied force F and for a particular sample of dimension $l_0 \times b_0 \times t_0$ and parameter combination α_{w} and β_{w}.

To determine the required mesh resolution for the numerical model, a convergence study is carried out as illustrated in Fig. A.3 and using the deterministic approach for parameter fitting. With average deviations of less than 1% with respect to the parameters computed on the finest
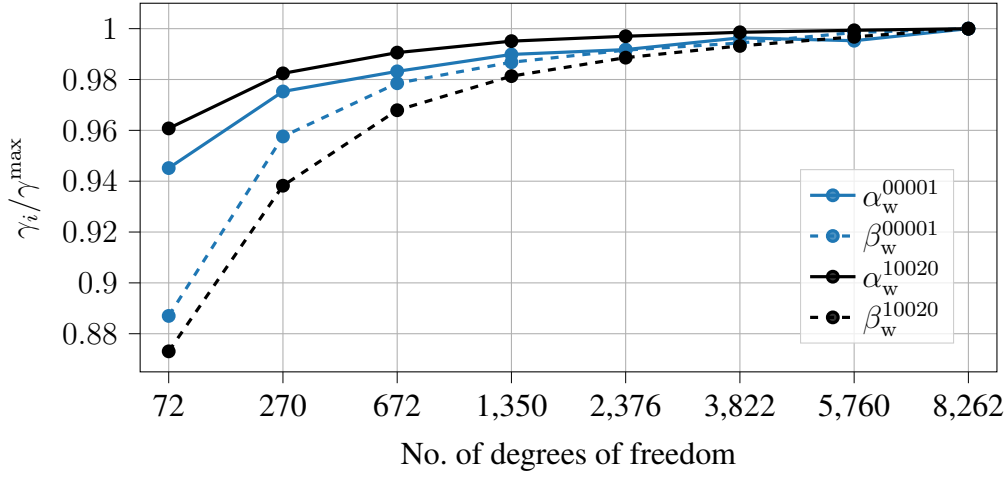
Figure A.3.: Convergence study for the numerical model. Samples 00001 and 10020 are fitted using an increasing number of degrees of freedom. The y-axis shows the ratio between the optimized parameters γ_i, with $\gamma = \{\alpha_{\mathrm{w}}^{00001}, \beta_{\mathrm{w}}^{00001}, \alpha_{\mathrm{w}}^{10020}, \beta_{\mathrm{w}}^{10020}\}$, at an increasing number i of degrees of freedom and the value at the finest resolution level $\gamma^{\mathrm{max}} = \gamma_i$ with $i = 8{,}262$.

resolution, a mesh consisting of 2,376 degrees of freedom is chosen for the experiments below. A finite element model of a typical tissue sample is visualized in Fig. A.4.
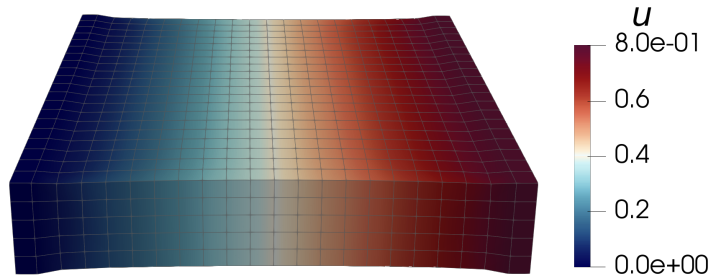
Figure A.4.: Finite element model of sample 10020, where the axial displacements u are visualized. The clamped surface is on the left, while the force is applied on the right side of the tissue sample. Making use of symmetries, only one quarter of the model is computed, consisting of 550 elements and 2,376 degrees of freedom.

Results

First, the deterministic approach is applied to all $n = 191$ tissue samples using both the analytical and numerical models. Force-displacement curves with optimized parameters for two exemplary samples along with the experimental data are shown in Fig. A.5. Histograms and KDEs for the cohort densities $\pi(\alpha_{\mathrm{w}})$ and $\pi(\beta_{\mathrm{w}})$ for the analytical and numerical model are shown in Fig. A.6 and Fig. A.7, respectively.

The Bayesian inverse analysis is then carried out using the analytical model for computational feasibility. 10,000 posterior realizations are computed for each tissue sample using the MCMC algorithm, where the first 10% are considered as burn-in and disregarded in the analysis. Results
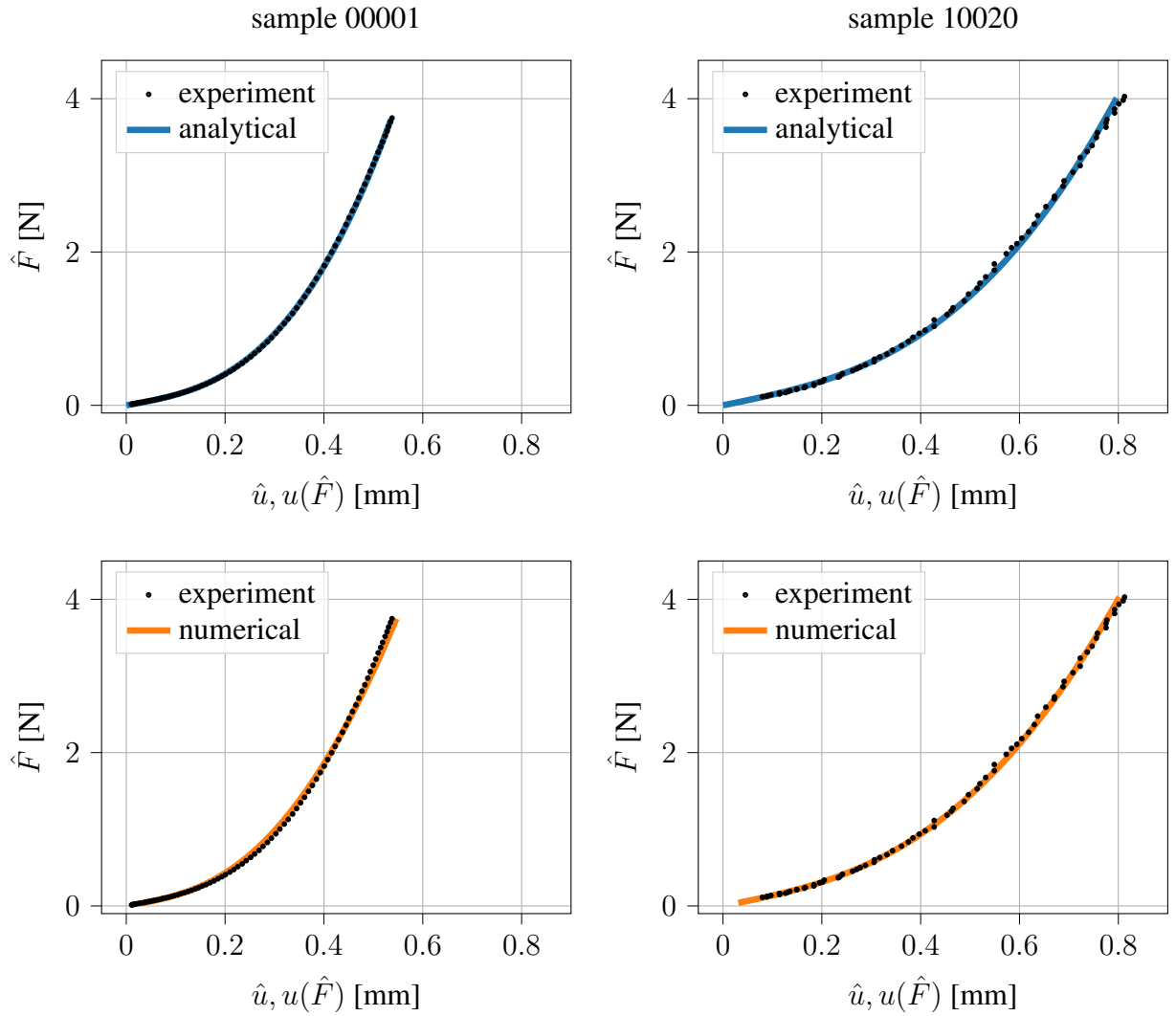
sample 00001   sample 10020

Figure A.5.: Measured and computed force-displacement curves for two exemplary samples using the analytical model. $\hat{u}$ is the clamp displacement and $\hat{F}$ the corresponding measured force, while $u(\hat{F})$ is the computed displacement using the optimized parameters. Left column: sample 00001 (ElectroForce 3100, $l_0 = 4.1$ mm, $b_0 = 10.0$ mm, $t_0 = 1.8$ mm, analytical model results: $\alpha_{\mathrm{w}}^{\star} = 44.303$ kPa, $\beta_{\mathrm{w}}^{\star} = 2660.155$ kPa, numerical model results: $\alpha_{\mathrm{w}}^{\star} = 33.016$ kPa, $\beta_{\mathrm{w}}^{\star} = 1896.868$ kPa). Right column: sample 10020 (Zwick/Roell mediX0.1, $l_0 = 7.3$ mm, $b_0 = 9.9$ mm, $t_0 = 1.7$ mm, analytical model results: $\alpha_{\mathrm{w}}^{\star} = 96.495$ kPa, $\beta_{\mathrm{w}}^{\star} = 4532.339$ kPa, numerical model results: $\alpha_{\mathrm{w}}^{\star} = 81.229$ kPa, $\beta_{\mathrm{w}}^{\star} = 3665.191$ kPa).

for the two samples from before are shown in Fig. A.8 in terms of a visualization of the computed posterior $\pi(\alpha_{\mathrm{w}}, \beta_{\mathrm{w}} | \hat{\boldsymbol{u}})$. A visualization of the measurement noise posterior means of all samples is provided in Fig. A.9.

    Lastly, the data-consistent approach is analyzed using the analytical model and $N = 20{,}000$ samples from the initial density π^{init}, which are used to compute the push-forward $\pi^{Q(\mathrm{init})}$. $n = 166$ QoI pairs were used for the computation of the observed density π^{obs}. The resulting
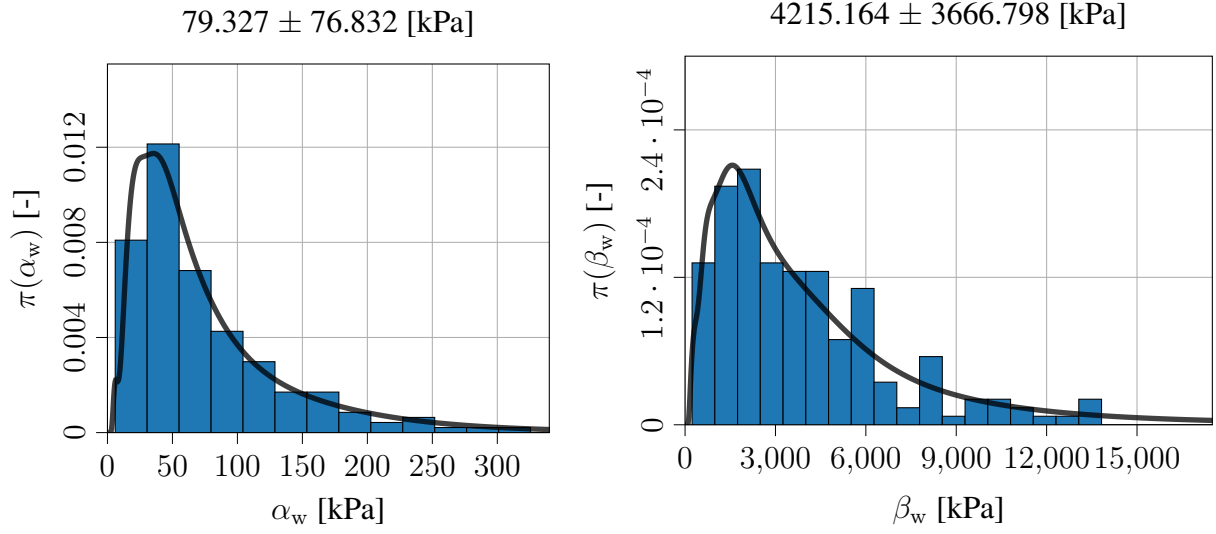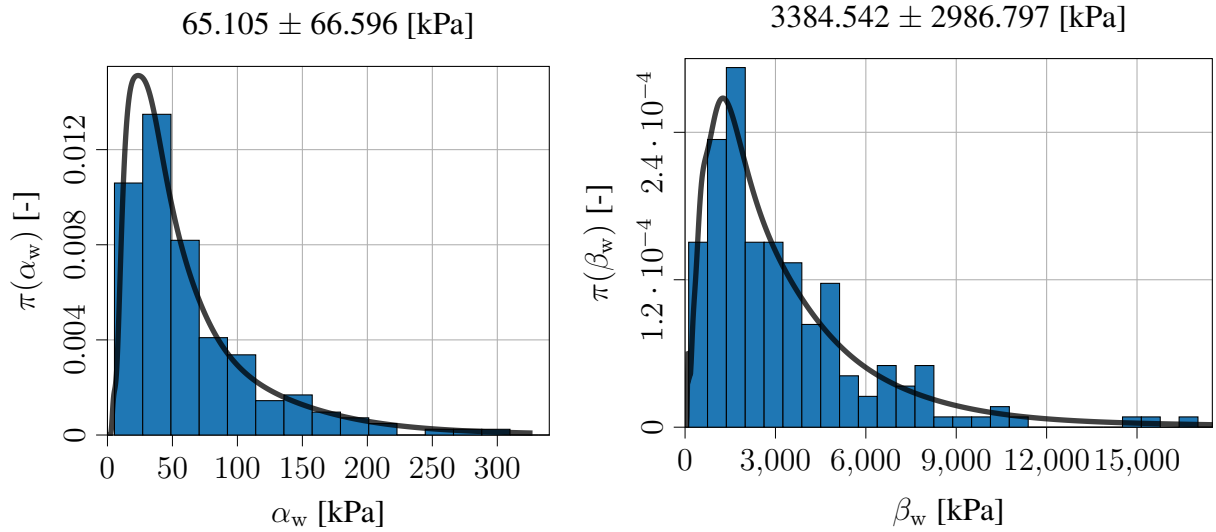
Figure A.6.: Visualization of the optimal parameter values obtained for $n = 191$ samples using the analytical model and NLS fit algorithm. Left: histogram and KDE for α_{w} (79.327 ± 76.832 [kPa]). Right: histogram and KDE for β_{w} (4215.164 ± 3666.798 [kPa]).

Figure A.7.: Visualization of the optimal parameter values obtained for $n = 191$ samples using the numerical model and NLS fit algorithm. Left: histogram and KDE for α_{w} (65.105 ± 66.596 [kPa]). Right: histogram and KDE for β_{w} (3384.542 ± 2986.797 [kPa]).

updated density π^{up} is visualized in histogram Fig. A.10, while diagnostics (cf. Section 2.5.6) for the method are provided in Table A.2. Accepted samples from the updated density are plotted in Fig. A.11 along with a scatter plot of the optimized parameters using the deterministic approach for comparison.
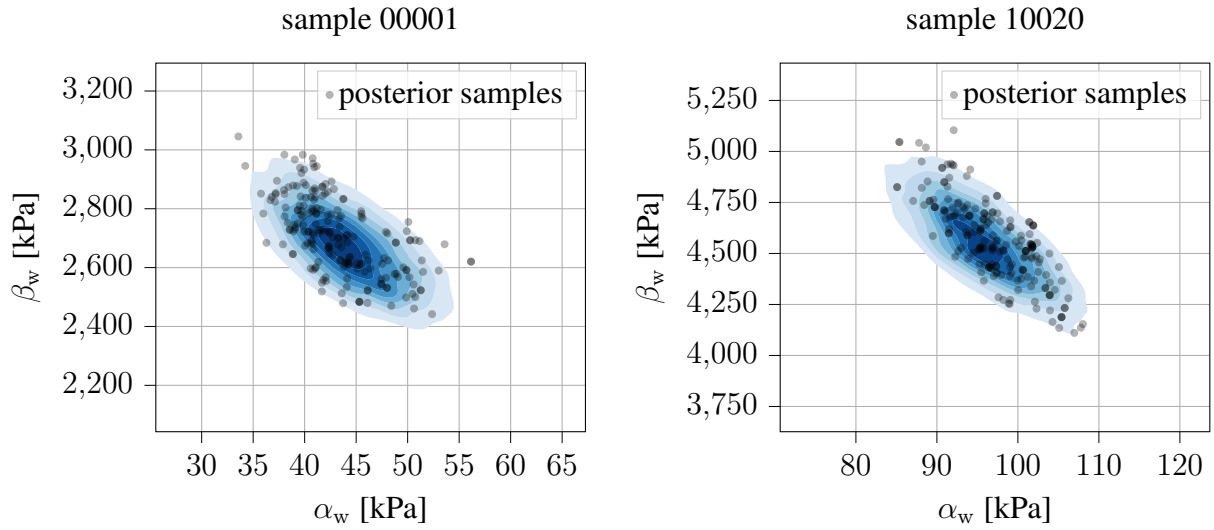
Figure A.8.: Computed posterior samples (black circles) and corresponding contours (shades of blue) from a KDE of the density $\pi(\alpha_{\mathrm{w}}, \beta_{\mathrm{w}}|\hat{\boldsymbol{u}})$ for two exemplary samples. Left: sample 00001 ($\alpha_{\mathrm{w}} = 44.267 \pm 4.656$ kPa, $\beta_{\mathrm{w}} = 2669.366 \pm 134.030$ kPa, $\sigma_u = 0.033 \pm 0.002$ mm). Right: sample 10020 ($\alpha_{\mathrm{w}} = 95.815 \pm 5.866$ kPa, $\beta_{\mathrm{w}} = 4553.745 \pm 194.647$ kPa, $\sigma_u = 0.036 \pm 0.003$ mm).
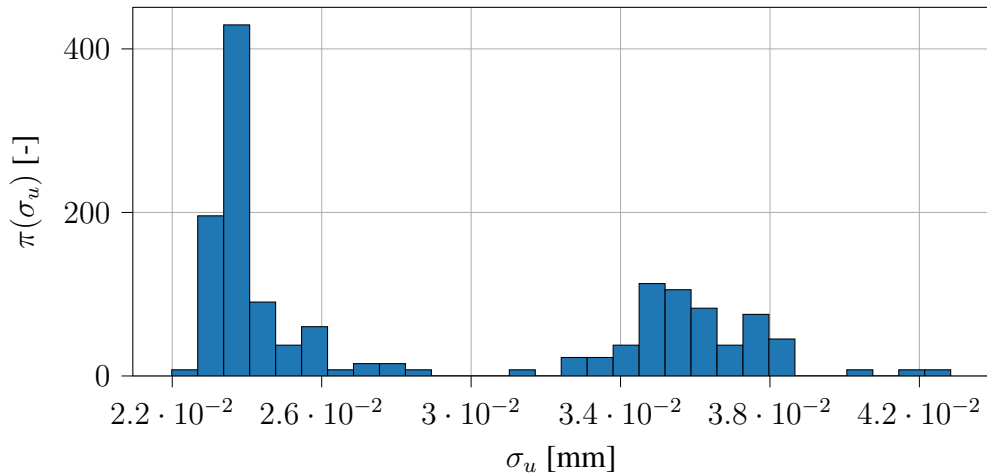
Figure A.9.: Histogram visualizing the measurement noise distribution of the cohort ($n = 191$), using the respective mean values of σ_u of each sample. The distribution is bimodal, where the left peak corresponds to the ElectroForce 3100 test machine ($n = 121$, $\sigma_u = 0.025 \pm 0.002$ mm) and the right peak to the Zwick/Roell mediX0.1 test machine ($n = 70$, $\sigma_u = 0.036 \pm 0.002$ mm).

Discussion

Both measured force-displacement curves in Fig. A.5 are fit equally well by the optimized analytical and numerical models. However, since the models are different, the fitted parameters of both models differ. For the first sample an alpha stiffness of 44.303 kPa vs. 33.016 kPa and a beta stiffness of 2660.155 kPa vs. 1896.868 kPa was obtained. For the second sample an alpha stiffness of 96.495 kPa vs. 81.229 kPa and a beta stiffness of 4532.339 kPa vs.
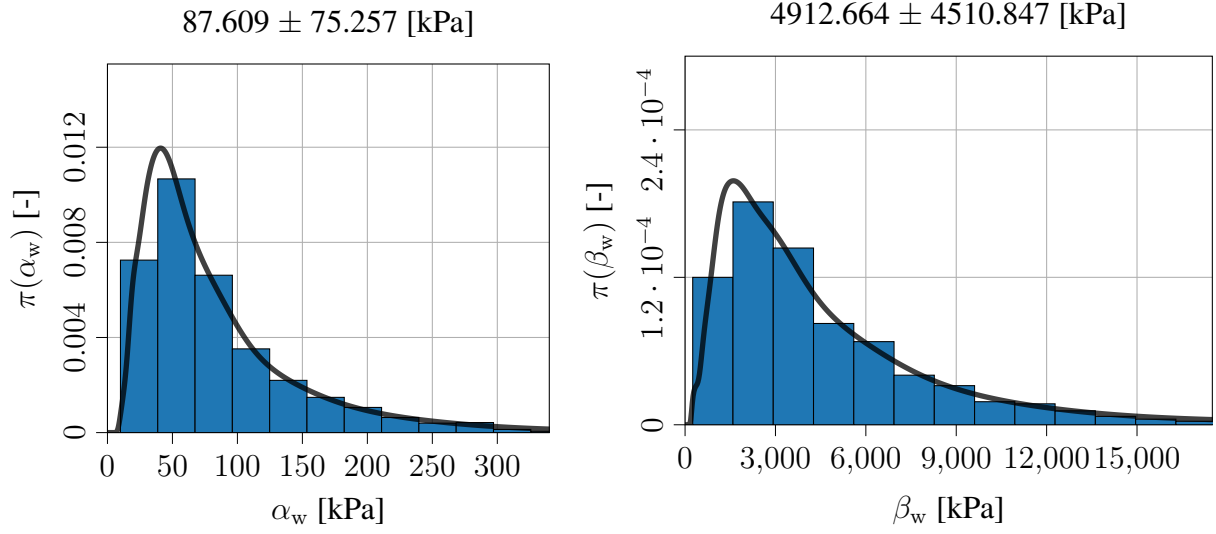
Figure A.10.: Visualization of the parameter values obtained for $N_{\mathrm{up}} = 1{,}316$ samples from the updated density $\pi^{\mathrm{up}}(\alpha_{\mathrm{w}}, \beta_{\mathrm{w}})$ using the analytical model and data-consistent approach. Left: histogram and KDE for α_{w} (87.609 ± 75.257 [kPa]). Right: histogram and KDE for β_{w} (4912.664 ± 4510.847 [kPa]).
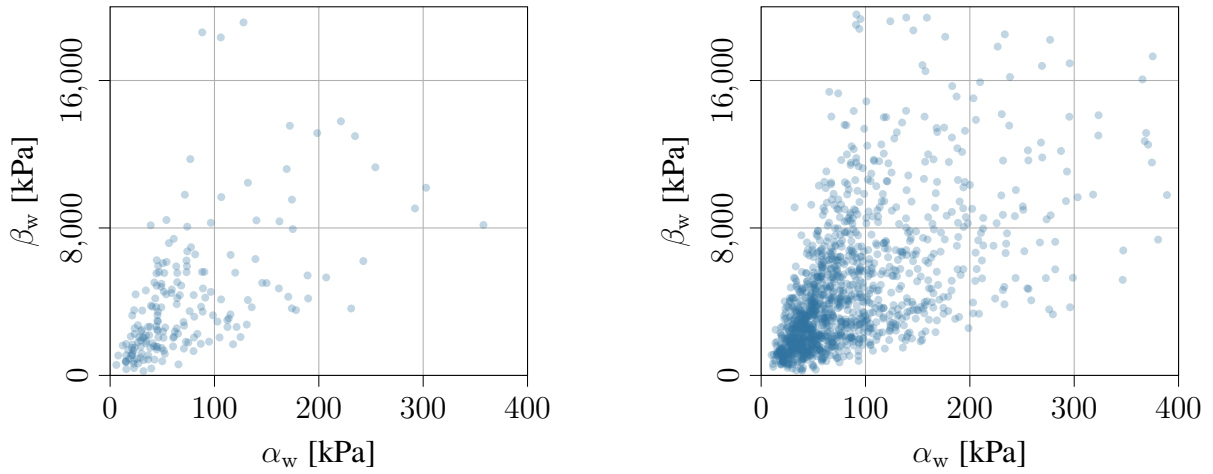

Figure A.11.: Scatter plots comparing the $n = 191$ optimized values using the deterministic approach (left) and the $N_{\mathrm{up}} = 1{,}316$ samples from the updated density $\pi^{\mathrm{up}}(\alpha_{\mathrm{w}}, \beta_{\mathrm{w}})$ (right). Corresponding correlation coefficients are $r_{\mathrm{S}}(\alpha_{\mathrm{w}}, \beta_{\mathrm{w}}) = 0.657163$ and 0.645944, respectively.

3665.191 kPa, respectively (analytical vs. numerical model). The stiffness parameters seem to be slightly higher for the analytical model. This observation is confirmed when comparing the histograms in Fig. A.6 and Fig. A.7. Reported mean values across all $n = 191$ investigated samples amount to 79.327 kPa vs. 65.105 kPa for α_{w} and 4215.164 kPa vs. 3384.542 kPa for β_{w}, corresponding to an increase of 21.8% and 24.5%. On the other hand, the coefficient of variation (CV), i.e. the ratio of the standard deviation to the mean, is approximately the same for both models (0.969 vs. 1.023 and 0.870 vs. 0.882).

(D1) Updated integral	0.990602
(D2) Consistency KL	0.022731
(D3) Information gain	0.330726
(D4) Acceptance rate	0.065800

Table A.2.: Diagnostic values for the data-consistent approach. $n = 166$ QoI pairs were used for the computation of the observed density. $N = 20{,}000$ samples from the initial density resulted in $N_{\mathrm{up}} = 1{,}316$ updated samples.

Moving on to the results from the Bayesian analysis, the inferred posterior means for the two examples in Fig. A.8 are almost identical to those from the NLS analysis. In light of the high-resolution force-displacement data, this can be expected and the likelihood will dominate over the a-priori assumptions. More interestingly, the posterior variance provides additional information about the sensitivity of the fit with respect to the parameters α_{w} and β_{w}. For the two examples, the standard deviations are 4.656 kPa and 5.866 kPa for the alpha stiffness, and 134.030 kPa and 194.647 kPa for the beta stiffness. This corresponds to CVs of 0.105 and 0.061 for α_{w}, and 0.050 and 0.043 for β_{w}, suggesting that the variability in the posterior is smaller than the variability between the analytical and numerical model. Furthermore, the noise levels of the two testing machines are clearly reflected in terms of the two modes of the histogram in Fig. A.9. For the ElectroForce 3100, σ_u concentrates around 2.4×10^{-2} mm and for the Zwick/Roell mediX0.1 around 3.5×10^{-2} mm.

Finally, the results for the data-consistent density $\pi^{\mathrm{up}}(\alpha_{\mathrm{w}}, \beta_{\mathrm{w}})$ show slightly higher mean values compared to those from the deterministic approach (87.609 kPa vs. 79.327 kPa and 4912.664 kPa vs. 4215.164 kPa), corresponding to an increase of 10.4% and 16.5%. Furthermore, Fig. A.11 shows an almost identical correlation structure between α_{w} and β_{w} resulting from the two methods. However, both results come from fundamentally different approaches, which makes a direct comparison difficult. The diagnostic values (D1) (close to one) and (D2) (close to zero) in Table A.2 indicate that a proper updated density was computed. The information gain, which is quantified by (D3), is significantly higher than using only Q_1 as a QoI, which results in an information gain of only 0.166920. This implies that Q_2 adds important additional information about the parameters α_{w} and β_{w}. However, it is unclear whether a further QoI would be necessary to correctly capture all the characteristics of the force-displacement curves. A third QoI would require a KDE over three parameters with only $n = 166$ available data points, which cannot be assumed to deliver meaningful results.

To summarize, the discrepancies between the numerical and analytical model cannot be explained with measurement uncertainties, but still remain modest. In particular, it is known that the alpha and beta stiffness parameters have a relatively low influence on the maximum von Mises stress in prestressed cardiovascular structures [7] and thus these differences are not expected to play a major role in the context of a rupture risk assessment. The lower values for α_{w} and β_{w} obtained using the numerical model are, however, in better agreement with biaxial testing results [143]. The Bayesian analysis provides additional information about the variance of the two stiffness parameters. Interestingly, α_{w} and β_{w} are negatively correlated among the two tissue samples in Fig. A.8, while positively correlated among all examined samples in Fig. A.11. This confirms the observation that the inter- and intra-patient variabilities in the stiffness pa-

rameters dominate over the uncertainties associated with the measurement noise. Finally, the data-consistent approach represents a non-parametric tool to obtain a population-based density $\pi(\alpha_\mathrm{w}, \beta_\mathrm{w})$. For a biomechanical rupture risk assessment, it could be used in place of Eq. (3.4) for patients, where no non-invasive properties are available, to provide a more accurate description of the correlation structure between α_w and β_w.

A.5. Overview: methods, implementations and publications

All computations and data processing tasks were performed using the C++ FEM code "Tartaros" and its Python wrapper "PyTartaros", which are developed at the Mechanics & High-Performance Computing Group.

- Section 3.1: Correlation analysis between invasive vessel wall properties and non-invasively accessible clinical parameters
  - Implementations:
    `pytartaros/applications/aaa_rupture_risk/patspec_data`

- Section 3.2: Patient-specific probabilistic modeling of invasive vessel wall properties
  - Related publications: Biehler et al. [8], Bruder et al. [19]
  - Methods: Multivariate Gaussian process regression (Section 2.5.2)
  - Implementations:
    `pytartaros/applications/aaa_rupture_risk/patspec_data`

- Section 3.3: Biomechanical rupture risk assessment at the time of data collection in the clinic
  - Related publications: Bruder et al. [17, 19]
  - Methods: Gaussian process surrogate modeling incorporating explicit basis functions (Section 2.5.2), Monte Carlo method (Section 2.5.3)
  - Implementations:
    `pytartaros/applications/aaa_rupture_risk/rupture_risk_framework`
    `tartaros/src/drt_uq`
  - Model parameters: $\boldsymbol{\theta} = [t_\mathrm{w}, \alpha_\mathrm{w}, \beta_\mathrm{w}]^\mathsf{T}$

- Section 3.4: Estimation of AAA growth based on consecutive imaging
  - Related publications: Bruder and Koutsourelakis [16], Kehl and Gee [69]
  - Methods: Stochastic variational inference (Section 2.5.5)
  - Implementations:
    `pytartaros/applications/aaa_rupture_risk/growth`
    `tartaros/src/drt_inv_analysis`
  - Model parameters: $\boldsymbol{\theta} = \mathbf{c}_\vartheta$

- Section 3.5: Predictive rupture risk assessment

    - Methods: Active subspace method (Section 2.5.7), Gaussian process regression (Section 2.5.2)

    - Implementations:
    `pytartaros/applications/aaa_rupture_risk/growth`
    `tartaros/src/drt_inv_analysis`

    - Model parameters: $\boldsymbol{\theta} = \mathbf{c}_\vartheta$

- Section A.4: Determining stiffness parameters based on tensile tests of AAA tissue samples

    - Related publications: Biehler et al. [8], Bruder et al. [18], Reeps et al. [117]

    - Methods: Markov chain Monte Carlo (Section 2.5.5), Unique solutions to stochastic inverse problems (Section 2.5.6)

    - Implementations:
    `pytartaros/applications/aaa_rupture_risk/mech_testing`

    - Model parameters: $\boldsymbol{\theta} = [\alpha_{\mathrm{w}}, \beta_{\mathrm{w}}]^{\mathsf{T}}$

Bibliography

[1] G. A. Antoniou, S. A. Antoniou, and F. Torella, Endovascular vs. Open Repair for Abdominal Aortic Aneurysm: Systematic Review and Meta-analysis of Updated Peri-operative and Long Term Data of Randomised Controlled Trials, *European Journal of Vascular and Endovascular Surgery* **59**, 385–397, 2020.

[2] S. Avril, M. W. Gee, A. Hemmler, and S. Rugonyi, Patient-specific computational modeling of endovascular aneurysm repair: State of the art and future directions, *International Journal for Numerical Methods in Biomedical Engineering*, 2021.

[3] T. Belytschko, W. K. Liu, B. Moran, and K. I. Elkhodary, *Nonlinear Finite Elements for Continua and Structures*, Wiley, Chichester, West Sussex, United Kingdon, second edition Edition, 2014.

[4] D. Bergqvist, M. Björck, and A. Wanhainen, Abdominal Aortic Aneurysm – To Screen or Not to Screen, *European Journal of Vascular and Endovascular Surgery* **35**, 13–18, 2008.

[5] J. Biehler and W. A. Wall, The impact of personalized probabilistic wall thickness models on peak wall stress in abdominal aortic aneurysms, *International Journal for Numerical Methods in Biomedical Engineering* **34**, e2922, 2018.

[6] J. Biehler, *Efficient Uncertainty Quantification for Large-Scale Biomechanical Models Using a Bayesian Multi-Fidelity Approach*, PhD thesis, Technical University of Munich, 2016.

[7] J. Biehler, M. W. Gee, and W. A. Wall, Towards efficient uncertainty quantification in complex and large-scale biomechanical problems based on a Bayesian multi-fidelity scheme, *Biomechanics and Modeling in Mechanobiology* **14**, 489–513, 2015.

[8] J. Biehler, S. Kehl, M. W. Gee, F. Schmies, J. Pelisek, A. Maier, C. Reeps, H.-H. Eckstein, and W. A. Wall, Probabilistic noninvasive prediction of wall properties of abdominal aortic aneurysms using Bayesian regression, *Biomechanics and Modeling in Mechanobiology* **16**, 45–61, 2017.

[9] C. Bierig and A. Chernov, Approximation of probability density functions by the Multilevel Monte Carlo Maximum Entropy method, *Journal of Computational Physics* **314**, 661–681, 2016.

[10] I. Bilionis and N. Zabaras, Bayesian Uncertainty Propagation Using Gaussian Processes, In R. Ghanem, D. Higdon, and H. Owhadi (eds.), *Handbook of Uncertainty Quantification*, pages 1–45, Springer International Publishing, Cham, 2015.

[11] P. Billingsley, *Probability and Measure*, Wiley Series in Probability and Mathematical Statistics, Wiley, New York, 3rd ed Edition, 1995.

[12] C. M. Bishop, *Pattern Recognition and Machine Learning*, Information Science and Statistics, Springer, New York, 2006.

[13] E. V. Bonilla, K. M. Chai, and C. Williams, Multi-task gaussian process prediction, In J. C. Platt, D. Koller, Y. Singer, and S. T. Roweis (eds.), *Advances in Neural Information Processing Systems 20*, pages 153–160, Curran Associates, Inc., 2008.

[14] F. S. Bott and M. W. Gee, A Strong Form Based Moving Kriging Collocation Method for the Numerical Solution of PDEs with Mixed Boundary Conditions, *International Journal for Numerical Methods in Engineering*, 2020.

[15] F. A. Braeu, A. Seitz, R. C. Aydin, and C. J. Cyron, Homogenized constrained mixture models for anisotropic volumetric growth and remodeling, *Biomechanics and Modeling in Mechanobiology* **16**, 889–906, 2017.

[16] L. Bruder and P.-S. Koutsourelakis, BEYOND BLACK-BOXES IN BAYESIAN INVERSE PROBLEMS AND MODEL VALIDATION: APPLICATIONS IN SOLID MECHANICS OF ELASTOGRAPHY, *International Journal for Uncertainty Quantification* **8**, 447–482, 2018.

[17] L. Bruder, B. Reutersberg, M. Bassilious, W. Schüttler, H.-H. Eckstein, and M. W. Gee, Methoden der künstlichen Intelligenz in der vaskulären Medizin: Status quo und Ausblick am Beispiel des AAAs, *Gefässchirurgie* **24**, 539–547, 2019.

[18] L. Bruder, M. W. Gee, and T. Wildey, DATA-CONSISTENT SOLUTIONS TO STOCHASTIC INVERSE PROBLEMS USING A PROBABILISTIC MULTI-FIDELITY METHOD BASED ON CONDITIONAL DENSITIES, *International Journal for Uncertainty Quantification* **10**, 399–424, 2020.

[19] L. Bruder, J. Pelisek, H.-H. Eckstein, and M. W. Gee, Biomechanical rupture risk assessment of abdominal aortic aneurysms using clinical data: A patient-specific, probabilistic framework and comparative case-control study, *PLOS ONE* **15**, e0242097, 2020.

[20] M. Bukač and S. C. Shadden, Quantifying the effects of intraluminal thrombi and their poroelastic properties on abdominal aortic aneurysms, *Archive of Applied Mechanics*, 2021.

[21] T. Butler, J. Jakeman, and T. Wildey, Combining Push-Forward Measures and Bayes' Rule to Construct Consistent Solutions to Stochastic Inverse Problems, *SIAM Journal on Scientific Computing* **40**, A984–A1011, 2018.

[22] T. Butler, J. Jakeman, and T. Wildey, Convergence of Probability Densities Using Approximate Models for Forward and Inverse Problems in Uncertainty Quantification, *SIAM Journal on Scientific Computing* **40**, A3523–A3548, 2018.

[23] T. Butler, J. Jakeman, and T. Wildey, Optimal experimental design for prediction based on push-forward probability measures, *Journal of Computational Physics* **416**, 109518, 2020.

[24] E. L. Chaikof, R. L. Dalman, M. K. Eskandari, B. M. Jackson, W. A. Lee, M. A. Mansour, T. M. Mastracci, M. Mell, M. H. Murad, L. L. Nguyen, G. S. Oderich, M. S. Patel, M. L. Schermerhorn, and B. W. Starnes, The Society for Vascular Surgery practice guidelines on the care of patients with an abdominal aortic aneurysm, *Journal of Vascular Surgery* **67**, 2–77.e2, 2018.

[25] Z. Chen, B. Wang, and A. N. Gorban, Multivariate Gaussian and Student-t process regression for multi-output prediction, *Neural Computing and Applications* **32**, 3005–3028, 2020.

[26] P. G. Constantine, *Active Subspaces: Emerging Ideas for Dimension Reduction in Parameter Studies*, number 2 in SIAM Spotlights, Society for Industrial and Applied Mathematics, Philadelphia, 2015.

[27] P. G. Constantine and P. Diaz, Global sensitivity metrics from active subspaces, *arXiv:1510.04361 [math]*, 2015.

[28] P. G. Constantine, C. Kent, and T. Bui-Thanh, Accelerating Markov Chain Monte Carlo with Active Subspaces, *SIAM Journal on Scientific Computing* **38**, A2779–A2805, 2016.

[29] E. S. Debus, W. Gross-Fengels, A. Mahlmann, E. Muhl, K. Pfister, S. Roth, C. Stroszczynski, N. Weiss, M. Wilhelmi, and R. T. Grundmann, S3-Leitlinie zu Screening, Diagnostik, Therapie und Nachsorge des Bauchaortenaneurysmas, Technical Report 004-14, AWMF, 2018.

[30] B. J. Doyle, N. Bappoo, M. B. Syed, R. O. Forsythe, J. T. Powell, N. Conlisk, P. R. Hoskins, G. R. Joldes, O. M. McBride, A. S. Shah, P. E. Norman, and D. E. Newby, Biomechanical Assessment Predicts Aneurysm Related Events in Patients with Abdominal Aortic Aneurysm, *European Journal of Vascular and Endovascular Surgery*, 2020.

[31] S. Durrleman, P. Fillard, X. Pennec, A. Trouvé, and N. Ayache, Registration, atlas estimation and variability analysis of white matter fiber bundles modeled as currents, *NeuroImage* **55**, 1073–1090, 2011.

[32] M. H. Faber, *Statistics and Probability Theory*, Volume 18 of *Topics in Safety, Risk, Reliability and Quality*, Springer Netherlands, Dordrecht, 2012.

[33] T. Fawcett, An introduction to ROC analysis, *Pattern Recognition Letters* **27**, 861–874, 2006.

[34] M. Fillinger, M. Raghavan, S. Marra, J. Croonenwett, and F. Kennedy, In vivo analysis of mechanical wall stress and abdominal aortic aneurysm rupture risk, *Journal of Vascular Surgery* **36**, 589–597, 2002.

[35] M. Fillinger, S. Marra, M. Raghavan, and F. Kennedy, Prediction of rupture risk in abdominal aortic aneurysm during observation: Wall stress versus diameter, *Journal of Vascular Surgery* **37**, 724–732, 2003.

[36] I. M. Franck and P. Koutsourelakis, Sparse Variational Bayesian approximations for nonlinear inverse problems: Applications in nonlinear elastography, *Computer Methods in Applied Mechanics and Engineering* **299**, 215–244, 2016.

[37] T. C. Gasser, Biomechanical Rupture Risk Assessment: A Consistent and Objective Decision-Making Tool for Abdominal Aortic Aneurysm Patients, *Aorta* **4**, 2016.

[38] T. C. Gasser, The Biomechanical Rupture Risk Assessment of Abdominal Aortic Aneurysms—Method and Clinical Relevance, In P. Wriggers and T. Lenarz (eds.), *Biomedical Technology*, Volume 84, pages 233–253, Springer International Publishing, Cham, 2018.

[39] T. C. Gasser, Modeling the Structural and Mechanical Properties of the Normal and Aneurysmatic Aortic Wall, In Y. Zhang (ed.), *Multi-Scale Extracellular Matrix Mechanics and Mechanobiology*, Volume 23, pages 55–82, Springer International Publishing, Cham, 2020.

[40] T. C. Gasser, R. W. Ogden, and G. A. Holzapfel, Hyperelastic modelling of arterial layers with distributed collagen fibre orientations, *Journal of The Royal Society Interface* **3**, 15–35, 2006.

[41] T. C. Gasser, G. Görgülü, M. Folkesson, and J. Swedenborg, Failure properties of intraluminal thrombus in abdominal aortic aneurysm under static and pulsating mechanical loads, *Journal of Vascular Surgery* **48**, 179–188, 2008.

[42] T. Gasser, M. Auer, F. Labruto, J. Swedenborg, and J. Roy, Biomechanical Rupture Risk Assessment of Abdominal Aortic Aneurysms: Model Complexity versus Predictability of Finite Element Simulations, *European Journal of Vascular and Endovascular Surgery* **40**, 176–185, 2010.

[43] M. W. Gee, C. Förster, and W. A. Wall, A computational strategy for prestressing patient-specific biomechanical problems under finite deformation, *International Journal for Numerical Methods in Biomedical Engineering* **26**, 52–72, 2010.

[44] M. W. Gee, C. T. Kelley, and R. B. Lehoucq, Pseudo-transient continuation for nonlinear transient elasticity, *International Journal for Numerical Methods in Engineering* **78**, 1209–1219, 2009.

[45] M. Gee, M. Sala, C. Siefert, J. Hu, and R. Tuminaro, ML 5.0 Smoothed Aggregation User's Guide, Technical Report SAND2006-2649, Sandia National Laboratories, 2006.

[46] M. Gee, C. Reeps, H. Eckstein, and W. Wall, Prestressing in finite deformation abdominal aortic aneurysm simulation, *Journal of Biomechanics* **42**, 1732–1739, 2009.

[47] O. Ghattas and K. Willcox, Learning physics-based models from data: Perspectives from inverse problems and model reduction, *Acta Numerica* **30**, 445–554, 2021.

[48] S. Giannopoulos, D. G. Kokkinidis, and E. J. Armstrong, Long term outcomes of endovascular vs open surgical repair for abdominal aortic aneurysms: A meta-analysis of randomized trials, *Cardiovascular Revascularization Medicine*, 2020.

[49] M. B. Giles, Multilevel Monte Carlo Path Simulation, *Operations Research* **56**, 607–617, 2008.

[50] M. B. Giles, Multilevel monte carlo methods, *Acta Numerica* **24**, 259–328, 2015.

[51] M. B. Giles, T. Nagapetyan, and K. Ritter, Multilevel Monte Carlo Approximation of Distribution Functions and Densities, *SIAM/ASA Journal on Uncertainty Quantification* **3**, 267–295, 2015.

[52] P. Gori, O. Colliot, L. Marrakchi-Kacem, Y. Worbe, C. Poupon, A. Hartmann, N. Ayache, and S. Durrleman, A Bayesian framework for joint morphometry of surface and curve meshes in multi-object complexes, *Medical Image Analysis* **35**, 458–474, 2017.

[53] R. B. Gramacy and H. K. H. Lee, Adaptive Design and Analysis of Supercomputer Experiments, *Technometrics* **51**, 130–145, 2009.

[54] R. M. Greenhalgh and J. T. Powell, Endovascular Repair of Abdominal Aortic Aneurysm, *New England Journal of Medicine* **358**, 494–501, 2008.

[55] J. M. Guirguis-Blake, T. L. Beil, C. A. Senger, and E. L. Coppola, Primary Care Screening for Abdominal Aortic Aneurysm: Updated Evidence Report and Systematic Review for the US Preventive Services Task Force, *JAMA* **322**, 2219, 2019.

[56] R. Hable, *Einführung in die Stochastik*, Springer-Lehrbuch, Springer Berlin Heidelberg, Berlin, Heidelberg, 2015.

[57] W. K. Hastings, Monte Carlo Sampling Methods Using Markov Chains and Their Applications, *Biometrika* **57**, 97–109, 1970.

[58] A. Hemmler, *In-Silico Endovascular Repair of Abdominal Aortic Aneurysms*, PhD thesis, Technical University of Munich, 2019.

[59] A. Hemmler, B. Lutz, C. Reeps, G. Kalender, and M. W. Gee, A methodology for in silico endovascular repair of abdominal aortic aneurysms, *Biomechanics and Modeling in Mechanobiology* **17**, 1139–1164, 2018.

[60] M. Hirschvogel, *Computational Modeling of Patient-Specific Cardiac Mechanics with Model Reduction-Based Parameter Estimation and Applications to Novel Heart Assist Technologies*, PhD thesis, Technical University of Munich, 2018.

[61] M. D. Hoffman, D. M. Blei, C. Wang, and J. Paisley, Stochastic variational inference, *The Journal of Machine Learning Research* **14**, 1303–1347, 2013.

[62] G. A. Holzapfel, J. A. Niestrawska, R. W. Ogden, A. J. Reinisch, and A. J. Schriefl, Modelling non-symmetric collagen fibre dispersion in arterial walls, *Journal of The Royal Society Interface* **12**, 20150188–20150188, 2015.

[63] G. Holzapfel and R. Ogden, Constitutive modelling of arteries, *Proceedings of the Royal Society A: Mathematical, Physical and Engineering Science* **466**, 1551–1597, 2010.

[64] G. A. Holzapfel, *Nonlinear Solid Mechanics: A Continuum Approach for Engineering*, Wiley, Chichester, New York, 2000.

[65] L. Jagschies, M. Hirschvogel, J. Matallo, A. Maier, K. Mild, H. Brunner, R. Hinkel, M. W. Gee, P. Radermacher, S. M. Wildhirt, and S. Hafner, Individualized Biventricular Epicardial Augmentation Technology in a Drug-Induced Porcine Failing Heart Model, *ASAIO Journal* **64**, 480–488, 2018.

[66] M. I. Jordan, Z. Ghahramani, T. S. Jaakkola, and L. K. Saul, An Introduction to Variational Methods for Graphical Models, *Mach. Learn.* **37**, 183–233, 1999.

[67] J. Kaipio and E. Somersalo, *Statistical and Computational Inverse Problems*, number v. 160 in Applied Mathematical Sciences, Springer, New York, 2005.

[68] S. Kehl, *Bayesian Calibration of Nonlinear Cardiovascular Models for the Predictive Simulation of Arterial Growth*, PhD thesis, Technical University of Munich, 2017.

[69] S. Kehl and M. W. Gee, Calibration of parameters for cardiovascular models with application to arterial growth, *International Journal for Numerical Methods in Biomedical Engineering* **33**, e2822, 2016.

[70] M. C. Kennedy and A. O'Hagan, Predicting the output from a complex computer code when fast approximations are available, *Biometrika* **87**, 1–13, 2000.

[71] J. Kim, B. Peruski, C. Hunley, S. Kwon, and S. Baek, Influence of surrounding tissues on biomechanics of aortic wall, *International Journal of Experimental and Computational Biomechanics* **2**, 105, 2013.

[72] D. P. Kingma and J. Ba, Adam: A Method for Stochastic Optimization, *arXiv:1412.6980 [cs]*, 2017.

[73] D. P. Kingma and M. Welling, Auto-Encoding Variational Bayes, 1–14, 2013.

[74] A. Klenke, *Wahrscheinlichkeitstheorie*, Springer Berlin Heidelberg, Berlin, Heidelberg, 2020.

[75] P.-S. Koutsourelakis, Accurate Uncertainty Quantification Using Inaccurate Computational Models, *SIAM Journal on Scientific Computing* **31**, 3274–3300, 2009.

[76] S. Kullback and R. A. Leibler, On Information and Sufficiency, *The Annals of Mathematical Statistics* **22**, 79–86, 1951.

[77] A. Lee and M. D. Dake, Abdominal and Thoracic Aortic Aneurysms, In N. A. Keefe, Z. J. Haskal, A. W. Park, and J. F. Angle (eds.), *IR Playbook*, pages 197–207, Springer International Publishing, Cham, 2018.

[78] J. H. Leung, A. R. Wright, N. Cheshire, J. Crane, S. A. Thom, A. D. Hughes, and Y. Xu, Fluid structure interaction of patient specific abdominal aortic aneurysms: A comparison with solid stress models, *Biomedical engineering online* **5**, 33, 2006.

[79] B. Li, S. Khan, K. Salata, M. A. Hussain, C. de Mestral, E. Greco, B. A. Aljabri, T. L. Forbes, S. Verma, and M. Al-Omran, A systematic review and meta-analysis of the long-term outcomes of endovascular versus open repair of abdominal aortic aneurysm, *Journal of Vascular Surgery* **70**, 954–969.e30, 2019.

[80] M. Lindquist Liljeqvist, M. Bogdanovic, A. Siika, T. C. Gasser, R. Hultgren, and J. Roy, Geometric and biomechanical modeling aided by machine learning improves the prediction of growth and rupture of small abdominal aortic aneurysms, *Scientific Reports* **11**, 18040, 2021.

[81] C. A. Mader, J. R. R. A. Martins, J. J. Alonso, and E. van der Weide, ADjoint: An Approach for the Rapid Development of Discrete Adjoint Solvers, *AIAA Journal* **46**, 863–873, 2008.

[82] A. Maier, M. W. Gee, C. Reeps, H.-H. Eckstein, and W. A. Wall, Impact of calcifications on patient-specific wall stress analysis of abdominal aortic aneurysms, *Biomechanics and Modeling in Mechanobiology* **9**, 511–521, 2010.

[83] A. Maier, M. W. Gee, C. Reeps, J. Pongratz, H.-H. Eckstein, and W. A. Wall, A Comparison of Diameter, Wall Stress, and Rupture Potential Index for Abdominal Aortic Aneurysm Rupture Risk Prediction, *Annals of Biomedical Engineering* **38**, 3124–3134, 2010.

[84] A. Maier, *Computational Modeling of Rupture Risk in Abdominal Aortic Aneurysms*, Dr. Hut, München, 2013.

[85] V. Man, S. Polzer, T. Gasser, T. Novotny, and J. Bursa, Impact of isotropic constitutive descriptions on the predicted peak wall stress in abdominal aortic aneurysms, *Medical Engineering & Physics* **53**, 49–57, 2018.

[86] M. Matsushita, T. Ikezawa, M. Sugimoto, and A. Idetsu, Management of symptomatic abdominal aortic aneurysms following emergency computed tomography, *Surgery Today* **44**, 620–625, 2014.

[87] E. O. Matthews, J. Pinchbeck, K. Elmore, R. E. Jones, J. V. Moxon, and J. Golledge, The reproducibility of measuring maximum abdominal aortic aneurysm diameter from ultrasound images, *The Ultrasound Journal* **13**, 13, 2021.

[88] N. Metropolis and S. Ulam, The Monte Carlo method, *Journal of the American Statistical Association* **44**, 335–341, 1949.

[89] N. Metropolis, A. W. Rosenbluth, M. N. Rosenbluth, A. H. Teller, and E. Teller, Equation of State Calculations by Fast Computing Machines, *The Journal of Chemical Physics* **21**, 1087–1092, 1953.

[90] P. Miles, Pymcmcstat: A Python Package for Bayesian Inference Using Delayed Rejection Adaptive Metropolis, *Journal of Open Source Software* **4**, 1417, 2019.

[91] A. C. Miller, N. Foti, and R. P. Adams, Variational Boosting: Iteratively Refining Posterior Approximations, 1–21, 2016.

[92] P. Moireau, N. Xiao, M. Astorino, C. A. Figueroa, D. Chapelle, C. A. Taylor, and J.-F. Gerbeau, External tissue support and fluid–structure simulation in blood flows, *Biomechanics and Modeling in Mechanobiology* **11**, 1–18, 2012.

[93] K. P. Murphy, *Machine Learning: A Probabilistic Perspective*, Adaptive Computation and Machine Learning Series, MIT Press, Cambridge, MA, 2012.

[94] R. M. Neal, Annealed Importance Sampling, 125–139, 1998.

[95] E. A. d. S. Neto, D. Perić, M. Dutko, and D. Owen, Design of simple low order finite elements for large strain analysis of nearly incompressible solids, *International Journal of Solids and Structures* **33**, 3277–3296, 1996.

[96] J. I. Ng, T. Nguyen, A. Tarpara, D. Salvatore, P. DiMuzio, and B. Abai, Giant abdominal aortic aneurysms, *Journal of Vascular Surgery Cases, Innovations and Techniques* **7**, 659–664, 2021.

[97] F. Nieto-Palomo, M.-Á. Pérez-Rueda, L.-M. Lipsa, C. Vaquero-Puerta, J.-A. Vilalta-Alonso, G. Vilalta-Alonso, and E. Soudah-Prieto, Statistical techniques for predicting rupture risk in abdominal aortic aneurysms: A contribution based on bootstrap, *Science Progress* **104**, 003685042110037, 2021.

[98] J. Nitzler, J. Biehler, N. Fehn, P.-S. Koutsourelakis, and W. A. Wall, A Generalized Probabilistic Learning Approach for Multi-Fidelity Uncertainty Propagation in Complex Physical Simulations, *arXiv:2001.02892 [cs]*, 2020.

[99] J. Nocedal, Updating quasi-Newton matrices with limited storage, *Mathematics of Computation* **35**, 773–782, 1980.

[100] S. A. O'Leary, J. J. Mulvihill, H. E. Barrett, E. G. Kavanagh, M. T. Walsh, T. M. McGloughlin, and B. J. Doyle, Determining the influence of calcification on the failure properties of abdominal aortic aneurysm (AAA) tissue, *Journal of the Mechanical Behavior of Biomedical Materials* **42**, 154–167, 2015.

[101] J. Oliveira-Pinto, N. Oliveira, F. Bastos-Gonçalves, S. Hoeks, M. J. VAN Rijn, S. Ten Raa, A. Mansilha, and H. J. Verhagen, Long-term results of outside "instructions for use" EVAR, *The Journal of Cardiovascular Surgery* **58**, 252–260, 2017.

[102] V. M.-H. Ong, D. J. Nott, and M. S. Smith, Gaussian variational approximation with a factor covariance structure, *arXiv:1701.03208 [stat]*, 2017.

[103] J. Paisley, D. Blei, and M. Jordan, Variational Bayesian Inference with Stochastic Search, *Icml*, 1367–1374, 2012.

[104] K. I. Paraskevas, H.-H. Eckstein, and F. J. Veith, Prevention and Treatment of Ruptured Abdominal Aortic Aneurysms, *Angiology* **71**, 586–588, 2020.

[105] T. U. S. A. T. Participants, Mortality results for randomised controlled trial of early elective surgery or ultrasonographic surveillance for small abdominal aortic aneurysms, *The Lancet* **352**, 1649–1655, 1998.

[106] B. Peherstorfer, K. Willcox, and M. Gunzburger, Survey of Multifidelity Methods in Uncertainty Propagation, Inference, and Optimization, *SIAM Review* **60**, 550–591, 2018.

[107] S. Polzer and T. C. Gasser, Biomechanical rupture risk assessment of abdominal aortic aneurysms based on a novel probabilistic rupture risk index, *Journal of The Royal Society Interface* **12**, 20150852, 2015.

[108] S. Polzer, T. C. Gasser, B. Markert, J. Bursa, and P. Skacel, Impact of poroelasticity of intraluminal thrombus on wall stress of abdominal aortic aneurysms, *Biomedical engineering online* **11**, 62, 2012.

[109] S. Polzer, T. Christian Gasser, J. Bursa, R. Staffa, R. Vlachovsky, V. Man, and P. Skacel, Importance of material model in wall stress prediction in abdominal aortic aneurysms, *Medical Engineering & Physics* **35**, 1282–1289, 2013.

[110] S. Polzer, T. C. Gasser, R. Vlachovský, L. Kubíček, L. Lambert, V. Man, K. Novák, M. Slažanský, J. Burša, and R. Staffa, Biomechanical indices are more sensitive than diameter in predicting rupture of asymptomatic abdominal aortic aneurysms, *Journal of Vascular Surgery* **71**, 617–626.e6, 2019.

[111] A. Quaglino, S. Pezzuto, P.-S. Koutsourelakis, A. Auricchio, and R. Krause, Fast uncertainty quantification of activation sequences in patient-specific cardiac electrophysiology meeting clinical time constraints, *International Journal for Numerical Methods in Biomedical Engineering*, 2018.

[112] A. Quarteroni, A. Manzoni, and F. Negri, *Reduced Basis Methods for Partial Differential Equations: An Introduction*, number volume 92 in UNITEXT, Springer, Cham ; New York, 2016.

[113] M. L. Raghavan and D. A. Vorp, Toward a biomechanical tool to evaluate rupture potential of abdominal aortic aneurysm: Identification of a finite strain constitutive model and evaluation of its applicability, *Journal of Biomechanics* **33**, 475–482, 2000.

[114] M. L. Raghavan, J. Kratzberg, E. M. Castro de Tolosa, M. M. Hanaoka, P. Walker, and E. S. da Silva, Regional distribution of wall thickness and failure properties of human abdominal aortic aneurysm, *Journal of Biomechanics* **39**, 3010–3016, 2006.

[115] C. E. Rasmussen and Z. Ghahramani, Bayesian Monte Carlo, In *Advances in Neural Information Processing Systems 15 - Proceedings of the 2002 Conference*, Cambridge, MA, 2003, MIT Press.

[116] C. E. Rasmussen and C. K. I. Williams, *Gaussian Processes for Machine Learning*, Adaptive Computation and Machine Learning, MIT Press, Cambridge, Massachusetts, 2006.

[117] C. Reeps, A. Maier, J. Pelisek, F. Härtl, V. Grabher-Meier, W. A. Wall, M. Essler, H.-H. Eckstein, and M. W. Gee, Measuring and modeling patient-specific distributions of material properties in abdominal aortic aneurysm wall, *Biomechanics and Modeling in Mechanobiology* **12**, 717–733, 2013.

[118] A. Reite, K. Søreide, J. T. Kvaløy, and M. Vetrhus, Long-Term Outcomes After Open Repair for Ruptured Abdominal Aortic Aneurysm, *World Journal of Surgery* **44**, 2020–2027, 2020.

[119] B. Rengarajan, S. S. Patnaik, and E. A. Finol, A Predictive Analysis of Wall Stress in Abdominal Aortic Aneurysms Using a Neural Network Model, *Journal of Biomechanical Engineering* **143**, 121004, 2021.

[120] D. J. Rezende, S. Mohamed, and D. Wierstra, Stochastic backpropagation and approximate inference in deep generative models, *Proceedings of The 31st ldots* **32**, 1278–1286, 2014.

[121] H. Robbins and S. Monro, A Stochastic Approximation Method, *The Annals of Mathematical Statistics* **22**, 400–407, 1951.

[122] G. O. Roberts and R. L. Tweedie, Exponential Convergence of Langevin Distributions and Their Discrete Approximations, *Bernoulli* **2**, 341–363, 1996.

[123] Y. Saad and M. H. Schultz, GMRES: A Generalized Minimal Residual Algorithm for Solving Nonsymmetric Linear Systems, *SIAM Journal on Scientific and Statistical Computing* **7**, 856–869, 1986.

[124] J. Sacks, W. J. Welch, T. J. Mitchell, and H. P. Wynn, Design and Analysis of Computer Experiments, *Statistical Science* **4**, 409–423, 1989.

[125] A. Saltelli (ed.), *Global Sensitivity Analysis: The Primer*, John Wiley, Chichester, England ; Hoboken, NJ, 2008.

[126] A. Schein and M. W. Gee, Greedy maximin distance sampling based model order reduction of prestressed and parametrized abdominal aortic aneurysms, *Adv. Model. and Simul. in Eng. Sci.* **8**, 2021.

[127] G. Schurink, J. van Baalen, M. Visser, and J. van Bockel, Thrombus within an aortic aneurysm does not reduce pressure on the aneurysmal wall, *Journal of Vascular Surgery* **31**, 501–506, 2000.

[128] I. Schuster, P. G. Constantine, and T. J. Sullivan, Exact active subspace Metropolis-Hastings, with applications to the Lorenz-96 system, *arXiv:1712.02749 [stat]*, 2017.

[129] R. C. Smith, *Uncertainty Quantification: Theory, Implementation, and Applications*, Computational Science and Engineering Series, Society for Industrial and Applied Mathematics, Philadelphia, 2013.

[130] I. Sobol, *The Monte Carlo Method*, Little Mathematics Library, Mir Publishers, Moscow, 1975.

[131] I. Sobol, Global sensitivity indices for nonlinear mathematical models and their Monte Carlo estimates, *Mathematics and Computers in Simulation* **55**, 271–280, 2001.

[132] K. Spanos, H.-H. Eckstein, and A. D. Giannoukas, Small Abdominal Aortic Aneurysms Are Not All the Same, *Angiology* **71**, 205–207, 2020.

[133] E. B. Tadmor, R. E. Miller, and R. S. Elliott, *Continuum Mechanics and Thermodynamics: From Fundamental Concepts to Governing Equations*, Cambridge University Press, New York, 2012.

[134] M. P. Thon, *Multiphysics Modeling and Quantification of Early Atherosclerosis*, PhD thesis, Technical University of Munich, 2018.

[135] M. K. Titsias and M. Lázaro-Gredilla, Doubly stochastic variational Bayes for non-conjugate inference. ICML, 2014.

[136] M. Trenner, B. Haller, M. Storck, B. Reutersberg, M. Kallmayer, and H.-H. Eckstein, Trends in Patient Safety of Intact Abdominal Aortic Aneurysm Repair: German Registry Data on 36,594 Procedures, *European Journal of Vascular and Endovascular Surgery* **53**, 641–647, 2017.

[137] M. Trenner, B. Reutersberg, M. Salvermoser, H.-H. Eckstein, and A. Kühnl, ”Under The Radar”- Over 35% of Patients Admitted with Ruptured Abdominal Aortic Aneurysm in Germany do not Qualify for Screening, *European Journal of Vascular and Endovascular Surgery* **58**, e654–e655, 2019.

[138] US Preventive Services Task Force, D. K. Owens, K. W. Davidson, A. H. Krist, M. J. Barry, M. Cabana, A. B. Caughey, C. A. Doubeni, J. W. Epling, M. Kubik, C. S. Landefeld, C. M. Mangione, L. Pbert, M. Silverstein, M. A. Simon, C.-W. Tseng, and J. B. Wong, Screening for Abdominal Aortic Aneurysm: US Preventive Services Task Force Recommendation Statement, *JAMA* **322**, 2211, 2019.

[139] J. P. Vande Geest, E. S. Di Martino, A. Bohra, M. S. Makaroun, and D. A. Vorp, A Biomechanics-Based Rupture Potential Index for Abdominal Aortic Aneurysm Risk Assessment: Demonstrative Application, *Annals of the New York Academy of Sciences* **1085**, 11–21, 2006.

[140] J. P. Vande Geest, M. S. Sacks, and D. A. Vorp, A planar biaxial constitutive relation for the luminal layer of intra-luminal thrombus in abdominal aortic aneurysms, *Journal of Biomechanics* **39**, 2347–2354, 2006.

[141] J. P. Vande Geest, D. H. J. Wang, S. R. Wisniewski, M. S. Makaroun, and D. A. Vorp, Towards A Noninvasive Method for Determination of Patient-Specific Wall Strength Distribution in Abdominal Aortic Aneurysms, *Annals of Biomedical Engineering* **34**, 1098–1106, 2006.

[142] B. Vidgen and T. Yasseri, P-Values: Misunderstood and Misused, *Frontiers in Physics* **4**, 2016.

[143] R. Vitásek, D. Gossiho, and S. Polzer, Sources of inconsistency in mean mechanical response of abdominal aortic aneurysm tissue, *Journal of the Mechanical Behavior of Biomedical Materials* **115**, 104274, 2021.

[144] D. A. Vorp, Biomechanics of abdominal aortic aneurysm, *Journal of Biomechanics* **40**, 1887–1902, 2007.

[145] M. J. Wainwright and M. I. Jordan, Graphical Models, Exponential Families, and Variational Inference, *Foundations and Trends® in Machine Learning* **1**, 1–305, 2007.

[146] B. Wang and T. Chen, Gaussian process regression with multiple response variables, *Chemometrics and Intelligent Laboratory Systems* **142**, 159–165, 2015.

[147] D. H. J. Wang, M. Makaroun, M. W. Webster, and D. A. Vorp, Mechanical Properties and Microstructure of Intraluminal Thrombus From Abdominal Aortic Aneurysm, *Journal of Biomechanical Engineering* **123**, 536–539, 2001.

[148] A. Wanhainen, How to Define an Abdominal Aortic Aneurysm — Influence on Epidemiology and Clinical Practice, *Scandinavian Journal of Surgery* **97**, 105–109, 2008.

[149] R. L. Wasserstein and N. A. Lazar, The ASA's Statement on p-Values: Context, Process, and Purpose, *The American Statistician* **70**, 129–133, 2016.

[150] J. S. Wilson, L. Virag, P. Di Achille, I. Karšaj, and J. D. Humphrey, Biochemomechanics of Intraluminal Thrombus in Abdominal Aortic Aneurysms, *Journal of Biomechanical Engineering* **135**, 021011, 2013.

[151] P. Wriggers, *Nichtlineare Finite-Element-Methoden*, Springer Berlin Heidelberg, Berlin, Heidelberg, 2001.